Ice Particle Impact Onto Dry, Wet and Granular Substrates

Experimental Investigation of Ice Impact Phenomena Relevant to Ice Crystal Icing of Aircraft Engines

Zur Erlangung des akademischen Grades Doktor-Ingenieur (Dr.-Ing.)
Genehmigte Dissertation von Louis Maximilian Reitter aus New York, NY
Tag der Einreichung: 18.04.2023, Tag der Prüfung: 28.06.2023

Erstreferentin: Prof. Dr.-Ing. Jeanette Hussong
Korreferent: Apl. Prof. Dr. Ilia Roisman
2. Korreferent: Prof. DPhil David Gillespie
Darmstadt, Technische Universität Darmstadt
Jahr der Veröffentlichung der Dissertation auf TUprints: 2023

TECHNISCHE
UNIVERSITÄT
DARMSTADT

Mechanical Engineering
Department

Ice Particle Impact Onto Dry, Wet and Granular Substrates
Experimental Investigation of Ice Impact Phenomena Relevant to Ice Crystal Icing of Aircraft Engines

Accepted doctoral thesis by Louis Maximilian Reitter

Erstreferentin: Prof. Dr.-Ing. Jeanette Hussong
Korreferent: Apl. Prof. Dr. Ilia Roisman
2. Korreferent: Prof. DPhil David Gillespie

Date of submission: 18.04.2023
Date of thesis defense: 28.06.2023

Darmstadt, Technische Universität Darmstadt
Jahr der Veröffentlichung der Dissertation auf TUprints: 2023

Bitte zitieren Sie dieses Dokument als:
URN: urn:nbn:de:tuda-tuprints-247525
URL: http://tuprints.ulb.tu-darmstadt.de/24752

For my Family

Erklärungen laut Promotionsordnung

§8 Abs. 1 lit. c PromO

Ich versichere hiermit, dass die elektronische Version meiner Dissertation mit der schriftlichen Version übereinstimmt.

§8 Abs. 1 lit. d PromO

Ich versichere hiermit, dass zu einem vorherigen Zeitpunkt noch keine Promotion versucht wurde. In diesem Fall sind nähere Angaben über Zeitpunkt, Hochschule, Dissertationsthema und Ergebnis dieses Versuchs mitzuteilen.

§9 Abs. 1 PromO

Ich versichere hiermit, dass die vorliegende Dissertation selbstständig und nur unter Verwendung der angegebenen Quellen verfasst wurde.

§9 Abs. 2 PromO

Die Arbeit hat bisher noch nicht zu Prüfungszwecken gedient.

Darmstadt, 18.04.2023

Louis

L. M. Reitter

Abstract

Icing of turbofan aircraft engines can occur when aircraft fly through atmospheric conditions with large concentrations of ice crystals. Under such conditions, ice accumulations of substantial thickness can develop inside the engine, causing a blockage of the flow path and reducing engine power. When shedding, the ice accretions impact the downstream engine parts, causing damage and possibly a complete engine shutdown, threatening flight airworthiness and safety. Manufacturers are highly interested in robust numerical tools to predict engine icing. However, various fundamental processes involved in ice crystal icing are not yet completely understood, and thus, the existing numerical tools lack accuracy. The present work is devoted to advancing the understanding of particle impact processes relevant to ice crystal icing. For three topics, separate experimental setups and methodologies are developed, allowing investigation of the involved physical phenomena beyond the state of the art.

Experimental investigations include the impact and fragmentation process of spherical ice particles. A small amount of residual ice fragments adheres to the impact target, which is quantified precisely for the first time. Employing an existing hydrodynamic model, characteristic length scales are proposed to estimate the adhering residual ice mass for sub-freezing target temperatures. Moreover, the size distribution of the fragment cloud is studied, which is of vital importance for several processes involved in engine icing. The obtained distributions are fitted with a power law, enabling a comparison with numerical simulations of generic brittle fracture and ice fracture processes observed on large scales. Furthermore, the ice particle impact onto wetted walls is investigated, focusing on the amount of energy dissipated during the collision. Existing models are modified and combined, explaining the observed low particle rebound velocity with a large dissipation during the plastic deformation of an ice particle. A dynamic strength measurement methodology is designed to investigate the material properties of ice accretions. Ice layers generated in a wind tunnel are studied and compared to artificial ice layers of various compositions generated in a laboratory environment. With the gained knowledge, ice layers with a realistic strength can be generated in the laboratory, enabling dedicated studies on ice layer erosion in the future. In summary, the present work contributes to a deeper understanding of ice particle impact phenomena relevant to aircraft engine icing, which may finally help to improve the accuracy of comprehensive numerical tools.

Zusammenfassung

Die Vereisung von Mantelstromtriebwerken kann auftreten, wenn Flugzeuge durch atmosphärische Bedingungen mit einer hohen Konzentration von Eiskristallen fliegen. Unter solchen Bedingungen können sich im Triebwerk Eisansammlungen von erheblicher Dicke bilden, die den Strömungsquerschnitt einengen und so die Triebwerksleistung verringern. Lösen sich diese Eisansammlungen ab, prallen sie auf stromabwärts gelegenen Triebwerksteile, was zu deren Schäden und sogar zu einer vollständigen Abschaltung des Triebwerks führen kann. Da eine Triebwerksvereisung die Lufttüchtigkeit eines Flugzeugs einschränkt und die Flugsicherheit gefährdet, sind Triebwerkshersteller sehr an robusten numerischen Vorhersagemodellen interessiert. Allerdings sind verschiedene grundlegende Prozesse, die bei der Eiskristallvereisung eine Rolle spielen, noch nicht vollständig verstanden, sodass es vorhandenen numerischen Modellen an Genauigkeit mangelt. Die vorliegende Arbeit widmet sich der Erweiterung des Verständnisses ausgewählter physikalischer Prozesse, die für die Eiskristallvereisung relevant sind. Für drei Themen wurden eigene Versuchsaufbauten und Methoden entwickelt, die es ermöglichen, die involvierten physikalischen Phänomene über den Stand der Technik hinaus zu untersuchen.

Die experimentellen Untersuchungen beinhalten den Aufprall- und Fragmentierungsprozess von kugelförmigen Eispartikeln. Hierbei haftet eine kleine Restmasse an Eisfragmenten an der Aufpralloberfläche, was zum ersten Mal präzise quantifiziert wird. Unter Verwendung eines bestehenden hydrodynamischen Partikelaufprallmodells werden charakteristische Längenskalen für eine Abschätzung der anhaftenden Resteismasse für Oberflächentemperaturen unter dem Gefrierpunkt vorgeschlagen. Daneben wird die Größenverteilung der entstehenden Fragment Wolke analysiert, welche von zentraler Bedeutung für verschiedene Prozesse ist, die bei der Eiskristallvereisung eine Rolle spielen. Ein Potenzgesetz wird an die ermittelten Größenverteilungen angepasst, was einen Vergleich sowohl mit numerischen Ergebnissen generischen Sprödbruchverhaltens als auch mit einer Eisfragmentierung auf großen Längenskalen erlaubt. Darüber hinaus wird der Aufprall von Eispartikeln auf benetzte Wände untersucht, wobei der Schwerpunkt auf der Menge an dissipierter Energie während des Aufprallvorgangs liegt. Bestehende Modelle werden modifiziert und kombiniert, wodurch die beobachtete geringe Rückprallgeschwindigkeit der Partikel mit einer großen Dissipation während der plastischen Verformung eines Eispartikels erklärt werden kann. Zur Untersuchung der Materialeigenschaften von angewachsenen Eisschichten wird eine Methode zur Messung derer dynamischen Festigkeit entwickelt. Eisschichten, die in einem Windkanal erzeugt wurden, wer-

den untersucht und mit künstlichen Eisschichten verschiedener Zusammensetzung verglichen, welche in einem Labor hergestellt wurden. Mit den gewonnenen Erkenntnissen kann die Festigkeit realistischer Eisschichten in einer Laborumgebung nachgebildet werden, was die gezielte Untersuchung von Eisschichterosionsprozessen in Zukunft ermöglicht.

Zusammenfassend lässt sich sagen, dass die vorliegende Arbeit zu einem besseren Verständnis von Eispartikelaufprallphänomenen beiträgt, die für die Vereisung von Flugzeugtriebwerken relevant sind. Dieses kann letztlich dazu beitragen, die Genauigkeit umfassender numerischer Vorhersagemodelle zu verbessern.

Acknowledgements

First of all, I would like to thank **Prof. Dr.-Ing. Cameron Tropea** for the opportunity to start working at the Institute for Fluid Mechanics and Aerodynamics at the Technical University of Darmstadt, and for the advice and supervision regarding my doctoral work. Second, I want to thank **Prof. Dr.-Ing. Jeanette Hussong** for enabling a continuation of my work at the institute, having taken over the supervision of my thesis and helpful discussions. I further want to express my gratitude to **Apl. Prof. Ilia V. Roisman** for reviewing this thesis and for his expertise, which was crucial for understanding the complex physical phenomena encountered during the present work. Additionally, I like to thank **Prof. David Gillespie** for acting as an external reviewer.

I would like to thank all my colleagues from the Institute of Fluid Mechanics and Aerodynamics who always showed great interest in discussing scientific topics during our coffee breaks, which were seldom related to my thesis. In particular, I want to thank **Dr.-Ing. Mark Gloerfeld**, **Dr.-Ing. Markus Schremb** and **Kilian Köbschall** for countless fruitful discussions and assistance whenever necessary, **Maximilian Lausch**, **Till Werner**, **Maximilian Bopp**, **Louis Krüger** and again **Dr.-Ing. Mark Gloerfeld** for their input and proofreading of this work. I thank **Monika Medina** and **Susanne Krüger** for helping with all funding and project management matters. Special thanks go to **Birgit Neuthe**, who solved all other administrative matters as quickly as possible. Furthermore, I would like to thank **Ilona Kaufhold** and the rest of the workshop team for manufacturing countless parts, without which the experiments in this work would not have been possible.

Moreover, I want to thank **Hannes Lohmann**, **Johannes Conrad**, **Max Lausch**, **Lion Oster**, **Mohammad Sämi Sbeitan**, **Andreas Mayrhofer**, **Aaron Jahn**, **Jurica Filipovic**, **Jan Lemmer**, **Manuel Metzger**, **Jonas Rüsch** and **Marius Petry**. The present work would not have been possible without their contribution in the scope of their theses, student projects and as assistants.

I want to gratefully acknowledge the financial support by the European Union Horizon 2020 Research and Innovation Programme under grant agreement No. 767560. It has been a great honour being part of the European research project MUSIC-haic, working with numerous talented people, which are too many to list. Within the project and beyond, it was a pleasure to work with **Norbert Karpen**, **Yasir Malik**, **Dr. Jonathan Connolly** and **Prof. Philippe Villedieu**, with whom I greatly enjoyed participating in project meetings and conferences.

My innermost gratitude belongs to my friends and family, particularly my parents **Barbara** and **Frithjof**, without whom I could not have accomplished everything I achieved so far. I want to thank my grandfather **Helmut**, who has encouraged my scientific curiosity from an early age through numerous radio controlled model aeroplanes built together. Finally, I am incredibly grateful to my fiancée **Sophie** for her continuous support, encouragement and love, not only during the preparation of this work. I dedicate this work to all of them.

Contents

Nomenclature

Acronyms

ANOVA	Analysis of variance
CDF	Cumulative distribution function
COR	Coefficient of restitution
DF	Degrees of freedom
EASA	European Union Aviation Safety Agency
FAA	Federal Aviation Administration
FFD	Full factorial design
ICI	Ice crystal icing
IL	Icing Laboratory
IWT	Icing wind tunnel
KAFTA	Kalman filter tracking algorithm
KS	Kolmogorov-Smirnov
MC	Monte-Carlo simulation
NASA	National Aeronautics and Space Administration
OLS	Ordinary least squares
PDF	Probability density function
PMMA	Polymethylmethacrylate
PSL	Propulsion Systems Laboratory
QLL	Quasi liquid layer
RANSAC	Random sample consensus regressor

RM	Residual mass	
ssE	Sum of squared errors	
TUBS	Technische Universität Braunschweig	
TUDa	Technische Universität Darmstadt	

Greek letters

α	Significance level	–
β	Constant for defining fragmentation mode boundaries	$\mathrm{m^{5/3}\,s^{-1}}$
δ^+	Dimensionless film thickness	–
ϵ	Pore filling ratio	–
Γ	Adjusted goodness-of-fit statistic	–
γ_s	Surface tension	$\mathrm{kg\,s^{-2}}$
ν	Poisson ratio	–
Φ	Dissipation function	$\mathrm{kg\,m^{-1}\,s^{-3}}$
Ψ	Power-law exponent	–
ψ	Porosity	–
σ_c	Critical stress for crack propagation	$\mathrm{kg\,m^{-1}\,s^{-2}}$
Θ	Elasticity parameter	–
ε	Fragment size threshold value	m
ς	Scale factor	–
ϑ	Thermal effusivity	$\mathrm{J\,K^{-1}\,m^{-2}\,s^{-1/2}}$
Ξ	Auxiliary variable	–

Latin letters

A	Area	$\mathrm{m^2}$
b_spread	Scaling factor for liquid drop spreading	–
Bn	Modified Bingham number	–
c	Speed of sound	$\mathrm{m\,s^{-1}}$

c_p	Isobaric heat capacity of ice	$\mathrm{m^2\,s^{-2}\,K^{-1}}$
Ca	Capillary number	–
D	Fractal dimension	–
d	Diameter	m
$\hat{D}$	Scaling exponent	–
$\overline{d}$	Estimated, volume equivalent diameter	m
$d_{\mathrm{f,max}}$	Maximum feret diameter	m
$d_{\mathrm{f,min}}$	Minimum feret diameter	m
d_{lam}	Lamella spreading diameter	m
E	Modulus of elasticity	$\mathrm{kg\,m^{-1}\,s^{-2}}$
e	Coefficient of restitution	–
E^*	Effective modulus of elasticity	$\mathrm{kg\,m^{-1}\,s^{-2}}$
$\mathcal{F}$	Generic function	–
$F(x)$	Cumulative distribution function of a doubly-truncated, power-law	–
$f(x)$	Probability density function of a doubly-truncated, power-law	–
F_{t}^{-1}	Inverse CDF of the Student's t-distribution	–
h	Film thickness	m
IWC	Ice water content	$\mathrm{g\,m^{-3}}$
k	Empirical constant	
l	Length descriptor	m
L, G	Auxiliary variables	–
LWC	Liquid water content	$\mathrm{g\,m^{-3}}$
M	Number of Monte-Carlo simulations	–
m	Mass	kg
$\mathcal{M}$	Characteristic shape parameter	–
$\overline{m_{\mathrm{RM}}}$	Transformed value of the residual mass	–

m_{RM}^{+}	Residual mass scaled with the initial particle mass	–
$n(>\varepsilon)$	Cumulative number of fragments larger than a threshold	–
p_{st}	p-value for significance testing	–
q_{diss}	Heat per unit volume produced through dissipation	$\mathrm{kg\,m^{-1}\,s^{-2}}$
R	Roundness	–
$\mathcal{R}$	Universal gas constant	$\mathrm{J\,mol^{-1}\,K^{-1}}$
Re	Reynolds number	–
S	Sphericity	–
s_{-}, s_{+}	Lower and upper bound for truncated dataset	–
St	Stokes number	–
T	Temperature	°C
t	Time	s
$\boldsymbol{T}$	Transformation matrix	–
ΔT	Temperature increment due to dissipative heating	K
t^{*}	Characteristic duration of a pressure pulse during a Hertz impact	s
t_1	Characteristic relaxation time	s
V	Volume	$\mathrm{m^3}$
$\hat{V}_{\mathrm{f}}$	Relative fragment volume of a synthetic volume distribution	–
$\overline{V}$	Estimated volume	$\mathrm{m^3}$
$\tilde{V}$	Relative volume	–
v_1	Particle velocity after impact	$\mathrm{m\,s^{-1}}$
We	Weber number	–
x_0	Characteristic particle - wall distance	m
Z	Cumulative, adjusted goodness-of-fit statistic	–
$\mathcal{U}$	Energy	$\mathrm{kg\,m^2\,s^{-2}}$

Subscripts

Al	Aluminium
char	Characteristic
co	Container
c	Critical
f	Fragment
lam	Lamella
l	Liquid
max	Maximum
min	Minimum
n	Normal
px	Pixel
p	Particle
qe	Quasi-elastic
RM	Residual mass
tg	Tangential
t	Target
w	Wetted

List of Figures

List of Tables

1 Introduction

Ice formation is a fascinating phenomenon that can be observed on multiple occasions in nature. Ice crystals and snow exist in a plethora of complex shapes (Libbrecht, 2005; Kikuchi et al., 2013; Grazioli et al., 2022) and their growth dynamics are still subject to active research (Libbrecht, 2019; Tan et al., 2022). While natural snow precipitation may be welcomed and even assisted by artificial snow production in winter sports regions, the formation of ice is in general more likely to impede every-day life. Ice accumulation can reduce the performance of engineering structures and applications or lead to their damage and failure. Adverse encounters with ice comprise icing of roads and bridges (Terry et al., 2020; Nasr et al., 2021), icing and possible collapse of power lines (Zhao et al., 2022; Farzaneh et al., 2022) and performance degradation of wind turbines (Jasinski et al., 1998; Caccia et al., 2023). Further hazards arise when transportation systems are affected by icing, comprising ice on automotive wind shields (Ene et al., 2021), saline water spray icing of ships (Makkonen, 1987; Ryerson et al., 2000; Samuelsen, 2018), and aircraft icing (Cao et al., 2018). A specific manifestation of aircraft icing is the performance degradation, damage and failure of aircraft engines and heated probes (Mason et al., 2006; Jäckel et al., 2021; Tetteh et al., 2022). Thus, the motivation for the present work is to enhance the current understanding of aircraft engine icing, since the involved physical processes are not yet completely understood.

Ice accumulation on solid structures can be caused by different physical processes, starting with water in the vapour, liquid or solid phase. Vapour re-sublimation on cold substrates (frost formation) is encountered in refrigerators or heat exchangers of various cooling systems (Anisimov et al., 2015; Koszut et al., 2022). In this case, the ice forms an insulating layer, reducing the heat exchanger efficiency. Severe weather conditions can lead to ice accretion caused by freezing of supercooled liquid water in the form of impinging atmospheric drops. In theory, supercooled water can exist at temperatures down to approximately $-40\,^{\circ}\mathrm{C}$ (Langham et al., 1958; Franks, 2003), which can start freezing spontaneously or when brought in contact with foreign substances. In this process, fine dendritic ice structures grow in the liquid fast, which has been studied in detail in recent works of Schremb (2018) and Gloerfeld (2022). These mechanisms play a crucial role in supercooled drop icing of aircraft, which is a threat to their flight safety (Cao et al., 2018). Ice accretion on aircraft surfaces can negatively affect their flight characteristics in multiple ways. They add weight and can change the aircraft flight stability and controllability (Ide et al., 1986). Furthermore, the change of the profile shape of an aircraft wing or helicopter blade modifies their aerodynamic behaviour, leading to increased drag and reduced lift (Cao et al., 2010; Cao et al., 2015).

A different mechanism dominates the ice formation inside aircraft engines or heated measurement probes. Here, icing is caused by a mix of solid and liquid water (mixed phase icing) or exclusively by atmospheric ice crystals, which is termed *ice crystal icing* (ICI). This problem gained attention during the 1990s since a number of high bypass ratio turbofan engines experienced powerloss events in atmospheric conditions where ice particles were present but not liquid water drops. Hence, Lawson et al. (1998) hypothesised that ice layers inside the engine core originate from ice crystals and it was conclusively reasoned to perturb the engine operation by Mason et al. (2006), who analysed a large database of engine events now attributed to ICI. Thereafter, fundamental research on ICI began and is still ongoing today. The present work is a part of this research effort on ICI and aims at enhancing the understanding of the involved micro-physical processes, namely the ice particle impact onto dry, wet and granular substrates.

1.1 Motivation and Background

Ice accretion inside of a turbofan engine can lead to multiple problems comprising damage of compressor blades, compressor stall and surge, a substantial, uncommanded thrust reduction (rollback) or a flameout of the combustion chamber. In the present section, a short overview is given about the hazards of ICI, the necessary environmental conditions for it to occur and the relevant physical mechanisms involved. For a more extensive, recent review, the reader is referred to Tetteh et al. (2022).

Vast knowledge of ICI has been gained by performing multiple full-scale engine icing tests with a heavily instrumented, geared turbofan ALF502 engine, which has experienced multiple ICI events. The engine was installed in the NASA Propulsion Systems Laboratory (PSL), which is capable of simulating ICI conditions (Goodwin et al., 2014; Oliver, 2014; Flegel, 2021). In an early test, Oliver (2014) showed that engine rollback events, previously documented in a flight test campaign, could be successfully reproduced at NASA PSL. Thereafter, multiple tests have been performed, aimed at expanding the knowledge of fundamental ICI physics. In Fig. 1.1, the flow path inside the ALF502 engine is illustrated, auxiliary to the discussion of the possibly encountered engine problems during ICI. The regions inside the engine which are affected by ICI are indicated with red dashed boxes. Furthermore, rotating and stationary engine parts are highlighted with different colours. It has been found that generally, the regions in a turbofan engine susceptible to ICI include the low pressure compressor and the region between it and the high pressure compressor. Furthermore, it is more likely for ice to accrete in areas behind stationary components, from where accretions may shed and impact downstream on the high pressure compressor blades (Tetteh et al., 2022). In order to visualise ICI in a

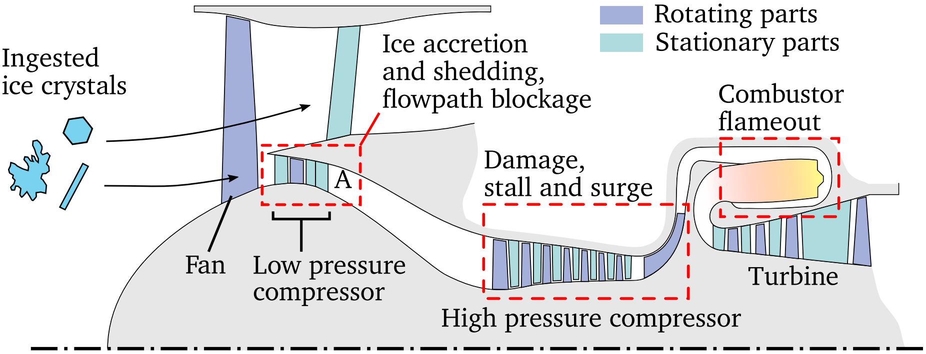

Figure 1.1: Sketch of the flowpath inside an ALF502 engine adapted from Goodwin et al. (2014). The rotational and stationary parts are highlighted with different colours. Regions where ICI induced phenomena are encountered are indicated with red dashed boxes. Video recordings of ice accretions developing at the point A were taken during tests at NASA PSL.

realistic engine environment, Goodwin et al. (2016) installed a video camera in the ALF502 engine, directed at a region directly behind the low pressure compressor outlet guide vanes, indicated by the letter *A* in Fig. 1.1. Two images taken during an ICI test at NASA PSL are shown in Fig. 1.2. In both images, ice accretion of substantial extent is visible, which continuously grows and sheds later on, representing a realistic ICI scenario. The left image in Fig. 1.2 is taken shortly after starting the

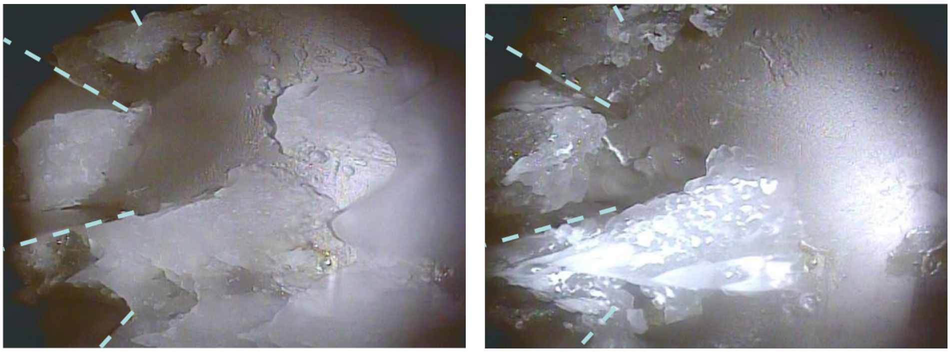

Figure 1.2: Images of macroscopic ice accretions located behind the low pressure compressor outlet guide vane of an ALF502 engine (Tsao, 2017). The images are rotated by 180° leading to the airflow coming from the left side. The trailing edges of the guide vanes are highlighted with blue dashed lines.

ice crystal ingestion, while the right image corresponds to a later instance in time, where the engine thrust has reduced to approximately half of its initial value (Tsao, 2017). Next to rollback events, ice accretion on low pressure compressor blades and damage of high pressure compressor blades was observed in earlier tests of Oliver (2014), as shown in Fig. 1.3. Apart from causing impact damage, ice accretion leads to a blockage of the compressor flow path. This can result in flow separation and thus, a departure from the compressor aerodynamic design point. In extreme cases, this can lead to compressor stall or surge. The latter occurs after enough compressor blades have experienced flow separation (stall), leading to a momentary reverse of the airflow direction. This phenomenon is highly damaging to multiple parts of the engine, possibly rendering it inoperable (Bräunling, 2009). Engine rollback, a substantial, uncommanded thrust reduction, possibly occurs when the compressor experiences a continuous flow path blockage during ICI, as shown in Fig. 1.2. Such an event starts with a reduced pressure build-up in the compressor and reduced airflow to the combustor. As a result, the turbine exit temperature tends to increase, which is ultimately prevented by the engine control unit by decreasing the fuel flow (Tetteh et al., 2022). Hence, the turbine power decreases along with the rotational speed (N1) of the shaft, which is connected to the fan, leading to a reduced engine thrust (Goodwin et al., 2014).

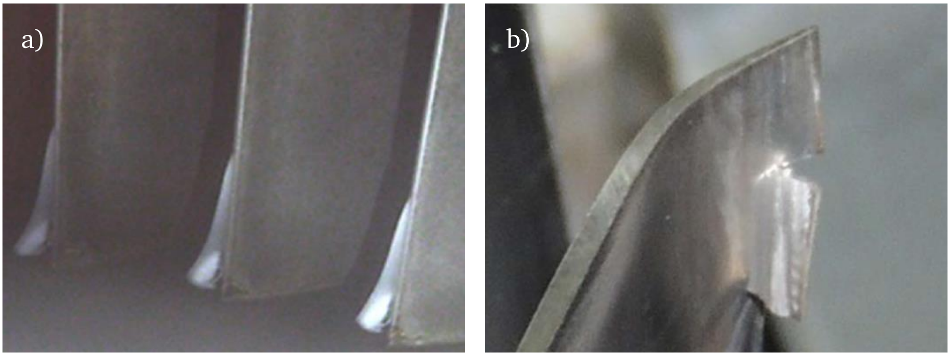

Figure 1.3: Ice accretion on the low pressure compressor inlet guide vane a), and mechanical damage of a high pressure compressor blade after an ice crystal icing test b) (Oliver, 2014).

In the most extreme case, ice accretion and shedding can lead to a flameout of the combustion chamber. In this case, an unwanted decrease of the air to fuel ratio occurs to such an extent, that stable combustion can no longer be maintained (Tetteh et al., 2022). Fuel rich conditions can be caused by a reduced air flow due to flowpath blockage. Additionally, ice in the flowpath can cause the combustor temperature to drop, which in turn causes the engine control unit to inject more fuel in order to raise the temperature, which again leads to fuel rich conditions and a possible flameout. In an extreme case, the pilots of a Raytheon Beechjet 400 experienced an ICI induced flameout of both engines in 2005 (Lacagnina, 2008). The incident occurred after the engine power was reduced while flying at a high altitude in ICI conditions. The pilots could not restart either engine and had to perform a landing without engine power. Fortunately, no harm was done to the crew in this case. Concluding, ICI can lead to damage of compressor blades, compressor stall and surge, engine rollback or combustor flameout, threatening flight airworthiness and safety when they are operated in ICI conditions.

Meteorological Conditions Leading to Ice Crystal Icing Ice crystal icing tends to occur in meteorological conditions near tropical convective systems, where larger mass concentrations of ice particles are present up to high altitudes (Bravin et al., 2015; Haggerty et al., 2019). The intensity of these convective systems varies both seasonally and longitudinally as presented in more detail by Grzych et al. (2010a). An extensive report on ice crystal concentration and their size distributions depending on the ambient conditions is given by Strapp et al. (2021). After analysing a large database of engine events attributed to ICI, Bravin et al. (2015) discuss certain similarities in the prevalent meteorological conditions: ICI events occur between the latitudes of 32°S and 52°N, occurring at typical altitudes above 22 000 ft (6.7 km) and up to 45 000 ft (13.7 km). The possible flight altitudes and ambient temperatures for ICI to occur have been summarised in the FAA (Federal Aviation Administration) and identical EASA (European Aviation Safety Agency) regulations concerning ICI (FAA, 2014; EASA, 2015). Therein, the flight altitudes and ambient temperatures are given as envelopes, which are illustrated in Fig. 1.4. Besides the

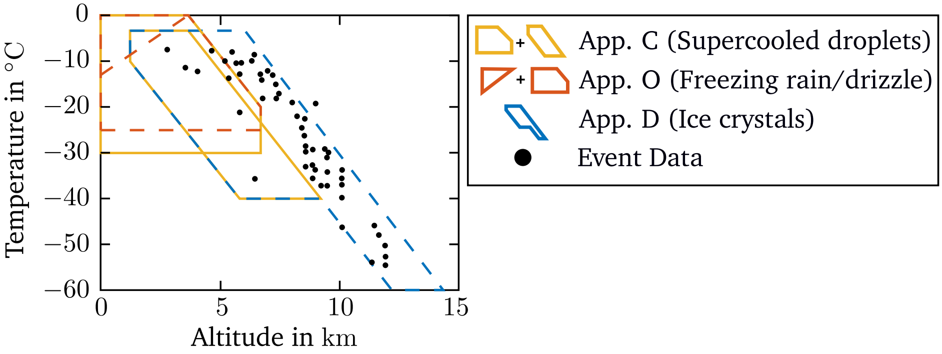

Figure 1.4: FAA and EASA icing envelopes with selected engine events, adapted from Tetteh et al. (2022). Included are FAA part 33, appendix D and the identical EASA CS 25 book 1 appendix P (ice crystal icing), FAA part 25, appendix C (freezing drizzle and rain) and FAA part 25, appendix O (supercooled droplets) (FAA, 2014; EASA, 2015).

envelope for ICI (blue line), the envelopes for freezing drizzle and rain (red lines), as well as supercooled drops (yellow lines), are included for a reference. As visible in Fig. 1.4, ICI conditions can be encountered at lower temperatures and significantly higher altitudes compared to liquid drop icing conditions. In general, it is harder to identify them from a pilot's perspective. The problem is that small ice crystals have a low radar reflectivity and are thus less visible on the aircraft weather radar. In Fig. 1.5, an encounter with a typical convective system is shown, with different levels of weather radar reflectivity indicated as coloured regions. Judging only from the radar data, overflying the highly reflective regions would be acceptable to avoid adverse weather effects. While maintaining the current altitude, heavy rain conditions corresponding to the highly reflective regions can be overflown. However, a large concentration of ice crystals would be encountered in this scenario, possibly leading to ICI. Additionally, an early identification of present ICI conditions is more difficult in contrast to supercooled drop icing, where ice formation on the airframe is visible. When ICI induced engine vibrations or a rollback are observed, substantial amounts of ice have already formed inside the engine. However, some phenomena can aid in identifying ICI conditions including the presence of electrostatic discharges (St.Elmo's Fire), an increase in flight deck temperature or humidity, an ozone-like odour in the flight deck during flight through the cloud, observation of liquid water on the windscreen caused by melting ice crystals or abnormal readings of an iced total air temperature probe (Bravin et al., 2015). Nevertheless, it is usually advised to totally avoid ICI conditions in the first place (Grzych, 2010b; Marconnet et al., 2016). In some cases, even specific restrictions have been issued like in 2013 for Boeing 747-8 and 787 aircraft, equipped with GEnx engines (Trimble, 2013). These aircraft were advised to stay clear of high altitude convective weather by 50 nautical

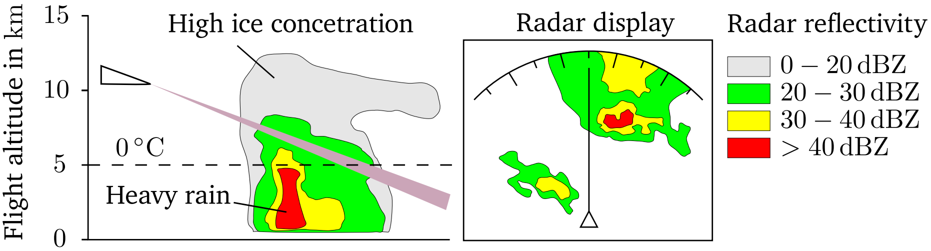

Figure 1.5: Conceptualized flight encounter with a strong convective system, alongside a typical aircraft weather radar display adapted from Strapp et al. (2016). Very low, low, medium and high levels of radar reflectivity are indicated as grey, green, yellow and red regions, respectively. Next to the green regions, the grey regions with very low radar reflectivity may contain large concentrations of ice crystals. The grey regions are usually not displayed in the pilots' radar display.

miles until the identified ICI issue was addressed. Concluding, ICI conditions can be encountered at high altitudes and low temperatures. From a pilot's perspective, these conditions are not as easily detectable as liquid icing conditions and demand special awareness. Even recently developed aircraft engines can be affected by ICI problems, illustrating the fact that ICI, being a complex problem involving multiple physical phenomena, is still not completely understood.

Physical Phenomena Involved in Ice Crystal Icing Ice crystal icing begins with the ingestion of ice particles present in the atmosphere and finally arrives at the formation of macroscopic ice agglomerations that accrete and shed inside of the engine core. In the present section, an overview of the relevant physical mechanisms is given and the specific phenomena are highlighted, which are investigated in the present work. In an ICI scenario, a mixture of water drops and ice particles or purely ice particles are ingested into the engine core, interacting with the engine surfaces and its internal gas flow. The concentration of ingested ice particles is quantified in ice water content (IWC), which is the mass of ice per volume of air. Correspondingly, the liquid water content (LWC) specifies the mass of liquid water per volume of air. Both variables add up to the total water content (TWC). Multiple circumstances have been identified that favour ice accretions at a specific location inside an engine as summarized by Tetteh et al. (2022), namely

- liquid water present at a substrate to initiate ice particle capture,
- a wet-bulb temperature[1] T_{wb} close to the freezing point,
- a melt ratio (LWC/TWC) in a characteristic range ($\approx 5\% - 25\%$)
- a sufficiently high TWC to initially cool down warm substrates to the melting temperature and
- small enough ice particles, that rather stick to an ice accretion than erode it for a given impact velocity.

ICI is a dynamic, multi-physics problem in which various parameters are closely coupled. In the following, important mechanisms and the corresponding parameters are elucidated. For a more detailed review, the reader is referred to Tetteh et al. (2022) and the references therein.

Ice particles experience a specific wet-bulb temperature history as they traverse the engine, possibly leading to a characteristic melt ratio LWC/TWC at an ice accretion site. At this location, the ice agglomeration is continuously subjected to the local wet-bulb temperature. Since the parameters humidity, pressure and temperature all affect the wet-bulb temperature, the coupling of multiple phenomena is already

---

[1] The wet-bulb temperature is defined as the temperature of an adiabatic, wet substrate in an airflow. It captures the evaporative cooling potential of the airflow and depends on the air temperature, humidity and the ambient pressure.

evident. All these parameters depend on the ambient flight conditions and the engine operating point. Furthermore, the wet-bulb temperature can vary across an aerodynamic surface in a compressible airflow. At the stagnation point of an object, the static temperature and thus, the wet-bulb temperature can be above freezing. When the air accelerates next to the stagnation point, the static temperature drops, possibly leading to a sub-freezing wet-bulb temperature. This phenomenon was observed by (Currie et al., 2016) on a hemispherical test article in an icing wind tunnel. During their investigation, well adhering ice accretions were produced due to the transition of the surface wet-bulb temperature from above freezing to sub freezing, anchoring the ice accretions.
Additionally, the local ice particle size distribution has a vital impact on multiple phenomena involved in ICI. The ice particle size influences its trajectory, since smaller ice particles tend to follow streamlines of the airflow more readily. Due to particle centrifuging effects, the total TWC can have local maxima in the engine flow path. The particle melting rate, which controls the local melt ratio LWC/TWC, is also affected by the particle size, since smaller particles melt faster. In addition, larger ice particles are observed to rather erode an ice layer than stick to it, illustrating another effect of the ice particle size. The local ice particle size distribution is a function of icing cloud particle size distribution, characterized in multiple flight campaigns as summarized by Strapp et al. (2021). Inside the engine, this size distribution is modified as the ice particles impact onto stationary and rotating engine parts and fragment to smaller particles. A graphic overview of the main phenomena involved in ICI is presented in Fig. 1.6. The present work explicitly

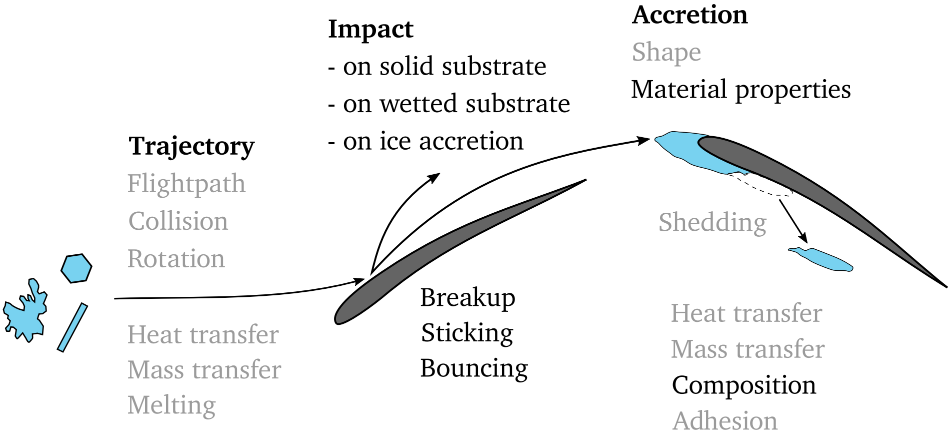

Figure 1.6: Overview of the physical mechanisms involved in ice crystal icing adapted from Kintea (2016). The mechanisms addressed in the present work are labelled in black, while mechanisms exceeding this work are labelled in grey.

addresses processes labelled in black, while mechanisms exceeding this work are labelled in grey. Some of the latter have been studied recently by (Kintea, 2016; Hauk, 2016; Baumert, 2019; Charton, 2020) on a fundamental level. The present thesis is devoted to advancing the knowledge of ice particle impact processes, since they are not completely understood yet and are of vital importance in a physical description of ICI. Ultimately, the findings can be used to improve existing numerical codes dedicated to ice accretion inside aircraft engines, like the ones developed by ONERA (Trontin et al., 2017; Refloch et al., 2011). Ice particle impact processes control the evolution of the particle size distribution in an engine which in turn is coupled with multiple processes comprising the particle trajectory evolution, their melting rates, sticking ability to wetted substrates and erosion ability of ice accretions.

One of the physical phenomena occurring first in an ICI scenario is the impact of atmospheric ice crystals on the engine casing, spinner and fan. Depending mainly on its diameter and impact velocity, an impacting ice particle may stay intact or break up into fragments of varying sizes. The combined effect of multiple parameters comprising the particle impact velocity, diameter, temperature and target temperature on the shape of the resulting fragment size distribution is still not completely understood. Thus, the fragment size distribution after a particle impact is studied experimentally within the present thesis, while systematically varying the aforementioned parameters. The diameters of the investigated ice particles are limited to a size of millimetres to obtain fragment size data with a given camera resolution, while the ice particle diameters in an ICI scenario vary from millimetres to tenths of micrometres (Tetteh et al., 2022). However, the comparability of the present results to an ICI scenario is supported by literature, suggesting that fragment size properties can be scaled with a characteristic strain rate during particle impact (Senoner et al., 2022). Furthermore, it is discussed in the present work that some processes involved in ice fragmentation may be scale invariant (Weiss, 2001), supporting comparability between the present results and an ICI scenario.

At the location inside an engine which is susceptible to ice accretion, ice particle fragments are impacting onto stationary substrates wetted with a water film. During impact, forces exerted by the fluid may lead to ice particle capture, initiating the formation of macroscopic ice agglomerations. The dynamic phenomena involved in a possible ice particle capturing process are complex and are another subject of the current investigations. Especially the material response of ice during this process is not yet understood, which is why ice particle impact experiments onto a wetted substrate are performed in the present thesis.

After the inception of ice accretion, heat transfer between ice particles, the liquid film and the corresponding engine surface eventually leads to the formation of a porous structure consisting of ice crystals wetted with meltwater. Further sticking of ice particles, and layer erosion due to impinging ice particles are affected by the ice layer composition and its material properties. However, information about a realistic ice layer composition and especially its material properties is lacking. Thus,

a dynamic ice layer strength testing method is developed in the present work and applied to different ice layers of varying composition to gather knowledge about their material properties.
Concluding, the physical processes related to ice particle impacts onto dry, wet surfaces and ice accretions are not yet completely understood and are thus investigated in the present thesis.

1.2 Thesis Outline

The outline of the present work follows three selected sequential physical processes an ice particle possibly encounters in an aero-engine icing scenario: First, the ice particle fragmentation after impact onto a **dry substrate**. After ingestion in the engine core, ice particle fragments may be captured after impact onto a **wet substrate**. Finally, impact phenomena on **granular ice layers** control the growth rate of ice accretion inside the engine core.

The present thesis is structured in four main parts, following this introduction.

Chapter 2 elucidates the theoretical background necessary for the discussion of the obtained experimental results. Theoretical concepts are outlined describing solid-solid collision phenomena for increasing impact velocities. Modelling efforts from the literature are discussed, especially for ice particle impacts on dry and wet substrates. Additionally, current literature is reviewed, highlighting evident research gaps.

Chapter 3 is devoted to the experimental setups and methodologies used for conducting the experiments in the present work. It is subdivided into three parts, corresponding to the three investigated impact scenarios.

Chapter 4 builds the main focus of the present work, comprising the experimental results for the three investigated phenomena. A mass of fragments adhering to the target after an ice particle impact onto a dry substrate is quantified and the shape of the fragment volume distribution is measured. Moreover, the ratio between the ice particle rebound and impact velocity is studied for impacts onto a wetted substrate. Additionally, for granular ice layers, the crater formation after impact is investigated.

Chapter 5 completes the present work with a summary and conclusion of the present experimental study. The most relevant findings are highlighted and an outlook is given, identifying open questions which can be addressed in future work of fundamental ice crystal icing studies.

2 Theoretical Background and State of the Art

Aircraft engine icing is rich in different physical phenomena combining various fields of research, namely structural dynamics and hydro- as well as thermodynamics. Despite recent advances in understanding aircraft engine icing, a detailed description of all involved physical processes is still lacking. Since an experimental investigation of ice particle impact phenomena is the focus of the present work, the following sections summarize the fundamentals and state of the art of the interaction of an ice particle with dry, wet and granular substrates.

Impact phenomena of solid materials in general are of interest in multiple areas of research. In planetary science, recent high-resolution simulations suggest that the Moon is formed in the timescale of hours after the early Earth was hit by a Mars size impactor, in contrast to a hypothesised formation process over months or years (Tavares, 2022; Kegerreis et al., 2022). On a small length scale, the formation of protoplanets is determined by repeated collisions and accretion of small, rigid bodies, including those made of ice. Hence, ice particle collisions with varying particle size, relative impact velocity and temperature have been investigated to study the mechanisms involved in the formation of planets (Higa et al., 1996; Yasui et al., 2014; Heißelmann et al., 2010; Shimaki et al., 2012; Uenishi et al., 2019; Uenishi et al., 2018). Just a few other examples for the relevance of studying solid collision phenomena include energy efficient particle breakage in different industries (Tavares, 2007; Cleary et al., 2008), improvement of material performance due to impact induced work hardening of surfaces (Hessert et al., 2008; Bagherifard, 2019), mechanical alloying processes e.g. creation of amorphous metal powders by ball milling (Koch et al., 1992; Weeber et al., 1988) or impact induced redirection of asteroid trajectories (Sarli et al., 2017; Nakano et al., 2022).

For the present work, collision phenomena of ice in the context of aeronautical science are of interest, specifically in the framework of ice crystal icing. Henceforth, the word *ice* is used for the hexagonal configuration of ice at ordinary pressures and temperatures in atmospheric conditions, termed ice Ih. In the following, the main occurring physical mechanisms during ice particle impact are presented as fundamentals for the discussion of the obtained experimental results.

2.1 Ice Particle Impact Onto a Dry Substrate

For the theoretical description of an ice particle impact onto dry surfaces, the ice particle is assumed to be spherical and impacting onto a wall considered as an infinite half-space. The collision is characterized by the particle diameter d_p, impact velocity v_p and impact angle relative to the surface. No rotational motion of the particle is considered and the particle and target surfaces are assumed to be perfectly smooth. The main particle and wall material properties affecting the collision dynamics are their density ρ, Elastic modulus E, Poisson's ratio ν and tensile and compressive strength. The ice material response to deformation is rather complex as reviewed in e.g. Schulson et al. (2009) or Petrenko et al. (1999). With an increasing deformation rate, single crystal ice under compression transitions from ductile to brittle behaviour at a strain rate threshold between $10^{-4} < \dot{\gamma} < 10^{-3}$ (Schulson et al., 2009, p. 239). Furthermore, ice exhibits a strain rate dependent brittle tensile strength and temperature and strain rate dependent compressive strength (Schulson et al., 2009).

The involved physical phenomena during the impact of spherical particles are reviewed in e.g. Johnson (1985) or Antonyuk et al. (2010) and the mechanisms relevant for the present work are introduced in the following. In order to classify the present investigated ice particle impact in the context of other studies, two characteristic scales are discussed. Firstly, it is of interest whether the particle deformation can be treated quasi-statically or whether the propagation of elastic waves in the materials has to be considered in the energy balance during a particle impact. Using the analysis of Hunter (1957), Johnson (1985, p. 354) utilises a ratio of two characteristic time scales to verify the assumption of a quasi-static deformation. Similarly, the concept is also applied by Higa et al. (1998) for the special case of ice-on-ice impacts, which is closely related to the present work. The dynamic response of the materials during impact is found to be approximated well with a system of a spring in parallel to a viscous damper. The energy absorbed by the viscous damper corresponds to the energy radiated away by elastic wave motion. For this spring-damper system, a relaxation time t_1 is derived. A ratio between t_1 and the duration of a pressure pulse applied to the material is used to check the assumption of a quasi-static response. For a Hertz impact (Hertz, 1882), this ratio can be expressed as (Johnson, 1985, p.354)

$$\frac{t_1}{t^*} \approx 0.3 \left(\frac{v_\mathrm{p}}{c}\right)^{3/5}, \tag{2.1}$$

where t^* is the characteristic duration of the pressure pulse and c is the longitudinal wave speed in the material. If the ratio t_1/t^* is small, the force variation during impact will be largely controlled by the spring and not the damper and thus, the material response can be considered quasi-statical to a good approximation. In this case, a negligible amount of elastic energy is radiated away from the impact point due to elastic wave motion. In the present experiments, the maximum impact velocity is

$v_\mathrm{p} \approx 80\,\mathrm{m\,s^{-1}}$ and with the speed of sound in ice at $T = -5\,^\circ\mathrm{C}$ of $c = 3850\,\mathrm{m\,s^{-1}}$ (Vogt et al., 2008), a value of $t_1/t^* \approx 0.03$ is obtained. Since the ratio t_1/t^* is small, quasi-static approximations are justified. A second dimensionless scale, a modified Bingham number, as introduced in Yarin et al. (2017, p.7), determines different regimes of the impact behaviour of solids (Johnson, 1985),

$$\mathrm{Bn}^{-1} = \frac{\rho v_\mathrm{p}^2}{Y} \tag{2.2}$$

where Y is the yield strength. For comparability to other works, the inverse modified Bingham number Bn^{-1} is discussed in the following, characterising the relation between inertia and plastic stresses in deforming bodies. For very small values of Bn^{-1}, the collision is considered completely elastic. From Hertzian impact theory, a critical value of the onset of plastic deformation can be derived, leading to a critical velocity $v_\mathrm{c} \propto Y^{5/2}\rho^{-1/2}E^{-2}$ (Johnson, 1985). Following the argument of Roisman (2022), this critical velocity is exceeded in most cases relevant to ice particle impacts in aeronautical applications, due to its rather low value for ice of $v_\mathrm{c} \approx 10^{-4}\mathrm{m\,s^{-1}}$. Johnson (1985, p. 361) states that the assumption of quasi-static conditions is still valid for plastic impacts at impact velocities which are small compared to the speed of sound in the material c, since the intensity of the contact pressure pulse is diminished when the particle yields. This is assumed to be the case for all present experiments where the maximum velocity $v_\mathrm{p} < 80\,\mathrm{m\,s^{-1}}$ is small compared to the speed of sound in ice of $c = 3850\,\mathrm{m\,s^{-1}}$ (at $T = -5\,^\circ\mathrm{C}$, (Vogt et al., 2008)).
With increasing values of Bn^{-1} for ice particle collisions, the observed phenomena are the following, with a terminology of different fragmentation modes adopted from Hauk et al. (2015):

- *no fragmentation*—Dissipation of a small amount of energy after transitioning from the elastic into the plastic regime.
- *minor fragmentation*—Appearance of cracks without macroscopic fragmentation, accompanied by an increasing amount of energy dissipation and the generation of small fragments.
- *major fragmentation*—Splitting of the particle by one or more radial cracks.
- *catastrophic fragmentation*—At even larger values of Bn^{-1}, the particle shatters into a fine fragment cloud.

In their work, Hauk et al. (2015) define the regimes minor, major and catastrophic fragmentation to occur when up to 20%, between 20% and 50%, or more than 50% of the original particle volume is shattered into fragments. Additional regimes, not relevant for the present work but for planetary sciences, include shock phenomena at impact velocities closer to the speed of sound or ultimately, impact-induced macroscopic melting, vaporisation or other phase transitions (Ramesh et al., 2015).

In the work of Hauk et al. (2015), regime boundaries between no and minor fragmentation and between minor and major fragmentation of ice particles are derived based on fracture mechanics arguments. They assume that a particle fragments when an estimation of a radial or lateral crack length is equal to the particle diameter. As a result, they obtain an expression of the critical impact velocity for lateral splitting,

$$v_\mathrm{p} = \beta\, d_\mathrm{p}^{2/3}, \tag{2.3}$$

where β is a constant, specifying the upper boundary of the no fragmentation regime with $\beta = 0.046\,\mathrm{m}^{5/3}\mathrm{s}^{-1}$, and the minor fragmentation regime with $\beta = 0.14\,\mathrm{m}^{5/3}\mathrm{s}^{-1}$. Additionally, Hauk et al. (2015) imply that the regime boundaries are in fact not sharp. Regime transitioning rather has to be viewed in a stochastic sense of increasing the probability of observing the next fragmentation mode.

Generally, at high strain rates typical for impact phenomena ice breaks as a brittle material. Ice breakup is studied in the framework of fracture mechanics, which is reviewed shortly. Following the discussion of Schulson et al. (2009, p. 190 ff.), it is necessary to understand the evolution of cracks in ice and in particular, their resistance to propagation. For this purpose, the principles of linear-elastic-fracture mechanics are applied (see e.g. Lawn (1993)), which are based on the work of Griffith (1924). Given that a crack of length $2c$ exists within an isotropic, linear elastic brittle body loaded under tension, an energy balance can be formulated to determine whether the crack propagates further. The total energy of a static crack system $\mathcal{U} = \mathcal{U}_\mathrm{E} + \mathcal{U}_\mathrm{S}$ is equal to the sum of the elastic energy of the strained body $\mathcal{U}_\mathrm{E}$ and the energy associated with the creation of the crack surfaces $\mathcal{U}_\mathrm{S}$. Hence, Griffith proposed that if for a small incremental increase in the crack length δc, more elastic energy is released than energy is needed to create new crack surfaces, the total energy of the system decreases ($\delta\mathcal{U}/\delta c < 0$) and the crack will propagate. The total energy $\mathcal{U}$ can be written as a function of the crack length c,

$$\mathcal{U} = \mathcal{U}_\mathrm{E} + \mathcal{U}_\mathrm{S} = -\frac{\pi c^2 \sigma^2}{E'} + 4c\gamma_\mathrm{s}, \tag{2.4}$$

where σ and γ_s are the applied tensile stress and the surface energy per unit area of the solid-vapor interface, respectively. E' is equal to Young's modulus E for thin bodies under plane stress, while E' is equal to $E/(1-\nu^2)$ for thick bodies under plane strain. When looking at the equilibrium condition of $\delta\mathcal{U}/\delta c = 0$, a critical stress σ_c for crack propagation can be derived from Eq. (2.4),

$$\sigma_\mathrm{c} = \sqrt{\frac{2E'\gamma_\mathrm{s}}{\pi c}}, \tag{2.5}$$

with the product $\sigma_\mathrm{c}\sqrt{\pi c}$ being a material constant. At the critical stress of σ_c, the energy of the static crack system (Eq. (2.4)) is at a maximum. Thus, the crack system is unstable and for a stress slightly greater than σ_c, the crack will propagate uncontrollably. This explains the rapid failure of brittle materials such as ice. Next to the tensile crack opening mode (*mode-I*) considered by Griffith (1924), two other modes exist, namely crack sliding (*mode-II*) and tearing (*mode-III*). However, for ice and most other brittle materials, cracks propagate with the least resistance in mode-I, which is why it is the most important mode for determining failure (Schulson et al., 2009, p.193). In fracture mechanics, a *stress intensity factor* for mode-I through-thickness cracks $K_{\mathrm{I}} = \sigma\sqrt{\pi c}$ is defined, incorporating both the effects of the crack length and the applied stress. Hence, both the combination of a low stress but long crack or a short crack but high stress can lead to a condition where the stress intensity factor reaches a critical value called *fracture toughness*, $K_{\mathrm{I}} = K_{\mathrm{Ic}}$, initiating crack propagation. Values for the fracture toughness of ice are relatively low ($K_{\mathrm{Ic}} \approx 100\,\mathrm{kPa\,m}^{1/2}$) (Schulson et al., 2009, p.199) compared to engineering ceramics ($K_{\mathrm{Ic}} \approx 2...10\,\mathrm{MPa\,m}^{1/2}$) or engineering alloys ($K_{\mathrm{Ic}} \approx 8...200\,\mathrm{MPa\,m}^{1/2}$) (Ashby, 1989), which is why linear elastic fracture mechanics works well for ice.

Since the *no fragmentation* and *minor fragmentation* regimes are important for the discussion of the present results for relatively slow ice particle impacts ($v_{\mathrm{p}} < 7\,\mathrm{m\,s}^{-1}$) on dry and wet walls, they are discussed in more detail in the following. In the no and minor fragmentation regime, it is of particular interest to quantify the loss of momentum during a particle-wall collision. The loss of momentum is usually characterized by the normal and tangential coefficients of restitution (COR), e_{n} and e_{tg}, which are defined as

$$e_{\mathrm{n}} = \frac{v_{1,\mathrm{n}}}{v_{\mathrm{p,n}}} \quad \text{and} \quad e_{\mathrm{tg}} = \frac{v_{1,\mathrm{tg}}}{v_{\mathrm{p,tg}}}, \tag{2.6}$$

where v_1 denotes the particle velocity after impact, and the subscripts n and tg denote the normal and tangential components relative to the target surface. In the following, a short review of existing models for particle collisions onto dry and wet surfaces, relevant to the present work is given. The models can be applied for ice particle impacts and are used in adapted form to compare them to the measured CORs of the present experimental data. Particle impacts onto dry surfaces have been extensively studied in literature for different impact angles with and without initial rotation (Kharaz et al., 2001; Kantak et al., 2005; Dong et al., 2006; Antonyuk et al., 2010; Eidevåg et al., 2021). At very low impact velocities where inter-molecular adhesion forces play a role, the value of the COR approaches zero, as e.g. modelled by Krijt et al. (2013). For impacts of ice particles at higher velocities than this adhesive limit, the COR typically remains constant in a quasi-elastic region up to a critical velocity v_{c}, where macroscopic cracks are observed in the particle, and the COR rapidly decreases with increasing impact velocity.

Various models for the COR are reviewed by Antonyuk et al. (2010), where different assumptions are made for the material response of the collision partners. Since a correct treatment of the material response is crucial, the model of Higa et al. (1998), which is explicitly derived for ice impacts, is utilized for the present work. In their accompanying experimental study, Higa et al. (1998) report on ice particles with diameters of $d_{\mathrm{p}} = 2.8\,\mathrm{mm}{-}72\,\mathrm{mm}$ impacting on ice targets over a wide range of velocities $v_{\mathrm{p,n}} = 0.01\,\mathrm{m\,s^{-1}} – 10\,\mathrm{m\,s^{-1}}$. For particles with diameters of $d_{\mathrm{p}} = 2.8\,\mathrm{mm}$, an average quasi-elastic COR of $e_{\mathrm{qe}} = 0.7$ is reported for $v_{\mathrm{p,n}} = 0.06\,\mathrm{m\,s^{-1}}$ up to a critical velocity of $v_{\mathrm{c}} = 0.124\,\mathrm{m\,s^{-1}}$ at a particle and target temperature of $-12\,°\mathrm{C}$. At higher velocities of $v_{\mathrm{p,n}} > v_{\mathrm{c}}$, cracks appear near the impact point of both ice particle and ice target, and the COR values decrease down to 0.1 at impact velocities of $v_{\mathrm{p}} = 10\,\mathrm{m\,s^{-1}}$. Above a critical velocity which can be determined using Eq. (2.3), ice particles break up into fragments (Hauk et al., 2015). For particle impacts in the quasi-elastic and inelastic region, a model for the normal COR is proposed by Higa et al. (1998),

$$e_{\mathrm{n}} = \begin{cases} e_{\mathrm{qe}} & v_{\mathrm{p,n}} < v_{\mathrm{c}} \\ e_{\mathrm{qe}} \left(\frac{v_{\mathrm{p,n}}}{v_{\mathrm{c}}}\right)^{-\log_{10}(v_{\mathrm{p,n}}/v_{\mathrm{c}})} & v_{\mathrm{p,n}} \geq v_{\mathrm{c}} \end{cases} \tag{2.7}$$

where the critical velocity v_{c} and the quasi-elastic COR, e_{qe}, are input parameters. For temperatures above $T = -41\,°\mathrm{C}$ and a flat target, the expression for the critical velocity derived by Higa et al. (1998) can be simplified to

$$v_{\mathrm{c}} = k_1 \exp\left(\frac{k_2}{2\mathcal{R}T}\right) d_{\mathrm{p}}^{-1/2}, \tag{2.8}$$

where $k_1 = 9.907 \times 10^{-7}\,\mathrm{m^{3/2}s^{-1}}$ and $k_2 = 48.2 \times 10^{3}\,\mathrm{J\,mol^{-1}}$ are empirical factors and $\mathcal{R} = 8.31446\,\mathrm{J\,mol^{-1}\,K^{-1}}$ and T_{p} are the universal gas constant and the particle temperature, respectively. Following Higa et al. (1998), the model of Dilley (1993) is used for the quasi-elastic COR of ice particle impacts onto a flat wall,

$$e_{\mathrm{qe}} = \exp\left(-\pi\Xi/\sqrt{1-\Xi^2}\right), \tag{2.9}$$

$$\Xi = 0.027\left(\frac{d_{\mathrm{p}}}{0.05\,\mathrm{m}}\right)^{-1/2}. \tag{2.10}$$

By inserting Eqs. (2.8),(2.9) and (2.10) into Eq. (2.7), particle size and temperature effects on the COR of ice particles impacting on dry ice surfaces can be captured. In contrast to the experiments of Higa et al. (1998), ice particle impacts onto an aluminium (EN AW-7075) surface are performed in the present work. Since aluminium has different material properties than an ice surface, it raises the question of whether the model of Higa et al. (1998) can be applied in this context. In a recent study, Eidevåg et al. (2021) report on ice particle impacts on a glass, ice, and ABS polymer wall, with different moduli of elasticity E. They observe that with an increasing elastic modulus of the target material, the normal COR decreases for identical impact velocities. This trend can be explained using Hertzian contact theory (Hertz, 1882), where the maximum pressure during impact p_{max} increases with an increasing effective modulus of elasticity E^*,

$$E^* = \left(\frac{1-\nu_{\mathrm{p}}^2}{E_{\mathrm{p}}} + \frac{1-\nu_{\mathrm{t}}^2}{E_{\mathrm{t}}}\right)^{-1}. \tag{2.11}$$

Here, E_p and E_t are the moduli of elasticity and ν_p and ν_t the Poisson ratios of the particle (p) and target material (t), respectively. With increasing target modulus of elasticity, E^* increases, ultimately resulting in a larger contact pressure for the same impact velocity. Hence, more energy is dissipated due to plastic deformation and crack formation, leading to a lower COR. Using the material properties $E_\mathrm{ice} = 9.3\,\mathrm{GPa}$, $\nu_\mathrm{ice} = 0.325$ (Gammon et al., 1983) and $E_\mathrm{Al} = 72\,\mathrm{GPa}$, $\nu_\mathrm{Al} = 0.33$ for aluminium the effective modulus of elasticity for an ice on ice impact at $E^* = 5.2\,\mathrm{GPa}$ is roughly half the effective modulus of elasticity for an ice particle impact on aluminium surfaces at $E^* = 9.2\,\mathrm{GPa}$. Therefore, the CORs reported in the present work are expected to be lower than the CORs reported in the work of Higa et al. (1998). In fact, in their model derivation, Higa et al. (1998) consider the effect of the effective modulus of E^*. However, they assume it to be constant and include the respective value of E^* in their empirical factor k_1. If E^* is kept as a variable during their model derivation, it follows that $v_\mathrm{c} \propto {E^*}^{-2}$ in Eq. (2.7). Consequently, a new empirical factor $k_3 = k_1/E^*_\mathrm{ice-ice} = 9.664 \times 10^{17}\,\mathrm{m}^{-1}\,\mathrm{s}^{-6}\,\mathrm{kg}^{5/2}$ can be defined, rewriting Eq. (2.7) as

$$v_\mathrm{c} = k_3 {E^*}^{-2} \exp\left(\frac{k_2}{2\mathcal{R}T}\right) d_\mathrm{p}^{-1/2}, \tag{2.12}$$

resulting in a formulation of the critical velocity v_c, sensitive to changes of the target material elastic modulus. In the present work this adapted model is compared to experimental results of ice particle impacts onto a dry aluminium surface.

2.2 Ice Particle Impact Onto a Wet Substrate

When the target surface is wetted by a fluid film, energy dissipation due to the fluid further reduces the COR compared to a particle impact onto a dry surface. In an approximate model, both the viscous dissipation in the liquid film and the dissipation in the solid can be combined into one expression for the COR (Joseph et al., 2001),

$$e_\mathrm{n} = e_\mathrm{dry} e_\mathrm{wet}, \tag{2.13}$$

where e_dry accounts for the dissipation in the solid and e_wet in the liquid. For ice particle impacts onto a water film, e_dry starts to significantly decrease above some critical velocity (v_c) with increasing impact velocity as discussed in the previous section. In the present section, the dissipation during impact of a perfectly elastic particle onto a thin fluid film characterised by e_wet is discussed in more detail.

Current modelling approaches for e_wet are reviewed by Buck et al. (2019) and can be subdivided into two groups, namely models relying on a Stokes number St to characterize the fluid film impact (Davis et al., 1986; Barnocky et al., 1988; Ennis et al., 1991; Davis et al., 1990; Ma et al., 2013; Müller et al., 2016) and more complex models involving force or energy balances of various sub-phenomena (Antonyuk et al., 2009; Gollwitzer et al., 2012; Sutkar et al., 2015; Buck et al., 2018).

The dimensionless parameters used to classify the impact of spherical particles onto liquid films are now introduced, following the discussion of Sutkar et al. (2015). Next to a dimensionless film thickness δ^+ relating the particle diameter d_p to fluid film thickness h,

$$\delta^+ = \frac{h}{d_\mathrm{p}}, \tag{2.14}$$

three dimensionless parameters can be derived, describing the relative importance of inertia, viscous and capillary forces of the liquid layer and the inertia force of the impacting particle. These include the Reynolds number Re, the capillary number Ca and the Stokes number St, which can be written as

$$\begin{aligned}
\mathrm{Re} &= \frac{\rho v_\mathrm{p} h}{\mu} \mathrel{\widehat{=}} \frac{\text{Fluid inertial force}}{\text{Fluid viscous force}}, && (2.15)\\
\mathrm{Ca} &= \frac{v_\mathrm{p} \mu}{\gamma_\mathrm{s}} \mathrel{\widehat{=}} \frac{\text{Fluid viscous force}}{\text{Fluid surface tension force}} \quad \text{and} && (2.16)\\
\mathrm{St} &= \frac{2 m v_\mathrm{p}}{3\pi\mu d_\mathrm{p}^2} \mathrel{\widehat{=}} \frac{\text{Particle inertial force}}{\text{Fluid viscous force}}, && (2.17)
\end{aligned}$$

where m and μ are the particle mass and the liquid dynamic viscosity, respectively. It can be noted that the capillary or Reynolds number can be replaced by the Weber number We, since it can be expressed as a linear combination of the introduced dimensionless parameters, $\mathrm{We} = \mathrm{Ca}\,\mathrm{Re}/\delta^+$. In most cases where the Reynolds number is rather low and the capillary number is large, considering only the Stokes number is enough, indicated by the success of Stokes number based models to fit experimental data (Davis et al., 1986; Barnocky et al., 1988; Ennis et al., 1991; Davis et al., 1990). In more recent approaches, a combination of the Stokes number and the dimensionless film thickness δ^+ is used to consider observed effects of the film thickness on the COR (Ma et al., 2013; Müller et al., 2016). However, these models are limited in certain cases, namely when capillary forces have to be considered (larger values of Ca). In the work of Darabi et al. (2009) a range of capillary numbers $0.01 < \mathrm{Ca} < 100$ is proposed, where both the capillary and viscous forces have to be considered. For liquid water near the freezing point, this corresponds to velocities of $0.4\,\mathrm{m\,s^{-1}} < v_\mathrm{p} < 4000\,\mathrm{m\,s^{-1}}$, spanning a very large range, which includes all relevant velocities for particle impacts in ice crystal icing. For a detailed description of the amount of energy dissipated by capillary forces and other contributions not captured by a Stokes number dependency, a force balance model like a recent one of Buck et al. (2018) has to be applied. For instance, they report that the ratio of the dissipated energy by capillary forces to the total dissipated energy can span from 44% for impact velocities of $v_\mathrm{p} = 0.8\,\mathrm{m\,s^{-1}}$ to 15% for $v_\mathrm{p} = 1.8\,\mathrm{m\,s^{-1}}$. They consider glass spheres with a diameter of $d_\mathrm{p} = 1.74\,\mathrm{mm}$

impacting on a $h = 400\,\mu\mathrm{m}$ water film, which is a comparable scenario to the experiments of the present work except for the response of the particle material. In particular, the plastic deformation during the impact of an ice particle is possibly highly dissipative as discussed in the previous section. Hence, the relative importance of plastic dissipation in the ice particle and dissipation due to the liquid film is of interest for the present work. For simplicity, the adapted COR model of Higa et al. (1998) is combined first with a more accessible Stokes model (Davis et al., 1986; Barnocky et al., 1988; Davis et al., 2002), which is presented in more detail in the following.

Davis et al. (1986) report that next to the Stokes number, viscous dissipation in an elastohydrodynamic collision process is governed by an elasticity parameter Θ,

$$\Theta = \frac{4\mu U_{x_0} (d_\mathrm{p}/2)^{3/2}}{\pi E^* x_0^{5/2}}. \tag{2.18}$$

The velocity U_{x_0} corresponds to the velocity of the particle at a characteristic distance x_0 to the surface. Similar to the recommendation of Barnocky et al. (1988), x_0 is set to two thirds of the initial water film thickness $x_0 = 2h/3$ in the present work. For $\mathrm{St} > 1$, it can be assumed that the initial particle velocity is reduced by only a small percentage at $x_0 = 2h/3$ after penetrating a third of the film thickness and consequently, U_{x_0} can be set to be equal to the particle impact velocity $U_{x_0} = v_\mathrm{p}$ (Barnocky et al., 1988). Since the Stokes number is a measure of the particle inertia relative to the viscous forces of the liquid, a critical Stokes number $\mathrm{St_c}$ is defined, below which the total particle kinetic energy is lost due to viscous dissipation, leading to it sticking to the wetted substrate (Davis et al., 1986). The elasticity parameter Θ provides a measure of the tendency of the particle to deform during impact onto the water film. Davis et al. (2002) investigated the impact of steel spheres ($\Theta = 10^{-6} - 10^{-4}$) and nylon spheres ($\Theta = 10^{-3} - 10^{-2}$) and report that the stiffer steel sphere with a smaller elasticity parameter penetrates further into the liquid film before elastic deformation is significant, leading to greater viscous losses; hence, a smaller COR compared to the nylon sphere impact. Consequently, also $\mathrm{St_c}$ increases with decreasing Θ (Davis et al., 2002),

$$\mathrm{St_c} = 0.40 \ln(1/\Theta) - 0.20, \tag{2.19}$$

where $\ln()$ is the natural logarithm. However, the dependence of $\mathrm{St_c}$ on Θ is rather weak ($5.6 < \mathrm{St_c} < 7.6$ for $3.6 \times 10^{-9} < \Theta < 4.9 \times 10^{-7}$ in the present experiments) and the critical Stokes number is assumed to be constant for the present work $\mathrm{St_c} = 6.6$. Finally, an expression for the COR of a perfectly elastic sphere depending on the Stokes number and critical Stokes number is introduced, reading

$$e_\mathrm{wet} = 1 - \mathrm{St_c}/\mathrm{St}, \tag{2.20}$$

which is utilized in the present work. The present equation is inserted into Eq. (2.13) together with Eq. (2.7) for e_dry presented in the previous chapter. As a result, an expression for the total COR of an ice particle impacting onto a wetted substrate is obtained. In the present study, this combined model (Eq. (2.13) with Eq. (2.7) and Eq. (2.20)) is compared to experiments of ice particle impacts onto a wetted wall. It can be noted that the plastic dissipation in the solid starts to significantly increase above some critical velocity v_c with increasing impact velocity, leading to decreasing values of e_dry as discussed in the previous section. The term e_wet on the other hand increases with increasing impact velocity, after a threshold value of the critical Stokes number St_c is exceeded. Therefore, at a certain impact velocity range, a plateau of higher CORs exists, while for smaller and larger velocities, the ice particle will stick to the wetted wall.

2.3 Current Knowledge of the Fragment Size Distribution After Ice Particle Impact

The fragment size distribution resulting from a single ice particle impact relevant to ICI has been studied in the context of earlier studies as summarized in Table 2.1. However, the most relevant influencing factors, the particle impact velocity v_p, diameter d_p, temperature T_p, and target temperature T_t, have not been varied systematically in a single study to the author's knowledge. Additionally, uncontrolled factors like the particle shape are seldom reported in detail. The current work aims at filling this research gap. More detailed information about the present knowledge on the ice fragment size distribution in the context of ICI is briefly summarized in the following.

Particle Impact Velocity and Impact Angle Depending on the impact velocity, Hauk et al. (2015) distinguish among four different fragmentation types corresponding to the loss of the original particle volume to smaller fragments. If between 20% up to 50% of the initial particle volume is shattered into airborne fragments, the break-up of the particle is termed major fragmentation. In accordance with the collisional break-up condition used in (Davis et al., 1990), the regime is referred to as catastrophic fragmentation if the volume portion of the fragments exceeds 50% of the initial volume (Hauk et al., 2015). Based on their experimental results, Hauk et al. (2015) linked the probability for the occurrence of these two regimes to a dimensionless variable defined using the velocity and diameter of the impacting particle. Given expected particle velocities inside aircraft engines, most studies are focused on break-up phenomena within the major and catastrophic regime. Fragment sizes after catastrophic fragmentation have been found to follow a non-normal, heavy-tailed distribution (Reitter et al., 2021; Vargas et al., 2015; Vargas et al., 2020; Senoner et al., 2022). Vargas et al. (2015) noted that the experimentally determined particle sizes resemble a log-normal distribution after binning.

Combescure et al. (2011) found the number of small fragments to increase with increasing impact velocity for the non-axisymmetric impact of ice machined into

Ref.	v_p in $\mathrm{m\,s^{-1}}$	d_p in mm	T_p in $^\circ\mathrm{C}$	T_t in $^\circ\mathrm{C}$
[1]	1 ... 5	12.9 ... 42	-10, -18, -25 (RT)	RT
[2]	66.1 ... 202.8	6.2, 12.9, 27.5	-25 ... -18 (NC)	RT
[3]	60 ... 127.3	20	NA	NA
[4]	6.5 ... 7.3	25, 50, 60	NA	NA
[5]	60.6 ... 189.2	38.1, 50.8, 61	-18.3 ... -16.7 (RT)	RT
[6]	76 ... 240	0.4 ... 0.9	-20	-18.9 ... 8.79 (NC)
[7]	1 ... 74	0.26 ... 3.5	-10 ... -20	-10 ... -20 (NC)
[8]	20 ... 130	1 ... 3.5	-20 (RT)	RT
[9]	33.9 ... 82.4	1.9 ... 3.3	-16, -10, -6 (C)	RT

Table 2.1: Range of investigated parameters in experimental studies relevant for the conditions during ICI. The abbreviations are: controlled (C), not controlled (NC), room temperature (RT), and unknown (NA). The following references are included in the table: [1](Guégan et al., 2012), [2] (Guégan et al., 2011),[3](Combescure et al., 2011), [4](Uenishi et al., 2018; Uenishi et al., 2019), [5](Tippmann et al., 2013),[6](Palacios et al., 2014), [7](Hauk et al., 2015), [8](Vargas et al., 2015),[9](Vargas et al., 2020).

a conical or cylindrical shape. For hailstones, the fragment sizes are assumed to follow a Weibull distribution in the model of AGARD (Garwood et al., 1995), in which the mass fraction of smaller fragments also increases with increasing impact velocity which is in agreement with observations from Pan et al. (1996).

Finally, also the impact angle changes the kinematics of the fragments after impact. The expanding fragment cloud moves with a velocity proportional to the tangential component of the impact velocity in the target plane (Guégan et al., 2011). However, the associated fragment size distribution seems to be influenced only indirectly by the impact angle namely through the reduction of the impact velocity normal to the target surface (Pan et al., 1996).

Particle Temperature Static air temperatures in icing clouds associated with the occurrence of ICI related impact events have been reported to range from $-58\,^\circ\mathrm{C}$ to $-3\,^\circ\mathrm{C}$ (Bravin et al., 2015). Fracture related material properties of ice, such as compressive and tensile strength, have been demonstrated to depend on temperature for strain rates up to 10^{-1} 1/s (Gold, 1977; Schulson, 2001). For strain rates associated with ice particle impact in the range of approx. 10^{3} 1/s, Shazly et al. (2009) concluded that decreasing the temperature from $-30\,^\circ\mathrm{C}$ to $-10\,^\circ\mathrm{C}$ leads to an increase in peak compressive strength. Therefore, the temperature dependence of the material properties of ice actually suggests a correlation of the fragmentation process with temperature.

The only experimental study of ice particle impact with a systematic variation of the particle temperature is reported in Vargas et al. (2020). For three initial particle temperatures of $-16\,^{\circ}\mathrm{C}$, $-10\,^{\circ}\mathrm{C}$ and $-6\,^{\circ}\mathrm{C}$, it has been shown qualitatively that the fraction of smaller fragments increases with decreasing temperature, i.e. with increasing compressive strength. Hauk et al. (2015) and Reitter et al. (2021) kept the initial particle temperature below the freezing point but did not actively control it. While it has been constrained between $-4\,^{\circ}\mathrm{C}$ and $0\,^{\circ}\mathrm{C}$ in the experiments of Guégan et al. (2011), both the surrounding air and the impact target have been at unspecified room temperature. Vargas et al. (2015) kept the initial particle temperature at $-16\,^{\circ}\mathrm{C}$, but the entire experimental setup was not temperature-controlled, which makes it difficult to assess the actual particle temperature on impact.

If the temperature of the air surrounding the ice particle is above freezing, the particle temperature rises, eventually leading to a phase change at the air-ice interface. Liquid water inside an aircraft engine serves as a precursor for ice accretion (Mason et al., 2010; Struk et al., 2012), which can originate from partially melted ice crystals. Therefore, ice particles may be enclosed by a water film in the engine region that is susceptible to ice accretion. This may alter their fracture and fragmentation dynamics. Palacios et al. (2014) studied the influence of the particle melt ratio on the ice accumulation area of a single particle by exposing the airborne particle to a heated air stream or oxygen/acetylene cross-flow flame during its propagation towards the impact surface. The ice accretion was shown to increase with an increasing melt ratio. Alvarez et al. (2019) found the threshold velocity for fragmentation to increase with particle melt ratio. However, to the author's knowledge, the influence of the particle melt ratio on the fragment size distribution resulting from a single particle impact has not yet been investigated. In the experiments of Guégan et al. (2011) and Guégan et al. (2012) and Vargas et al. (2015) and Vargas et al. (2020), the air and the impact target are at room temperature, presumably creating a non-negligible layer of liquid water around the particle prior to its impact. However, the effect of that layer has not been considered, let alone quantified.

Target Temperature Engine parts susceptible to ICI have been shown to be at temperatures above freezing during the operation of a research gas turbine similar to modern turbofan engines (Veres et al., 2016; Jorgenson et al., 2020). However, despite its importance for ICI, to the author's knowledge, the influence of the target temperature on the fragmentation process within the scope of a single ice particle impact has not yet been studied systematically.

2.4 Particle Impact Onto a Wet Granular Ice Layer

In an aero-engine or probe icing scenario, ice accretion may form as a porous structure of ice crystals wetted with meltwater. For advanced modelling of the ice layer growth and erosion due to impinging ice crystals, information about the ice layer composition and material properties is crucial. Despite recent advances in understanding aircraft engine icing, a detailed description of the material properties of wet granular ice layers is still lacking. Furthermore, dedicated single particle impact experiments on wet granular ice layers for their strength quantification have not been performed in literature to the knowledge of the author. However, the strength of granular media in general is of interest in multiple fields of research. Hence, a short literature review is now presented for identifying the main physical mechanisms involved in a particle impact onto a wet granular ice layer.

Related phenomena of impacts onto granular media include meteorite impact or probe retrieval on asteroids (Burchell et al., 2005; Schultz et al., 2007; Arakawa et al., 2011; Tsujido et al., 2015; Nakamura, 2017), subsurface investigation of soil and rock (Caudle et al., 1967; Hearst et al., 1994; Bless et al., 2020) or military applications (Børvik et al., 2015; Savvateev et al., 2001). Next to the impactor density, velocity, shape and impact angle relative to the target surface, the properties of the granular medium control the resistance to penetration and final crater geometry as reviewed by (Ruiz-Suárez, 2013) or (Omidvar et al., 2014). Moreover, the packing fraction or porosity of a dry granular material is an important parameter, as investigated by (Umbanhowar et al., 2010). By measuring the crater geometry and volume change of a bed of $300\,\mu\mathrm{m}$ glass spheres after the impact of a $19.8\,\mathrm{mm}$ steel sphere, they found that at a critical packing fraction, the post-impact change of the bed volume is zero. With a more dense initial packing, the bed is diluted after impact, forming a larger ridge next to the crater, and the steel sphere penetrates deeper compared to a loose initial packing. (Marston et al., 2012) dropped a $20\,\mathrm{mm}$ steel sphere onto dry and wet sand and also found that the penetration depth was greater with a looser packing fraction. Additionally, they observed that depending on the water saturation, the penetration depth was either smaller or greater compared to dry sand penetration. In wet granular media, cohesive forces between individual grains can exist due to the surface tension of the wetting liquid, as e.g. described by (Mitarai et al., 2006). Four wetting regimes can be identified:

- *pendular*—liquid bridges between the contact points of the grains,
- *funicular*—both liquid bridges and liquid-filled pores,
- *capillary*—almost all the pores filled with liquid and
- *slurry*—grains are fully immersed, no capillary action.

As expected, the resistance to deformation of a wet granular medium is affected by its wetting state. In the pendular state, Pierrat et al. (1998) found different granular materials to be more resistant to shearing compared to the samples of the dry materials. The mechanical response of the funicular state on the water saturation however, is not well understood (Mitarai et al., 2006), since for different materials, their strength is either enhanced or diminished with increasing saturation (Schubert et al., 1975; Kristensen et al., 1985). Several other strength tests of wet granular materials are reviewed by Iveson et al. (2001), where the effect of particle size on the reciprocity of cohesion and lubrication inside the material was considered to be one of the causes of the ambiguous influence of the water saturation. When transitioning from a fully saturated into the capillary state, the shear strength of clay as granular medium was observed to increase, since the compressive stress inside the material increases, originating from the liquid surface tension at the surface of the material (Vanapalli et al., 1996; Mitarai et al., 2006). It can be concluded that modelling of the material response of a wet granular layer is complex even with an exact knowledge of the layer composition.

Quantifying the strength of wetted granular ice layers in the context of ICI poses additional difficulties, since the porosity and water saturation are not easily measurable in icing wind tunnel tests, where realistic ice layers are accreting, although first attempts have been made to measure their water content (Currie et al., 2015). Hence, it is not yet feasible to re-create ice layers with the same properties in the laboratory. Additionally, the ice layers generated in the wind tunnel are of irregular shape and are not easily transferable to a controlled laboratory environment, since heat exchange with the surrounding may lead to melting or freezing with the result of alternated mechanical properties. In order to gain knowledge of the material response of a wet granular ice layer, a particle impact based strength measurement method is proposed in the present work. It can be applied directly in an icing wind tunnel and in a laboratory environment, where the porosity and water saturation are at least controllable during the ice layer manufacturing.

3 Experimental Materials and Methods

Impact processes relevant to aircraft engine icing are studied experimentally in the present work. Three distinct physical phenomena are investigated, ice particle fragmentation after impact onto a dry, cold and heated substrate, ice particle sticking and rebound after impact onto a wetted substrate, and the crater formation after particle impact onto dry and wet granular ice layers. For each phenomenon, separate experimental setups and methodologies are developed that are presented in detail in the following.

3.1 Ice Particle Impact Onto a Dry Substrate[1]

All experiments are conducted inside a cooling chamber[2] operating at sub freezing temperature to ensure no unwanted phase change is happening. The experimental setup consists of four major parts comprising a pneumatic gun to accelerate the ice particle, a high-speed video system with a sufficient spatial and temporal resolution to capture the particle size and velocity distribution, a cooling system to control the particle temperature and a transparent, temperature controlled target. A computer control and monitoring unit is utilized for temperature measurements and for controlling high-speed cameras. In Fig. 3.1, the experimental setup is shown in its entirety. In the following, all relevant sub-systems are introduced in more detail.

Pneumatic Ice Particle Shooting Setup Investigating ice particle impacts with varying impact velocities necessitates a device for accelerating them towards an impact target in a repeatable manner. The device consists of an $300\,\mathrm{mm}$ long aluminium tube with inner diameter of $8\,\mathrm{mm}$ connected to an aluminium block (magazine) with a $8\,\mathrm{mm}$ borehole constricting to a $7\,\mathrm{mm}$ borehole. An ice particle is inserted into a $10\,\mathrm{mm}$ long plastic cup (sabot), with an outer diameter of $7.3\,\mathrm{mm}$ that is stopped at the constriction inside the magazine when inserted through the

---

[1] Parts of this chapter are based on the Bachelor-Thesis of Hannes Lohmann and the Master-Thesis of Maximilian Lausch and have been published (Reitter et al., 2022a; Reitter et al., 2021) or are currently submitted for publication (Lausch* et al., 2023). The original contents have been edited and/or extended for this work.

[2] The cooling chamber has been designed in the framework of Gloerfeld (2022).

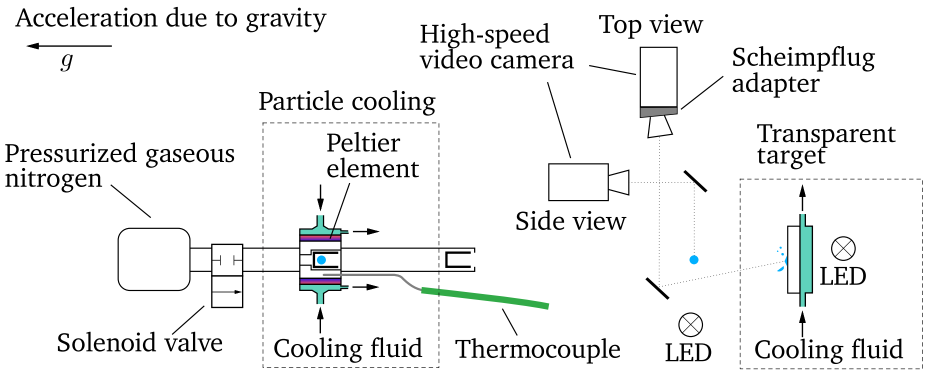

Figure 3.1: Schematic of the experimental setup comprising a pneumatic ice particle shooting setup, cooling systems for the ice particle and transparent target and a high-speed video system.

aluminium tube. The ice particle gun is driven by pressurized gaseous nitrogen supplied to a small buffer tank of the volume of $4 \times 10^{-4}\mathrm{m}^3$. The tank is connected to a solenoid valve which is in turn fitted to the magazine containing the sabot. The firing tube points vertically upwards and is aimed at the impact target. By activating a solenoid valve, the ice particle, shielded by the sabot, is accelerated inside the aluminium tube. At the end of the tube, the sabot is stopped by a removable aperture while the ice particle is ejected through the aperture hole. The impact velocity is set by adjusting the supply pressure ranging from $0.06\,\mathrm{MPa}$ to $1.6\,\mathrm{MPa}$ using a manually operated pressure regulator with an attached digital manometer. The achievable ice particle impact velocity v_p ranges from $10\,\mathrm{m\,s^{-1}}$ to $79\,\mathrm{m\,s^{-1}}$ and can be approximated as a function of the driving nitrogen gas pressure p by the following empirical correlation,

$$v_\mathrm{p} = 20.30\,\mathrm{m\,s^{-1}} \left(\frac{p - 0.034\,19\,\mathrm{MPa}}{0.1\,\mathrm{MPa}} \right)^{0.4713} . \tag{3.1}$$

It should be noted that the present relation has no universal applicability but is viable only for the estimation of an impact velocity for the present experimental setup.

High-Speed Video System A high-speed video camera (*Photron SA1.1*) is used to determine the impact velocity and volume of the impacting ice particles from a view parallel to the impact surface (side-view). It is operated with a frame rate of 15000 frames per second and a spatial resolution of $58.66\,\mathrm{\mu m/pixel}$ with 960 pixel × 416 pixel per frame. A second high-speed camera (*Phantom V2012*, $46.63\,\mathrm{\mu m/pixel}$,

34000 frames per second, 768 pixels × 768 pixels per frame) is used to capture the particle impact onto the target and the emerging fragments in a top-view almost normal to the target surface. A Scheimpflug adapter is used with this camera to tilt its focal plane and align it parallel to the target surface. Two LED light sources (*Veritas Constellation 120E*) are used for shadowgraphy imaging. The light source positioned behind the target is pulsed with the same frequency ($34\,\mathrm{kHz}$) as the recording frequency of the high-speed camera to obtain flicker-free video sequences.

Ice Particle Cooling System Two separate cooling systems are operated to control the particle and target temperature independently. The ice particle temperature is controlled by regulating the magazine temperature. Since the ice particle inside the sabot is located at the centre of the magazine prior to an experiment, it will reach thermal equilibrium with the magazine after a given time. The magazine is cooled or heated using two Peltier elements attached to opposite faces of it. The Peltier elements are connected to an external power supply (*Manson, HCS 3300 USB*) that is operated using a PID-controller implemented in a commercial data acquisition software (*National Instruments, LabVIEW*). Two heat exchangers (*Alphacool XP*^{3} *LIGHT*) are attached to the Peltier elements, and an external chiller (*Huber, UC020TW*) is used to pump a cooling fluid through them. A calibrated type-K thermocouple inserted into a borehole in the magazine, located at a distance of 1.5 mm from the sabot, is used to monitor the magazine temperature. In preliminary tests, a calibrated type-K thermocouple is frozen in the centre of an ice particle to correlate its temperature with the measured magazine temperature. Additionally, the time for the ice particle to reach thermal equilibrium with the magazine is determined for magazine temperatures ranging from $-5\,^\circ\mathrm{C}$ to $-50\,^\circ\mathrm{C}$. It is found that the ice particle reaches thermal equilibrium after a maximum of $300\,\mathrm{s}$ in all cases, which is accordingly considered for the experiments. The particle temperature is always measured to be higher than the magazine temperature due to heat flux inside the magazine. This temperature offset is determined and introduced in the automatic control unit, allowing the desired particle temperature to be set precisely for each experimental run. The cooling system enables a variation of the particle temperature between $-5\,^\circ\mathrm{C}$ to $-50\,^\circ\mathrm{C}$ with an uncertainty of ± 0.3 K.

Temperature Controlled Impact Target To allow capturing of high contrast videos using back lighting, the impact target, schematically shown in Fig. 3.2, is fully transparent while still enabling precise control of the surface temperature. The hollow impact target is made completely from transparent materials and is incorporated into a closed circuit of a transparent thermo-fluid (mixture of ethylene glycol and water), temperature controlled using a liquid chiller (*Lauda RC20 CS*). The system is used to either heat or cool the impact surface for the experiments by directing the coolant through a channel formed between an acrylic glass back plate and a sapphire glass plate serving as the impact target. The sapphire glass with a

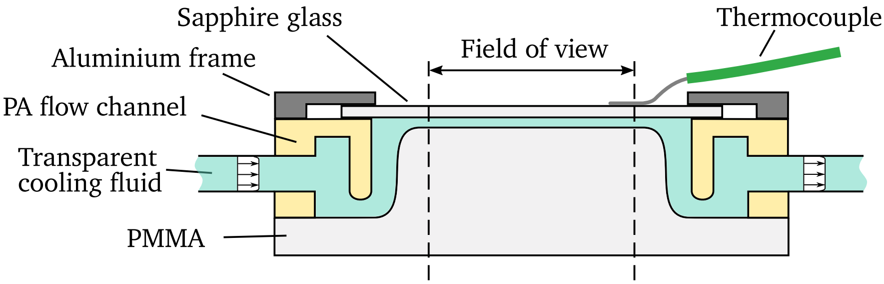

Figure 3.2: Schematic side-view of the transparent impact target enabling temperature control of the sapphire impact surface and backlight shadowgraphy imaging of the impact process in a top-view.

thickness of $4\,\mathrm{mm}$ is held in place by an aluminium retaining frame and the surface temperature is measured using a calibrated type K surface-thermocouple attached to the target at the outer edge of the camera field of view. Two manual 3-way valves are included in the coolant circuit directly before and after the target. They are connected to a second coolant circuit which is utilized to rapidly heat up the target surface above the melting temperature. In this manner, ice adhering to the target can be melted quickly. In order to investigate the temperature uniformity on the surface, its temperature is measured once in a preliminary test using an infrared camera (*Optris PI 160*). For this purpose, the infrared transmissive sapphire glass target is replaced with a sandblasted PMMA target. Since the infrared transmission of PMMA tends to zero for the operational spectral range of the utilized thermal imaging camera, only the infrared emission from the surface is captured without superimposing the infrared emission of the cooling fluid flowing through the target. Additionally, the sandblasting diminishes errors due to the reflection of infrared light sources in the surroundings.

For a calibration of the PMMA thermal emissivity, a sticker with a known emissivity of 0.95 was applied to the target surface. After matching the temperature of the sticker with the temperature of the PMMA target next to it, a target emissivity of 0.96 was determined. In Fig. 3.3, an example image taken using the infrared camera is shown. It was found that the temperature is indeed uniform in a large area of the target surface with dimensions of $36\,\mathrm{mm} \times 36\,\mathrm{mm}$, corresponding to the field of view of the high-speed camera. Temperature uniformity has been demonstrated for a maximum difference of 25 K between the mean target temperature and the ambient temperature, revealing a variation of the target temperature around its mean in the field of view of the top-view high-speed camera of ± 0.3 K. In the present work, the surface temperature is varied between $-10\,^{\circ}\mathrm{C}$ and $10\,^{\circ}\mathrm{C}$ while the entire setup is placed inside a cooling chamber providing an ambient temperature of $-15\,^{\circ}\mathrm{C}$. In the following section, the experimental procedure is explained in detail, comprising the manufacturing of spherical ice particles, the measurement method to obtain the

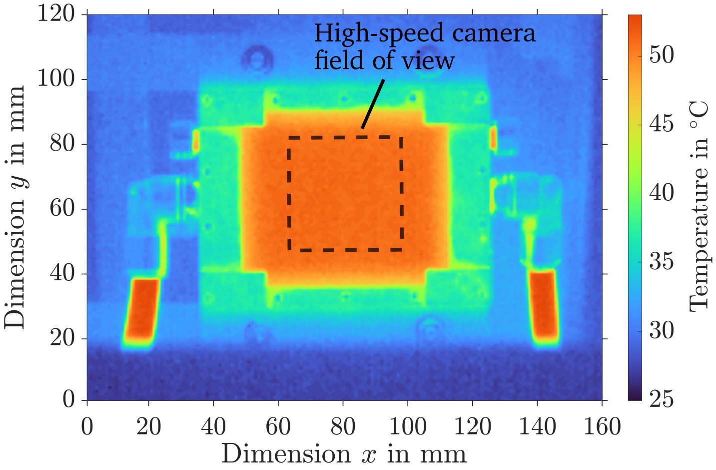

Figure 3.3: Thermographic imaging of the transparent impact target in a top-view. At the centre of the target, the field of view of the high-speed camera is depicted as black dashed box.

particle diameter d_p and impact velocity v_p prior to impact and the mass of small ice fragments adhering to the target after particle impact. The methodology for measuring the particle size distribution is presented as well as the procedure for fitting a doubly-truncated, power-law size distribution to the data.

Ice Particle Generation Near spherical ice particles are made from purified and de-ionised water (*Millipore, Milli-Q*). The water is additionally degassed by reducing the pressure in the water vessel below $0.2\,\mathrm{kPa}$ using a vacuum pump (*Adixen AMD4*). Repeatedly striking the vessel enhances the degassing process through induction of cavitation (Juan Gallego-Juarez, 2015). This process finally minimizes the presence of gas inclusions inside the prepared particles, which may affect fragmentation. After preparation of the water, a defined volume is deposited onto a 3D-printed, superhydrophobically coated (*Evonik, Tegotop 210*) polyamide plate with hemispherical depressions whose diameters match the particle diameters used in the present study. The coated plate with the water droplets in the depressions is placed into the cooling chamber providing a constant ambient temperature of $-15\,^\circ\mathrm{C}$. In this case, the freezing process is mainly directional, with a freezing front propagating from the bottom upwards. In this case, a conical protrusion is formed after freezing due to the volume expansion during solidification, as visualized by e.g. Jung et al. (2012). The ice particles prepared in this way appear dark in the video recordings during the experiments because the surface roughness of the plate partially imprints on the particles. However, the resulting small-scale surface roughness of the ice particles is assumed not to affect the fragmentation process. Compared to dispensing the water droplets into a liquid nitrogen reservoir, as reported by Vargas et al. (2015) or in a first experimental campaign, the present method ensures higher repeatability of the particle diameters and shape. When using liquid nitrogen, volume expansion during solidification from the outside causes the build-up of tensile stress in the ice shell, encapsulating a remaining liquid water volume in the centre. This may result in cracks and even an explosive like partition of the freezing drop, as shown by Wildeman et al. (2017). Cracks formed in the ice can actually be visually identified, and thus, damaged particles are sorted out during the analysis. Nevertheless, the absence of obvious cracks in the recorded particles during an experiment is no guarantee for the actual absence of residual internal stresses introduced during the freezing, which may also affect fragmentation. However, the present method is deemed to be more robust in avoiding these unidentified stresses, since it more likely leads to parallel solidification of the water drop in contrast to radial freezing starting from the outside, which is more likely associated with the liquid nitrogen method.

Impact Velocity and Particle Diameter Measurement Using the high-speed video recording of the ice particle before impact from the side view perspective, the initial particle diameter and velocity are measured via image processing. With the present setup, a minimum of four images are obtained from the particle in a video sequence. The data processing is performed with an in-house code implemented in the commercial software package *MATLAB*. A GUI allows the selection of all images in which the still intact ice particle is visible before impact. After background subtraction and black and white (BW) conversion of these images, the position of the particle centroid and the projected area of the particle is obtained. In the next step, the travelled distance of the particle centroid with respect to its position in the first image is plotted against time for all relevant images. Since the ice particle appears to travel with a constant velocity, the plotted data exhibits a linear increasing trend. This suggests that drag and gravitational forces do not decelerate the particle to a measurable extent. Thus, a linear function is fitted to this data set using an ordinary least squares (OLS) regression in order to obtain the slope of the observed trend, which yields a robust measurement of particle velocity prior to impact.

The uncertainty of the particle velocity is estimated as follows. Prior to impact, the particle is observed to travel at least half the distance of the image field of view, which is equal to a distance of 480 pixels using the present optical setup. If the particle deviates from a perfect spherical shape and rotates slightly during its flight, the centroid of the recorded 2D projection of the particle may deviate from its true centre of mass. As a conservative estimate, the measured centroid of the particle is assumed to be shifted by a distance less than 5 pixels from its true centre of mass during its flight path. As the time between the video frames is known precisely, the uncertainty of the measured velocity is directly proportional to the uncertainty of the position of the particle centroid, leading to an uncertainty of $5\,\text{pixels} / 480\,\text{pixels} \approx 1\%$. After their generation, ice particles with a clearly visible, non-spherical shape are immediately discarded. However, the ice particles used for the experiments may exhibit a minor conical protrusion, as discussed in the previous section. A possible deviation from a perfectly spherical shape is quantified via image processing, defining a sphericity S and roundness R of 2D projections of the particle. For the present work, the particle sphericity S is defined as the ratio of the diameter of a circle area, equivalent with the projection of the particle, and the diameter of the smallest circumscribing circle of the particle projection. The roundness R is determined according to the method of Zheng et al. (2015). After smoothing out the surface roughness with a robust automatic procedure, pronounced corners of the particle are determined. The average radius of these corners is divided by the maximum inscribed circle resulting in a value for the particle roundness. In the experiments, ice particles having a roundness value below a threshold of $R = 0.75$, or a sphericity value is below $S = 0.9$ are discarded. To a good approximation, a particle with a conical protrusion can be assumed as rotationally symmetric. Then, its geometry can be defined entirely by a single video frame in which the particle symmetry axis is aligned with the focal plane as illustrated in Fig. 3.4. The video image best capturing a view of the symmetry axis is selected by comparing the ratio between the maximum and minimum feret diameter, $d_{\mathrm{f,max}}/d_{\mathrm{f,min}}$, for all frames before the impact and choosing the largest ratio. The symmetry axis through the particle centroid is determined and the distance of each pixel inside the particle to this axis, r_{i}, is computed. The particle volume V_0 is then computed as

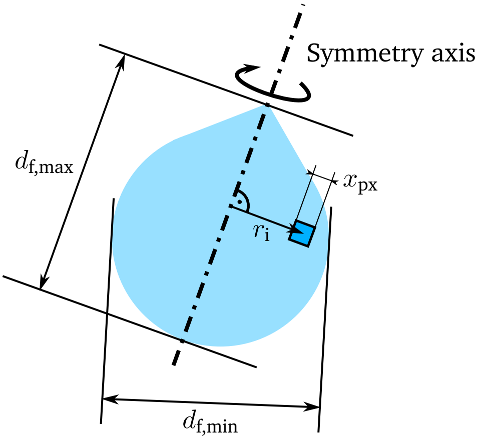

Figure 3.4: Sketch of a rotational symmetric ice particle with a small deviation from a spherical shape.

$$V_0 = \sum_{i=1}^{N} \frac{\pi\, x_{\mathrm{px}}}{2} \left[(r_{\mathrm{i}} + x_{\mathrm{px}}/2)^2 - (r_{\mathrm{i}} - x_{\mathrm{px}}/2)^2 \right], \tag{3.2}$$

where x_{px} is the width of one pixel in metres and N is the number of all pixels in the ice particle image. The particle diameter d_{p} is then defined as the volume equivalent spherical diameter using V_0 as the particle volume

$$d_{\mathrm{p}} = \sqrt[3]{\frac{6V_0}{\pi}}. \tag{3.3}$$

Measurement of the Residual Ice Cone Mass and Base Diameter Ice particle impact experiments of the present work and in literature (Palacios et al., 2014; Hauk, 2016) have shown that some of the particle fragments stick to the impact surface. If the impact surface is at a temperature above the freezing temperature, this sticking residual mass (RM) partially melts. Otherwise, strong cohesive forces between the sintered fragments and adhesive forces between the target and the RM make it difficult to remove it from the target surface.

In this case, it is difficult to directly measure the residual mass using a laboratory precision balance. The strongly adhering residual mass would have to be removed from the target surface and transferred to a balance while ensuring no mass is lost. Detaching the solid residual mass mechanically is very difficult due to its strong bonding to the surface and parts of the ice could either remain on the surface, or on the tool used for removing the ice. Melting the residual mass prior to its transfer is disadvantageous since liquid water wets the target made of sapphire glass very well, making it difficult to remove the residual mass. Furthermore, it must be ensured that an insignificant amount of water evaporates during this process. To measure the mass of the residual cone sticking to the target precisely, a novel indirect measurement technique was developed, which is illustrated in Fig. 3.5. After an impact experiment is conducted at subfreezing target temperatures, the target is heated up first, melting the RM. Then, a heated glass plate with a thin tissue

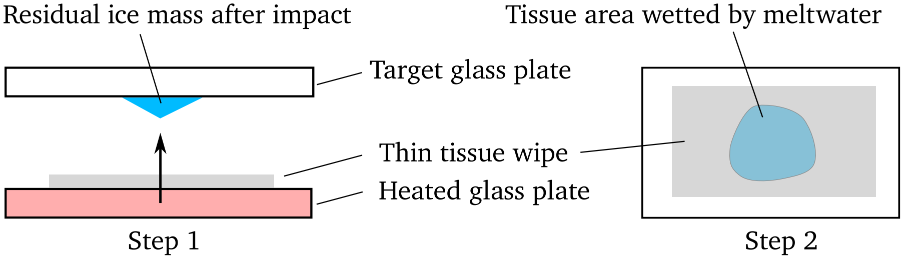

Figure 3.5: Method for the measuring the RM adhering to the target after an impact experiment. For the studied subfreezing target temperatures, the target is heated up first, melting the RM. Afterwards, a heated glass plate with a thin tissue wipe on top is pressed onto the target, and the residual mass wets the tissue, which is visible in the camera view.

wipe (*Kimtech Science*) on top is pressed against the target glass plate. As a result, the residual ice cone melts and wets the tissue leading to a higher transparency of the wetted tissue area. This process is recorded in a view orthogonal to the target surface with a spatial resolution of $46.63\,\mu\mathrm{m}/\mathrm{pixel}$. The wetted tissue area is measured using image processing and can be related to the melted water volume. This wetted area - melted water volume relationship is calibrated for the tissue paper by placing drops of known volume between $0.2\,\mu\mathrm{l}$ and $1.4\,\mu\mathrm{l}$ onto the glass target using a $5\,\mu\mathrm{l}$ Hamilton syringe. The wetted tissue area is measured using the same procedure as for the residual ice cone mass measurement. In Fig. 3.6, the results of the calibration measurements are shown. The expression for the linear calibration curve is

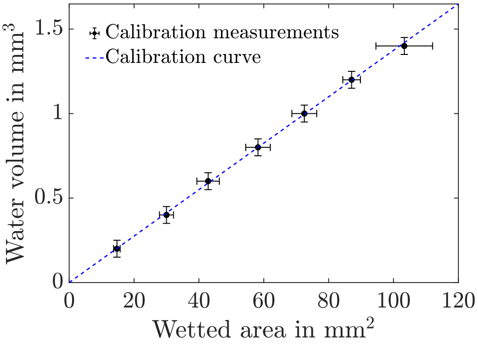

Figure 3.6: Calibration measurements (symbols) and linear calibration curve (dashed line) for the measurement of the mass of a residual ice cone. The dispensed water volume is plotted against the measured wetted area of the used tissue wipe and each symbol represents 6 experimental repetitions. The vertical error bars of $\pm 0.05\,\mathrm{mm}^3$ are based on assuming the accuracy of the dispensed drop volume to be in the order of one syringe graduation step and the horizontal error bars represent the standard deviation of the experimental repetitions.

$$V_\mathrm{w} = 1.374 \times 10^{-2}\,\mathrm{mm} \times A_\mathrm{w}, \tag{3.4}$$

where V_w is the imbibed melt-water volume and A_w is the wetted tissue area. The error of the dispensed drop volume in the calibration measurements cannot be directly quantified. Therefore, the error is assumed to be in the order of one graduation step of $0.05\,\mathrm{mm}^3$ of the syringe, which is shown as vertical error bars in Fig. 3.6. The horizontal error bars correspond to one standard deviation of 6 experimental repetitions. The calibration curve is found by fitting a linear function to the measurements. In addition to the residual mass measurement, the area of the residual mass A_RM visible in the view normal to the impact surface is measured using image processing. For this purpose, the same camera as for the measurement of the wetted tissue is used, having a spatial resolution of $46.63\,\mu\mathrm{m/pixel}$. Using the measured area A_{RM}, a circle equivalent diameter of the residual mass can be computed as $d_{\mathrm{RM,max}} = \sqrt{4A_{\mathrm{RM}}/\pi}$.

Multi-Object Tracking for Fragment Size Analysis After the impact and subsequent fragmentation of an ice particle, a cloud of fragments is ejected radially outwards from the impact location as depicted in Fig. 3.7. Starting with a dense cloud of particles, individual fragments become visible with increasing time after impact. A small amount of ice fragments adheres to the target near the point of impact, as will be discussed in detail in section 4.1.1. At $t = 3.50\,\mathrm{ms}$ after impact, a part of this residual ice mass has already melted, forming transparent drops on the target surface. At its centre, the residual mass is still solid; hence non-transparent, but at later times ($t = 22.00\,\mathrm{ms}$) the last residuals of ice are also melted.

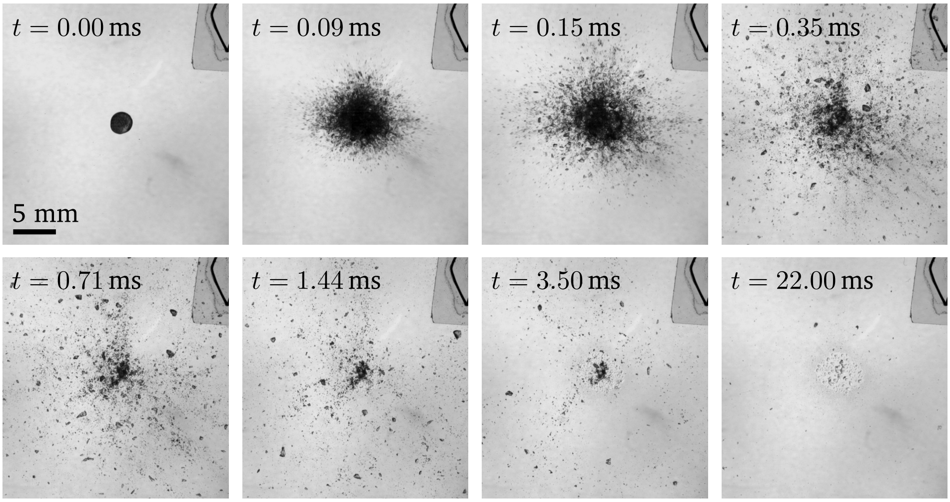

Figure 3.7: Example image sequence of an ice particle impact with $v_{\mathrm{p}} = 73.54\,\mathrm{m\,s^{-1}}$, $d_{\mathrm{p}} = 2.67\,\mathrm{mm}$, $T_{\mathrm{p}} = -34.9\,^{\circ}\mathrm{C}$ and $T_{\mathrm{t}} = 10\,^{\circ}\mathrm{C}$, recorded in a view almost normal to the transparent target. Time $t = 0$ refers to the moment of first contact between the particle and the target as determined from the video material. The surface-thermocouple is visible in the top right corner of the images.

Since the camera recording speed is relatively high, even the fastest detectable fragments in the present experiments are visible at least in 5 video frames before leaving the field of view. Hence, multiple views of the same fragment exist in the high-speed videos, which can be utilized for a more precise fragment size estimation compared to using a single image for fragment size measurements. To do so, a modified version of a Kalman filter tracking algorithm (KAFTA), is used to track all detectable fragments. The algorithm, which originates from a software library pre-implemented in the commercial software *MATLAB*, has been extensively modified to enable accurate motion-based tracking of multiple objects. Due to the high spatial density of fragments emanating from the impact area, a user selected rectangular area near the impact point is excluded from the analysis to reduce incorrect detections and mappings, which may also be associated with the residual ice mass adhering to the impact surface which is not considered for the fragment size distribution. At remote locations from the point of impact, particles are more dispersed, allowing more reliable tracking. During video analysis, all detected fragments are assigned an individual ID, as illustrated in Fig. 3.8, and are tracked along their trajectories through analysis of the entire high-speed video. To ensure the correct evaluation of the fragment size distribution, the data obtained using KAFTA, i.e. the trajectories and measured size of all detected and tracked fragments, are subjected to an improved quality control to ensure a robust analysis. For that, a semi-automatic sorting algorithm is used to discard false or multiple detections of the same fragment based on five selection criteria. If the trajectory of the fragment is not intersecting with the area of impact, its direction of flight is not orientated towards the area of impact or its estimated trajectory length is smaller than $1.5\,\mathrm{mm}$, the data of the fragment is discarded. These false detections to a large extent

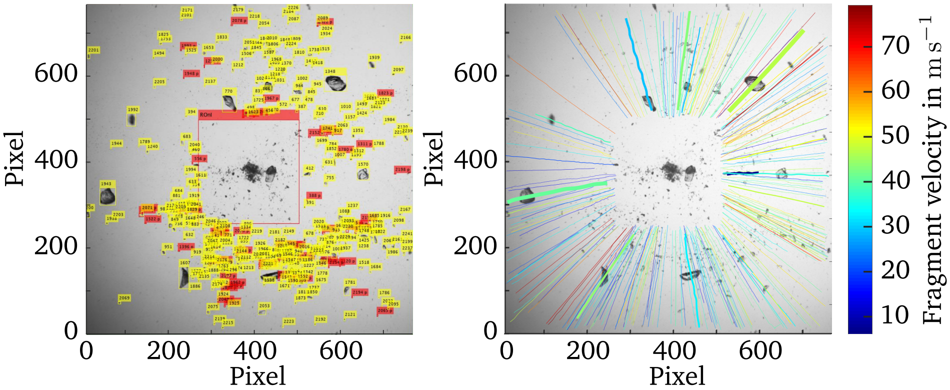

Figure 3.8: Example image of a high-speed video frame, analysed using KAFTA. While the yellow labels correspond to track IDs correctly assigned to the fragments in the video frame, the red labels correspond to tracks which could not be correctly assigned and whose position is therefore only predicted in the current video frame based on the individual equations of motion of the known tracks. On the right side, the obtained fragment trajectories are shown as curves, where the color indicates the average fragment velocity.

originate in high-speed fragments that bounced off from peripheral parts of the experimental setup and subsequently crossed the camera field of view a second time.

A large deviation of the current fragment position from a straight extension of the previous flight direction is considered as the fourth selection criterion. The actual flight direction of a fragment is allowed to deviate from the predicted flight direction by only up to 25° for fragments smaller than $d_\mathrm{f} = 0.4\,\mathrm{mm}$ and up to 45° for larger fragments. Distinguishing fragments according to their size is to prevent dust from the ambient air from being mistaken as an ice fragment. Small ice particles generally tend to be more easily affected by an airflow accompanying the particle impact. During initial stages after impact, the airflow on the target is presumably a well posed stagnation flow; thus, the straight ballistic fragment trajectories are not affected. However, after a certain time, the flow on the target presumably becomes more chaotic, eventually also ingesting dust particles from the ambient into the field of view. These dust particles are associated with a more irregular trajectory, while those of larger fragments originating from initial fragmentation remain straight, also for a more chaotic surrounding flow field. Moreover, for fragments larger than $0.4\,\mathrm{mm}$ in diameter, the rotation of the fragment may cause the centroid to deviate more from a straight line than for smaller fragments which is also accounted for through the distinction.

Over-detection, i.e. consideration of the same fragment as several ones, mainly originates from fragments being obscured by other fragments for more than five consecutive frames, or from a tracked fragment breaking up into smaller fragments. In these cases, the algorithm considers the initially tracked fragment as lost and eventually initializes a new fragment track and thus, the same fragment may be considered as several fragments in the raw tracking data. In order to include a fragment only once in the analysis, a further assignment criterion is defined. During the experiments, it is observed that the rotation rate of a fragment remains almost constant. Thus, the measured centroid trajectory prescribes a straight line superimposed on a sinusoidal motion with almost constant amplitude for all detections of the same fragment. To obtain a robust indicator regarding this phenomenon, a linear OLS regression of the two-dimensional fluctuating centroid position is performed to estimate the 85% confidence region coverage for subsequent fragment positions. Only fragment detections within this envelope are actually considered to potentially be the currently tracked fragment. Deviations of up to 40% in diameter and 50% in velocity are tolerated during candidate selection. Finally, identification as a duplicate is further based on the distance between the end point of the centroid of the original detection where the fragment track is lost and the starting point of the candidate at which it was first detected. If the two trajectories both belong to the same fragment, the distance in flight direction between the impact area and the candidate starting point must be greater than the distance between the end point of the original fragment trajectory and the impact area; i.e. a fragment is required to move radially outwards.

Fragment Volume Estimation A distinguishing feature of the algorithm is its extension with the volume estimation method of Presles et al. (2012) on a per-fragment basis. In this process, a maximum-likelihood estimate based on two geometric descriptors for the size and shape of the projection of a fragment assumed as either a square bipyramidal or an ellipsoidal three-dimensional object is used. It allows to derive not only the estimated fragment volume $\overline{V}_{\mathrm{f}}$, but also its tendency to resemble one of these two convex objects, which are shown in Fig. 3.9. For a comparison of the measured fragments to the test objects, the area A_{f} and two shape parameters $\mathcal{M}_1$ and $\mathcal{M}_2$ of a 2D projection are used,

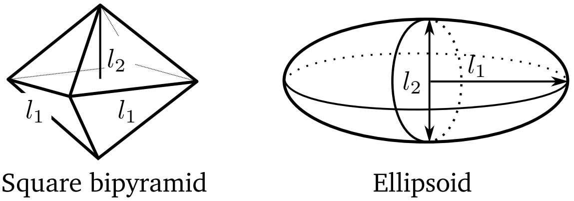

Figure 3.9: Illustration of two test geometries that are used for comparison to the ice particle fragments. On the left, a square bipyramid is shown with edge length l_1 and height of one pyramid l_2. An ellipsoid is shown on the right with minor axis l_2 and major half axis l_1.

$$\mathcal{M}_1 = \frac{d_{\mathrm{f,min}}}{d_{\mathrm{f,max}}}, \quad \mathcal{M}_2 = \frac{4A}{\pi d_{\mathrm{f,max}}^2}, \tag{3.5}$$

where $d_{\mathrm{f,min}}$ and $d_{\mathrm{f,max}}$ are the minimum and maximum Feret diameters, respectively. A large data base of generic square bipyramids and ellipsoids is generated where the parameters l_1 and l_2 are varied systematically. For each object, $655\,362$ 2D-projections from equidistant view points are computed to obtain a statistic for the parameters A, M_1 and M_2 for each combination of l_1 and l_2.
As a result, probability density functions $f^{A}_{\mathrm{l_1,l_2}}(A)$ and $f^{\mathcal{M}}_{\mathrm{l_1,l_2}}(\mathcal{M}_1, \mathcal{M}_2)$ for the parameters A, $\mathcal{M}_1$ and $\mathcal{M}_2$ are obtained for a random 2D-projection of each test object. Here, $f^{\mathcal{M}}_{\mathrm{l_1,l_2}}$ is a combined function for both $\mathcal{M}_1$ and $\mathcal{M}_2$. In order to determine the likelihood of a test shape matching the combination of all measured fragment areas and shapes in i consecutive high-speed video images, all experimentally measured values A^i, $\mathcal{M}_{1,i}$ and $\mathcal{M}_{2,i}$ are inserted in the respective probability density functions. The results are multiplied, leading to a single value for the likelihood. After repeating this process for all test objects in the database, the object with the highest likelihood is chosen and the respective values of l_1 and l_2 are used for an estimation of the fragment volume $\overline{V}_{\mathrm{f}}$. For further details on the computational method, the reader is referred to Presles et al. (2012). Finally, the fragment diameter $\overline{d}_{\mathrm{f}}$ is assumed as the diameter of a volume equivalent sphere as

$$\overline{d}_{\mathrm{f}} = \sqrt[3]{6\overline{V}_{\mathrm{f}}/\pi}. \tag{3.6}$$

When comparing the measured particle volume V_0 with the sum of all measured fragment volumes $\sum_j \overline{V}_0$, it is found that the particle volume is generally over-predicted by the sum of all fragment volumes. Hence, this over-prediction is corrected in a calibration procedure. 15 experiments with low impact velocities are selected, where it can be easily verified that all fragments are robustly tracked and few fine fragments exist. In these experiments, the cumulative volume of all detected fragments over-predicts the volume of the unbroken ice particle by 43% on average. Thus, all fragment volumes are corrected by 43% for the analysis.

Statistical Fit of the Fragment Size Distribution After fragment tracking and cleaning of the data, the shape of the obtained fragment size distribution can be analysed. In Fig. 3.10, two example histograms are shown, resulting from particle impacts with different impact velocities of $27.22\,\mathrm{m\,s^{-1}}$ (Fig. 3.10a) and $73.54\,\mathrm{m\,s^{-1}}$ (Fig. 3.10b) but otherwise similar parameters ($d_\mathrm{p} = 2.7\,\mathrm{mm}$, $T_\mathrm{p} = -35\,°\mathrm{C}$, $T_\mathrm{t} = 10\,°\mathrm{C}$). With increasing impact velocity, absolutely more and relatively smaller fragments are generated after impact, thus altering the shape of the fragment size distribution. A distribution function is fitted to each experimental data set to quantify this shape change as a function of the varied parameters. However, it is generally not unambiguous which type of distribution function is best suited for matching the experimental data and which method is to be used for fitting the respective distribution function.

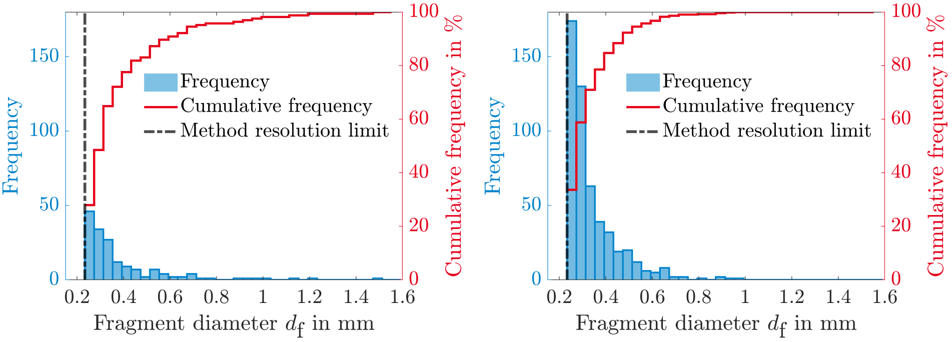

(a) $v_\mathrm{p} = 27.22\,\mathrm{m\,s^{-1}}$; $d_\mathrm{p} = 2.71\,\mathrm{mm}$ **(b)** $v_\mathrm{p} = 73.54\,\mathrm{m\,s^{-1}}$; $d_\mathrm{p} = 2.67\,\mathrm{mm}$

Figure 3.10: Example fragment diameter distribution obtained for particle impact experiments with different velocities. The blue bars represent number frequencies for a bin size of $40\,\mu\mathrm{m}$, while the red curve depicts the cumulative frequency of the fragment diameters. Fragments with an equivalent diameter smaller than 5 pixels are disregarded as indicated by the black dashed line.

For the description of a fragment size distribution, traditionally log-normal, Weibull, and power-law distributions have been assumed (Turcotte, 1997). Based on experimental data for hail particle impact with particle sizes ranging from $12.5\,\mathrm{mm}$ to $50\,\mathrm{mm}$, velocities between $75\,\mathrm{m\,s^{-1}}$ and $275\,\mathrm{m\,s^{-1}}$, and particle temperatures between $-20\,°\mathrm{C}$ and $0\,°\mathrm{C}$, a Rosin-Rammler distribution, which is an integral form of the Weibull distribution, is assumed to describe the resulting fragment sizes in the AGARD model (Garwood et al., 1995). Pan et al. (1996) also fitted a Weibull distribution by applying an OLS algorithm to the experimental data, and they derived empirical models for the two distribution parameters. The shape parameter is thereby approximated by a linear function depending on the normal impact velocity, while the second parameter, the scale parameter, is related to the mean fragment size.

Senoner et al. (2022) utilized the combined experimental data from Reitter et al. (2021), Hauk et al. (2015), Karpen et al. (2021), Vargas et al. (2020), and Guégan et al. (2011) to compare different fitting procedures and distribution functions. They found that the Weibull fit yields unacceptable errors for smaller particle diameters and suggested instead using a power-law function. They utilize a maximum-likelihood estimator for fitting the distribution function to the experimental data for large data sets and a random sample consensus regressor (RANSAC) according to Pedregosa et al. (2011) for small data sets.

The occurrence of a power-law distributed data set may imply scale-invariance of the investigated phenomenon. Accordingly, ice fracture and fragmentation processes indeed appear to exhibit the same characteristic shapes and topologies regardless of the scale involved, whether observed in laboratory specimens on the order of millimetres or in Arctic ice sheets on the order of kilometres. Scale invariance of fracture and fragmentation patterns in ice is originally suggested in Schulson et al. (1991) and Schulson (2001) and evidence for its occurrence is summarised and reviewed in Weiss (2001). Therefore, the existence of scale invariance not only consolidates the use of the power-law distribution purely for statistical data fitting but may also imply a physical meaning.

In the given context, the term "scaling" refers to all functions $\mathcal{F}$ that satisfy the homogeneity relation (Feder, 2013)

$$\mathcal{F}(\varsigma\varepsilon) = \varsigma^{\hat{D}}\mathcal{F}(\varepsilon), \tag{3.7}$$

with a scale factor $\varsigma \geq 0$ and a scaling exponent $\hat{D}$ (Feder, 2013). For a fragment size distribution, the definition of fractals can be extended to be applicable to distinct objects, such as fragments with varying sizes. Introducing the fractal dimension D, which can be determined by counting the number of fragments being larger than a certain threshold value ε, $n(>\varepsilon)$ (Turcotte, 1997), a fractal set obeying Eq. (3.7) is associated with a power-law for the number of fragments as (Weiss, 2001)

$$n(>\varepsilon) \sim \varepsilon^{-D}. \tag{3.8}$$

Accordingly, in the present work, experimentally obtained fragment size distributions are fitted using a power-law ansatz function. It has to be noted that both fragment volume and diameter distributions are analysed, actually leading to different values in each case. For clarity, the power-law parameters for the fragment volume distribution are denoted Ψ and for the fragment diameter distribution Ψ_{d}. From a data analysis point of view, a data set distributed according to a power-law is expressed by the fact that it follows a linear trend in a double logarithmic plot. The slope of this trend provides the exponent of the respective power-law. Data of some physical processes may deviate from a perfect power-law shape through two other characteristic features.

The first is a characteristic (length) scale of the process, for example, a minimum possible fragment size which may lead to a plateau of the distribution at the lower end of the measured parameter. The second feature at the upper end of the scale relates to the maximum fragment size that cannot be larger than the size of the impacting ice particle itself. The latter feature is sometimes referred to as "fall-off" (Burroughs et al., 2001) and leads to a steep decline in the distribution function at the upper end of the measured parameter. The distributions of fragment diameter obtained in the present work in principle exhibit both properties, but show additional characteristics related to the fragment tracking algorithm and volume estimation.

The present fragment volume estimation relies on the morphology of the projected fragment shape. The smaller the projected area of a detected fragment becomes, the less accurate is the estimate of its shape as the three-dimensional convex object assigned to it. One may imagine a small fragment resulting in only one pixel of the projected area. While the true shape may e.g. resemble a flat bipyramid, the assigned shape and subsequent volume calculation are performed for a sphere. To limit the influence of such miss-assignments, a lower bound for the fragment size is introduced in order to improve the accuracy of the measurement. All fragments with a volume equivalent diameter less or equal to five pixels are discarded prior to evaluation, resulting in an artificially and non-physically truncated lower end of the distribution. However, truncation of the data does not necessarily prevent the estimation of the characteristic power-law parameter of the fragmentation process from the experimental data. Depending on the characteristics of the process itself, the data remaining after truncation which is not yet affected by discrete effects from fragment sizes being in the order of the impacting particle at the upper end of the distribution may still allow resolving the scale invariance of the process.

The power-law ansatz function is fitted to the experimental distribution data utilizing the maximum-likelihood method since linear OLS fits are prone to inaccurate estimates, particularly for the case of truncated distribution data (Deluca et al., 2013; Clauset et al., 2009). Moreover, the smallest impact velocity in the experiments only encompasses comparably few (in the order of $\mathcal{O}(10^1)$ - $\mathcal{O}(10^2)$) fragments tracked, which might implicate further difficulties in fitting a power-law, since observed finite-number effects at the upper end of the scale presumably gain increased importance. Since this effect is caused by too sparse data rather than by a change in the involved physics, a power-law is still assumed to be the most appropriate ansatz function. Furthermore, assuming a power-law for the approximation of the distribution of ice fragmentation processes caused by impact allows interpretation of the results in terms of the physical phenomenon of scale invariance for fragmentation processes (Senoner et al., 2022). To mitigate the effects of the fall-off at the upper end of the distribution and still retain the truncation at the lower end, a doubly-truncated, power-law is chosen as the most appropriate distribution function, whose probability density function (PDF), $f(x)$, and cumulative distribution function (CDF), $F(x)$, read as (Deluca et al., 2013)

$$f(\tilde{V}_\mathrm{f}) = \frac{\Psi - 1}{s_-^{1-\Psi} - 1/s_+^{\Psi-1}} \left(\tilde{V}_\mathrm{f}\right)^{-\Psi}, \tag{3.9}$$

$$F(\tilde{V}_\mathrm{f}) = \frac{1/\left(\tilde{V}_\mathrm{f}\right)^{\Psi-1} - 1/s_+^{\Psi-1}}{s_-^{1-\Psi} - 1/s_+^{\Psi-1}}, \tag{3.10}$$

where Ψ is the power-law exponent of the distribution, and s_- and s_+ are the lower and upper cut-off position, respectively. In this relation, $\tilde{V}_\mathrm{f}$ is the distribution of relative fragment volumes, estimated as

$$\tilde{V}_\mathrm{f} = \frac{\overline{V}_\mathrm{f}}{\sum_{i=1}^{N} \overline{V}_{\mathrm{f},i}}, \tag{3.11}$$

where $\overline{V}_\mathrm{f}$ refers to the fragment volume distribution determined using the method of Presles et al. (2012) as described above, which is normalized with the initial particle volume computed as the sum of all individual fragment volumes. Eq. (3.10) is used to obtain a maximum-likelihood estimator according to (Deluca et al., 2013). The maximum of this estimator yields the most accurate value for $\overline{\Psi}$ for a given set of data, based on finding the root of its derivative as (Deluca et al., 2013)

$$\frac{1}{\overline{\Psi} - 1} + \frac{L^{\overline{\Psi}-1} \ln(L)}{1 - L^{\overline{\Psi}-1}} - \ln \frac{G}{s_-} = 0, \tag{3.12}$$

where $\ln(x)$ denotes the natural logarithm, and L and G are defined as

$$L = \frac{s_-}{s_+}, \quad \text{and} \quad G = \exp\left(N^{-1} \sum_{i=1}^{N} \ln\left(\tilde{V}_{\mathrm{f},i}\right)\right). \tag{3.13}$$

While solving Eq. (3.12) yields the most accurate value for the estimated power-law exponent $\overline{\Psi}$, the values for s_- and s_+ are assumed to be known *apriori*. Thus, the task of finding an optimal interval, $V_\mathrm{f} \in [s_-, s_+]$, for which the most accurate fit is obtained, remains. Deluca et al. (2013) suggest using the Kolmogorov-Smirnov (KS) statistic in conjunction with a Monte-Carlo simulation to determine the optimum interval. The KS statistic or KS distance Γ_KS is defined as the maximum absolute difference between the CDF obtained from Eq. (3.10) for a given $\overline{\Psi}$ and the empirical CDF of the data set. In the method, first, a power-law exponent $\overline{\Psi}_0$ is obtained for the non-truncated data set using the maximum-likelihood estimator, and the KS statistic $\Gamma_{\mathrm{KS},0}$ is computed. Afterwards, a large number of M synthetic data sets with the same sample size N as the experimental data are generated using the obtained power-law exponent $\overline{\Psi}_0$ while varying the lower and upper cutoff values s_- and s_+. Such a synthetic volume distribution is obtained by evaluating the following equation N times

$$\hat{V}_\mathrm{f} = s_- \left(1 - \left(1 - L^{\overline{\Psi}-1}\right) \mathrm{rand}\left([0,1[\right)\right)^{-1/\left(\overline{\Psi}-1\right)}. \tag{3.14}$$

By evaluation of the KS distance for each synthetic data set, $\Gamma_{\mathrm{KS,i}}$, the distribution of Γ_{KS} is estimated. If the KS distance for the initial fit $\Gamma_{\mathrm{KS},0}$ is large compared to its estimated distribution using the synthetic data, the fit is considered insufficient, and the assumption of a power-law behaviour should be rejected. Whether this is the case, is quantified using a p-value defined as

$$\mathrm{p_{st}} = \frac{\text{number of simulations with } \Gamma_{\mathrm{KS,i}} \geq \Gamma_{\mathrm{KS},0}}{M}. \tag{3.15}$$

Then, a threshold for p is defined as e.g. $p_\mathrm{c} = 0.05$, below which the initial fit is rejected. Preliminary tests showed the proposed algorithm of Deluca et al. (2013) to yield insufficient results when being applied to some data sets obtained in the present work. The reason lies in the premise of their proposed goodness-of-fit test utilizing the KS distance. Since the KS distance is a single value characterising the goodness of the fit, namely the maximum distance between the fit and the experimental data, it is not robust against noisy data. Thus, large values of p are required, unattainable from the available experimental data, especially for low values of the particle impact velocity where the number of detected fragments is minimal.

Nevertheless, the applicability of their proposed method is possible after minor modifications, namely a replacement of the KS distance as an optimality criterion. So far, the algorithm operates on the premise that testing for specific limits s_-, s_+ is only possible as long as the simulated statistic of the KS distance confirms with a predetermined probability that the tested data set follows a power-law distribution. Under the assumption that the size distribution for the fragmentation process of ice particles follows this distribution, a criterion instead of the KS distance is needed that quantifies the quality of the fit. Thus, a modified optimality criterion is proposed, which is based on the mean absolute difference between the estimated and empirical CDF as

$$\Gamma = N^{-1} \sum_{i=1}^{N} \left| F(\tilde{V}_\mathrm{f}, \overline{\Psi}) - \frac{n(\geq \tilde{V}_\mathrm{f})}{N} \right|, \tag{3.16}$$

where $n(\geq \tilde{V}_\mathrm{f})$ denotes the number of observations with a value larger or equal $\tilde{V}_\mathrm{f}$.
Finally, the full algorithm operates as follows: First, $\overline{\Psi}$ is determined by invoking Eq. (3.12) for the non-truncated data set (s_- and s_+ are equal to the lower and upper limit of the data). By evaluating Eq. (3.16), the proposed goodness of fit criterion Γ is calculated. A Monte Carlo simulation is performed to generate $M = 1000$ sets of random synthetic data fulfilling Eq. (3.9), using $\overline{\Psi}$ from the previous step, still keeping s_- and s_+ equal to the lower and upper limit of the data. For each set of synthetic random data, $\overline{\Psi}_\mathrm{MC}$ and $\Gamma_\mathrm{MC}(\overline{\Psi}_\mathrm{MC})$ are calculated in turn. The value obtained for $\overline{\Psi}_\mathrm{MC}$ will be close to $\overline{\Psi}$, but not equal since the data used to estimate Ψ_MC were randomly generated. These steps so far are consistent with the algorithm originally proposed by Deluca et al. (2013). Now, instead of relying on the threshold p_c for the assessment of the goodness-of-fit, the difference between the Γ for the original $\overline{\Psi}$ and the mean of all Monte Carlo simulations, $\overline{\Psi}_\mathrm{MC}$, is determined as

$$\mathrm{Z}(s_-, s_+) = \left| \Gamma(a, b, \overline{\Psi}) - M^{-1} \sum_{i=1}^{M} \Gamma_{\mathrm{MC},i}(s_-, s_+, \overline{\Psi}_{\mathrm{MC},i}) \right| , \tag{3.17}$$

thus quantifying the goodness of fit for the distribution value Ψ. The criterion Z may now be used to obtain optimal values of s_- and s_+. In the next step, Eq. (3.17) is evaluated for every combination of s_- and s_+ which are varied in discrete steps for every successive $\tilde{V}_\mathrm{f}$, limited by $\tilde{V}_\mathrm{f}$ values of the 10th and 90th percentile, respectively. These limits are invoked to prevent discarding too much data by truncation. Again, $M = 1000$ sets of random synthetic data are generated for each combination of s_- and s_+.

The optimal values of s_- and s_+ with a corresponding value of $\overline{\Psi}$ are finally found from solving the optimization problem to find the combination of s_-, s_+ for which Z is minimal, i.e. $\overline{\Psi}(s_-, s_+)|_{\mathrm{Z}_\mathrm{min}}$. This way, a set of truncation limits is found for which the difference between the optimality criterion for the initially obtained distribution parameter $\overline{\Psi}$ and that for the random data with the same distribution parameter $\overline{\Psi}$ is minimal.

Results of such an optimized distribution fit are shown as an example in Fig. 3.11 for the same experimental run already shown in Fig. 3.7. The cumulative normalized number distribution of the measured relative fragment volumes, $\mathrm{F}(\tilde{V}_\mathrm{f})$, is plotted against the relative fragment volume in Fig. 3.11a), which can also be expressed as the probability of a fragment being larger than a specific volume, $\mathrm{F}(\tilde{V}_\mathrm{f}) = n(\geq \tilde{V}_\mathrm{f})/N$. It can be observed that the doubly-truncated, power-law fit denoted by the red dashed line describes well the experimental data. When compared with a lower-truncated power-law fit, indicated by the black dashed line, it becomes clear that accounting for the upper truncation is necessary to describe the fall-off for large $\tilde{V}_\mathrm{f}$. The same data set as is displayed in Fig. 3.11b) in the form of a histogram of the fragment volume probability density. It can be observed that the doubly-truncated,

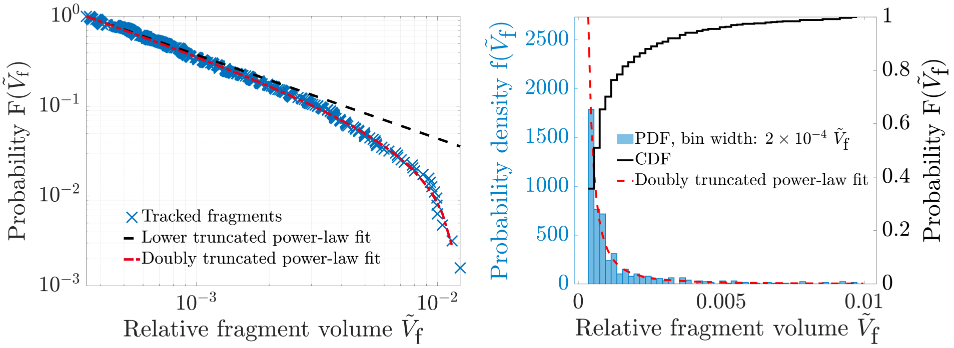

(a) The experimental data is denoted as blue dots, where one dot corresponds to an individual fragment. The black and red dashed lines denote a lower-truncated (for $s_+ \rightarrow \infty$) and doubly-truncated, power-law fit of the data, respectively.

(b) The blue bars represent the probability density for a bin size of 2×10^{-4}, while the black curve depicts the cumulative distribution. The red dashed line denotes the doubly-truncated, power-law fit.

Figure 3.11: Example of a cumulative normalized number distribution (a) and probability density function (b) of measured relative fragment volumes. For the shown data, a value of $\overline{\Psi} = 1.91$ is obtained using the present statistical method. The experimental conditions for the given experiment are $v_\mathrm{p} = 73.54\,\mathrm{m\,s^{-1}}$, $d_\mathrm{p} = 2.67$ mm, $T_\mathrm{p} = -34.9\,°\mathrm{C}$ and $T_\mathrm{t} = 10.0\,°\mathrm{C}$.

power-law fit denoted by the red dashed line again describes well the experimental data. However, the fall-off effect clearly observable in Fig. 3.11a) is no longer visible in this data representation.

3.2 Ice Particle Impact Onto a Wetted Substrate[3]

An experimental methodology is developed to measure the normal and tangential coefficients of restitution, e_{n} and e_{tg}, for ice particles impacting onto a polished aluminium target wetted with a water film of varying thickness. The experimental setup, schematically shown in Fig. 3.12, consists of a temperature controlled aluminium target with a cylindrical water pool. The setup is operated at room temperature, but all crucial parts of the experimental setup are temperature controlled. A cooling fluid circle powered by an external chiller (*Huber, UC020TW*) in combination with a Peltier element is operated to keep the water film temperature at $(0.5 \pm 0.3)\,^{\circ}\mathrm{C}$. The temperature is monitored using a calibrated type K thermocouple

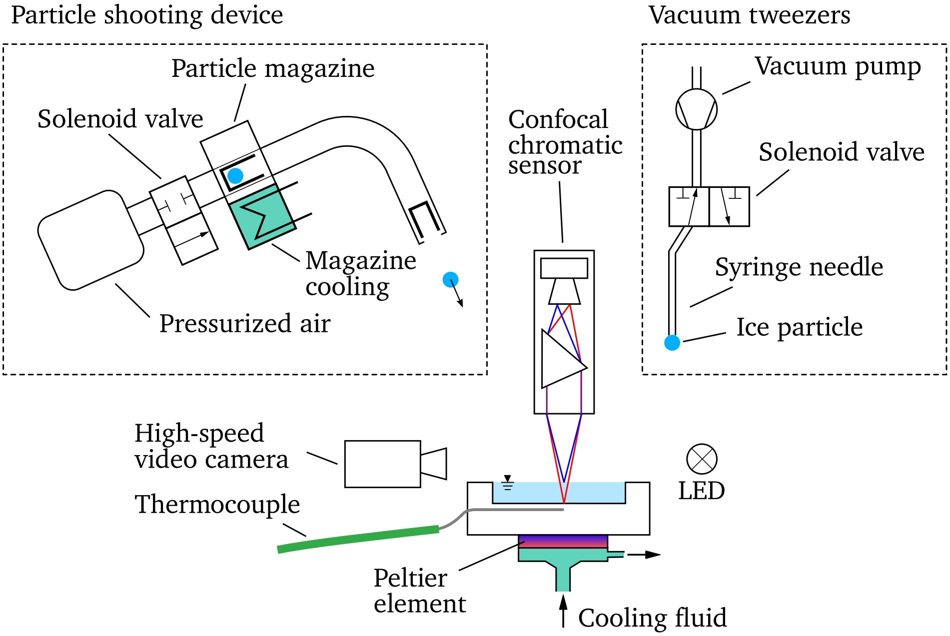

Figure 3.12: Schematic of the experimental setup used to investigate the normal and oblique ice particle impact onto a wetted target. A pneumatic gun is used to accelerate the ice particle to high impact velocities, while vacuum tweezers are used to drop it onto the target at lower velocities. A high-speed video system is used to capture the ice particle impact and the film thickness is measured using a confocal chromatic sensor.

---

[3] The present chapter is based on the Bachelor-Theses of Johannes Heinrich Conrad, Mohammad Sämi Sbeitan, the Master-Thesis of Andreas Mayrhofer and have been published (Reitter et al., 2022b). The original contents have been edited and/or extended for this work.

which is inserted into a drill hole in the target. The temperature sensitive end of the thermocouple is positioned at the target centre, $1\,\mathrm{mm}$ below the target surface as depicted in Fig. 3.12.

Particle Preparation and Acceleration Method Either a pneumatic gun is used to accelerate the ice particles towards the target or vacuum tweezers are used to release ice particles above the target. The particle impact dynamics are captured using a high-speed camera (*Phantom V12* or *Photron SA1.1*) and a continuous LED back light (*Veritas Constellation 120E*). The recording speed is set to 6000 to 8000 frames per second, and the spatial resolution of the camera is $36.94\,\mathrm{\mu m}$/pixel to $48.96\,\mathrm{\mu m}$/pixel, depending on the used setup.
Ice particles are prepared from de-ionised, de-gassed water as described in section 3.1, and stored inside an external insulated box at a temperature of $-5\,^{\circ}\mathrm{C}$. Vacuum tweezers, as schematically shown in Fig. 3.12, are installed in the lid of the box with an air-tight movable ball joint. They are used to pick up the ice particles, reposition them or release them through a hole in the insulated box. This way, low impact velocities with impact angles of 90° can be achieved. The pneumatic gun is used to achieve impact velocities larger than the velocity of an ice particle accelerated only by gravity. In addition, oblique impact angles can be realized when the ejection brass tube (barrel) of the pneumatic gun is tilted. The barrel itself is bent in an angle of 115° to make sure that an ice particle does not fall out through the barrel before an experiment.
For an impact experiment with the pneumatic gun, an ice particle is inserted into a $10\,\mathrm{mm}$ long plastic cup (sabot), with outer diameter of $7.3\,\mathrm{mm}$. The sabot is stored inside the cooled magazine, which is placed in the same box as the ice particles. The magazine is transferred to the particle shooting device and inserted into an insulated aluminium block cooled to a temperature of $-5\,^{\circ}\mathrm{C}$ using a Peltier element and a ventilated radiator, connected to the Peltier element with heat pipes. The ice particle shooting device is driven by pressurized air, supplied to a small buffer tank containing a volume of $4 \times 10^{-4}\mathrm{m}^3$. The tank is connected to a solenoid valve, which is in turn fitted to the aluminium block containing the magazine. The firing tube can be aimed at the impact target at an angle between 90° and 45° relative to the target surface. By activating the solenoid valve, the sabot and ice particle are accelerated inside the brass barrel. At the end of the barrel, the sabot is retained by a removable aperture while the ice particle is ejected through the aperture hole. The impact velocity is set by adjusting the supply pressure using a manually operated pressure regulator with an attached digital manometer.

Wetted, Temperature Controlled Target An impact target is made of aluminium (EN AW-7075), having a thickness of $8\,\mathrm{mm}$. A cylindrical pocket having a depth of $0.7\,\mathrm{mm}$ and a diameter of $50\,\mathrm{mm}$ is milled into the target to serve as a water pool. Using a syringe pump, the pocket is filled with purified, de-ionized water. At the beginning of each experimental day or if changes are made to the experimental setup, the water film thickness is measured at various points next to the target centre to ensure that the target is horizontal. During experiments, the water film thickness at the centre of the target is measured using a confocal chromatic sensor (*Micro-epsilon IFS2406-3*). In case of experiments performed with the vacuum tweezers setup, the liquid film thickness is determined prior to each particle impact. If the pneumatic gun is used, the compressed air used for accelerating the ice particle disturbs the water film, leading to a temporary varying film thickness at the impact point. In order to obtain the exact film thickness the ice particle is impacting, time resolved film thickness measurements are performed during each experiment with a data acquisition rate of $2000\,\mathrm{Hz}$. The measurement is synchronized with the captured high-speed videos, enabling the determination of the actual film thickness at the instance of impact which is used for further analysis. Example measurement data of the film thickness during an ice particle impact event is shown in Fig. 3.13. It can be observed that the film thickness is relatively constant at first ($h = 0.51\,\mathrm{mm}$), until the pneumatic gun is triggered and accelerates the sabot with the ice particle inside the shooting tube. The air displaced by the accelerated sabot exits the shooting tube, disturbing the smooth water surface and decreasing the film thickness, as it can be observed in Fig. 3.13. At the instance of particle impact ($t = 0.345\,\mathrm{s}$), determined visually using the synchronized high-speed video, the film thickness has reached a value of $h = 0.467\,\mathrm{mm}$. Afterwards, large scatter and missing data can be observed due to the particle obscuring the sensor view, before the data quality increases again and the film thickness is observed to tend towards its initial value.

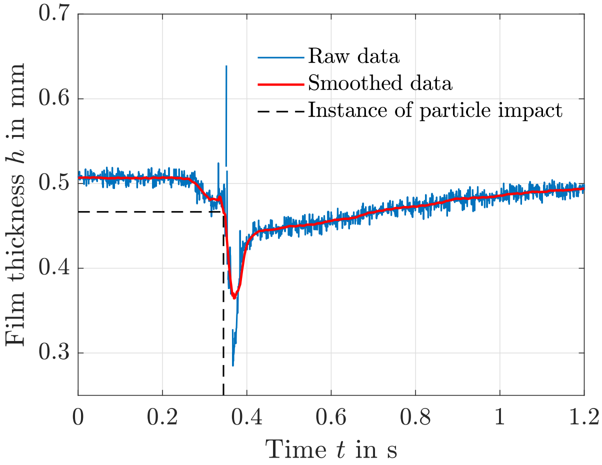

Figure 3.13: Example measurement data of the film thickness. The film thickness corresponding to the instance of particle impact is indicated by the black dashed line.

Coefficient of Restitution Measurement The normal and tangential coefficient of restitution, e_{n} and e_{tg}, are determined for each experiment via image processing of the recorded high-speed videos using an in-house code implemented in the commercial software package *MATLAB*. Prior to impact, the particle centroid is used to determine the particle position in each video frame. After the particle makes contact with the film, a circle is fitted to the particle contour using a pre-implemented function which utilizes the Hough transform; the circle centroid then is used for further analysis.

In the next step, the particle centroid displacement with respect to its position in the first relevant image is plotted against time. Here, a differentiation is made between the travelled distance in the normal and tangential directions relative to the target surface to obtain the normal and tangential CORs, e_{n} and e_{tg}, respectively. In addition, the exact impact angle can be determined this way. In Fig. 3.14, an exemplary particle displacement over time is shown for the direction perpendicular to the target surface. Two linear curves are fitted to the particle displacement over time prior to, and after impact. The actual time of impact, which can be in between two video frames, is determined as the intersection point of the two fitted curves and set to $t = 0\,\mathrm{s}$. As it can be observed in Fig. 3.14, the assumption of a constant particle velocity corresponding to a linear curve fit is reasonable in this case. The slopes of

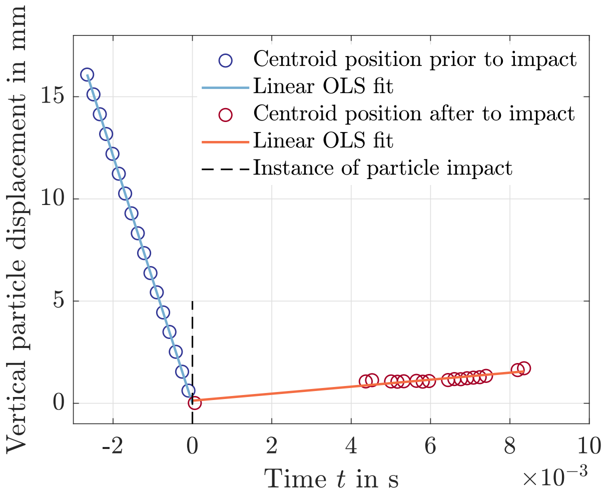

Figure 3.14: Example plot of the particle centroid displacement in the direction normal to the target surface plotted against time for an impact onto a wetted surface. The blue markers correspond to data prior to impact, while the red markers indicate the particle position post impact. Two linear functions are fitted to the data in order to evaluate the particle velocity from their slope.

both curves are evaluated, which are equal to the particle velocity prior to and after impact, and finally, the COR in normal direction to the surface, e_{n}, can be obtained. If the particle is significantly accelerated or decelerated, quadratic functions are used for fitting. Then, the particle velocities prior to and after impact are evaluated using the slope of the fitting functions at the instance of particle impact. For determining the tangential COR e_{tg}, the same methodology as for determining e_{n} is applied. At higher impact velocities, a fragmentation of the particle may be observed. In these cases, the velocity of the largest non-sticking fragment is tracked after impact and used for the determination of the COR.

3.3 Particle Impact Onto a Granular Ice Layer[4]

The experimental setup consists of a device that is able to shoot ice and nylon spheres onto ice accretions generated in the icing wind tunnel (IWT) at Technische Universität Braunschweig (TUBS) and artificial ice layers generated at Technische Universität Darmstadt Icing Laboratory (TUDa IL). In the wind tunnel campaign, all equipment used has been designed in other studies, except for the particle shooting device.

For a realistic ice layer generation in the IWT facilities, an ice crystal generation and conveyance mechanism is used for feeding a cloud of ice crystals into the wind tunnel. The ice crystal cloud impacts onto a metallic flat plate setup with embedded heaters, temperature and heat flux sensors mounted inside the test section of the wind tunnel. Under ambient conditions favouring ice crystal accretion, a macroscopic ice layer forms on the flat plate setup. After the generation of an ice layer, the top wall of the test section is removed and the particle shooting device is introduced into the wind tunnel. Nylon spheres are impacted at different velocities onto the ice layer, leading to craters of varying sizes. A commercial 3D scanner is utilized to determine the crater depth.

At the TUDa IL, the same particle shooting device is used to generate craters in artificial dry and water-filled granular ice layers, manufactured by compressing a defined amount of ice crystals inside a small container. Using this method, the goal is to create granular ice layers with less experimental effort but mechanical properties comparable to ice layers generated in an ICI-representative environment like in the IWT. Similar to the methodology for the ice layers in the IWT, a custom-developed crater scanner is used to determine the crater depth.

Artificial Ice Layer Generation To fabricate reproducible granular ice layers in the laboratory at TUDa, a sufficient number of ice crystals with well-characterized size is necessary. Similar to the procedure reported on by Schremb et al., 2019, ice crystals are generated by vapour deposition at the walls inside a chest freezer, operated at a temperature of $-25\,^{\circ}\mathrm{C}$. The crystals are scraped off several times during a day of experiments and stored in a container, leading to a consistent mixture of old and new crystals that minimizes the influence of possible effects of ice crystal metamorphism (Pinzer et al., 2009) on their shape and size distribution. The crystals are sieved inside the chest freezer using mesh sizes of $1\,\mathrm{mm}$ and $0.71\,\mathrm{mm}$ or $0.45\,\mathrm{mm}$ and $0.15\,\mathrm{mm}$ for obtaining two different size distributions. Ice crystals are either taken from the sieve with a mesh size of $0.71\,\mathrm{mm}$ or $0.15\,\mathrm{mm}$ for sample preparation. The crystals have a mean area equivalent diameter of $1.02\,\mathrm{mm}$, or $0.365\,\mathrm{mm}$ measured in a sample of 1526 and 974 2D crystal images recorded using a microscope. For more

---

[4] Parts of this chapter are based on the Bachelor-Theses of Lion Oster and Aaron Basil Jahn and have been published (Schremb et al., 2019; Reitter et al., 2023). The original contents have been edited and/or extended for this work. The work in the icing wind tunnel of the Technische Universität Braunschweig has been performed in collaboration with Yasir A. Malik.

details about the ice crystal characterization, the reader is referred to Schremb et al., 2019. After sieving, a specific mass of crystals, determined using a scale inside the chest freezer, is taken from the respective sieve. The crystals are carefully poured into a PMMA container with an aluminium guiding sleeve on top as visualized in Figure 3.15. After inserting an aluminium stamp into the guiding sleeve, the whole

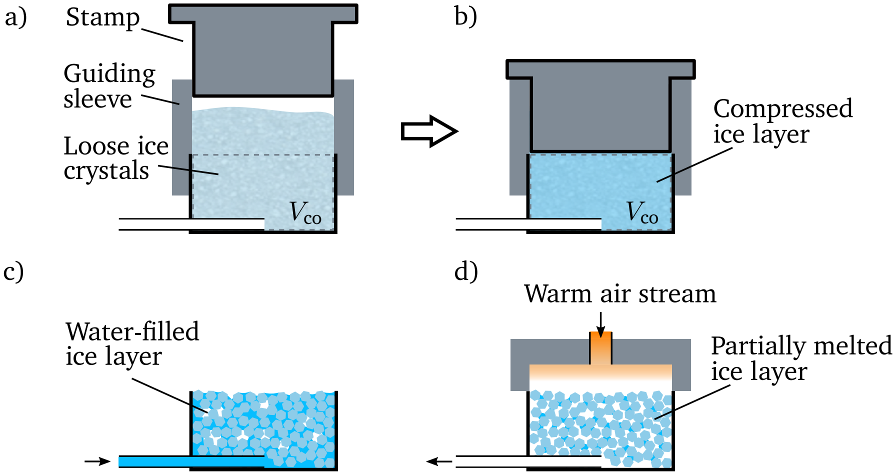

Figure 3.15: Sketch of the procedure for manufacturing artificial ice layers at TUDa IL. An aluminium stamp is used for compressing loose ice crystals inside a container. It has a defined length such that the ice crystals are compressed to a fixed volume V_{c}. After compression, the ice layer can be filled with water through a pipe attached to the ice layer container. Additionally, a warm air stream can be directed through the ice layer, partially melting the ice crystals.

structure is put inside an insulated box. For the generation of the ice layer, all components are placed under a manually operated press outside the chest freezer. The loose ice crystals are compressed to a fixed volume V_{co}, such that the top of the ice layer is at the same level as the top of the PMMA container. The exact mass of ice crystals inside the container is determined by weighing the apparatus before and after inserting the ice crystals using a precision scale (*Kern PNS 600*, measurement accuracy and repeatability of $1\,\mathrm{mg}$). By measuring the container volume V_{co} and the ice crystal mass m_{ice}, the ice layer porosity ψ can be determined as:

$$\psi = 1 - \frac{m_{\mathrm{ice}}}{\rho_{\mathrm{ice}} V_{\mathrm{co}}}, \tag{3.18}$$

where ρ_{ice} is the ice density. When loosely pouring the ice crystals into the container, a large porosity of approximately 0.7 is achieved, typical for the irregular shape of the ice crystals. For the impact experiments, dry layer porosities of 0.4 and 0.6 are manufactured, corresponding to the upper and lower limits of reasonably realizable porosities using the compression method. During the compression procedure, the temperature of the ice layer is monitored using a thermocouple and never exceeded $-6\,^{\circ}\mathrm{C}$ in the experiments. In the present work, several methods are used for altering the ice layer composition. A device is designed to direct a stream of warm nitrogen gas at a temperature of $15\,^{\circ}\mathrm{C}$ through the ice layer, partially melting the ice crystals, as illustrated in Fig. 3.15. The melt water is retained between the ice crystals and frozen afterwards with the goal of enhancing the strength of the ice crystal matrix while keeping the porosity constant. To enable the manufacturing of wetted ice layers, a small pipe is attached to the ice layer container, through which distilled water near the freezing temperature can be infused. In order to achieve lower porosities and a larger crystal matrix strength, the water is drawn out of the layer again after infusion using a syringe. Using this method, a larger quantity of water is retained inside of the ice layer. After freezing the interstitial water, porosities down to $\psi = 0.15$ can be achieved. The water infusion and finally the particle impact experiments are conducted inside a small, temperature-controlled cooling chamber which is presented in more detail in the following.

Cooling Chamber Setup for Impact Experiments It is of the utmost importance that no unwanted phase change happens during experimentation, next to other changes of the ice layer properties that may affect its strength like sintering (Blackford, 2007) or frost build up on the surface of dry ice layers. Hence, a dedicated small cooling chamber is utilized for conducting impact experiments aiming for a strength characterization of artificial ice layers generated at TUDa IL. The experimental setup, which is schematically shown in Fig. 3.16, consists of 3 major parts: a temperature-controlled housing with a separately cooled copper block that serves as a mount for the ice layer, a device to shoot nylon spheres of $3.18\,\mathrm{mm}$ diameter onto the ice layer and a high-speed video system to record the impact process. The ambient air inside the setup is temperature controlled using a bath thermostat (*Lauda, RC 20 CS*) and its temperature is kept in the range of $-1.5\ ^{\circ}\mathrm{C} \pm 0.5\ \mathrm{K}$. Styrofoam walls provide thermal insulation from the surrounding laboratory environment. After a dry ice layer is manufactured, it is stored inside a small insulated box located inside the chest freezer. Prior to each experiment, the insulated box is removed from the chest freezer and the ice layer is transferred quickly from the box to the cooling chamber and put inside a temperature-controlled copper block. Additionally, a thermocouple is inserted $0.5\,\mathrm{mm}$ into the ice layer, $0.5\,\mathrm{mm}$ below its surface as depicted in Fig. 3.16. While transferring the ice layer to the cooling chamber, it is in contact with the warm ($\approx 25\,^{\circ}\mathrm{C}$) laboratory air for less than $5\,\mathrm{s}$ before the cooling chamber is closed again. It is assumed that during that time, the amount of heat transferred to the layer is negligibly small and does not lead to any significant phase

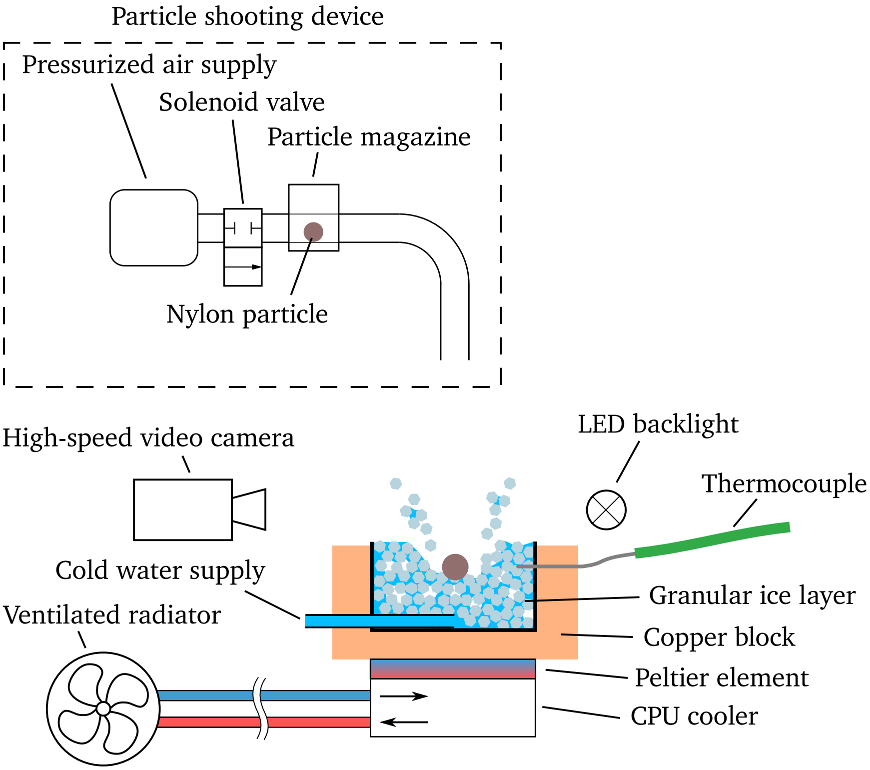

Figure 3.16: Sketch of the cooling chamber setup used for conducting impact experiments in the TUDa IL. It consists of an ice layer cooling apparatus, a device to shoot nylon spheres and a high-speed video system, located inside a styrofoam housing, which, for clarity, is not displayed.

change at the layer surface.

At a sub freezing temperature of a dry ice layer, three other mechanisms may affect its strength, possibly leading to non-repeatable experiments. First, the unconfined brittle compressive strength of ice is temperature dependent, ranging from e.g. $14\,\mathrm{MPa}$ at $-35\,^{\circ}\mathrm{C}$ to $2\,\mathrm{MPa}$ at $0\,^{\circ}\mathrm{C}$ (Schulson et al., 2009, p. 246). Second, starting from the instance of the ice layer compression, single ice particles sinter together (Blackford, 2007), forming stronger inter-particle bonds with increasing time. Arakawa et al. (2011) showed in their experiments, that the dynamic strength of dry porous ice targets, similar to the ones used in the present work, increases with sintering time, following a power-law relationship $\sigma \propto t^{0.28\pm0.03}$. According to this relation, the ice layer strength they measured increases by e.g. $21\,\%$, if the sintering time is increased from $10\,\mathrm{min}$ to $20\,\mathrm{min}$. Third, if the humid air surrounding the ice layer is over-saturated with respect to the ice surface temperature, frost forms at the ice layer, possibly altering the ice layer strength. By controlling the boundary conditions in the experiment as precisely as possible, the effect of these mechanisms on the repeatability of the ice layer strength is minimized. After inserting the ice layer into the cooling chamber, its measured temperature varies between $-6\,^{\circ}\mathrm{C}$ and $-11\,^{\circ}\mathrm{C}$. Inside the cooling chamber, the ice layer is warmed up for $20\,\mathrm{min}$ by setting the temperature of the copper block to $-1\,^{\circ}\mathrm{C}$, reaching a final temperature varying between $-2.7\,^{\circ}\mathrm{C}$ and $-1\,^{\circ}\mathrm{C}$. By constantly flooding the cooling chamber with a stream of pre-cooled gaseous nitrogen, the relative humidity inside the chamber is kept between $39\,\%$ and $58\,\%$ at a maximum ambient temperature of $-1\ ^{\circ}\mathrm{C}$, leading to a minimum dew point temperature of $-11.9\ ^{\circ}\mathrm{C}$ (Wagner et al., 2011). As a result, no frost growth is observed, since it is ensured that the ice layer temperature is always above the dew point temperature. In the laboratory experiments, impacts onto dry and wetted ice layers are investigated. In order to investigate the influence of water saturation of a porous ice layer on its strength, distilled water is pumped into the ice layer through the small pipe attached to the ice layer container. For the quantification of the water amount inserted into the ice layer, a pore filling ratio ϵ is defined,

$$\epsilon = \frac{V_{\mathrm{l}}}{\psi V_{\mathrm{co}}}, \tag{3.19}$$

where V_{l} is the liquid water volume. The water is supplied from a reservoir surrounded by an ice-water mixture to keep its temperature near the freezing point. As sketched in Fig. 3.16, the tube attached to the ice layer cup is connected to the cold water reservoir. The reservoir is airtight and connected to a syringe pump which displaces a defined volume of water V_{l} from the reservoir into the ice layer. All wetted ice layers are filled to such an extent, that the water level is observed to reach the top of the layer. By measuring V_{l} using the syringe pump displacement and having computed the ice layer porosity Φ, the pore filling ratio ϵ can be derived for all wetted ice layers.

In order to conduct an impact experiment, the solenoid valve connecting the pressurized air supply and shooting tube (see Fig. 3.16) is opened for a fixed time of $\approx\,100\,\mathrm{ms}$. Thereafter, the pressurized air accelerates the nylon sphere having a diameter of $3.18\,\mathrm{mm}$ towards the ice layer. By setting the air pressure to values between 0.4 bar and 10 bar, impact velocities between $5\,\mathrm{m\,s^{-1}}$ and $90\,\mathrm{m\,s^{-1}}$ can be achieved. The impact dynamics are captured using a high-speed camera (*Phantom V12* or *Photron SaX2*) recording at a frame rate between 6000 fps and $20\,000$ fps with a spatial resolution of $38.84\,\mathrm{\mu m}$/pixel in order to measure the particle velocity prior to impact via image processing.

Crater Depth Measurement of Artificial Ice Layers Determination of the crater depth is performed using a custom built laser profilometer. The scanning device is portable and can be operated inside the chest freezer in order to prevent the melting of the ice layers. It consists of a miniature line laser, a system to hold the ice layer cup and a high resolution camera (*JAI SP-5000M*), recording images with an average spatial resolution of $25\,\mu\mathrm{m}$. The camera is mounted at a fixed angle of 45° relative to the ice layer surface, capturing the reflection of the laser line. Before scanning, the ice layers are spray-coated with a thin layer of white pigments (*AESUB white*), making the ice layer surface non-transparent. The laser is mounted above the ice layer on a linear translation stage, as schematically shown in Fig. 3.17, allowing it to be moved across the ice layer surface in the direction of the depicted y-axis. In the centre of Fig. 3.17, a recorded image is sketched along with an image coordinate system (x', y'). Since the ice layer surface is always placed at the same height ($z = 0$), the y position of the laser line is an explicit function of the horizontal laser position in the recorded images ($y_0 = f(y'_0)$). Via image processing, y'_0 is determined by averaging the laser position in an area next to the crater as indicated by the blue area in Fig. 3.17. In order to obtain the correct contour of the laser line $z_l(x)$, all camera images are transformed using existing *MATLAB* functions, leading to an image of the laser line in the transformed coordinate system (x'', y''). The projective transformation matrix $\boldsymbol{T}(y)$ is dependent on the y coordinate since the camera magnification and image distortion are changing along it. $\boldsymbol{T}(y)$ is determined via traversing a checkerboard target oriented parallel to the $x-z$ plane a distance of $25\,\mathrm{mm}$ along the y axis in steps of $2.5\,\mathrm{mm}$. $\boldsymbol{T}(y)$ is a 3-by-3 matrix which can be written as

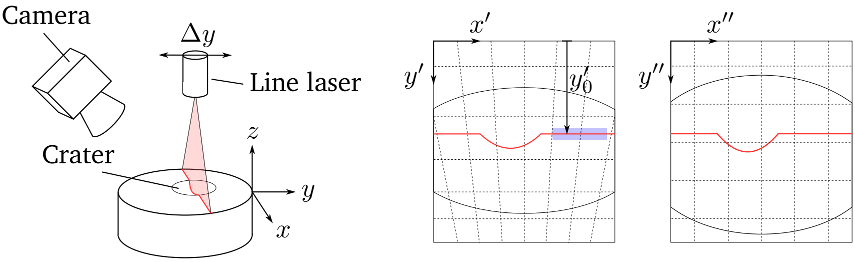

Figure 3.17: Sketch of the laser scanner working principle.

$$\boldsymbol{T}(y) = \begin{bmatrix} T_{1,1} & T_{1,2} & T_{1,3} \\ T_{2,1} & T_{2,2} & T_{2,3} \\ T_{3,1} & T_{3,2} & T_{3,3} \end{bmatrix} . \tag{3.20}$$

The individual matrix entries $T_{i,j}$ can be written as

$$\begin{aligned}
T_{1,1} &= T_{sc,x'}(y)\cos(q(y)) && (3.21a)\\
T_{1,2} &= T_{sc,x'}(y)\sin(q(y)) && (3.21b)\\
T_{1,3} &= T_{vp,x'}(y) && (3.21c)\\
T_{2,1} &= T_{sh,x'}(y)T_{sc,y'}(y)\cos(q(y)) - T_{sc,y'}(y)\sin(q(y)) && (3.21d)\\
T_{2,2} &= T_{sh,x'}(y)T_{sc,y'}(y)\sin(q(y)) + T_{sc,y'}(y)\cos(q(y)) && (3.21e)\\
T_{2,3} &= T_{vp,y'}(y) && (3.21f)\\
T_{3,1} &= T_{tr,x'}(y) && (3.21g)\\
T_{3,2} &= T_{tr,y'}(y) && (3.21h)\\
T_{3,3} &= 1 && (3.21i)
\end{aligned}$$

where $T_{sc}(y)$ and $T_{sh}(y)$ denote the scaling and shear factors in x' and y' direction, respectively. $T_{vp}(y)$ denotes the vanishing point coordinates and $q(y)$ denotes a clockwise image rotation angle. At each step the checkerboard image is traversed, and the obtained transformation matrix is decomposed in the factors $T_{sc,x'}, T_{sc,y'}, T_{sh,x'}, T_{sh,y'}, T_{vp,x'}, T_{vp,y'}$ and q, obtaining a total of 11 values per factor. Finally, the expressions for each factor depending on the y-position, e.g. $T_{sc,x'}(y)$, are obtained by fitting linear functions to 11 data points, $T_{sc,x'}(y) = T_{sc,x',0} + y\,T_{sc,x',1}$.
For a reconstruction of the impact crater, in all video frames the parameter y'_0, the distorted laser contour $y'_\text{l}(x')$ and the transformation matrix $\boldsymbol{T}(y_0)$ are determined. They are used to transform all recorded laser contours $y'_\text{l}(x')$ to non-distorted contours $z_\text{l}(x) = y''_\text{l}(x'') = \boldsymbol{T}(y_0)y'_\text{l}(x')$. All transformed laser contours are combined into a point cloud. The values of this point cloud are interpolated on an equidistant $x-y$ grid with $10\,\mu\text{m}$ spacing. After applying a median filter on the z values with $300\,\mu\text{m}$ window size in x and y directions, the crater depth is computed. For this purpose, a first-degree polynomial surface is fitted to the measured points outside the crater area in order to obtain the position of the undisturbed ice layer. Subsequently, the crater depth is computed as the maximum distance between the fitted surface and the crater surface.

Icing Wind Tunnel Facility A part of the experimental results is obtained from experiments performed at the Icing Wind Tunnel (IWT) of Technische Universität Braunschweig (TUBS). An elaborate overview of the testing facility with details concerning the design, construction and commissioning of the wind tunnel is documented in detail by Bansmer et al. (2018). In Fig. 3.18 an illustration of the TUBS IWT is shown, comprising the details important for the present work. The closed loop tunnel schematically shown in Fig. 3.18a) enables flow velocities reaching up to $40\,\text{m}\,\text{s}^{-1}$ in a test section with a cross-sectional area of $500\,\text{mm} \times 500\,\text{mm}$. The static temperature inside the tunnel can be maintained in the range of $-20\,^\circ\text{C}$ to $30\,^\circ\text{C}$.

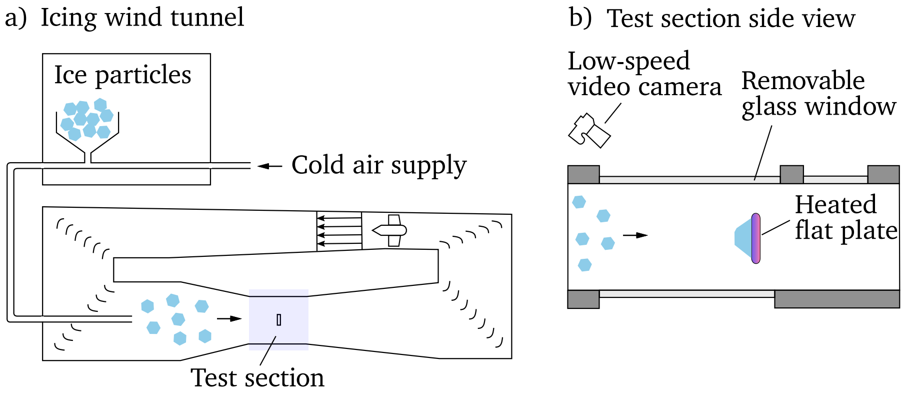

Figure 3.18: Schematics of the icing wind tunnel a) next to a detailed sketch of the test section b) based on Baumert et al. (2016) and Bansmer et al. (2018). Ice particles are generated in a separate cooling chamber and fed into the wind tunnel via a cold air stream. The test section is visually accessible via glass windows that can be removed. A low-speed camera is installed to record the ice accretion process onto a heated flat plate.

Since the air is saturated with water vapour in all experiments for the present work, the static temperate is equal to the wet-bulb temperature in all cases. Ice crystals are generated inside a separate cooling chamber whereas the generation, dosing, sieving and finally transport of the ice crystals to the wind tunnel test section takes place. The cooling chamber has an independent cooling unit providing an ambient temperature of $-15\,^{\circ}\mathrm{C}$. For ice crystal generation, a cloud chamber technology is employed to simulate the naturally occurring process in atmospheric clouds. Inside the cooling chamber, atomized water droplets are fed by an air stream into balloons where they mix with cooled air. Pressure impulses are generated inside the balloons, promoting nucleation of the supercooled droplets. Ice crystals start to grow in expense of the ambient vapour or due to collisions with other liquid droplets, ice crystals or the balloon walls. Once the ice crystals reach a critical size, they settle into the bottom of a freezer placed below the balloons. From there, the ice particles are taken and injected into the wind tunnel through a pipe using a stream of cold air. The ice particles arrive at the test section shown in detail in Fig. 3.18b) in the form of an icing cloud which impinges onto a heated flat plate. A low-speed video camera, recording at a frame rate of $25\,\mathrm{s}^{-1}$, is directed at the flat plate. It is used to obtain a qualitative observation of the ice accretion growth from an oblique perspective.

The ice crystal feeding system enables a variation of the ice water content in the

range of 3 to 20 $\mathrm{g\,m^{-3}}$ inside the test section. In an icing cloud characterization study, the particle size distribution in the test section was found to have a median mass diameter of $\mathrm{D_{50}} = 80\,\mathrm{\mu m}$. The particle diameter at 10 and 90 percent of the cumulative mass distribution was found to be $\mathrm{D_{10}} = 20\,\mathrm{\mu m}$ and $\mathrm{D_{90}} = 220\,\mathrm{\mu m}$, respectively (Bansmer et al., 2018).
To study heat transfer physics and ice accretion phenomena on a heatable metallic substrate, a flat plate test article was designed in other studies[5]. The flat plate setup is composed of multiple layers with a base support structure responsible for providing structural strength. It has a cross section of $100\,\mathrm{mm}$ x $20\,\mathrm{mm}$ with semicircular edges and a span of $500\,\mathrm{mm}$. In the wind tunnel experiments, its face is directed perpendicular to the stream of impacting ice particles. A rectangular pocket is milled into the support structure, into which heaters, temperature and heat flux sensors are inserted. To avoid any heat loss to the sides of the pocket, Teflon strips are installed. For insulation in the bottom direction, an layer with low thermal conductivity (*Multitherm Insulation 550M*, $\lambda = 0.023\,\mathrm{W\,m^{-1}\,K^{-1}}$) is installed. This ensures heat flux mainly in one direction i.e., towards the impinging ice crystals. To provide the heating capability, a total of six heat foils are glued to the aluminium plate. The heat foils are placed such that they are able to provide uniform heating to the flat plate model, providing a total heating power of $326\,\mathrm{W}$ leading to a maximum heat flux of approximately $15\,\mathrm{kW\,m^{-2}}$. To measure the temperature evolution and heat flux inside the test article as a result of impinging ice crystals, a total of 34 PT1000 temperature sensors and five heat flux sensors (Differential-Temperature Thermopile) are installed $0.3\,\mathrm{mm}$ below the target surface.

Ice Layer Generation in the Wind Tunnel For a generation of ice layers under different regimes (slushy and glaciated ice layers), the focus was set on the influential parameters heat flux, tunnel wet-bulb temperature and ice water content. The airflow speed was set to $40\,\mathrm{m\,s^{-1}}$ in all experiments. In Table 3.1, all varied parameters of the wind tunnel settings are summarized. These settings were chosen after preliminary tests, since they led to fast-growing ice accretion on the test article in either the slushy or glaciated layer regime. While a positive wet-bulb temperature

ICE LAYER ID	1	2	3	4
T_{wb} in °C	2	2	2	−2
$\dot{q}_{\mathrm{heater}}$ in $\mathrm{kW\,m^{-2}}$	2.8	5.6	8.3	8.3
IWC in $\mathrm{g\,m^{-3}}$	5	5	5	10

Table 3.1: Varied parameters wet-bulb temperature T_{wb}, heat flux $\dot{q}_{\mathrm{heater}}$ and ice water content IWC in the wind tunnel experiments.

---

[5] The test article was designed by Yasir A. Malik and is presented in more detail in Malik et al. (2023).

of $T_{\mathrm{wb}} = 2\,^{\circ}\mathrm{C}$ (ID 1,2,3) led to slushy ice layers with low cohesion between the individual particles of the porous ice matrix, a negative wet-bulb temperature of $T_{\mathrm{wb}} = -2\,^{\circ}\mathrm{C}$ (ID 4) led to a strong porous ice matrix. Although no quantitative measure was performed, the pore volume of all ice layers appeared to be filled with water to a large extent, with only a few air bubbles trapped inside the porous ice matrix.

All experiments are performed in such a way, that the heated model is first allowed to reach thermal equilibrium with the running wind tunnel, while a removable windshield is installed in a location upstream of the model. In order to start an experiment, particles are fed into the air stream for 30 seconds to obtain a constant max flux of ice crystals in the test section after an initial ramp-up. Afterwards, the windshield is removed, allowing for ice crystal impingement onto the heated model. In Fig. 3.19, a temperature evolution plot is shown along with images of the test article, corresponding to an experiment with a heating power of $50\,\mathrm{W}$, tunnel wet-bulb temperature of $-2\,^{\circ}\mathrm{C}$, ice water content of $10\,\mathrm{g\,m^{-3}}$ and a flow speed of

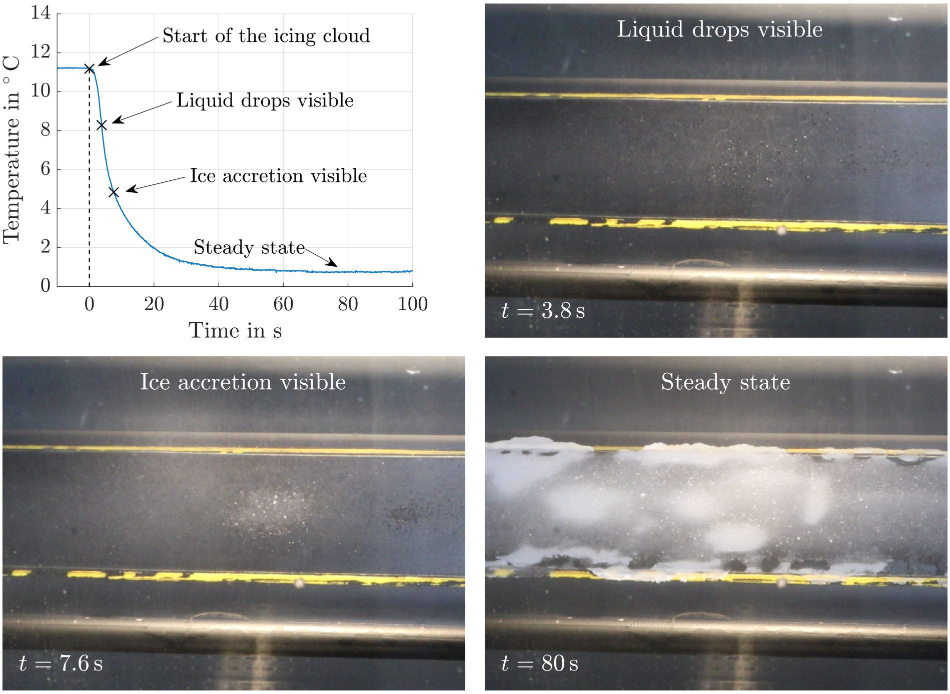

Figure 3.19: Temperature evolution plot along with example images of different stages of the ice accretion process. The time $t = 0\,\mathrm{s}$ corresponds to the instance the icing cloud shield is removed. Temperature measurements are taken using a PT 1000 sensor located below the test article surface.

$40\,\mathrm{m\,s^{-1}}$. Here, the measurement of just one temperature sensor located in the centre of the model is shown for simplicity, the other temperature readings show a similar trend. As it can be seen in Fig. 3.19, the test article has reached thermal equilibrium at $t < 0\,\mathrm{s}$. When the icing cloud shield is removed at $t = 0\,\mathrm{s}$, the impact of ice crystals cools down the surface fast, with liquid drops visible on the surface at first ($t = 3.8\,\mathrm{s}$). Thereafter, ice crystals are captured by the liquid water, visible as a brighter appearance of the accretion ($t = 7.6\,\mathrm{s}$). After an initially large temperature gradient, the temperature measured below the test article surface tends to a value close to the freezing point, while a larger ice accretion is developing.
Once the ice layer is generated, the tunnel is turned off and the flat plate model is rotated 90 degrees with the ice layer facing the top window of the test section as shown in Fig. 3.20a). The top window is taken off for access and similar to the procedure with the artificial ice layers, $3.18\,\mathrm{mm}$ nylon spheres are shot onto the ice layers at velocities between $18.1\,\mathrm{m\,s^{-1}}$ and $88.7\,\mathrm{m\,s^{-1}}$. For shooting the nylon spheres, a modified version of the particle shooting device depicted in Fig. 3.20a) is lowered into the test section. It is equipped with a Peltier cooled magazine, to lower the nylon sphere temperature to $-5\,^{\circ}\mathrm{C}$ before each experiment in order to prevent the melting of the ice layer during and after impact. Furthermore, two

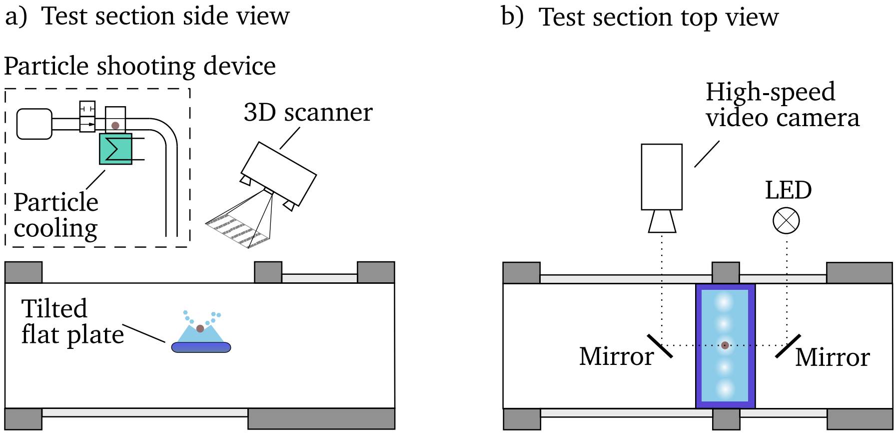

Figure 3.20: Illustration of the methodology for generating impact craters in an ice layer generated in the wind tunnel. In a side view of the test section a) a sketch of the particle shooting device is shown which can be lowered into the test section. Afterwards, a 3D scanner is used to measure the ice layer geometry. In a top view of the test section b) the high-speed video system is displayed, which is used to measure the particle impact velocity.

mirrors are mounted beside the shooting tube, to be able to observe the impact process through the side window of the test section using a high-speed camera (*Photron Sa-Z*, recording at 20 000 frames per second) and LED illumination (*Veritas Constellation 120E*).

Since the ice layers extend over a large region along the span of the flat plate model, nylon spheres are shot at 5 different spanwise positions onto the ice layers while varying the impact velocity. Afterwards, the ice layers are spray coated with a thin layer of white pigments (*AESUB white*). A commercial 3D scanner (*GOM Atos Core*) is introduced into the test section which captures the entire ice layer topography.

4 Experimental Results

In the present work, impact processes relevant to aircraft engine icing are studied. The experimental results of three investigated phenomena are presented in the following sections: ice particle fragmentation after impact onto a dry, cold and heated substrate, ice particle sticking and rebound after impact onto a wetted substrate and the crater formation after particle impact onto dry and wet granular ice layers.
Ice particle fragmentation leads to a change of the fragment size distribution inside the engine, affecting fragment trajectories and melting rates. These quantities control the local ice and liquid water mass flux, key parameters for determining engine areas prone to ice accretions. Due to its importance for the prediction of ice crystal icing, the fragmentation of single ice particles is investigated experimentally with significantly higher accuracy compared to present literature. Results for a mass of ice fragments adhering to the target at sub-freezing temperatures, quantified for first time, are discussed. An empirical model is proposed for the fragment size distribution as well as a semi-empirical model for the fragment mass adhering to the target at a sub-freezing target temperature.
Inception of ice accretion starts with a liquid film wetting an engine surface, enabling the capture of impinging ice particles. The number of captured ice particles controls the cooling rate of the liquid film and the surface beneath. If the freezing temperature is reached, macroscopic fragment agglomerations strongly adhere to the substrate and ice accretion is initiated. In this context, the ice particle impact onto a liquid film is studied experimentally with a focus on the coefficient of restitution. Since the particle impact on wetted substrates is intensively studied in literature, the present focus is set on the specific material response of ice in this case.
Ice accretion growth is a balance between adhering fragments and erosive effects of large fragment impacts. Currently, ice layer accretion and erosion modelling relies on adjustable parameters for the ice layer material properties. In order to advance this practice, a dynamic strength testing method for dry and wet granular ice layers is proposed. The method is applied to obtain characteristic strength values of ice accretion generated in an icing wind tunnel and of artificial ice layers generated in the laboratory.

4.1 Ice Particle Impact Onto a Dry Substrate[1]

Ice particles first impact onto dry surfaces at a sub-freezing temperature in an engine icing scenario. They fragment, and a debris cloud further traverses the engine. As the fragments subsequently impact onto rotating and stationary parts of the engine core, they encounter surfaces at above freezing temperatures, yet no liquid film has to be present. Thus, the ice particle impact onto a dry substrate is of vital importance for accurately modelling the particle size distribution for predicting ice crystal icing.

Ice particle impact experiments have shown that some of the particle fragments stick to the impact surface even with the particle and target being at subfreezing temperatures (Palacios et al., 2014; Hauk, 2016). Thus, this sticking mechanism does not depend on a macroscopic liquid layer neither on the ice particle nor the target. If the impact surface is at a temperature above the freezing temperature, this sticking residual mass partially melts and acts as an additional source for liquid water, promoting the adhesion of subsequent impacting ice particles. In the present work, the quantity of a residual ice mass deposited after normal impact of a nearly spherical ice particle onto a dry solid substrate is studied experimentally and modelled theoretically. A full factorial experimental design (FFD) is employed to determine the significance of the varied parameters impact velocity, particle diameter, particle temperature and target temperature on the resulting residual mass (RM). The strength of each effect is quantified and discussed afterwards. Finally, a semi-empirical model is proposed for the amount of residual mass for sub-freezing temperatures.

Additionally, the ice particle fragmentation is studied, while particle and substrate temperatures are varied systematically without introducing any liquid water before impact. A FFD is employed again to determine the effect of the parameters impact velocity, particle diameter, particle temperature and target temperature on the resulting fragment size distribution. A maximum-likelihood estimation is performed to fit a doubly-truncated power-law to the fragment size distributions and the power-law parameter is used to quantify the effect of the varied experimental parameters on the size distribution. By analyzing the dependency of the power-law parameter on the impact velocity, implications for the underlying fracturing process are discussed and compared to numerical investigations in literature. Under the premise that ice fragmentation processes are fractal in nature, a comparison between the present observations and findings for low strain-rate ice fracture at large scales is made.

---

[1] Parts of this chapter are based on the Bachelor-Thesis of Hannes Lohmann and the Master-Thesis of Maximilian Lausch and have been published (Reitter et al., 2021; Reitter et al., 2022a; Lausch* et al., 2023). The original contents have been edited and/or extended for this work.

4.1.1 Formation of a Residual Ice Mass

Ice accretion mechanisms in aeronautical engineering typically involve freezing of liquid water deposited by impinging drops or start with mixed-phase conditions when a surface water film leads to the capture of ice particles. However, experiments on ice particle impact revealed that some of the particle fragments stick to the impact surface even when the particles and the target are below the freezing point (Palacios et al., 2014; Hauk, 2016). Thus, this adhesion mechanism seems not dependent on a macroscopic liquid layer on the ice particle or target prior to impact. If the impact surface has a temperature above the freezing point, this adherent residual mass partially melts and acts as an additional source of liquid water, promoting the adhesion of subsequent impacting ice particles.

In the present study, the formation of a residual ice mass after the normal impact of a nearly spherical ice particle onto a dry solid substrate is studied experimentally and modelled theoretically. The impact, deformation and fragmentation of the ice particle are observed using a high-speed video system. The mass of the nearly conical residual ice agglomerate and its area on the target surface are then measured for different particle diameters, impact velocities, temperatures and target temperatures.

Based on a simplified hydrodynamic model of Roisman (2022), a theoretical description of the particle deformation during an impact is used to describe the residual ice cone size. In the model, the velocity field in the deforming particle is approximated by a kinematically admissible inviscid flow. The pressure field in the particle is integrated, accounting for the rheology of the material, including hardening effects during plastic deformation, namely the dependence of the yield strength of ice on the local strain rate. Finally, the equations of motion of the particle are solved, which allows a prediction of the maximum dimensionless particle dislodging, which can be viewed as the dimensionless distance of the particle rear from the target (see Roisman (2022)). The dimensionless particle dislodging parameter is then used for the development of an appropriate scale for the typical size of the residual ice cone. A semi-empirical model for the cone height is proposed at the end of the section that can be used in engineering applications for a prediction of the residual ice mass.

4.1.1.1 Qualitative Analysis and Experimental Observations

In Fig. 4.1, an example image sequence of an impacting ice particle is shown. As described in section 3.1, the ice particle gun is oriented vertically such that the particles are ejected against the direction of the acceleration due to gravity. In the moment of impact at $t = 0\,\mathrm{s}$, an ejection of fine fragments near the impact surfaces can be seen, analogous to a prompt splash during a liquid drop impact. The impact leads to particle fragmentation and formation of a cloud of large fragments, which is investigated in section 4.1.2. As shown in Fig. 4.1, some of the ice particle fragments form a conical shape and remain adhered to the target long after the

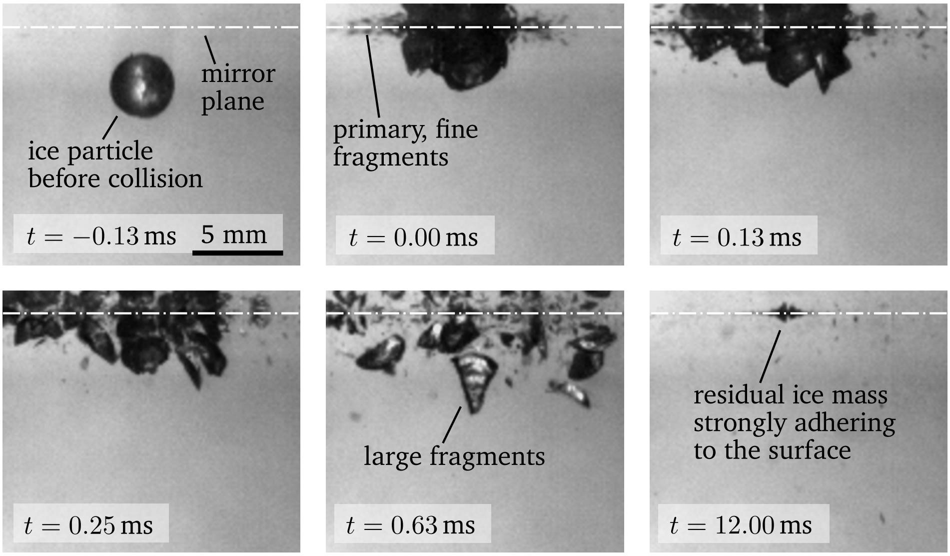

Figure 4.1: Example image sequence of an ice particle impacting onto the glass target, showing the particle before impact ($t = -0.13\,\mathrm{ms}$), the ejection of fine fragments ($t = 0\,\mathrm{ms}$) and ejected fragments of the particle after break-up. After the collision of the ice particle, a residual ice cone is formed which adheres to the target surface. In this example the particle diameter is $d_\mathrm{p} = 2.30\,\mathrm{mm}$ and the impact velocity is $v_\mathrm{p} = 21.63\,\mathrm{m\,s^{-1}}$.

impact, resisting the influence of gravity. This residual mass is also observed to adhere strongly to the target surface, although the particle and target temperature are at sub-freezing temperature. These observations are discussed in detail in the following.

It is assumed that a cone of finely crushed ice in contact with the target surface forms in the initial moments of impact. The assumption that the adhering mass is composed of small crushed fragments formed into a cone is corroborated by phenomenological observations of Tomas et al. (1999) and numerical simulations of Ma et al. (2018a) and Ma et al. (2018b) for rock fragmentation, which according to Schulson (2001) exhibits similar phenomenological fracture processes as ice. In Fig. 4.2 these observations are presented with the focus on the cone of fine fragments in the immediate vicinity of the impact point. In Fig. 4.2a), a sketch of a fracturing brittle sphere, redrawn from Tomas et al. (1999), is shown to illustrate the main occurring fragmentation features. Next to meridian cracks, secondary (lateral) cracks and a remaining cone, a conical region near the impact point (cone of fines) are formed. In this region, plastic compression in combination with shearing leads to a high spatial density of cracks and thus fine fragments (Tomas et al., 1999).

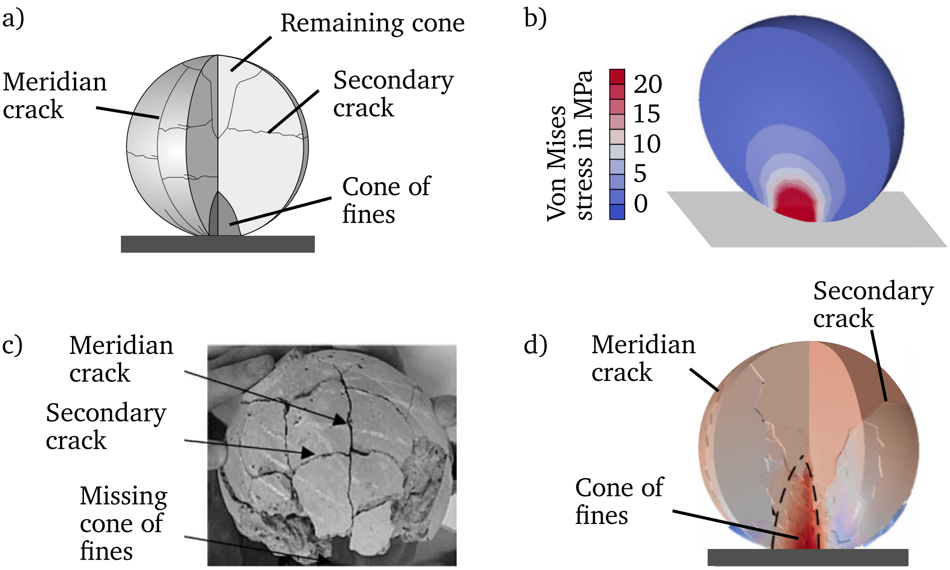

Figure 4.2: Phenomenological evidence for the generation of fine fragments for a brittle sphere impact. A sketch of a fracturing brittle sphere a), redrawn from Tomas et al. (1999), is shown to illustrate the occurring main fragmentation features. The same features are observed in experiments, e.g. with concrete spheres of Khanal et al. (2004) c). Fine fragments termed *cone of fines* are generated in a conical region near the impact point in a zone subjected to intense shear forces indicated by the magnitude of von Mises stresses that are present for the purely elastic case b) of Ma et al. (2018a). In a simulation with a fracture model d), the same cone of fines is obtained (Ma et al., 2018a). All figures are reprinted with permission.

The same fragmentation features are observed, e.g. in experiments with concrete spheres of Khanal et al. (2004) as shown in Fig. 4.2c). Meridian and lateral cracks can be observed in the re-assembled sphere with missing fragment mass in the region of the cone of fines, which are not recovered for the reassembly.
In order to investigate an approximate of the stress state in the initial moments of impact, Ma et al. (2018b) obtained the von Mises stress distribution in a purely elastic finite element simulation of an impacting sphere. The results are shown in Fig. 4.2b). It can be seen that von Mises stress is concentrated near the impact point, promoting the generation of numerous fine fragments in a highly sheared area. In a simulation with a fracture model, the same authors show that fine fragments are actually obtained in this region as indicated in Fig. 4.2d). These phenomenological

observations suggest the similarity of processes that take place in the formation of the present RM, which is assumed to consist of small fragments. This assumption is further supported by its opaque appearance, which indicates a high spatial density of reflective surfaces and therefore small fragments.

Impact Induced Sintering of the Residual Mass The strong cohesion of finely crushed material inside the cone and its strong adhesion to the target suggests that impact induced sintering is taking place. Otherwise, the majority of the fragments in the cone would be ejected radially outwards with the debris cloud or would detach from the target due to the acceleration due to gravity. As noted by Szabo et al. (2007), the timescales of diffusion limited processes contributing to ice sintering like vapour diffusion, surface diffusion, volume diffusion (Kingery, 1960; Hobbs et al., 1964) are too large to contribute to the sintering process in case of an ice particle impact with timescale in the order of milliseconds. Hence, freezing of liquid water is assumed to cause the strong adhesive and cohesive forces. Three physical phenomena are candidates for explaining the existence of liquid water in the zone of the particle near the impact point, where the fragments of the RM are formed. These are namely the presence of a quasi-liquid layer (QLL) on the ice surface (Wettlaufer, 1999; Petrenko et al., 1999; Fan et al., 2003; Dash et al., 2006), frictional heating, and melting point depression due to high pressures inside the particle during impact, which are discussed in the following.

As reviewed by Dash et al. (2006), experiments show robust evidence that a disordered, liquid-like layer of water molecules is wetting an ice surface near the melting temperature. They review that the experimental evidence from different studies displays a great variation in the magnitude of the QLL thickness and its temperature dependency. The behaviour of QLLs on ice is still not completely understood and is an active area of research (Slater et al., 2019; Li et al., 2022). From thermodynamic arguments, it can be reasoned that the existence of a QLL stems from the reduction of the total free energy if a liquid film is wetting the ice surface compared to a dry ice surface (e.g. Dash et al. (2006)). For a more detailed explanation of the underlying mechanisms, the reader is referred to Dzyaloshinskii et al. (1961), Elbaum et al. (1991), and Li et al. (2022). For the present discussion, it is sufficient to consider the experimental results showing that the maximum measured QLL thickness is in the order of $\mathcal{O}(1\,\mu\mathrm{m})$ close to the melting temperature and decreases to $\mathcal{O}(5\,\mathrm{nm})$ at $-10\,^{\circ}\mathrm{C}$.

For the evaluation of the contribution of QLL freezing to the strong RM cohesion and adhesion, the sintering experiments of Szabo et al. (2007) are reviewed. They attribute the fast sintering process in the order of $100\,\mathrm{ms}$ of two contacting ice cones to the freezing of the contacting QLLs, based on their observation of fast, sub-second sintering, cohesion in the limit of vanishing contact pressure and the stronger sintering force at temperatures closer to the melting point. However, the shortest contact time is $20\,\mathrm{ms}$ in the experiments of Szabo et al. (2007), which is large compared to an estimated contact time below $0.1\,\mathrm{ms}$ for the present experiments, a similar sintering process could be involved in the RM formation, with a QLL freezing at the contact between the fine fragments inside the RM. For the present case of the RM formation, similar compact conical shapes of a strongly adhering RM are observed for ice particle temperatures of $-5\,^\circ\mathrm{C}$ and $-35\,^\circ\mathrm{C}$. Since there is no apparent regime change at particle temperatures of $-35\,^\circ\mathrm{C}$ where the QLL thickness is in the order of nanometers (e.g. Dash et al. (2006)) and thus negligibly small, it is assumed that the QLL freezing process alone cannot explain the present strong RM.

Frictional heating at the fragment contacts may be a complementary explanation for a liquid water source, similar to the process causing low friction during ice skating as reviewed by Rosenberg (2005). It is assumed that in the vicinity of the impact point, the mass of small fragments is strongly deformed before coming to rest, finally forming the RM. Hence, frictional heating at the fragment contact points presumably leads to the generation of liquid water at short times. After the deformation process, the RM tends towards thermal equilibrium. The liquid water may freeze again as heat is transferred from the liquid at the interfaces to the fragment cores, being still at sub-freezing temperature. For an estimation of the heat generated during particle impact leading to local melting, the model of Roisman (2022) is utilized. It is assumed that deviatoric stresses inside the particle are present during its plastic deformation and after its fragmentation, where the fragment mass resists further deformation. If the stress originates from inter-particle friction, the work performed against this stress is dissipated as heat, which may then lead to the discussed fragment melting. In order to estimate the contribution of the dissipation process to the generation of water, a dissipation function for the model of Roisman (2022) is formulated. When the stress $\boldsymbol{\sigma}'$ near the particle central axis is multiplied with the local strain rate $\boldsymbol{E}$, derived from the proposed deformation field, the dissipation function $\Phi \equiv \sigma'_{ij}E_{ij}$ is obtained having the units of a specific work,

$$\Phi = \frac{8a^3UY}{\pi(a^2+z^2)^2}, \quad \text{at} \quad r = 0. \tag{4.1}$$

The particle deformation is assumed to be too fast for macroscopic heat transfer processes to dominate. Hence, the deformation work leads locally to adiabatic heating of the ice fragments. For the estimation of a characteristic total amount of heat produced through dissipation, the dissipation function is evaluated at the central axis of the particle. The characteristic value is then obtained by integrating the dissipation function from the time of impact to the time of the maximum deformation to obtain the total amount of generated heat

$$q_{\mathrm{diss}}(\zeta) = \int_0^t \Phi \,\mathrm{d}t = \int_0^\zeta \frac{16\sqrt{2}\zeta^{3/2}R^4Y}{\pi(2R^2\zeta+z^2)^2}\,\mathrm{d}\zeta. \tag{4.2}$$

In order to obtain the heat generation inside the moving particle, Eq. (4.2) has to be integrated along a material point inside the particle. The position of a material point starting at the coordinate $z = 0$ at $t = 0$ as a function of the instantaneous particle deformation ζ can be written as

$$z = z_0 + R \int_0^{\zeta} \frac{u_z(\zeta)}{U(\zeta)}\,\mathrm{d}\zeta. \tag{4.3}$$

Finally, the temperature increment ΔT can be estimated assuming adiabatic heating

$$\Delta T \approx \frac{q_{\mathrm{diss}}}{\rho\, c_p}. \tag{4.4}$$

The predicted temperature elevation due to dissipation is shown in Fig. 4.3 as a function of the axial coordinate z for various values of ζ_{max}. Since the value of the effective rate-of-strain is relatively high in the present experiments, the constant maximum yield strength $Y = 6Y_0$ is used for the analysis. The values shown in Fig. 4.3 can be considered as an upper bound for the temperature increment due to dissipative heating due to particle impact, since the energy sink of fragmentation is not taken into account. However, Ma et al. (2018b) report in their study on the fragmentation of generic brittle spheres that the energy spent on fragmentation did not exceed 1% of the initial sphere kinetic energy. Thus, the temperature estimations utilizing the model of Roisman (2022) in Fig. 4.3 clearly suggest that the temperature rise can be significant and could lead to partial melting of the fragments.

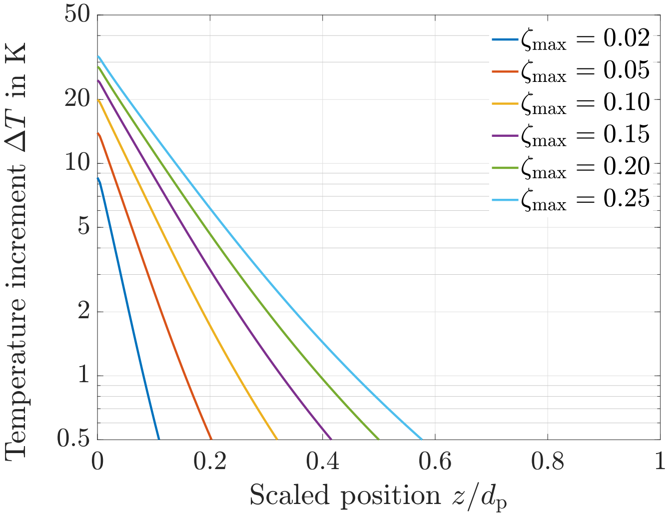

Figure 4.3: Theoretical predictions for the upper bound of the temperature increment after particle impact. Computations for different values of the maximum particle dislodging are shown in different colors.

The third phenomenon potentially contributing to the generation of liquid water is the melting point depression of ice for increasing pressure. One of the unique properties of water is its expansion upon solidification at moderate pressures. Hence, according to Le Chatelier's principle, an increased pressure leads to a decrease of the equilibrium melting temperature (Petrenko et al., 1999). This leads to a negative slope of the solid-liquid phase boundary in the water p-T phase diagram as visualized in Fig. 4.4. For the present experiments this means that due to the

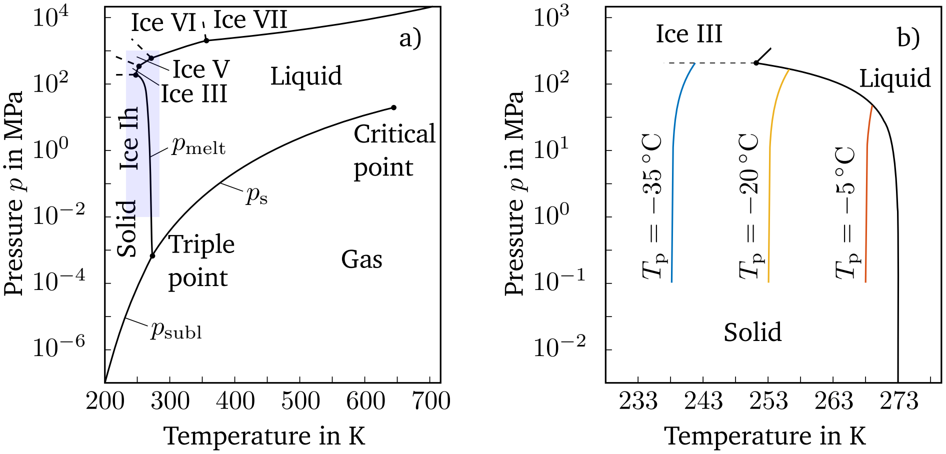

Figure 4.4: Phase-boundary curves of water in a p-T diagram over a wider range of pressures and temperatures a), redrawn from Wagner et al. (2011) with permission. The relevant region for the present work, indicated as a blue area in a), is shown again in an enlarged view on the right hand side b). The coloured lines correspond to isentropic changes of state starting at a pressure of $0.1\,\mathrm{MPa}$ and temperatures of $-35\,°\mathrm{C}$, $-20\,°\mathrm{C}$ and $-5\,°\mathrm{C}$, respectively. The lines are calculated using the water equation of state reported in Feistel et al. (2006).

increased pressures during impact, the melting temperature decreases, which may assist in localized melting. The region in the phase diagram that is most relevant for the present work is indicated as a blue area in Fig. 4.4a) and is shown again in an enlarged view in Fig. 4.4b). In addition to the equilibrium phase boundaries indicated as black curves, isentropic changes of state are indicated as coloured curves. They start at a pressure of $0.1\,\mathrm{MPa}$ and temperatures of $-35\,°\mathrm{C}$, $-20\,°\mathrm{C}$ and $-5\,°\mathrm{C}$, indicated by the blue, orange and red curves, respectively. These correspond to the ice particle temperatures investigated in the present work. The curves are shown only for illustration purposes, since the impact process is assumed to be dissipative and hence non-isentropic. However, they indicate that at least for the particle temperatures of $T_{\mathrm{p}} = -20\,°\mathrm{C}$ and $T_{\mathrm{p}} = -5\,°\mathrm{C}$, pressure melting is possible without dissipative heating at sufficiently large pressures. With dissipation, the curves indicating the actual change of state are located on the right hand side of the isentropic curves. Hence, with sufficient dissipative heating for particle temperatures of $T_\mathrm{p} = -35\,^\circ\mathrm{C}$, the corresponding change of state curve can also enter the liquid region. After releasing the pressure again to $p \approx 0.1\,\mathrm{MPa}$ after the particle impact, some of the generated water freezes, if the change of state curve ends up again in solid region.

For this process to activate, the pressures during impact have to be in the order of $\mathcal{O}(100\,\mathrm{MPa})$. As argued by e.g. Colbeck (1995), the ice failure strength limits the maximum achievable pressure which poses an argument against pressure melting leading to water generation during ice skating. However, in the present situation, the ice is confined in the region where the RM is formed. Hence, it is assumed that larger hydrostatic pressures can be encountered before material failure, making pressure melting possible. For an estimation of the encountered pressure during particle impact in the present experiments, the compressive stress σ_{zz} at the central axis of the particle ($r = 0$) is estimated, using the model of Roisman (2022). The stress obtained for a particle of $d_\mathrm{p} = 2\,\mathrm{mm}$ impacting at a velocity of $v_\mathrm{p} = 70\,\mathrm{m\,s^{-1}}$ is shown in Fig. 4.5. The model diverges at the limit of zero contact time, which can be seen in Fig. 4.5 at the large values for σ_{zz} at $t = 0\,\mathrm{s}$. However, at larger times where the model is mathematically valid, the pressure is still in the order of $\mathcal{O}(100\,\mathrm{MPa})$ up to a time of $t = 1\,\mu\mathrm{s}$. Hence, the pressure is sufficiently large for pressure melting to possibly occur.

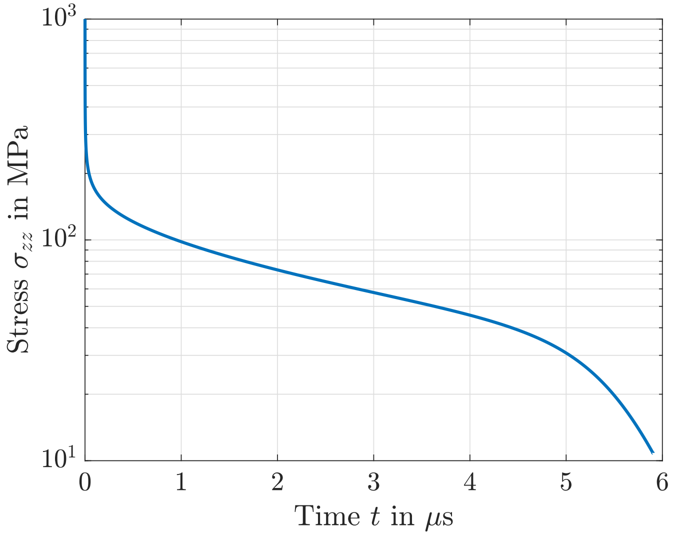

Figure 4.5: Temporal evolution of the stress σ_{zz} at the central axis of a particle with a diameter of $d_\mathrm{p} = 2\,\mathrm{mm}$ and an impact velocity of $v_\mathrm{p} = 70\,\mathrm{m\,s^{-1}}$.

Concluding, the contribution of all three discussed physical phenomena in the RM generation process can not be ruled out in general. However, the QLL is assumed to be not the main source for (quasi) liquid water, since a strong RM is still observed at low particle temperatures of $-35\,^\circ\mathrm{C}$ where the QLL thickness is negligible. More likely frictional heating in combination with melting point depression leads to the generation of liquid water during impact. Either a release from the pressurized state or local heat transfer then causes refreezing of the temporary liquid water.

Effect of the Impact Velocity With increasing impact velocity, a relatively larger amount of RM is deposited on the target surface, compared to the impacting particle mass. This dependence can already be visually observed as demonstrated in Fig. 4.6. All shown experiments are conducted with similar ice particle diameter $d_\mathrm{p} = (2.89 \pm 0.14)\,\mathrm{mm}$, particle $T_\mathrm{p} = (-20.0 \pm 0.4)\,^\circ\mathrm{C}$ and target temperature $T_\mathrm{t} = (-10.0 \pm 0.5)\,^\circ\mathrm{C}$, while the impact velocity is varied between $v_\mathrm{p} = 11.72\,\mathrm{m\,s^{-1}}$ and $v_\mathrm{p} = 75.78\,\mathrm{m\,s^{-1}}$. Since the RM exhibits approximately a conical shape in all cases, a larger dark area observed in Fig. 4.6 directly corresponds to a larger mass of ice adhering to the target. A quantitative analysis of this clearly observable influence of the impact velocity is performed in the following section 4.1.1.4. As mentioned in section 4.1.1.1, the opaque appearance of the residual ice mass indicates a high spatial density of reflective surfaces and therefore small fragments in the RM in all images.

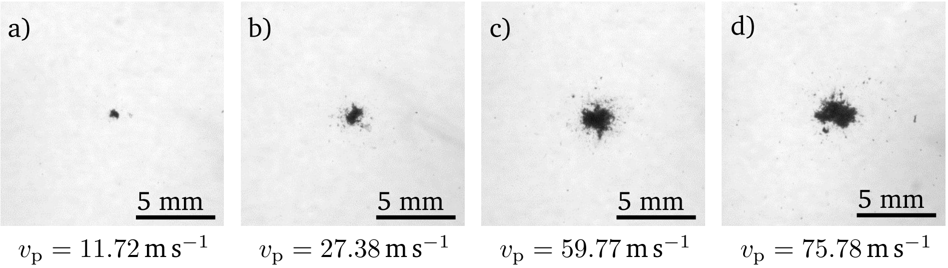

Figure 4.6: Example images of the residual ice mass adhering to the target substrate, recorded in a top-view. All experiments are conducted with similar ice particle diameter $d_\mathrm{p} = (2.89 \pm 0.14)\,\mathrm{mm}$, particle $T_\mathrm{p} = (-20.0 \pm 0.4)\,^\circ\mathrm{C}$ and target temperature $T_\mathrm{t} = (-10.0 \pm 0.5)\,^\circ\mathrm{C}$. The impact velocity is varied between $v_\mathrm{p} = 11.72\,\mathrm{m\,s^{-1}}$ and $v_\mathrm{p} = 75.78\,\mathrm{m\,s^{-1}}$, shown in ascending order in the images a) to d).

Effect of the Target Temperature In the experiments conducted with target temperatures above freezing, the RM is observed to melt in a short period of time, as shown in Fig. 4.7. In order to differentiate between air-born fragments and the sticking RM in the leftmost image of Fig. 4.7, the area of the RM is indicated with a blue dashed line. Immediately after impact, the RM exhibits an opaque appearance, like in the case of a sub-freezing target temperature. This indicates that although the target temperature is at $T_\mathrm{t} = 10\,^\circ\mathrm{C}$, the bulk of the RM remains frozen at short times ($t = 2\,\mathrm{ms}$) after impact. When comparing the RM appearance in Fig. 4.7 to Fig. 4.6d), it can be observed that the RM is not a compact spot on the target anymore, but scattered across a larger area as many individual fragment clusters. This behaviour can be explained when the thermal contact problem between ice and sapphire glass is taken into account. The contact temperature T_c at the interface between ice and the sapphire glass target can be computed as (Baehr et al., 2011, pp.156-158)

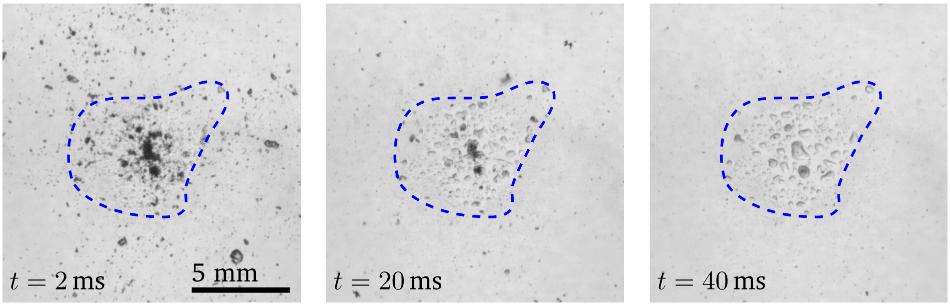

Figure 4.7: Image sequence of an experiment with above freezing target temperature $T_\mathrm{t} = 10\,^\circ\mathrm{C}$. The particle diameter, impact velocity and temperature are $d_\mathrm{p} = 2.84\,\mathrm{mm}$, $v_\mathrm{p} = 75.40\,\mathrm{m\,s^{-1}}$ and $T_\mathrm{p} = -20.0\,^\circ\mathrm{C}$, respectively. Directly after the particle impact ($t = 2\,\mathrm{ms}$) the RM appears opaque but finally becomes transparent as it melts almost completely after $t = 40\,\mathrm{ms}$. The area finally wetted with the melted RM is indicated with a blue dashed line to differentiate between airborne fragments and sticking RM in the leftmost image.

$$T_{\mathrm{p|t}} = \frac{T_\mathrm{p}\vartheta_\mathrm{ice} + T_\mathrm{t}\vartheta_\mathrm{t}}{\vartheta_\mathrm{ice} + \vartheta_\mathrm{t}}, \tag{4.5}$$

with the thermal effusivity $\vartheta = \sqrt{\rho\lambda c_p}$. The variables ρ, λ and c_p denote the density, thermal conductivity and isobaric heat capacity, respectively. For the experiment shown in Fig. 4.7, a contact temperature of $T_{\mathrm{p|t}} = 5.4\,^\circ\mathrm{C}$ is computed when using Eq. (4.5). It has to be noted, that phase change is not considered in this analysis, violating the underlying assumptions of Eq. (4.5). Instead of obtaining the contact temperature at the interface, the interface temperature will first rise to the melting temperature before the melting front propagates in direction of the bulk ice. Then, the temperature at the water-sapphire interface will exceed the melting temperature. However, the analysis using the classical contact temperature still allows the conclusion that at the moment of contact between the ice particle and the warm sapphire glass, melting immediately begins at the interface. This changes the dynamics of the disintegrating ice particle during impact, decreasing friction due to a lubricating water film. Fragmentation of the initially compact RM is facilitated and hence, it radially spreads over a larger area on the target surface, as observed in Fig. 4.7. At larger time scales, heat is transferred from the target to the RM, melting successively bigger portions. Smaller parts of the fragmented RM melt first, becoming transparent drops ($t = 20\,\mathrm{ms}$). After a time of $t = 40\,\mathrm{ms}$ after impact, most of the RM is melted while only a few darker spots still indicate non-melted ice fragments.

4.1.1.2 Design of Experiments

The amount of RM is examined for varying impact velocity, particle diameter, and particle and target temperature in a quantitative analysis. The experimental conditions are determined based on a full factorial design (FFD), where all possible combinations of the varied experimental parameters (factors) are investigated. The advantages consist of the ability to resolve interactions of the factors completely, without confounding and the option to add more than two discrete values (levels) of an experimental parameter for the following statistical analysis. They are considered to outweigh potential disadvantages such as the high experimental effort compared to other experimental designs. The experimental conditions are summarized in Table 4.1, where the displayed values are calculated for each factor as the mean of all experimental runs for the given level. In addition to intentionally varied experimental conditions, another source of potentially influential effects are non-controllable parameters, which are further classified into measured and unmeasured parameters. By visual examination and selection of the ice particles, high aspect ratios or obvious deformations are discarded prior to firing. Yet no specific values for the sphericity S or the roundness R are adjustable. Therefore, experimental runs are discarded where the roundness value is below a threshold of $R = 0.75$, and the sphericity value is below $S = 0.9$. While the particle morphology and air temperature are measured for each experimental run, the crystallisation structure of the particles and the angular velocity remain unknown. However, the latter is assumed to be negligible, as a visual examination of the video material does not reveal any rotation which could be of significance in the process compared to the translational motion of the particle. Three replications are performed for each factor level combination, resulting in a total of 216 experimental runs.

The combinations of particle diameter, d_p, and impact velocity, v_p, for all experimental runs are summarized in Fig. 4.8, where factor levels are visible as local clusters. For each experimental run, measured velocities and diameters are indicated by blue markers scattered around the mean value of each factor level combination (cluster),

Controlled parameters	Level 1	Level 2	Level 3	Level 4
Particle velocity v_p in $\mathrm{m\,s^{-1}}$	11.94	26.55	57.90	73.66
Particle diameter d_p in mm	1.86	2.83	3.94	
Particle temperature T_p in °C	-34.98	-20.01	-5.04	
Target temperature T_t in °C	-9.97	9.98		

Uncontrolled parameters, measured	Lower limit	Upper limit
Sphericity S	0.9	1
Roundness R	0.75	1
Ambient temperature T_air in °C	-15	-7
Impact angle	Normal to surface	

Uncontrolled parameters, unmeasured	Assumption
Particle angular velocity in $\mathrm{s^{-1}}$	≈ 0
Particle crystallization structure	Polycrystalline

Table 4.1: Summary of all experimental parameters eventually influential for the formation of a residual ice mass adhering to the target substrate. All parameters are subdivided into three categories. For the controlled parameters, the mean values of all corresponding experiments are displayed.

which is indicated by a yellow circle. Within a given cluster, the particle and target temperature remain as varying parameters. Each factor level combination is repeated three times and thus three blue markers are combined into one red marker for each factor level combination, where the six resulting red dots represent the possible combinations of the particle and target temperature. Ideally, the difference between the impact velocity and particle diameter values of each experimental run and the mean factor level values is minimal. In extreme cases, however, these differences exceed ten percent deviation from the desired mean factor level values. This can be seen in Fig. 4.8 by comparing the distance between the blue markers and the mean factor value, which is indicated by a dashed black line. The impact on the statistical analysis is mitigated by conducting three replicates for each factor combination. This results in a smaller difference between the calculated mean of that factor level combination and the mean factor value, represented as the distance of the red circles from the dashed black lines.

All mean replication values of the particle diameter deviate from the mean factor level value by a maximum of 6%. The initial statistical evaluation to determine the statistical significance of the factors is performed such that each factor level combination is treated categorically, assuming for the analysis the mean level values

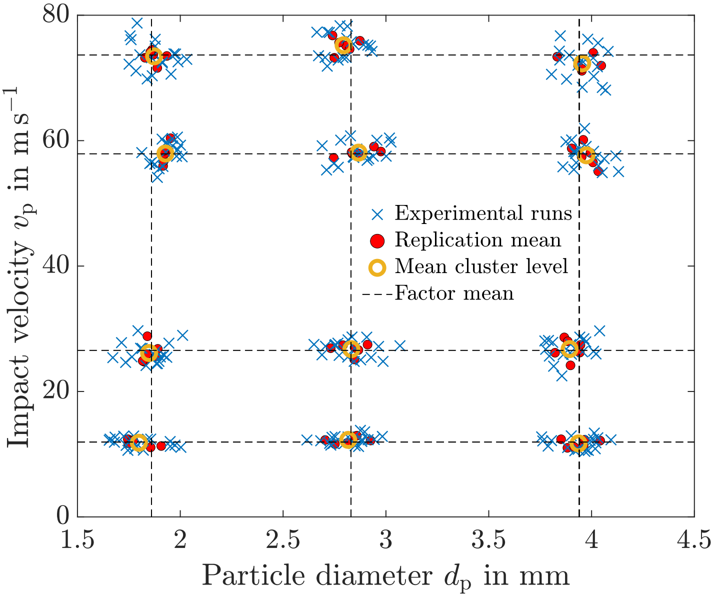

Figure 4.8: Distribution of the measured particle diameter d_p and impact velocity v_p for all experimental runs for investigating the residual ice mass, visualized with blue markers. For each factor level combination, the cluster of experimental runs contains three replications for each possible combination of the particle and target temperature level. The replication means are indicated with red markers. Six replication means are combined to obtain a cluster mean, denoted by a yellow circle. Finally, the mean factor values as summarized in Table 4.1 are indicated as black dashed lines.

as summarized in Table 4.1. However, for the regression analysis in later stages, the true measured velocity and diameter values of each experimental run are used instead. The particle and target temperature can be controlled more precisely, such that they only vary within the described uncertainty of ± 0.3 K. It can be concluded that the particle geometry and impact velocity in the experiments are associated with minor variations, which are considered acceptable. Thus, the present experimental design allows a statistically founded analysis of the significance of the varied factors for the amount of RM.

4.1.1.3 Statistical Data Analysis

For determining whether the varied factors of particle diameter, impact velocity as well as particle and target temperature have any statistically significant influence on the amount of RM remaining on the target surface after impact, an analysis of variance (ANOVA) is performed. The orthogonal structure of the experimental design allows an unconfounded calculation of possible interaction effects between the experimental factors. This is in contrast to a commonly employed experimental design following the One-Factor-At-A-Time approach, where one factor is varied while all other factor levels remain the same to rule out their effects during variation. The presence of an interaction effect means that the values of the response cannot be attributed solely to the individual influence of the varied experimental parameters. The significance of an effect or interaction effect on the response $\overline{\Psi}$ is determined by performing an ANOVA, for which the null hypothesis is that an effect has no influence on the measured response, the residual mass, m_{RM} (Dean et al., 2017).

Checking Model Assumptions for an Analysis of Variance The results of the ANOVA are analysed by assessing the resulting effect strengths which are displayed in a Pareto chart. Prior to drawing any conclusions based on the Pareto chart, it is necessary to confirm the model assumptions for an ANOVA. These include equal variances of the error variable, a normal distribution of the error variable and independence of individual experiments, each tested by scrutinizing standardized residuals. Absolute residuals are obtained by calculating the differences between each individual, i-th measured value of the RM, $m_{\mathrm{RM},i}$, and an OLS fit of an empirical, linear model to all data, $m_{\mathrm{RM,fit}}(v_{\mathrm{p}}, d_{\mathrm{p}}, T_{\mathrm{p}}, T_{\mathrm{t}})$. Standardized residuals z_i are obtained by dividing the absolute residuals by their standard deviation (Dean et al., 2017, pp.143-144),

$$z_i = \frac{m_{\mathrm{RM},i} - m_{\mathrm{RM,fit}}(v_{\mathrm{p},i}, d_{\mathrm{p},i}, T_{\mathrm{p},i}, T_{\mathrm{t},i})}{\sqrt{\mathrm{ssE}/(n-1)}}, \tag{4.6}$$

where ssE denotes the total sum of the squared errors and n is the total number of experiments. In Fig. 4.9a, the standardized residuals are plotted against the empirical model prediction for the amount of RM for each experimental parameter combination for an investigation of data homoscedasticity.

In Fig. 4.9b, a normal probability plot is shown for an investigation of the error variable distribution. In Fig. 4.9a it can be observed that the variance of the standardized residuals increases with increasing values of the predicted RM, indicating heteroscedasticity. This behaviour can be attributed to a constant relative error of the measurement method presented in section 3.1. Additionally, the standardized residuals do not follow a normal distribution as can be seen in Fig. 4.9b. For small and large values of the standardized residuals, their distribution deviates from a normal distribution (red line in Fig. 4.9b). Hence, two prerequisites for a rigorous statistical analysis of the experimental data, homoscedasticity and a

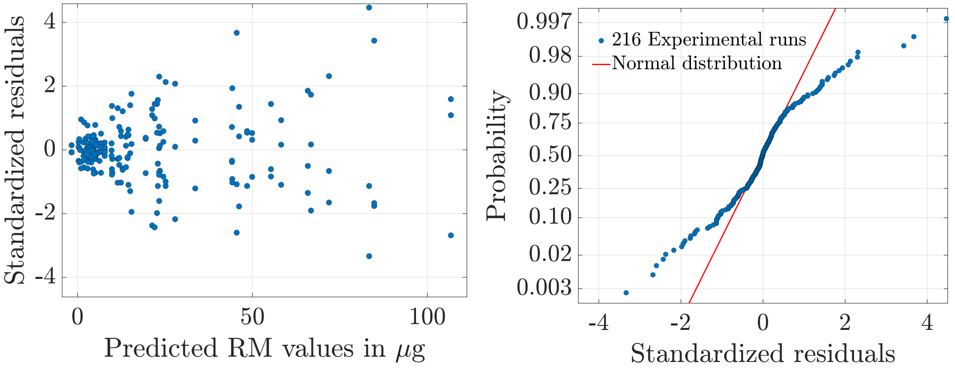

(a) Standardized residuals plotted against the RM values predicted by fitting a linear model to all available data using an OLS regression. The plot is used to check for data homoscedasticity.

(b) Cumulative probability distribution of the standardized residuals for investigation of their distribution. For comparison, a normal distribution is indicated as red line.

Figure 4.9: Plots for visual assessment of data homoscedasticity and normal distribution of the error variable for the RM.

normal distribution of the residuals, are violated in the present case. However, the experimental data can be transformed in such a way, that these prerequisites are not violated anymore. A non-linear Johnson transformation (Johnson, 1949) is performed, leading to the transformed value of the residual mass $\overline{m_{\mathrm{RM}}}$,

$$\overline{m_{\mathrm{RM}}} = 1.80849 + 0.690612 \log\left(\frac{m_{\mathrm{RM}} \times 10^8 + 0.321\,538\,\mathrm{kg}}{169.879\,\mathrm{kg} - m_{\mathrm{RM}} \times 10^8}\right). \tag{4.7}$$

The non-dimensional values of $\overline{m_{\mathrm{RM}}}$ span a range between -2 and 2. These values are difficult to interpret due to the applied non-linear transformation. However, each statement made about the significance of effects, e.g. the impact velocity significantly affecting $\overline{m_{\mathrm{RM}}}$, is transferable to a statement about the non-transformed quantity m_{RM}. After transformation, the data homoscedasticity and normal distribution of the error are investigated again. The corresponding plots are shown in Fig. 4.10.

A small non-uniformity of the standardized residuals is still observable in Fig. 4.10a, which is considered acceptable. The distribution of the standardized residuals, shown in Fig. 4.10b, is much closer to a normal distribution when compared to Fig. 4.9b. The deviation at small values of the standardized residuals is considered acceptable. Accepting small deviations from the optimal prerequisites is reasonable, since an ANOVA is robust against these small deviations (Schmider et al., 2010).

The last missing test is the one for the independence of individual experiments, which is conducted by randomly changing the experimental parameters for each subsequent experiment. In Fig. 4.11, the standardized residuals for the experiments are plotted in the same order as they were conducted. Since no increasing or decreasing trend can be observed, the prerequisite of mutual independence is considered to be fulfilled.

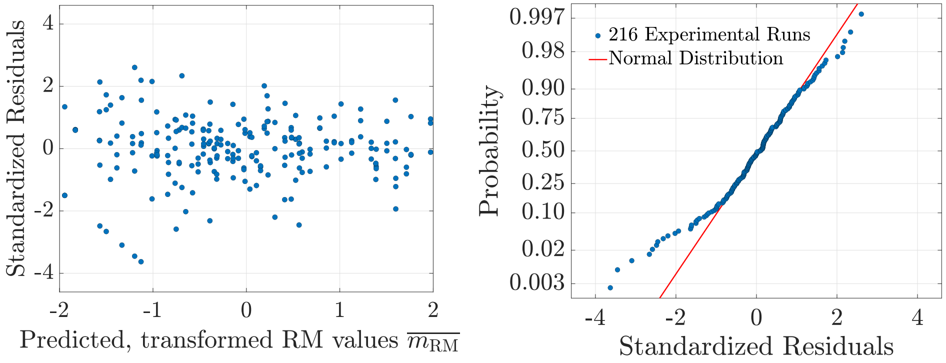

(a) Standardized residuals plotted against the predicted values of the transformed RM, $\overline{m_{\mathrm{RM}}}$. The predicted values are obtained by fitting a linear OLS model to the transformed data. The plot is used to check for data homoscedasticity.

(b) Cumulative probability distribution of the standardized residuals for investigation of their distribution. The residuals of the transformed RM values, $\overline{m_{\mathrm{RM}}}$, are displayed. For comparison, a normal distribution is indicated as red line.

Figure 4.10: Plots for visual assessment of data homoscedasticity and normal distribution of the error variable for the transformed RM values.

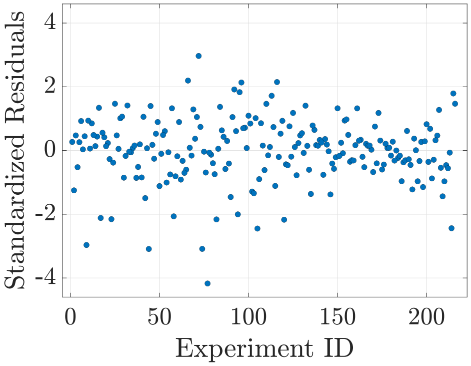

Figure 4.11: Distribution of the standardized residuals for increasing experimental run order.

Effect of the Controlled Parameters After verifying the underlying model assumptions, the results of the ANOVA are analysed to determine the significance of experimental parameters for the amount of RM left on the target surface after impact. The underlying null hypothesis consists of the assumption that an experimental parameter has no influence on the amount of residual mass, m_{RM} (Dean et al., 2017). The null hypothesis is rejected and an effect is considered significant when the standardized effect strength represented by a t-value is above a threshold value associated with the global significance level taken at 5%.

The t-value of an effect or interaction is calculated by first determining the p-value, p_{ANOVA}, and the degrees of freedom from the ANOVA. If the degrees of freedom for an effect equals one, the t-value is determined by performing a two-sample t-test. For effects or interactions with more than one degree of freedom, the t-value is defined as the inverse CDF of the Student's t-distribution as

$$\text{t-value} = F_{\mathrm{t}}^{-1}\left(\left(1 - \frac{p_{\mathrm{ANOVA}}}{2}\right) \middle| \, \mathrm{DF}_{\mathrm{Error}}\right), \tag{4.8}$$

where F_{t}^{-1} denotes the inverse Student's t CDF, p_{ANOVA} is the p-value of the corresponding F-statistic and $\mathrm{DF}_{\mathrm{Error}}$ represents the error degrees of freedom for the chosen model. The standardized effect strength (t-values) of all factors and factor combinations can be summarized and compared to a threshold t-value in a Pareto chart, as shown in Fig. 4.12. Five terms exceed the t-value of 1.97 for the global significance level of $\alpha = 0.05$. These include all varied experimental parameters individually, the particle impact velocity (A), diameter (B), temperature (C) and target temperature (D) as well as an interaction effect of the impact velocity and particle diameter (AB). For the assessment of the significance of each factor, non-significant terms from Fig. 4.12 are excluded in a step-wise procedure, beginning with the term with the smallest t-value. The factorial regression is repeated as long as terms with insignificant contributions are left in the model. At the significance level $\alpha = 0.05$, five terms remain in the model as A, B, C, D and AB, that were already identified in the initial analysis of factor insignificance and shown in Fig. 4.12.

Concluding, a rigorous statistical analysis has shown that all varied parameters particle impact velocity v_{p}, diameter d_{p}, temperature T_{p} and target temperature T_{t} significantly affect the amount of RM.

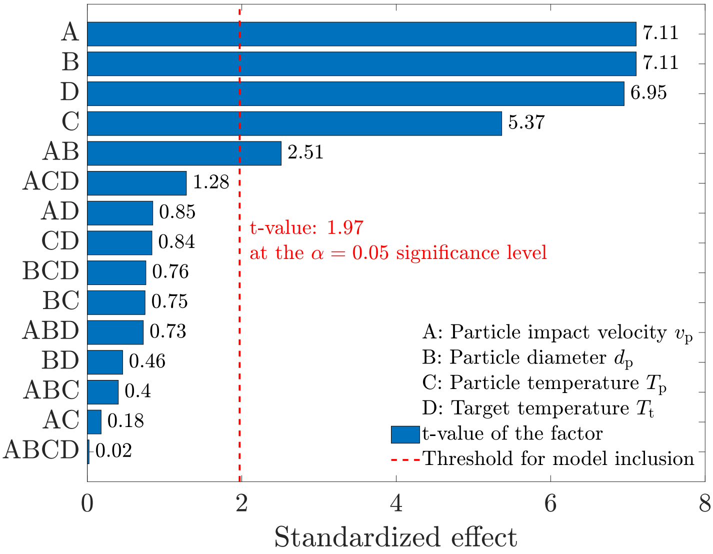

Figure 4.12: Pareto chart summarizing the t-values for all experimental parameters and their interactions. The significance of an effect or interaction effect on the mean $\overline{m_\mathrm{RM}}$ is determined by comparison of the individual t-values against the t-value at a global significance level of $\alpha = 0.05$. Five terms exceed this t-value of 1.97: A, B, C, D and AB.

Effect of the Uncontrolled Parameters Additionally, it is investigated whether the uncontrolled experimental parameters summarized in Table 4.1, the air temperature T_air, the particle sphericity S and roundness R, have any significant effect on the results of the RM. For this purpose, plots of the respective standardized residuals are shown in Fig. 4.13. No observable trend in the data for the air temperature, roundness and sphericity suggests that $\overline{m_\mathrm{RM}}$ is correlated with these parameters. This is confirmed by the calculation of Pearson correlation coefficients. For each uncontrolled experimental parameter, the null hypothesis has been tested that there is no relationship between the observed phenomena null hypothesis at the $\alpha = 0.05$ significance level. Since the p-value of the test for each parameter is greater than the threshold, it can be concluded that the covariates roundness, sphericity and air temperature have no influence on $\overline{m_\mathrm{RM}}$ for the chosen parameter range.

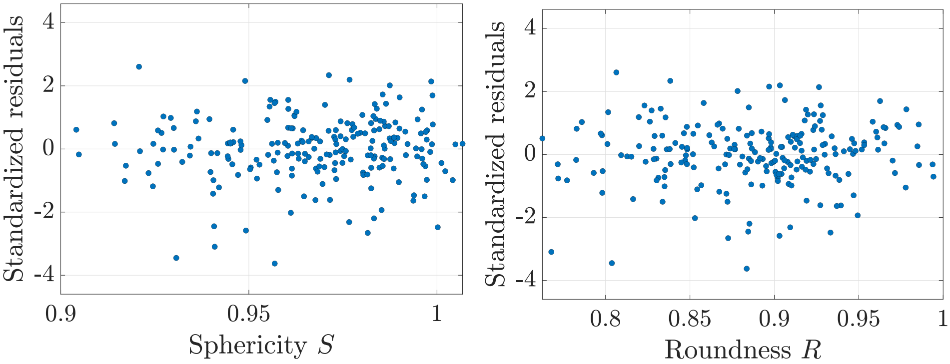

(a) Standardized residuals plotted against the sphericity S of the impacting ice particle.

(b) Standardized residuals plotted against the roundness R of the impacting ice particle.

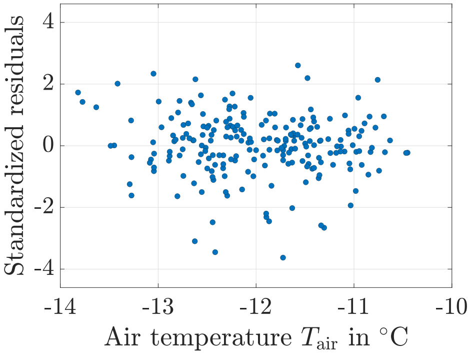

(c) Standardized residuals plotted against the air temperature T_{air}.

Figure 4.13: Standardized residuals calculated as the difference between the measured response and the Ordinary Least Squares (OLS) fit for that factor level combination, respectively rationalized using its estimated standard deviation. The potential influence on m_{RM} is determined by visual inspection for signs of correlations with the covariates ambient temperature, T_{air}, roundness R, and sphericity S.

4.1.1.4 Quantitative Analysis and Discussion

So far, no quantitative statements have been made about the correlation between the varied experimental parameters and the RM or about the strength of these effects. It has just been evaluated that all varied experimental parameters have an effect on the RM that is significantly different from random experimental errors at a significance level of $\alpha = 0.05$. This statement is valuable for the following quantitative discussion, where only the strength of the effect and its nature need to be determined (linear, non-linear and direction of the effect on RM).

Effect of the Impact Velocity and Particle Diameter The effect of increasing impact velocities leading to increasing amounts of RM is already observed by visual inspection of the size of the RM on the target (see section 4.1.1.1). In Fig. 4.14, quantitative data for the effect of the impact velocity and particle diameter on the RM is presented. In Fig. 4.14a), the residual mass m_{RM} is plotted against the particle impact velocity v_{p}, while the three levels of the particle diameter d_{p} are displayed separately, indicated by different colours. Linear OLS fits to the individual data sets are displayed as dashed lines. The residual mass increases with both increasing particle diameter and impact velocity. It has to be noted that each marker

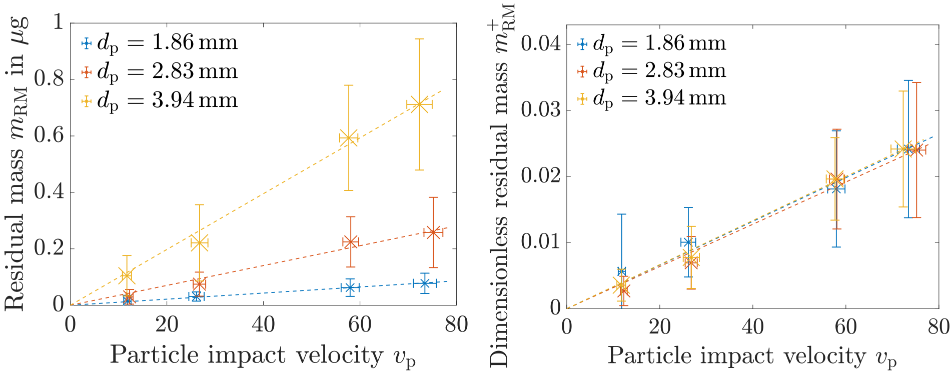

(a) Residual mass m_{RM} plotted against the particle impact velocity v_{p}.

(b) Dimensionless residual mass m^+_{RM} plotted against the particle impact velocity v_{p}.

Figure 4.14: Comparison of the effect of the particle impact velocity and diameter on the residual mass before and after scaling. The experimental data for the three levels of the particle diameter d_{p} are displayed separately, as indicated by different colours. One marker corresponds to 18 experiments, including all variations of the particle and target temperature. Linear OLS fits to the individual data sets are displayed as dashed lines.

corresponds to 18 experiments, including all variations of the particle and target temperature. Hence, the error bars, representing one standard deviation, indicate both the random error of the experiments and the variation of the RM due to the effect of the particle and target temperature. Since the experimental design is orthogonal, an inclusion of all 18 measurement points per cluster does not affect the statement that can be made about the effect of the e.g. velocity. For example, if a larger particle temperature leads to larger amounts of RM, both larger and smaller amounts of RM due to this effect are included in the same cluster. A cluster mean, represented by individual markers in Fig. 4.14a, is not affected if the particle temperature effect is more pronounced, as long as it centres around the same mean. Hence, the particle temperature effect is neutralized for each cluster mean and when the mean values are compared, exclusively the effects of the impact velocity and particle diameter are observed. However, the errorbar sizes are affected by the combination of all experimental runs since their size would increase for a stronger effect of the particle temperature. For interpretation of the data, the existence of an effect of all experimental parameters has been shown already in section 4.1.1.1, which is why it is not necessary to resort to visual inspection of the errorbars in this case. Both the particle diameter and impact velocity significantly influence the amount of RM, which is also evident from a visual inspection of Fig. 4.14a. The amount of RM is assumed to be correlated with the initial particle mass, since a larger particle size leads to a larger amount of RM. In order to test this hypothesis, the dimensionless residual mass $m_{\mathrm{RM}}^{+} = m_{\mathrm{RM}}/m_0$ is introduced, which is the RM, m_{RM}, scaled with the mass of the initial particle m_0. In Fig. 4.14b, m_{RM}^{+} is plotted against the impact velocity. It can be observed that all three trend lines perfectly align to one increasing trend of m_{RM}^{+} with an increasing impact velocity, supporting the hypothesis that the RM can be scaled with the initial particle mass. Therefore, only the dimensionless RM is considered in the following analysis. The trend of m_{RM}^{+} appears to increase linearly with increasing velocity. In the analysis based on the model of Roisman (2022) presented in the following section 4.1.1.5, the observed diameter of the RM is modelled as a function of the impact velocity, coinciding with the observed trend.

Effect of the Particle and Target Temperature Both the particle and target temperature significantly influence the amount of RM as shown in section 4.1.1.1. The strength of these effects is shown in Fig. 4.15. When comparing the values of m_{RM}^{+} for different particle temperatures at a subfreezing target temperature of $T_{\mathrm{t}} = -9.97\,^{\circ}\mathrm{C}$ in Fig. 4.15a), no noticeable effect of the particle temperature is observed. In contrast, an effect of the particle temperature is observed for a target temperature of $T_{\mathrm{t}} = 9.98\,^{\circ}\mathrm{C}$, as shown in Fig. 4.15b). It seems that only at an above freezing target temperature, does an increasing particle temperature lead to an increasing dimensionless residual mass. As already shown in the qualitative analysis section 4.1.1.1, the different target temperatures lead to a regime change in the appearance of the RM. The RM forms a compact cone on a sub freezing target,

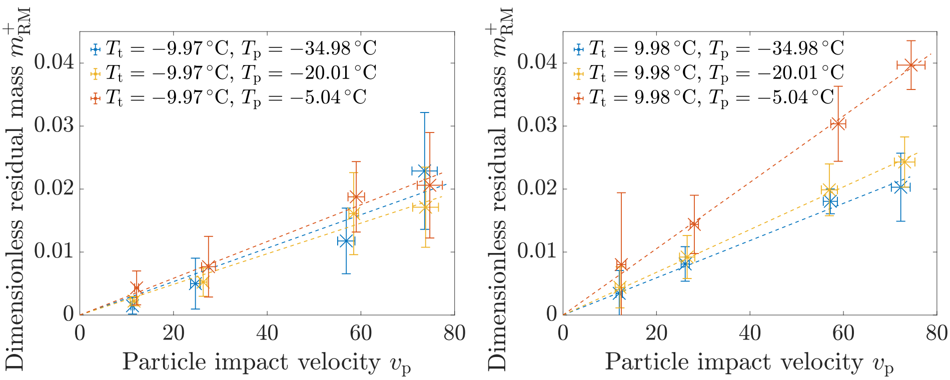

(a) Dimensionless residual mass m_{RM}^{+} plotted against the particle impact velocity v_p for a target temperature of $T_\mathrm{t} = -9.97\,°\mathrm{C}$.

(b) Dimensionless residual mass m_{RM}^{+} plotted against the particle impact velocity v_p for a target temperature of $T_\mathrm{t} = 9.98\,°\mathrm{C}$.

Figure 4.15: Comparison of the effect of the particle and target temperature on the dimensionless residual mass. The experimental data for particle temperature levels are displayed separately, as indicated by different colours. One marker corresponds to 9 experiments, including all variations of the particle diameter. Linear OLS fits to the individual data sets are displayed as dashed lines.

but fragments and spreads out on an above freezing target. For an illustration of this phenomenon, example images of the RM are shown in Fig. 4.16, captured 9 ms after the impact of ice particles with comparable particle diameters of $3.85\,\mathrm{mm} < d_\mathrm{p} < 4.08\,\mathrm{mm}$ and impact velocities of $68.5\,\mathrm{m\,s^{-1}} < v_\mathrm{p} < 76.7\,\mathrm{m\,s^{-1}}$. Despite the regime change visible in Fig. 4.16, the values of m_{RM}^{+} for the target temperature of $-9.97\,°\mathrm{C}$ (Fig. 4.16 a), b) and c)) are similar to the values for the target temperature of $9.98\,°\mathrm{C}$ and the lowest particle temperature (Fig. 4.16 d)). The values of m_{RM}^{+} noticeably increase for a combination of the largest target and particle temperatures (Fig. 4.16 e)). Additionally, the area of the RM wetting the target increases, as visualized with the blue shaded areas and area-equivalent circles with diameters d_{RM}. A phenomenological explanation for these phenomena is proposed in the following.

Whether the compact RM cone breaks up or not, does not have to mean that the volume of ice adhering to the target increases. This assumption is supported by the observation of similar RM values in Figs. 4.16 a) and d). However, the above freezing target temperature leads to lubrication of the particle-wall contact, facilitating a break-up of the RM as discussed in section 4.1.1.1. Within the regime of the disintegrating RM (Fig. 4.16 d) e) and f)), an increasing particle temperature leads to an increasing amount of RM. This suggests that the phenomena involved in

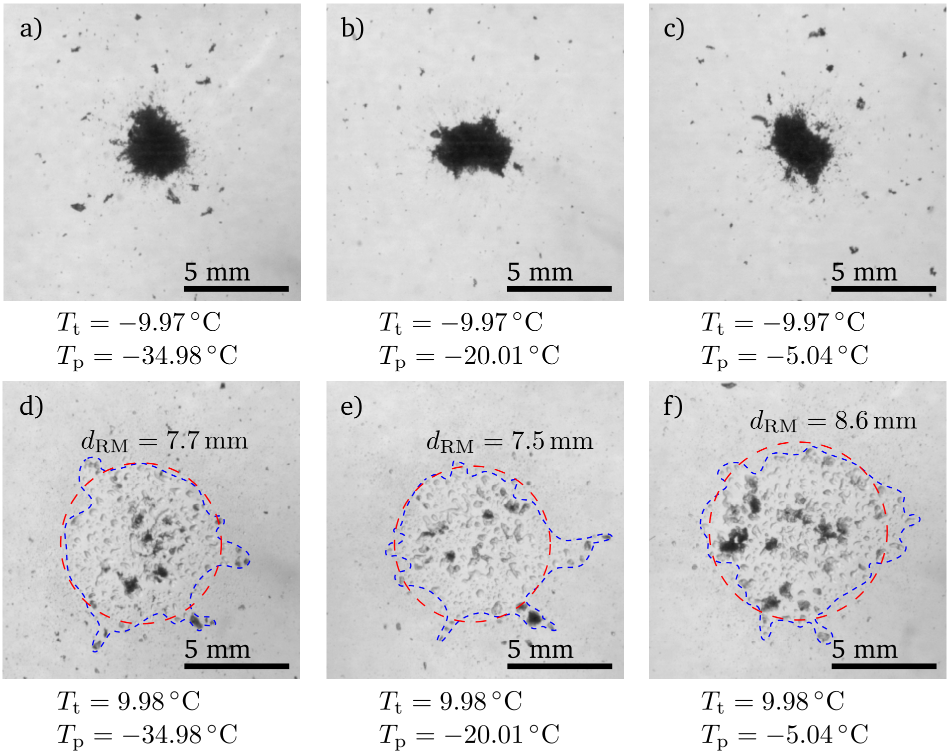

$T_{\mathrm{t}} = -9.97\,°\mathrm{C}$
$T_{\mathrm{p}} = -34.98\,°\mathrm{C}$

$T_{\mathrm{t}} = -9.97\,°\mathrm{C}$
$T_{\mathrm{p}} = -20.01\,°\mathrm{C}$

$T_{\mathrm{t}} = -9.97\,°\mathrm{C}$
$T_{\mathrm{p}} = -5.04\,°\mathrm{C}$

$T_{\mathrm{t}} = 9.98\,°\mathrm{C}$
$T_{\mathrm{p}} = -34.98\,°\mathrm{C}$

$T_{\mathrm{t}} = 9.98\,°\mathrm{C}$
$T_{\mathrm{p}} = -20.01\,°\mathrm{C}$

$T_{\mathrm{t}} = 9.98\,°\mathrm{C}$
$T_{\mathrm{p}} = -5.04\,°\mathrm{C}$

Figure 4.16: Example images of the RM captured $9\,\mathrm{ms}$ after the impact of ice particles with comparable particle diameters of $3.85\,\mathrm{mm} < d_{\mathrm{p}} < 4.08\,\mathrm{mm}$ and impact velocities of $68.5\,\mathrm{m\,s^{-1}} < v_{\mathrm{p}} < 76.7\,\mathrm{m\,s^{-1}}$. The particle temperature T_{p} was set to $-34.98\,°\mathrm{C}$, $-20.01\,°\mathrm{C}$ and $-5.04\,°\mathrm{C}$ (represented by the three columns) while the target temperature T_{t} was set to $-9.97\,°\mathrm{C}$ and $9.98\,°\mathrm{C}$ (represented by the two rows). The blue dashed line indicates the target area wetted with residual mass. The red dashed circles have the same area, visualizing the RM size with a more intuitive measure, the area equivalent diameter d_{RM}.

the secondary RM break-up, which are affected by the particle temperature, lead to an increasing RM. Thus, it is suspected that the RM increase is not caused by the generation of more fine fragments during the primary RM formation process. One possible explanation is, that the temperature dependent strength properties of bulk ice, like the brittle compressive failure strength (Schulson et al., 2009, pp.245-246), do not control the process.
Three possible mechanisms can be identified that increase the RM break-up propensity, namely a temperature dependent fragment cohesion inside the sintered RM

or a decreased friction at the particle-wall contact due to an increased lubricating water film for larger particle temperatures. The former mechanism seems implausible, since the force required to break a bond between two ice particles created by compressive sintering is observed to increase with increasing ice temperature, besides other influencing factors like contact time and contact load (Szabo et al., 2007; Bahaloo et al., 2022). As discussed in the context of QLL freezing inside the RM in section 4.1.1.1, the observed temperature dependent bond strength is still assumed to be not the dominant mechanism leading to the present observations. Thus, the decreased friction at the particle-wall contact is favoured for an explanation of an earlier break-up of the RM at larger particle temperatures. This hypothesis is supported by the observation of a larger area of the RM wetting the impact surface in this case. However, this phenomenon alone cannot explain larger amounts of RM sticking to the target surface if reduced friction would just lead to a RM spreading over a wider area. It is hypothesized that an earlier RM break-up allows more fragments originating from the rear of the particle to impact the target at a normal angle, instead of being re-directed by an intact RM cone. As a result, more fragments stick to the target, finally increasing the amount of RM.

4.1.1.5 Estimation of the Residual Mass at Low Temperature Conditions

In the case of above freezing target temperatures, the dynamic process of RM formation involves several sub-processes, like the initial formation of fine fragments, RM break-up and spreading, lubrication by a melt-water film, and presumably secondary particle impact and sticking. At sub-freezing target temperatures, the formation process of a compact, conical RM is assumed to be governed by less physical phenomena and the amount of RM can be estimated utilizing the model of Roisman (2022). In the following, a subset of 108 experiments is analyzed, corresponding to the experiments with a negative target temperature, combined with the data set of 62 experiments reported on in Reitter et al. (2022a). In this data set, the experimental parameters impact velocity and particle diameter were varied, ranging from $11.2\,\mathrm{m\,s^{-1}} < v_\mathrm{p} < 73.2\,\mathrm{m\,s^{-1}}$ and $1.89\,\mathrm{mm} < d_\mathrm{p} < 4.44\,\mathrm{mm}$, respectively. The measured, but uncontrolled particle and target temperature varied between $-10.9\,^\circ\mathrm{C} < T_\mathrm{p} < -9.4\,^\circ\mathrm{C}$ and $-10.6\,^\circ\mathrm{C} < T_\mathrm{t} < -6.7\,^\circ\mathrm{C}$, respectively.

In the present experiments, the base diameter of the residual ice cone $d_\mathrm{RM,max}$ is measured. It can be compared to the lamella spreading diameter d_lam for a liquid drop impact, since the deformation of the ice particle is assumed to be similar to the deformation of a liquid drop at small dimensionless times as discussed in Roisman (2022). The kinematics of the drop spreading diameter d_lam have been investigated in detail by Rioboo et al. (2002). It has been shown that for relatively small drop deformations, $\zeta < 0.2$, the spreading diameter scaled with the drop diameter $d^+_\mathrm{lam} = d_\mathrm{lam}/d_\mathrm{p}$ does not depend on the drop material properties like viscosity or surface tension. The dependence of d^+_lam on the drop dislodging parameter ζ is determined as

$$d^+_{\text{lam}} \approx b_{\text{spread}}\sqrt{\zeta}, \tag{4.9}$$

where the factor $b_{\text{spread}} \approx 2.05$ was determined by Rioboo et al. (2002). In Fig. 4.17, the measured base diameter of the residual ice cone $d_{\text{RM,max}}$, scaled by the initial particle diameter d_{p} is displayed as a function of the characteristic final particle dislodging parameter ζ_{max} obtained by evaluation of the model of Roisman (2022). Additionally, the evolution of a liquid drop spreading diameter as a function of the drop dislodging, determined in Eq. (4.9), is represented by a black dashed line in the same graph. The agreement between the present measurements and the predictions for a liquid drop impact supports the hypothesis of a residual ice cone formed after a spreading motion of fine fragments near the impact point. It is considered as a validation of the theory and of the assumed dynamic material properties of the ice particles. As shown in Fig. 4.17, the diameter of the residual ice cone, $d_{\text{RM,max}}$, can be modelled as the spreading diameter of a liquid drop lamella at the same dimensionless dislodging parameter ζ_{max}. In order to predict the total residual mass, it is assumed that it has the shape of a cone. The base diameter of the cone is then equal to the diameter $d_{\text{RM,max}}$, leaving just the cone height h_{RM} to be modelled. The cone height is not directly measured in the present experiments. However, from the measured RM diameter and mass, an expression for the cone height can be derived using geometric arguments. With the present assumptions,

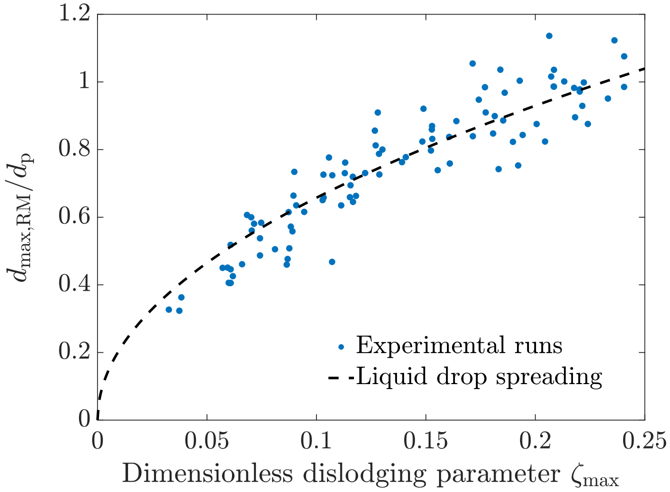

Figure 4.17: The spreading diameter of the residual ice cone d_{max} scaled by the initial particle diameter d_{p} as a function of the characteristic final particle dislodging parameter ζ_{max}. The dashed line corresponds to the spreading diameter of a liquid drop (Rioboo et al., 2002), defined in Eq. (4.9).

the amount of dimensionless RM, m^+_{RM}, can be expressed as

$$m^+_{\mathrm{RM}} = \frac{h^+_{\mathrm{RM}}(d^+_{\mathrm{RM,max}})^2}{2}, \tag{4.10}$$

where $h^+_{\mathrm{RM}} = h_{\mathrm{RM}}/d_{\mathrm{p}}$ is the scaled cone height and $d^+_{\mathrm{RM,max}} = d_{\mathrm{RM,max}}/d_{\mathrm{p}}$ is the scaled cone diameter. Rearranging the expression for h^+_{RM}, with use of Eq. (4.9) leads to a relation

$$h^+_{\mathrm{RM}} = \frac{2\,m^+_{\mathrm{RM}}}{(d^+_{\mathrm{RM,max}})^2} = \frac{2\,m^+_{\mathrm{RM}}}{b^2_{\mathrm{spread}}\zeta_{\mathrm{max}}}. \tag{4.11}$$

In order to investigate the cone shape, the relation of the cone height to the cone diameter $h^+_{\mathrm{RM}}/d^+_{\mathrm{RM,max}}$ is of interest, which finally leads to the expression

$$\frac{h^+_{\mathrm{RM}}}{d^+_{\mathrm{RM,max}}} \approx \frac{0.68\,m^+_{\mathrm{RM}}}{\zeta^{3/2}_{\mathrm{max}}}, \tag{4.12}$$

representing the angle of the cone. In Fig. 4.18, experimental results for this estimated cone angle are shown as a function of the scaled cone diameter. It seems

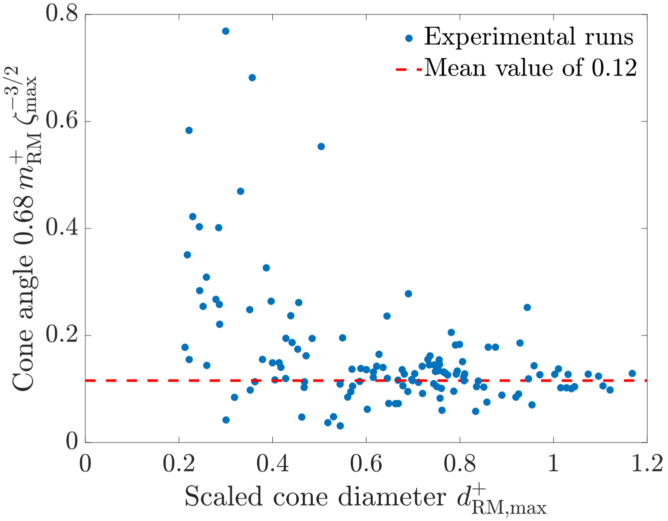

Figure 4.18: Experimental data for the scaled height of the residual ice cone h^+_{RM}, obtained using Eq. (4.11), plotted against the scaled residual cone diameter $d^+_{\mathrm{RM,max}}$.

that the cone angle tends to a constant value for larger cone diameters. Thus, as a working hypothesis, a constant ratio of $h^+_{\mathrm{RM}}/d^+_{\mathrm{RM,max}} = 0.12$ is used for modelling the scaled cone height. Finally, an approximation of the dimensionless mass m^+_{RM} as a function of the maximum dislodging parameter $\zeta_{\max}$ can be obtained as

$$m^+_{\mathrm{RM}} = \frac{0.12\, b^2_{\mathrm{spread}} \zeta^{3/2}_{\max}}{2\sqrt{2}} \approx 0.1773\, \zeta^{3/2}_{\max}. \tag{4.13}$$

In Fig. 4.19, the predicted values of m^+_{RM} are compared to the experimental results. Although a deviation of the predicted from the measured residual mass exists, the general trend of the data is predicted well and Eq. (4.13) can be used for the engineering modelling of the processes involved in ice accretion. The present results are already incorporated in numerical codes for ice accretion prediction as used by Malik et al. (2023). They modify the ice mass sticking efficiency in such a way, that 2% of an ice particle mass sticks to the surface, even without liquid water present.

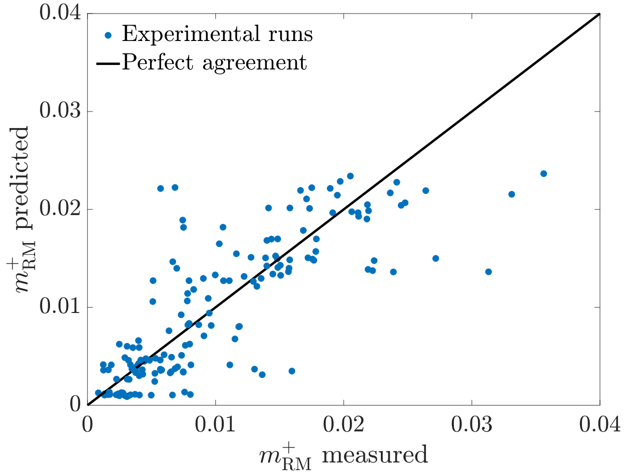

Figure 4.19: Prediction of the dimensionless residual mass m^+_{RM} using expression (4.13) plotted against the experimental measurements. Perfect agreement between the model and experiments is illustrated as black solid line.

4.1.1.6 Conclusion

The focus of the present section has been on the formation of a residual mass after ice particle impact and fragmentation. Applying a full factorial design of experiments, the particle diameter, impact velocity, temperature and target temperature were varied systematically. The ice mass and surface area covered by ice after the impact were measured. It was found that all varied parameters significantly influence the amount of residual mass at a 5% significance level. Quantitative analysis showed that an appropriate scale for the residual mass is the initial ice particle mass, allowing a description of the phenomenon using the dimensionless residual mass. Assuming a conical shape for the dimensionless residual mass, the theoretical model for particle deformation of Roisman (2022) is used to predict the geometry and thus the amount of dimensionless residual mass for sub-freezing target temperatures. The physics behind the formation of the residual ice cone remains unclear, yet several potential explanations have been identified. It can be a result of dissipation in the deforming particle, combined with a pressure induced melting point depression, leading to local melting of the fragments and subsequent fast solidification after impact. In the statistical analysis, it has been shown that both the particle and target temperature significantly affect the amount of dimensionless residual mass. Thus, the model for the amount of residual mass should be extended in future work to incorporate these effects. Finally, the model can then be utilized for the heat flux estimation during the collision of an ice particle with a hot solid substrate, associated with the ice crystal accretion problem.

4.1.2 Analysis of the Fragment Size Distribution

The experimental results for the fragment size distribution are examined both qualitatively and quantitatively. The fragmentation process depending on the impact conditions, is qualitatively assessed based on visual inspection of the captured video data and the measured particle size distributions are characterized with respect to their shape using the power-law parameter Ψ. A statistical analysis is performed to investigate which parameters control Ψ significantly at the $\alpha = 0.05$ level, and the results are discussed in the context of findings reported in literature about ice fragmentation.

4.1.2.1 Qualitative Analysis and Experimental Observations

Within the parameter range of the present experiments, four different fragmentation modes are encountered. Typical examples of each type are presented in Fig. 4.20, actually resembling the types described by Hauk et al. (2015) and Uenishi et al. (2019). The latter specifically describe types (a) and (c), whose occurrence they explain based on a model that relates to the time required to reach a pressure threshold during impact. This in turn determines the evolution of the amplitudes of shear stress waves leading to specific fracture types. No correlation is found between the occurrence of types (a)-(c) and neither the particle nor the target temperature in the present work. For the present range of particle impact velocities, fragmentation types (a)-(c) are encountered exclusively for small particles with $d_\mathrm{p} < 3\,\mathrm{mm}$ and impact velocities of approximately $10\,\mathrm{m\,s^{-1}}$. Faulting of the particle at the lowest impact velocity level is caused mostly by splitting due to radial cracks, as shown in Fig. 4.20b), with some expressing characteristics of type (c). This observation is in

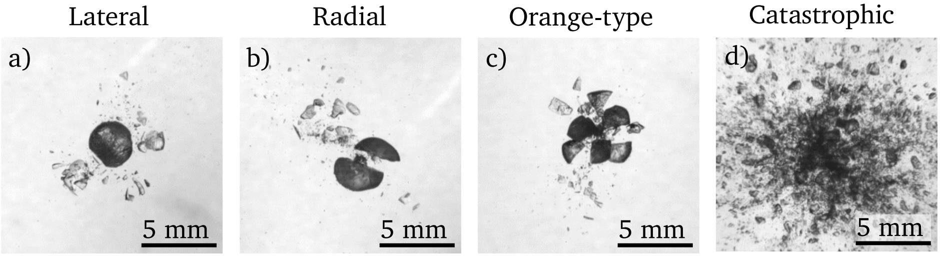

Figure 4.20: Encountered types of particle fragmentation classified according to Hauk et al. (2015) and Uenishi et al. (2019). Experimental parameters for:
a) $v_\mathrm{p} = 12.31\,\mathrm{m\,s^{-1}}$, $d_\mathrm{p} = 2.88$ mm, $T_\mathrm{p} = -5.0\,°\mathrm{C}$, $T_\mathrm{t} = 10.1\,°\mathrm{C}$,
b) $v_\mathrm{p} = 11.34\,\mathrm{m\,s^{-1}}$, $d_\mathrm{p} = 2.85$ mm, $T_\mathrm{p} = -34.9\,°\mathrm{C}$, $T_\mathrm{t} = 10.1\,°\mathrm{C}$,
c) $v_\mathrm{p} = 11.22\,\mathrm{m\,s^{-1}}$, $d_\mathrm{p} = 2.87$ mm, $T_\mathrm{p} = -5.0\,°\mathrm{C}$, $T_\mathrm{t} = 10.0\,°\mathrm{C}$,
d) $v_\mathrm{p} = 72.85\,\mathrm{m\,s^{-1}}$, $d_\mathrm{p} = 2.77$ mm, $T_\mathrm{p} = -35.0\,°\mathrm{C}$, $T_\mathrm{t} = 9.7\,°\mathrm{C}$.

agreement with predictions for the occurrence of the fragmentation types by Hauk et al. (2015). Based on their analysis, they postulate a minimum velocity for the onset of particle damage and the transition to major fragmentation, and likelihood functions for the appearance of the different fragmentation types depending on the impact conditions. For the present experiments, impact velocities for particles with mean diameter $2.83\,\mathrm{mm}$ are above both the upper boundary for no fragmentation with approx. $2.3\,\mathrm{m\,s^{-1}}$ and the upper boundary for transition to major/catastrophic fragmentation with approx. $7\,\mathrm{m\,s^{-1}}$. Using the model from Hauk et al. (2015), it is thus predicted as highly unlikely to encounter type (a) for the range of velocities in the present experiments, which is in agreement with the present observations. For particles with diameters on the lower level of the present work, fragmentation due to lateral cracks is predicted as more likely to occur and the transition velocity from minor to major fragmentation is predicted as approx. $9.3\,\mathrm{m\,s^{-1}}$.

In accordance with reports of Guégan et al. (2011), the phenomenon of a two-stage ejection of fragments during impact is observed, whose distinction generally becomes more pronounced with increasing particle impact velocity. As shown for example in Fig. 4.21, a first wave of small fragments with high velocity precedes a second, denser wave of fragments that expands continuously until the end of the fragmentation process. The distinction between a first and second wave generally becomes more pronounced with increasing particle impact velocity. In contrast to the homogeneous distribution of fragments, also spatial fragment clustering in pronounced geometrical shapes can be observed, as shown for example in Fig. 4.22. Spatially localized fragment clusters are exclusively observed at impact velocities greater than $50\,\mathrm{m\,s^{-1}}$ and particle temperatures equal or below $-20\,°\mathrm{C}$. Based on phenomenological observations in the captured video data, the interaction of

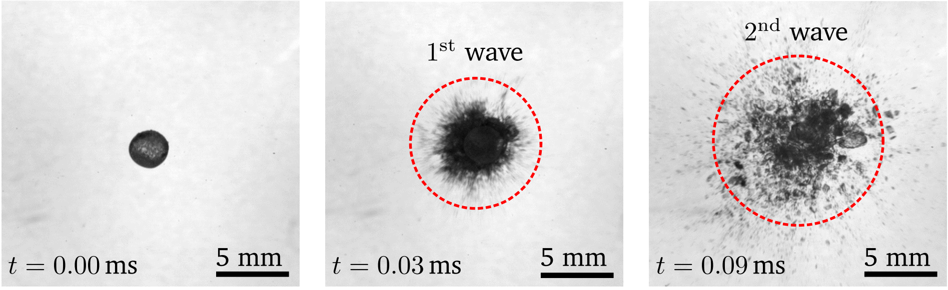

Figure 4.21: Illustration of the two-stage ejection of fragments during particle impact with $v_\mathrm{p} = 77.32\,\mathrm{m\,s^{-1}}$, $d_\mathrm{p} = 2.72\,\mathrm{mm}$, $T_\mathrm{p} = -5.1\,°\mathrm{C}$ $T_\mathrm{t} = -10.1\,°\mathrm{C}$, as also described in Guégan et al. (2011). Shortly after impact, a first wave of finely crushed fragments emerges with a high radial velocity from the point of impact which is followed by a second wave of fragments with larger fragment size and lower velocity.

fragments of the disintegrating particle with the RM adhering to the target during impact turns out to be the origin of these fragment clusters. As discussed in the previous section and visible in Fig. 4.22, some of the ice particle mass adheres to the impact surface during impact. For the case of ice particle impact, the cone of finely crushed material is presumably fused together by a sintering process facilitated through frictional heating and melting point depression due to high pressures inside

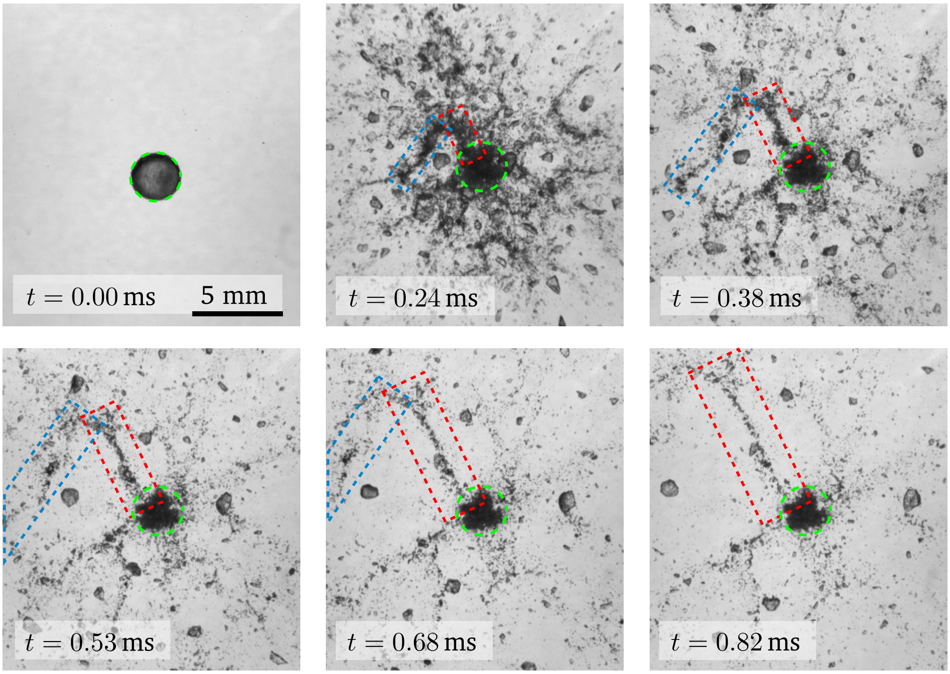

Figure 4.22: Impact of an ice particle with $v_\mathrm{p} = 75.28\,\mathrm{m\,s^{-1}}$, $d_\mathrm{p} = 2.89$ mm, $T_\mathrm{p} = -34.9\,°\mathrm{C}$, $T_\mathrm{p} = -10.0\,°\mathrm{C}$. During the initial stages after impact, a residual ice mass starts adhering to the impact surface. The ice mass is composed of finely crushed fragments originating from the leading edge of the impacting particle and is visible as a black convex region around the point of impact. Depending on the impact conditions, subsequent larger fragments originating from the trailing edge of the particle and being associated with a significant momentum eventually impinge on the adhering ice mass resulting in the ejection of large clusters of fragments originating from the adhering ice mass. The clusters eventually further disintegrate during their radial motion in the global flow field. For comparison, the green dashed line indicates the contour of the impacting particle.

the particle during impact as discussed in section 4.1.1.1. The residual ice mass then refreezes and either remains frozen and attached to the target if $T_\mathrm{t} < 0\,^\circ\mathrm{C}$ or melts slowly on the target if $T_\mathrm{t} > 0\,^\circ\mathrm{C}$.

During the formation of the residual ice cone, fragments originating from the trailing edge of the particle may subsequently impinge on and interact with the adhering cone. While the initial impact conditions can be assumed to primarily control the dynamics and size distribution of fragments eventually further interacting with the ice cone, the particle and substrate temperature may alter the response of the ice cone to the impinging fragments through the temperature dependence of its material properties.

The force exerted on the ice cone by impinging fragments significantly depends on the size distribution and momentum in the portion of fragments interacting with the ice cone, which in turn depends on the initial impact conditions. For the case of a stream of a large number of small fragments homogeneously impinging onto the ice cone, the ice cone is presumably homogeneously eroded. In contrast, the impingement of fewer but larger fragments is associated with a discrete behaviour. Depending on the fragment impact velocity and mass, the impact forces associated with larger fragments may not only overcome the cohesive forces between individual sintered fragments at the surface of the cone, it may also overcome the cohesive force between larger portions of the sintered cone and the impact target below, resulting in the separation of large clusters of sintered fragments from the cone. The subsequent cluster behaviour is mainly controlled by temperature, affecting the associated properties and cohesive forces of the fragment clusters. Additionally, the impact position of the fragment onto the ice cone plays a role.

A cluster may stay intact and thus follow a common trajectory which is affected by both the flow field resulting from the initial particle impact, interactions with the surrounding fragments and the momentum transfer from the interaction with the impinging fragment. In contrast, a fragment cluster may also further disintegrate into individual fragments, which is either associated with the formation of a pronounced circumferential rim around the impacting fragment or a radial line consisting of fine fragments along the trajectory of the cluster, indicated by the blue and red box in Fig. 4.22, respectively. The clusters originate from the adhering ice cone below the impinging fragment and are emitted radially outwards from the interaction point. However, this radial spreading of fragments and the associated formation of a rim of fragments are also affected by the global flow field resulting from the initial particle impact. As a consequence, the rim is stretched in the circumferential direction as it transitions in the radial direction over time, as shown in Fig. 4.22.

The ice mass adhering to the impact target is actually not considered as part of the fragment population in the present work. Therefore, in particular intact clusters, which are erroneously interpreted as one large fragment even though they actually contain a large number of small fragments, are prone to add a certain error to the measured size distribution. The analysis of the power-law parameter $\overline{\Psi}$ is performed to minimize the associated error for the set of experiments with a combination of

parameters that facilitates this fragmentation process.
The phenomenon of a pronounced ejection of fragment clusters forming the initial ice mass adhering to the target is primarily observed for low temperatures. The force required to break a bond between two ice particles created by compressive sintering was observed to decrease with decreasing temperature next to other influencing factors like contact time and contact load (Szabo et al., 2007; Bahaloo et al., 2022) as already discussed in section 4.1.1.1 for the RM generation processes. It was reasoned that although the shortest contact time is 20 ms in the experiments of Szabo et al. (2007), which is large compared to an estimated contact time below 0.1 ms for the present experiments, the observed trends can be extrapolated for the present work. Szabo et al. (2007) observe an increased ice particle bond strength with increasing temperature. While this dependency was not considered to play a role in the primary RM break-up process at above freezing target temperatures, it may affect the secondary process of RM erosion and poses a possible explanation for the resulting ejection of fragment clusters at low temperatures.

4.1.2.2 Design of Experiments

Similar to the procedure for the investigation of the RM, reported on in section 4.1.1.2, an experimental FFD is applied. In fact, the same experiments are used for the analysis of the fragment size distribution, as for the investigation of the RM. However, only a subset of 96 experiments is analyzed. The largest level of the particle diameter, $d_\mathrm{p} = 3.94\,\mathrm{mm}$, and the intermediate level of the particle temperature, $T_\mathrm{p} = -20.01\,°\mathrm{C}$, are omitted. The reason for omitting large particles is the inability to robustly track and analyse all fragments in this case. Since the fragment number and density emerging from the point of impact increase for large particles and impact velocities, the chosen FOV is too small to allow for a sufficient separation of individual fragments. Hence, excluding this level of particle diameters from evaluation prohibits a potentially introduced bias on the investigated distribution parameter Ψ as not all fragments can be robustly tracked.
The intermediate level of the particle temperature, $T_\mathrm{p} = -20.01\,°\mathrm{C}$, is omitted. In the analysis, the possible presence of an effect of the particle temperature on $\overline{\Psi}$ is investigated first, only using the extreme values $T_\mathrm{p} = -34.98\,°\mathrm{C}$ and $T_\mathrm{p} = -5.04\,°\mathrm{C}$. Only if an effect is present, which was not the case, the level of $T_\mathrm{p} = -20.01\,°\mathrm{C}$ would have been included to investigate the influence of T_p in more detail. The experimental conditions of the reduced FFD are summarized in 4.2, where the displayed values are calculated for each factor as the mean of all experimental runs for the given level. Since the experiments are a subset of all experiments reported on in section 4.1.1.2, ice particles with high aspect ratios or obvious deformations have been discarded by visual examination. Similarly, only particles are considered that exhibit roundness values above a threshold of $R = 0.75$, and sphericity values above $S = 0.9$. The crystallisation structure of the particles and their vanishing angular velocity are assumed not to be of significance. Three replications are per-

<table>
<tr><th>Controlled parameters</th><th>Level 1</th><th>Level 2</th><th>Level 3</th><th>Level 4</th></tr>
<tr><td>Particle velocity v_p in $\mathrm{m\,s^{-1}}$</td><td>12.05</td><td>26.44</td><td>58.02</td><td>74.33</td></tr>
<tr><td>Particle diameter d_p in mm</td><td>1.86</td><td>2.83</td><td></td><td></td></tr>
<tr><td>Particle temperature T_p in $^\circ\mathrm{C}$</td><td>-34.98</td><td>-5.04</td><td></td><td></td></tr>
<tr><td>Target temperature T_t in $^\circ\mathrm{C}$</td><td>-9.97</td><td>9.98</td><td></td><td></td></tr>
<tr><th colspan="2">Uncontrolled parameters, measured</th><th colspan="2">Lower limit</th><th>Upper limit</th></tr>
<tr><td colspan="2">Sphericity S</td><td colspan="2">0.9</td><td>1</td></tr>
<tr><td colspan="2">Roundness R</td><td colspan="2">0.75</td><td>1</td></tr>
<tr><td colspan="2">Ambient temperature T_air in $^\circ\mathrm{C}$</td><td colspan="2">-15</td><td>-7</td></tr>
<tr><td colspan="2">Impact angle</td><td colspan="2">Normal to surface</td><td></td></tr>
<tr><th colspan="4">Uncontrolled parameters, unmeasured</th><th>Assumption</th></tr>
<tr><td colspan="4">Particle angular velocity in $\mathrm{s^{-1}}$</td><td>≈ 0</td></tr>
<tr><td colspan="4">Particle crystallization structure</td><td>Polycrystalline</td></tr>
</table>

Table 4.2: Summary of all experimental parameters eventually being influential for ice particle fragmentation subdivided into three categories. For the controlled parameters, the mean values of all corresponding experiments are displayed.

formed for each factor level combination, resulting in a total of 96 experimental runs. The combinations of particle diameter, d_p, and impact velocity, v_p, for all experimental runs are summarized in Fig. 4.23, where factor levels are visible as local clusters. For each experimental run, measured velocities and diameters are indicated by blue markers scattered around the mean value of each factor level combination (cluster), which is indicated by a yellow circle. Within a given cluster, the particle and target temperature remain as varying parameters. Each factor level combination is repeated three times and thus, three blue markers are combined into one red marker for each factor level combination, where the four resulting red dots represent the possible combinations of the particle and target temperature.
The initial statistical evaluation to determine the statistical significance of the factors is performed such that each factor level combination is treated categorically, assuming the mean level values as summarized in Table 4.2. For the regression analysis in later stages, the true measured velocity and diameter values of each experimental run are used instead in order to mitigate the potential influence of the associated bias.

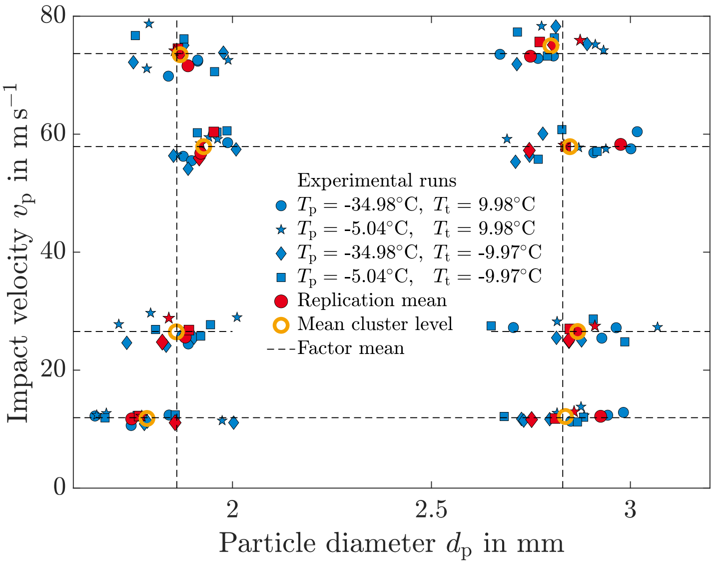

Figure 4.23: Distribution of the measured particle diameter d_p and impact velocity v_p for all experimental runs visualized with blue markers. For each displayed factor level combination, the cluster of experimental runs contains three replications for each possible combination of the particle and target temperature level. The replication means are indicated with red markers. Four replication means are combined to obtain the mean cluster level, denoted by a yellow circle. The global level value of each factor is calculated as the mean of all experimental runs on that level, visualized by the dashed black lines.

4.1.2.3 Statistical Data Analysis

The reduced FFD again exhibits an orthogonal structure of the varied factors, allowing a rigorous statistical analysis of the experimental data. It is determined, whether the particle diameter, impact velocity as well as particle and target temperature have any statistically significant influence on the shape of the fragment size distribution characterized by the power-law distribution parameter $\overline{\Psi}$. An ANOVA is performed in order to determine the significance of an effect or interaction effect on the response $\overline{\Psi}$ with the null hypothesis that an effect has no influence on the measured response $\overline{\Psi}$. The null hypothesis is rejected and an effect is considered significant when the standardized effect strength represented by a t-value defined in Eq. (4.8) is above the threshold value associated with the global significance level taken at 5%.

Determination of Statistically Significant Influencing Factors The prerequisites for an ANOVA comprising mutual independence, normal distribution and equal variances of the error variable, are scrutinized by analyzing the standardized residuals of $\overline{\Psi}$, similar to the procedure reported on in section 4.1.1.2. In contrast to the analysis of the RM, the discussed prerequisites are fulfilled immediately for the analysis of $\overline{\Psi}$. Hence, no data transformation is needed and the effect significance can be directly analysed utilizing the Pareto chart shown in Fig. 4.24. Only three of the effects and their mutual interaction exceed the global significance level of approximately 2. These include the particle impact velocity (A) and its interaction effect with the particle diameter (AB) and target temperature (AD). Note that the t-value for particle impact velocity v_p tends towards infinity, as the corresponding p-value, p_ANOVA is close to zero. Therefore, the corresponding t-value in Fig. 4.24 is arbitrarily limited to 7.5. To assess the significance of each factor, non-significant terms from Fig. 4.24 are excluded in a step-wise procedure, beginning with the term with the smallest t-value. The factorial regression is repeated as long as terms with insignificant contributions are left in the model. At the significance level $\alpha = 0.05$, three terms remain in the model as A, AB and AD, that were already identified in

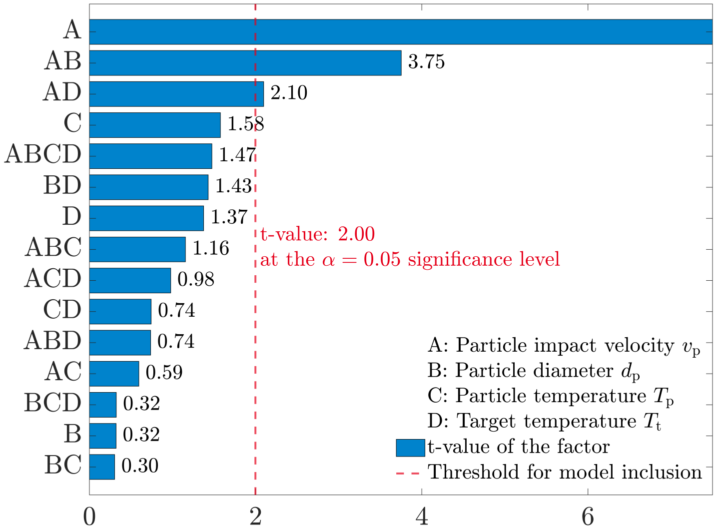

Figure 4.24: Pareto chart summarizing the t-values for all experimental parameters and their interactions. The significance of an effect or interaction effect on the mean $\overline{\Psi}$ is determined by comparison of the individual t-values against the t-value at a global significance level of $\alpha = 0.05$. Three terms exceed this t-value of 2.00: A, AB and AD, where the p_ANOVA value for A is close to zero, causing its t-value obtained from Eq. (4.8) to tend towards infinity.

the initial analysis of factor insignificance and shown in Fig. 4.24. In addition to the determination of a significant influence of systematically varied and controlled factors on $\overline{\Psi}$ in Fig. 4.24, the influence of the uncontrolled factors as summarized in Table 4.2 is examined. The standardized residuals are shown for each measured uncontrolled experimental parameter in Fig. 4.25. No trend in the data for the air temperature, roundness and sphericity suggests that $\overline{\Psi}$ is not correlated with these parameters. This is confirmed by the calculation of the Pearson correlation

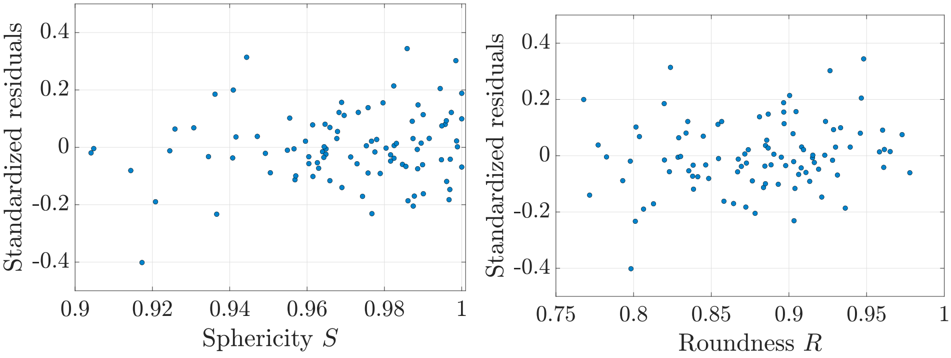

(a) Standardized residuals plotted against the sphericity S of the impacting ice particle.

(b) Standardized residuals plotted against the roundness R of the impacting ice particle.

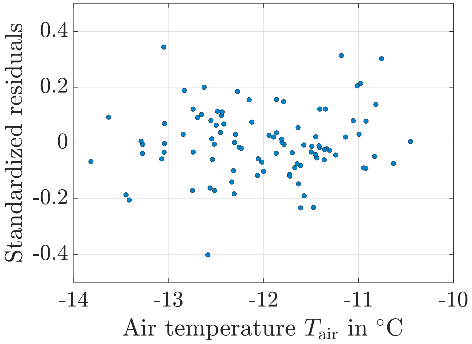

(c) Standardized residuals plotted against the air temperature T_{air}.

Figure 4.25: Standardized residuals calculated as the difference between the measured response and the Ordinary Least Squares (OLS) fit for that factor level combination, respectively rationalized using its estimated standard deviation. The potential influence on $\overline{\Psi}$ is determined by visual inspection for signs of correlations with the covariates ambient temperature, T_{air}, roundness R, and sphericity S.

coefficient. For each uncontrolled experimental parameter, the null hypothesis has been tested that there is no relationship between the observed phenomena null hypothesis at the $\alpha = 0.05$ significance level. Since the p-value of the test for each parameter is greater than the threshold, it can be concluded that the covariates roundness, sphericity and air temperature have no influence on $\overline{\Psi}$ for the chosen parameter range and accordingly, their influence is neglected in the further statistical analysis.

Interaction plots are shown in Fig. 4.26 for the model terms AB, comprising the interaction of the parameters v_p and d_p, and AD that reflects the interaction between v_p and T_t. The mean values of $\overline{\Psi}$ obtained for all particle impact velocity levels and both diameter and target temperature levels are shown as large red and blue markers. An interaction is present if the lines connecting the mean values for each factor combination are not parallel (Dean et al., 2017), actually implying the dependence of the effect of a factor on $\overline{\Psi}$ on the respective other factor. As can be seen in Fig. 4.26a), interactions for the term AB only occur for larger particle impact velocities. No interaction is observed for the two lower velocity levels. For combinations of large particle diameter and high impact velocity, fragment detection and size evaluation becomes an increasingly difficult task. Fragments are obscured more often partly or fully by other fragments due to their higher spatial density

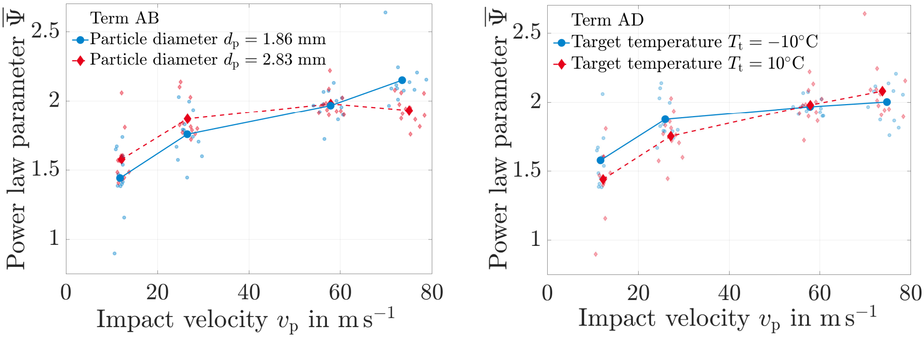

(a) Interaction plot showing the mean power-law parameter $\overline{\Psi}$ for four levels of the particle impact velocity v_p and two levels of particle diameter d_p.

(b) Interaction plot showing the mean power-law parameter $\overline{\Psi}$ for four levels of particle impact velocity v_p and two levels of the target temperature T_t.

Figure 4.26: Interaction plots for the mean power-law parameter $\overline{\Psi}$. Small markers indicate individual experimental runs that result in the mean values finally connected through lines. Interactions are present if the difference between the level mean values obtained for a given impact velocity for the different levels of d_p or T_t significantly changes with varying v_p.

in comparison to low impact velocities. This is exacerbated by the appearance of localized spatial clusters of fragments at particle temperatures below $-20\,^{\circ}\mathrm{C}$, since these are sometimes misidentified as a single large fragment. For particles of the smaller diameter level, the current field of view is chosen sufficiently large to allow fragment separation and subsequent tracking using KAFTA. Yet, for the combination of the highest level in particle diameter and impact velocity, smaller fragments may be lost in the cloud of fragments by the detection algorithm. Fewer tracked fragments of small diameter lead to an artificial decrease in the computed value of $\overline{\Psi}$. Considering the increasing difficulties in detecting fragments, the calculated significance of the interaction term for larger impact velocities is rather attributed to technical limitations of the evaluation procedure, rather than representing a truly occurring, physical effect. The model term AB comprising the interaction of the parameters v_{p} and d_{p} is thus excluded from the significant terms that participate in the data fitting.

The difference in the mean values of $\overline{\Psi}$ for different target temperatures, as shown in Fig. 4.26b) for the term AD comprising the interaction between v_{p} and T_{t}, is not constant over the examined range of particle velocities, indicating the presence of an interaction. However, a closer examination of all the experimental runs shows that the apparent interaction can be attributed to the influence of outliers on the mean value. For example, the mean $\overline{\Psi}$ for $T_{\mathrm{t}} = 10\,^{\circ}\mathrm{C}$ for the lower velocity level at $v_{\mathrm{p}} = 12.05\,\mathrm{m\,s^{-1}}$ contains the two lowest measured values, while $T_{\mathrm{t}} = -10\,^{\circ}\mathrm{C}$ contains an outlier with the highest measured $\overline{\Psi}$ at this velocity level. Conversely, at $v_{\mathrm{p}} = 74.33\,\mathrm{m\,s^{-1}}$ the mean of $\overline{\Psi}$ at $T_{\mathrm{t}} = 10\,^{\circ}\mathrm{C}$ is overly effected by one outlier. Except for the intermediate level of velocity at $v_{\mathrm{p}} = 26.44\,\mathrm{m\,s^{-1}}$, the distribution of $\overline{\Psi}$ suggests no difference in the velocity level specific mean for varying target temperature if the outliers are not taken into consideration. Within the limits of achievable experimental parameters and under consideration of the statistical evaluation of the data, the fragment distribution is hence assumed to be solely dependent on the particle impact velocity.

Effect of the Particle Temperature Remarkably, the particle temperature apparently has no effect on the distribution coefficient $\overline{\Psi}$ as shown in Fig. 4.24, although the temperature of ice has been reported to affect its strength Schulson (2001). The ice compressive strength is affected by temperature even for strain rates up to an order of $\mathcal{O}(10^3)\mathrm{s}^{-1}$ as reported by Wu et al. (2015) and Shazly et al. (2009). While a correct treatment of the compressive strength is important for the prediction of the force development during ice particle impacts numerically (Tippmann et al., 2013) or theoretically (Roisman, 2022), the independence of $\overline{\Psi}$ from the temperature-dependent compressive strength suggests that it is not the main influencing quantity controlling the particle size distribution for the present range of investigated experimental parameters.

To the author's knowledge, the influence of ice temperature on the fractal dimension has not yet been investigated; the specimen temperature is not specified for the data reported in Weiss (2001). Also for ice particle fragment size distributions, reported data for the particle temperature is rare, as summarised in the introduction. Only Vargas et al. (2020) phenomenologically report an increase of the portion of smaller particles with decreasing temperature. Assuming this trend generally can be captured using the power-law fitting procedure performed in the present work, this would correspond to higher values of $\overline{\Psi}$ for decreasing temperatures. However, a dependence of $\overline{\Psi}$ on temperature has been demonstrated to be negligible based on the present data.

Effect of the Particle Impact Velocity For a combination of a large particle impact velocity and diameter, the values of $\overline{\Psi}$ are artificially decreased, as discussed in connection with Fig. 4.22. The phenomenon is attributed to technical limitations related to the fragment detection. When dense clusters of fine fragments are not separated enough within the camera field of view, the detection of individual fragments is not possible. This poses a challenge for an empirical description of the dependence of Ψ on v_p. In order to minimize the influence of suspected technical limitations and outliers on the empirical regression coefficients, in total two levels for the combination of the upper two impact velocity levels at the upper particle diameter level are excluded. The regression analysis is subsequently performed using the 72 remaining measured values of $\overline{\Psi}$ and the true measured values of d_p and v_p as shown in Fig. 4.23, instead of using mean level values. The dependence of the experimentally obtained values of $\overline{\Psi}$ on particle impact velocity are shown in Fig. 4.27. In order to reduce the effect of outliers, a robust OLS regression procedure with a bisquare weight function is used for an estimation of the functional relation between impact velocity and $\overline{\Psi}$. The fit is shown as red curve in Fig. 4.27 and can be expressed by the relation

$$\overline{\Psi} = 1.3312 + 0.0195 \frac{v_\mathrm{p}}{\mathrm{m\,s^{-1}}} - 1.26 \times 10^{-4} \frac{v_\mathrm{p}^2}{\mathrm{m^2\,s^{-2}}} \, . \tag{4.14}$$

As summarized in section 2.3, comparatively few studies are devoted to fragment size distribution measurements for ice particle impacts with diameters less than typical hailstone diameters. However, the non-linearity of velocity effect on the fragment size distributions and an increase in $\overline{\Psi}$ with increasing particle impact velocity are consistent with reports from Vargas et al. (2015), Vargas et al. (2020), and Combescure et al. (2011), even though no specific values are available for comparison. Moreover, also the experimental data presented in Senoner et al. (2022) suggests a distribution of d_f that follows a power-law.

4.1.2.4 Implications for the Occurring Fracture Processes

Similarities between rock and ice fracture processes have been identified in earlier studies (Schulson, 2001). Hence, additional studies of rock impacts are included in the following discussion. For example, Ma et al. (2018a) and Ma et al. (2018b)

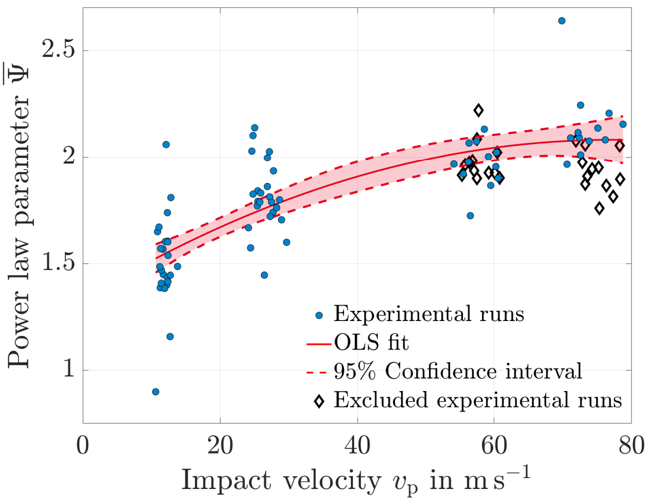

Figure 4.27: Dependence of experimental data for $\overline{\Psi}$ on the particle impact velocity. The robust fit of the dependence of the fragment volume power-law parameter is obtained by applying an OLS fit with a bisquared weight function. The shaded region indicates the 95% confidence interval of the model. Experiments with a combination of the upper two impact velocity levels and the large particle diameter level are indicated by diamond markers. These values are excluded from the fitting procedure because of suspected technical limitations leading to a non-detection of small fragments.

numerically find a similar increase in $\overline{\Psi}$ with increasing velocity for the impact of spheres of a generic brittle heterogeneous material onto a rigid wall. They studied the shape and mass distribution of the resulting fragments after impact via Finite-Discrete Element Method simulations at velocities comparable to the present work. A striking similarity is the nonlinear increase of $\overline{\Psi}$ with increasing velocity both in the present work and the results from Ma et al. (2018b). For impact velocities of $10\,\mathrm{m\,s^{-1}}$, the power-law exponent takes on a value $\overline{\Psi} = 1.59$ in their work. Similar to the functional relationship in the present work, $\overline{\Psi}$ calculated with all rock fragments increases with increasing impact velocity and seems to tend asymptotically to an upper bound of $\overline{\Psi} \approx 2$ at $v_0 = 50\,\mathrm{m\,s^{-1}}$. Additionally, Ma et al. (2018b) analyzed the power-law exponent of exclusively fine debris with diameters smaller than 10% of the initial particle diameter, where they found $\overline{\Psi} \approx 2$ to remain almost constant over the range of velocities studied, coinciding with the upper bound value for all fragments at high impact velocity in the present work.

They hypothesise that this phenomenon originates from two possible cracking mechanisms leading to particle fracture. While a mixture of mode I fracture (tensile fracture) and mode II fracture (shear fracture) occurs at low impact velocities, mode II fracture becomes more dominant at high impact velocities. Since the fine debris ($\overline{\Psi} \approx 2$) originates from the zones of high shear in the particle, $\overline{\Psi}$ is assumed to approach this value for all fragments at high impact velocities as mode II fracture begins to dominate throughout the particle. The method of data collection used in the present work precludes any conclusions about fragment diameters smaller than approx. $0.23\,\mathrm{mm}$ and thus, the link between an upper bound for $\overline{\Psi}$ associated with the smallest fragments cannot be verified. Additionally, a larger amount of small ice particles generated in the high shear zone near the impact point forms the residual mass and cannot be included in the analysis. However, assuming an evolution of $\overline{\Psi}$ similar to the results of Ma et al. (2018b) considering all fragments, a theoretical limit of $\overline{\Psi}$ may be postulated as $\overline{\Psi}_{\max} \approx 2.1$, obtained from extrapolation of the available data.

An additional interpretation of increasing values of $\overline{\Psi}$ with increasing impact velocity is given by Hartmann (1969) in the context of the fragmentation of rock. They associated lower values of $\overline{\Psi}$ with a single fragmenting blow and higher values of $\overline{\Psi}$ with a repetitive break-up process, such as grinding. This finding may be combined with the simulation results of Carmona et al. (2008), who used the discrete element method to refine the understanding of brittle fracture processes. After initial cracking, the total kinetic energy of the particle determines whether or not emerging fragments are further broken up by secondary, oblique cracks. Therefore, the observed increase of $\overline{\Psi}$ for increasing impact velocity could indicate a shift in fragmentation mainly due to secondary cracks. Similarly to Ma et al. (2018b), Carmona et al. (2008) also find a power-law distribution parameter of $\Psi = 2.2 \pm 0.2$ for small fragments, which seems to be robust against changes in the impact velocity and material properties. Whether a shift from mode I to mode II fracture or a repetitive break-up of fragments with high kinetic energy is the cause for larger values of $\overline{\Psi}$ is still open for debate. However, the increase of $\overline{\Psi}$ with larger ice particle impact velocities is clearly demonstrated with the present data, approaching a value of $\overline{\Psi}_{\max} \approx 2$, equal to the value found for small fragments in the numerical studies of Ma et al. (2018b) and Carmona et al. (2008).

4.1.2.5 Scale Invariance and the Effect of Strain Rate

It is well known that fragmentation processes in many cases exhibit scale invariance, as summarised e.g. by Turcotte (1997), and specifically for ice by Weiss (2001). However, conclusions regarding the scale invariance of fragmentation and associated fractal dimension require the measurement of at least two decades of $\tilde{V}_{\mathrm{f}}$ (Gonzato et al., 1998), which is not the case in the present work with the current fragment detection limit (see Fig. 3.11). Although the present data itself does not allow distinct conclusions about the scale invariance, the assumption of the fractal nature of ice particle fragmentation is actually consistent with the observed statistically insignificant effect of the particle diameter on $\overline{\Psi}$, since scale invariance inherently precludes any size effect. Therefore, the present results actually appear to confirm the assumption of scale invariance underlying the present data.

Still, a connection between the reported findings on scale invariant ice fracture of Weiss (2001) and the present work can be made, if the present results are analysed with respect to the strain rates present during fragmentation. Instead of the fragment volume, the fragment diameter has been used to determine the power-law parameter $\overline{\Psi}_d$ for data comparability. While Weiss (2001) reports a universal fractal dimension lower than the presently observed one, the corresponding strain rates are small when compared to ice particle impact events. However, the increasing ratio of smaller fragments, and thus larger values of $\overline{\Psi}_d$ and $\overline{\Psi}$, has been correlated with greater impact velocities and thus strain rates by Ma et al. (2018b) and Carmona et al. (2015). Their numerical results attribute this phenomenon at higher strain rates to the increased occurrence of micro-cracks in the particle core during the initial stages of impact. To investigate the influence of strain rate on $\overline{\Psi}_d$, its characteristic value during the impact and fragmentation process is estimated utilizing the model of Roisman (2022). It describes the motion of the disintegrating particle during its impact onto a rigid wall by employing quasi one-dimensional models from fluid mechanics. Using the model, a characteristic value for the strain rate $\dot{\gamma}_{\mathrm{char}} = \dot{\gamma}(t = t_{\mathrm{char}})$ is obtained for the characteristic time t_{char}, corresponding to the instance when the impact force reaches its maximum value after first contact between the particle and the target. The strain rate is approximated for the radial expansion of the impacting particle, which leads to tensile stresses inside the particle, ultimately initiating fracture. The resulting characteristic strain rates are in the order of $\mathcal{O}(10^4)\mathrm{s}^{-1}$ - $\mathcal{O}(10^5)\mathrm{s}^{-1}$, thus still being one order of magnitude larger than strain rates investigated in laboratory strength tests (Shazly et al., 2009).

In contrast, power-law values for ice fragmentation based on the fragment diameter instead of volume are summarized for comparably low strain rates in the order of $3\times10^{-2}\ \mathrm{s}^{-1}$ by Weiss (2001). The power-law exponent $\overline{\Psi}_d$ obtained from the present data for the distribution of $\tilde{d}_f$, which is calculated from $\tilde{V}_{\mathrm{f}}$ using Eq. (3.6), is shown in Fig. 4.28 for varying strain-rate. Similar to the trend for increasing velocity, the power-law exponent $\overline{\Psi}_d$ increases with increasing strain rate. From a robust regression procedure for the data using a bisquare weight function, the dependence of $\overline{\Psi}_d$ on $\dot{\gamma}_{\mathrm{char}}$ is obtained as

$$\overline{\Psi}_d = 2.246 + 2.418 \times 10^{-5}\,\mathrm{s}\,\dot{\gamma}_{\mathrm{char}}, \tag{4.15}$$

which is shown in the figure as solid red line. In qualitative agreement with the numerical results of Ma et al. (2018b) and Carmona et al. (2015), an increasing strain rate results in an increased proportion of smaller fragments for ice particle impacts, i.e. an increasing power-law exponent $\overline{\Psi}_d$. It should be noted that the simulated material of Carmona et al. (2015) resembles the behavior of a polymer at low temperatures. While also exhibiting brittle behaviour, this may actually lead to qualitatively different fragmentation processes. However, in their simulation, the

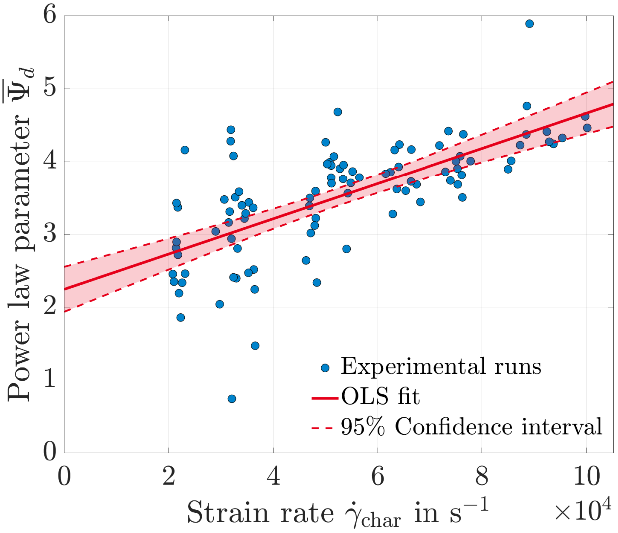

Figure 4.28: Experimental data of the fragment diameter power-law parameter $\overline{\Psi}_{\text{d}}$ obtained for varying strain rate $\dot{\gamma}_{\text{char}}$. The values of $\dot{\gamma}_{\text{char}}$ are calculated according to a model of Roisman (2022) at the point of impact and at the time of maximum force exerted onto the target. A robust regression procedure based on a bisquare weight function is used to obtain the OLS fit.

particle starts to break into orange-type fragments generated by meridian cracks similar to the present observation for faulting ice particles as shown in Fig. 4.20c). This is believed to originate from tensile failure inside the particle and was also identified for the failure of brittle ceramics by Andrews et al. (1998), where orange-type fragmentation was observed.

From the OLS fit of the experimental data, the power-law exponent in the low strain rate regime, $\dot{\gamma}_{\text{char}} = 0$, is found as $\overline{\Psi}_d|_{\dot{\gamma}_{\text{char}}=0} \approx 2.246$, which is in agreement with power-law exponents reported in literature for large scale ice fragmentation processes at low strain rates. For example, the break-up of ice floes in the large-scale ice shield in the Arctic Ocean is associated with scaling exponents between $D = 1.7$ and 2.16, with most values close to $D = 2$ (Weiss, 2001). The analysis of these break-up processes was performed based on image analysis and an one-dimensional length for the structural element ε in Eq. (3.8) such as the mean radius or diameter of the floes. Similar to these large-scale observations, also for the small scale regime, the fragment distribution obtained from laboratory uniaxial compressive failure experiments for strain rates close to zero exhibits a fractal behaviour with $D = 2.09 \pm 0.15$. Moreover, it turned out to be apparently unaffected by the type of loading mode (creep, constant strain rate, constant stress rate), the applied strain rate ($7 \times 10^{-5}\,\mathrm{s}^{-1}$ - $3 \times 10^{-2}\,\mathrm{s}^{-1}$), resulting stress rate ($0.05\,\mathrm{MPa\,s}^{-1}$- $0.2\,\mathrm{MPa\,s}^{-1}$), and the actual crystallisation structure and grain size, as reviewed by (Weiss, 2001). As shown in Fig. 4.28, the scatter of the present experimental data used for the robust OLS fit is high, especially for experimental runs with low impact velocity and small particle diameter, which are usually associated with only small numbers of detected fragments. However, considering the experimental data for higher strain rates, the 95% confidence interval for $\overline{\Psi}_d|_{\dot{\gamma}_{\mathrm{char}}=0}$ of approx. $[1.94,\ 2.55]$ agrees well with the data reported by Weiss (2001), $[1.7,\ 2.16]$.

Although the eventual scale invariance for ice fracturing at a small strain rate cannot be proven using the present data, the good agreement of the estimated data for vanishing strain rate with literature data appears to confirm the assumption of the fractal nature of ice particle fragmentation also for the present work. Finally, the present results for small ice particle impacts onto a rigid surface provide further insights into the fragmentation processes of ice in the high strain-rate regime, for which only little information is reported in literature.

4.1.2.6 Conclusion

In the present section, the effect of the particle impact velocity, diameter, temperature, and target temperature on the fragmentation process resulting from a single ice particle impact has been experimentally examined, representing a systematic variation of these four parameters. The quantification of a fragment distribution parameter for the experimental data required an advanced measurement procedure, including an experimental setup for controlling the temperature of the particle and the target and the evaluation software for fragment detection and estimation of the fragment volume distribution. Preliminary tests and literature research revealed variances and statistical properties that necessitated the use of a full factorial experimental design with a total of 96 experimental runs to reliably determine the significance of the effects of the experimental conditions.

The fragmentation types observed in the present work and their dependence on the impact conditions are consistent with empirical models of Hauk et al. (2015), Uenishi et al. (2018), and Uenishi et al. (2019), and the qualitative observation of a two-stage ejection of particle fragments for high impact velocities are in line with descriptions of Guégan et al. (2011). A spatial fragment clustering in radial and circumferential lines around the point of impact are reported at impact velocities greater than $50\,\mathrm{m\,s}^{-1}$ and particle temperatures equal or below $-20\,^{\circ}\mathrm{C}$. Phenomenological observations in the video data revealed that these clusters were detached pieces of a sintered cone of finely crushed ice mass that initially adhered to the target during impact. The separation of these pieces from the cone is presumed to be caused by fragments originating from the trailing edge of the particle, which impact onto the cone that forms during initial stages of impact. The impact velocity determines whether the forces associated with fragment impact overcome the cohesive forces between the individual sintered fragments in the cone or even the adhesive forces between the cone and the impact target. It is assumed that the initial particle temperature controls the final strength of the cohesive and adhesive forces resulting from the sintering process between the fragments in the cone. After detachment from the cone, the pieces disintegrate into smaller parts as they are ejected radially away from the point of impact, forming circumferential and radial lines of fragments in the process.

Evaluation of the fragment volume distribution is based on a maximum-likelihood estimation of a doubly-truncated power-law fit of the data. Optimal truncation points for the data have been estimated based on a statistical approach employing Monte Carlo simulations. The obtained fragment volume distributions of all experimental runs were subjected to statistical analysis by performing an analysis of variance (ANOVA) including all four varied experimental parameters. Out of all investigated experimental parameters, the particle impact velocity dominates the fragment size distribution within the investigated parameter range. A temperature variation of the particle and target within a range of $-35\,^{\circ}\mathrm{C}$ to $-5\,^{\circ}\mathrm{C}$ and $-10\,^{\circ}\mathrm{C}$ to $10\,^{\circ}\mathrm{C}$, respectively, showed no significant effect on the fragment volume distribution. Considering the temperature dependence of fracture-related ice material properties such as compressive and tensile strength (Gold, 1977; Schulson, 2001; Shazly et al., 2009), the found invariance towards the particle temperature in the present study is actually remarkable. Presumably, the strain rate dominates the mechanical behaviour of ice for the present experiments, rather than a combination of ice temperature and strain rate, since even for the minimum particle impact velocity of approx. $11\,\mathrm{m\,s^{-1}}$, still no effect of the temperature is measurable.

Impacting particles disintegrate into smaller fragments with increasing velocity, which is in agreement with reported distributions for hail impact (Pan et al., 1996). The dependence of the fragment distribution parameter on the particle impact velocity is found to be nonlinear for the studied range, and asymptotically approaches a limit at ≈ 2.1 for impact velocities of $\approx 70\,\mathrm{m\,s^{-1}}$. This asymptotic dependency is in agreement with numerical simulations of impacts of generic brittle spheres (Ma et al., 2018a; Ma et al., 2018b) in a comparable impact velocity range. A regression model has been derived that allows empirical prediction of the power-law values corresponding to a given impact velocity for ice spheres for the first time. Using this, the fragment size distribution can be estimated in order to improve the modelling of ice particle impacts causing ice crystal icing (ICI) events.

Although findings reported in literature can be linked to the present observations and partially explain the obtained relations, so far no theoretical models are available that explain the fragmentation process in its entirety. Consequently, predictions regarding the fragment distribution for ice particle impacts still mostly rely on empirical data fits.

Assuming that ice particle fragmentation is governed by the same mechanisms as fragmentation of rock, a shift in fracture mode towards shear fracture may be a contributing factor for a higher number of smaller fragments observed for increasing impact velocity, such as observed for rock in (Ma et al., 2018b; Ma et al., 2018a). Under the premise that ice fragmentation processes are fractal in nature, the observed increase of the fragmentation distribution parameter with rising impact velocity may additionally be attributed to the increasing dominance of secondary cracks that form after the initial break-up. The premise is supported by the limit of an established linear relation between the strain rate and the fragment distribution parameter: for strain rates approaching zero, the extrapolated value of the linear relation in the present work well coincides with the fractal dimension reported by Weiss (2001) for lower strain-rate ice fracture of ice floes. Finally, the dependence of the fragment diameter distribution on occurring strain rates is also in qualitative agreement with numerical results reported by Carmona et al. (2015).

4.1.3 Summary

A gas gun has been used to accelerate almost spherical, temperature controlled ice particles towards a transparent, temperature controlled target. The ice particles were made from de-ionized, degassed water. Their impact onto the target has been recorded using a high-speed video system and emerging fragments were detected and tracked during video post-processing by means of a Kalman-filter tracking algorithm. Post-processing of the recorded videos finally provided an estimate for the volume of each detected fragment used to determine the fragment size distribution in the debris cloud. The particle size, impact velocity, temperature and target temperature were varied systematically.

A small mass of ice fragments, termed residual mass, was observed to adhere to the target even at subfreezing target temperatures. At a 5% significance level, all varied parameters were found to significantly influence the amount of adhering residual mass. Finally, a theoretical model for particle deformation was used to model the amount of residual mass adhering to the target for sub-freezing target temperatures. The present results have already been incorporated in numerical codes for ice accretion prediction as used by Malik et al. (2023). Hereby, the ice mass sticking efficiency was modified in such a way, that 2% of an ice particle mass sticks to the surface even without liquid water present. In future work, the model can be potentially used for the description of the heat flux during the collision of an ice particle with a hot solid substrate.

The shape of the fragment volume distribution is dominated by the particle impact velocity within the investigated parameter range. A temperature variation of the particle and target within a range of $-35\,^{\circ}\mathrm{C}$ to $-5\,^{\circ}\mathrm{C}$ and $-10\,^{\circ}\mathrm{C}$ to $10\,^{\circ}\mathrm{C}$, respectively, showed no significant effect on the fragment volume distribution at a 5% significance level. Phenomenological observations of the interplay between the portion of crushed fragments adhering to the surface during impact and fragments originating from the trailing edge of the particle further complement the current understanding of the mechanisms involved in ICI. The fragmentation distribution is fitted with a doubly-truncated power-law. The power-law parameter increases with increasing impact velocity, which may be attributed to the increasing dominance of secondary cracks that form after the initial break-up. Under the premise that all ice fragmentation processes are fractal in nature and thus scale invariant, the present high strain-rate experiments are compared to lower strain-rate ice fracture of ice floes.

The premise of scale invariance is supported by the limit of an established linear relation between the strain rate and the fragment distribution parameter: for strain rates approaching zero, the extrapolated value of the linear relation in the present work well coincides with the fractal dimension reported by Weiss (2001) for the lower strain-rate ice fracture of ice floes. Concluding, the present work contributes to a better understanding of the fragmentation of small ice particles during their impact on a rigid surface, which may finally help to improve the accuracy of ICI models; both qualitatively and quantitatively.

4.2 Ice Particle Impact Onto a Wetted Substrate[2]

Accretion of macroscopic ice layers in aircraft engines usually starts with the capture of ingested ice particles in a liquid water film wetting the engine core surfaces. The amount of captured ice particles controls the cooling rate of the liquid film and the surface beneath. If the freezing temperature is reached, macroscopic fragment agglomerations strongly adhere to the substrate and ice accretion is initiated. Depending on the ice particle geometry, impact velocity and the liquid film thickness, the impacting particle either remains in the film or rebounds with a diminished velocity.

The dissipation of energy during a particle wall collision is usually characterized by the coefficient of restitution (COR), a ratio of the particle velocity after and prior to impact. During impact, mainly viscous forces in the water film, plastic deformation of the ice particle and surface tension forces cause the dissipation of the energy of the ice particle, which rebounds with a lower velocity. In the present chapter, the normal and oblique impact of ice spheres onto a wetted wall is studied experimentally to advance the knowledge of phenomena leading to ice particle capture and thus, the inception of ice accretion. Subsequently, existing models for the dry and wet coefficient of restitution, which are based on the main parameters influencing the impact outcomes are adapted, combined and compared to the experimental results. In the investigated parameter range, the plastic behaviour of the ice particles dominates the energy dissipation during impact, leading to a low COR in the direction perpendicular to the target surface.

4.2.1 Qualitative Observations

An example image sequence of an ice particle impacting onto the wetted target is shown in Fig. 4.29. It can be observed that the ice particle is not perfectly spherical. However, it is assumed that the observed asphericity of the particle does not influence the experimental outcome in this case. Therefore, similar experimental runs are used for the analysis. In the first video frame where the ice particle has made contact with the water film ($t = 0\,\mathrm{ms}$), a small mass of liquid is visible, which is ejected upwards, similar to the observations of Hauk et al. (2014) for the impact of a sanded glass sphere onto a water pool. The water initially forms a thin sheet, which breaks up into small droplets at later stages ($t = 0.64\,\mathrm{ms}$). As time progresses, it becomes clear that the particle has lost its momentum in the direction perpendicular to the surface and slides across the wetted surface horizontally, further displacing the water film. This behaviour is termed *sticking* for the present work. In the last displayed image in the time series ($t = 4.47\,\mathrm{ms}$), a protrusion is visible on top of the particle. This stems from a small volume of liquid water wetting the ice particle,

---

[2] Parts of this chapter are based on the Bachelor-Theses of Johannes Heinrich Conrad and Mohammad Sämi Sbeitan, and the Master-Thesis of Andreas Mayrhofer, and have been published (Reitter et al., 2022b). The original contents have been edited and/or extended for this work.

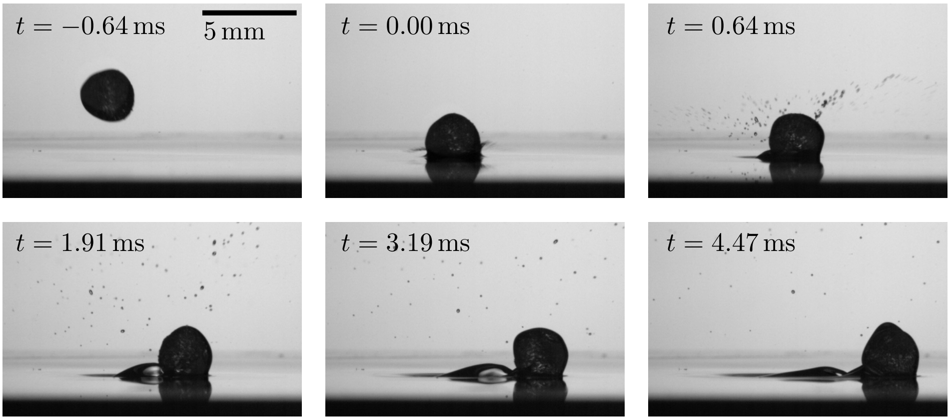

Figure 4.29: Example image sequence of a sticking ice particle after impact onto a $h = 0.442\,\mathrm{mm}$ thick water film with a normal velocity of $v_{\mathrm{p,n}} = 3.90\,\mathrm{m\,s^{-1}}$. In this example, the impact angle is $66°$ and the particle diameter is $d_{\mathrm{p}} = 2.88\,\mathrm{mm}$.

which migrates to the top of the particle.

Despite the rich phenomena observable in Fig. 4.29, only the change of the particle velocity is of interest for the present work. For comparison, a time series of a rebounding particle is shown in Fig. 4.30. Similar to the case of a sticking particle, a splash with the ejection of fine droplets can be observed shortly after impact. All experimental parameters are similar, except for the absolute impact velocity $v_{\mathrm{p,n}} = 4.93\,\mathrm{m\,s^{-1}}$, which is larger than for the sticking case ($v_{\mathrm{p,n}} = 3.90\,\mathrm{m\,s^{-1}}$). In related literature on particle impact onto liquid films, the Stokes number is used successfully to describe the present phenomena (Davis et al., 1986; Ennis et al., 1991; Davis et al., 2002; Ma et al., 2013; Müller et al., 2016). For the rebounding particle shown in Fig. 4.30, the Stokes number is larger compared to the sticking case, which corresponds to a larger ratio between the particle inertia and the viscous forces in the liquid film, decelerating the particle. Hence, the particle does not lose as much momentum and is able to rebound again from the wetted substrate. For larger impact velocities, the particle fragments, as shown in Fig. 4.31. Next to the generation of fine droplets observed at the smaller impact velocities, a macroscopic liquid film is generated that persists for longer times. The generation of such crown-shaped fluid films is intensively studied for the case of a liquid drop impacting a liquid film (Yarin, 2006; Liang et al., 2016; Yarin et al., 2017). In the present experiment, it also leads to the generation of secondary drops at the unstable rim of the crown. The ice particle fragments after contact with the substrate, which is clearly visible in the last image in Fig. 4.31 ($t = 5.11\,\mathrm{ms}$). The particle splits into two half-spheres, one of which flies on without touching the water film again, while

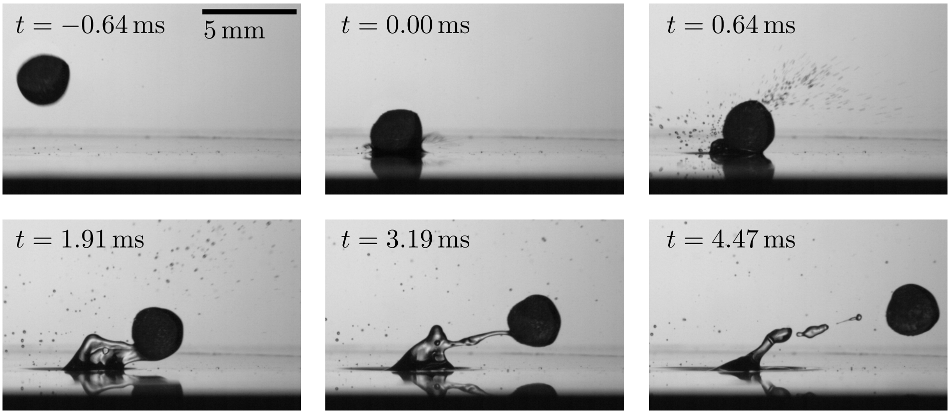

Figure 4.30: Example image sequence of a rebounding ice particle after impact onto a $h = 0.444\,\mathrm{mm}$ thick water film with a normal velocity of $v_{\mathrm{p,n}} = 4.93\,\mathrm{m\,s^{-1}}$. In this example, the impact angle is $63°$ and the particle diameter is $d_{\mathrm{p}} = 2.93\,\mathrm{mm}$.

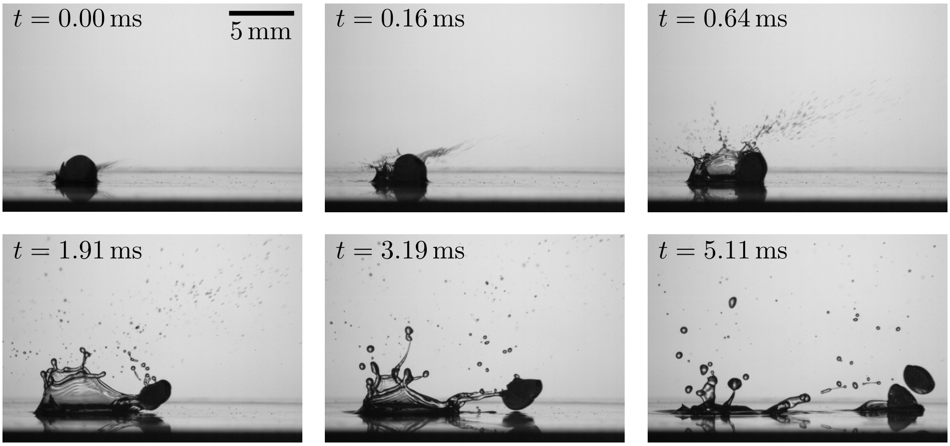

Figure 4.31: Example image sequence of an ice particle fragmenting, after impact with an absolute velocity of $v_{\mathrm{p,n}} = 6.77\,\mathrm{m\,s^{-1}}$ onto a water film with a thickness of $h = 0.471\,\mathrm{mm}$. In this example, the impact angle is $64°$ and the particle diameter is $d_{\mathrm{p}} = 2.72\,\mathrm{mm}$.

the other is caught in the film. In these cases, the fragment with the largest velocity perpendicular to the substrate is considered in the analysis to estimate a COR as maximum COR of the fragments.

4.2.2 Quantitative Data Analysis

The focus of the quantitative data analysis is the effect of the varied experimental parameters on the normal and tangential COR. Experiments are conducted with near-spherical ice particles of varying diameter $d_\mathrm{p} = 1.85\,\mathrm{mm}$ - $d_\mathrm{p} = 3.35\,\mathrm{mm}$. The normal impact velocity is varied between $v_\mathrm{p,n} = 0.58\,\mathrm{m\,s^{-1}}$ and $v_\mathrm{p,n} = 6.72\,\mathrm{m\,s^{-1}}$ and the impact angles are varied from normal up to 42.4° impacts. In addition to impact experiments on a water film with varying thickness between $h = 0.095\,\mathrm{mm}$ and $h = 0.902\,\mathrm{mm}$, reference experiments with a dry surface are conducted.

4.2.2.1 Experimental Test Matrix

Multiple circumstances prevented a precise systematic variation of the experimental parameters and thus the application of a full factorial design of experiments for example. The largest contributors are the uncontrollable film thickness due to the air jet disturbing the water surface prior to a particle impact and a larger scatter of the achieved impact velocity at similar air pressures of the shooting device. The latter phenomenon is most likely caused by a varying friction coefficient for the sabot-barrel contact. In summary, a quantitative analysis is performed for the scattering experimental parameters, but without an accompanying rigorous statistical analysis. In Table 4.3, the varied experimental parameters are shown. The experiments are subdivided into three groups based on the particle acceleration method and whether or not a liquid water film is present. In the first experimental campaign, the vacuum

Experimental campaign	1	2	3
Acceleration method	Gravity	Pneumatic gun	Pneumatic gun
Impact velocity $v_\mathrm{p,n}$ in $\mathrm{m\,s^{-1}}$	$0.576\ldots3.45$	$1.63\ldots6.72$	$2.07\ldots6.66$
Particle diameter d_p in mm	$1.85\ldots3.35$	$2.58\ldots3.08$	$2.39\ldots3.22$
Film thickness h in mm	$0.095\ldots0.902$	0	$0.287\ldots0.550$
Impact angle in °	90	$\begin{Bmatrix} 88.4 \pm 1.6 \\ 59.2 \pm 5.7 \\ 46.5 \pm 4.1 \end{Bmatrix}$	$\begin{Bmatrix} 63.9 \pm 3.4 \\ 47.0 \pm 3.7 \end{Bmatrix}$
Particle temperature T_p in $^\circ\mathrm{C}$	$-1.3\ldots-14.9$	-4.5 ± 0.5	-4.5 ± 0.9
Target temperature T_t in $^\circ\mathrm{C}$	$-2.8\ldots3.0$	0.5 ± 0.3	0.5 ± 0.3
Number of experiments	62	43	65

Table 4.3: Summary of all varied experimental parameters. The experiments are subdivided into three groups based on the particle acceleration method and whether or not the target is wetted with a liquid film.

tweezers are used to release the particles that are then accelerated by gravity. In the second and third campaigns, the particle is accelerated using the pneumatic gun, while experiments with and without a liquid film are conducted.

4.2.2.2 Effect of the Particle Temperature

In impact experiments specifically with ice spheres on ice blocks and different dry materials, it was found that the COR is a function of the ice particle temperature (Higa et al., 1996; Eidevåg et al., 2021). No studies are known to the author, where single ice particles impact onto a rigid wall with the presence of a macroscopic water film while systematically varying the particle temperature. A related study is the one of Hauk (2016), who found that ice spheres fragment at larger velocities when impacting onto a wetted wall. He rationalised this observation with the fact that the particle impacts onto the rigid wall with an effective lower velocity due to its deceleration in the liquid film. Similarly, Alvarez et al. (2019) made the same observation for ice particles partially melted in an acoustic levitator prior to impacting them with a rigid projectile. However, a possible effect of the particle temperature was not investigated in the studies of Hauk (2016) and Alvarez et al. (2019), which is the subject of the following discussion. In Fig. 4.32, the effect of the particle temperature on the normal COR is shown for a wetted aluminium target.

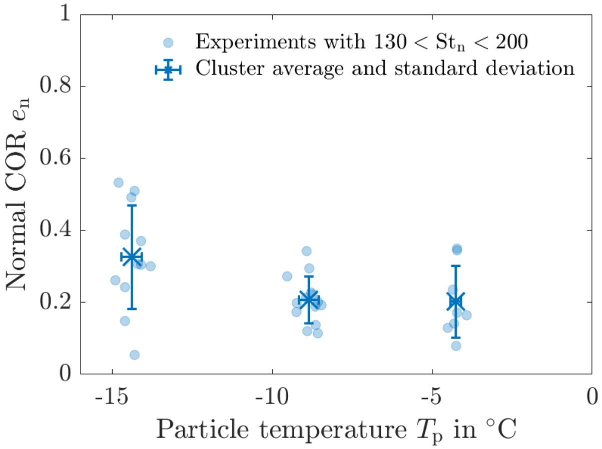

Figure 4.32: Normal COR e_n plotted against the particle temperature T_p. The blue circles correspond to a reduced data set of campaign 1 with particle diameters of $1.97\,\mathrm{mm} < d_\mathrm{p} < 3.31\,\mathrm{mm}$, normal impact velocities of $1.05\,\mathrm{m\,s^{-1}} < v_\mathrm{p,n} < 1.32\,\mathrm{m\,s^{-1}}$ and a film thickness of $0.095\,\mathrm{mm} < h < 0.332\,\mathrm{mm}$.

Two experimental clusters with the largest average particle temperatures of $-8.87\,^{\circ}\mathrm{C}$ and $-4.25\,^{\circ}\mathrm{C}$, share a similar value of the normal COR, $e_{\mathrm{n}} = 0.207$ and $e_{\mathrm{n}} = 0.201$, respectively. Only the cluster with the lowest particle temperature of $-14.4\,^{\circ}\mathrm{C}$ exhibits a larger average normal COR of $e_{\mathrm{n}} = 0.325$. This observation is in agreement with literature on dry ice particle impacts (Higa et al., 1996; Eidevåg et al., 2021) since the COR decreases with increasing particle temperature. However, the trend is not very pronounced for the present investigated parameter range, in contrast to the results of Higa et al. (1996), where larger particle temperature differences are investigated ($-160 < T_{\mathrm{p}} < -4$), motivated by studying ice particle collisions in Saturn's rings. For the present work, it is assumed that the particle temperature has no significant effect on the COR above a temperature of $T_{\mathrm{p}} = -12^{\circ}\mathrm{C}$, supported by the results presented in Fig. 4.32. In the further analysis, all experiments with lower particle temperatures are excluded.

4.2.2.3 Effect of the Target Stiffness

As a reference, impact experiments on the dry aluminium target (campaign 2) are discussed next. In Fig. 4.33, the results for the normal COR e_{n}, plotted against the normal impact velocity $v_{\mathrm{p,n}}$ are compared to literature data of ice on ice impacts (Higa et al., 1998). For the present discussion, it is not differentiated between results for the inclined and non-inclined impact since no significant differences regarding e_{n} are observed. Significantly lower values of e_{n} are observed for the impact experiments on aluminium of the present work (red markers), compared to the values of e_{n} for ice on ice impacts from Higa et al. (1998)(black and blue markers).

This effect can be explained when the effective modulus of elasticity E^{*} defined in Eq. (2.11) is considered for both cases. The effective modulus of elasticity for the present ice particle impact on aluminium, $E^{*}_{\mathrm{ice-Al}} = 9.2\,\mathrm{GPa}$, is almost double the effective modulus of elasticity for an ice on ice impact $E^{*}_{\mathrm{ice-ice}} = 5.2\,\mathrm{GPa}$ at a temperature of $-12\,^{\circ}\mathrm{C}$. As discussed in Section 2.1, an increasing effective modulus of elasticity E^{*} leads to a larger contact pressure for the same impact velocity. In this case, more energy is dissipated due to plastic deformation and crack formation; hence, a lower COR is obtained. This phenomenon is observed in Fig. 4.33. By including the modulus of elasticity E^{*} as a variable in the model of Higa et al. (1998), the trend of a lower COR for a larger effective modulus of elasticity can be predicted as described in Section 2.1. The model for the COR is repeated here for clarity,

$$e_{\mathrm{n}} = \begin{cases} e_{\mathrm{qe}} & v_{\mathrm{p,n}} < v_{\mathrm{c}} \\ e_{\mathrm{qe}} \left(\frac{v_{\mathrm{p,n}}}{v_{\mathrm{c}}} \right)^{-\log_{10}(v_{\mathrm{p,n}}/v_{\mathrm{c}})} & v_{\mathrm{p,n}} \geq v_{\mathrm{c}} \end{cases} \tag{4.16}$$

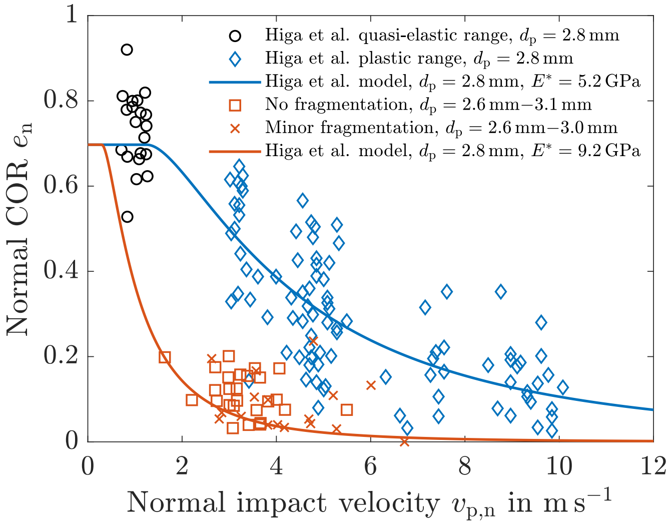

Figure 4.33: Normal COR e_n plotted against the impact velocity normal to the target surface. The black an blue markers correspond to data from Higa et al. (1998) for particle diameters of $d_\mathrm{p} = 2.8\,\mathrm{mm}$ while the red markers correspondent to impact experiments of the present work with diameters $d_\mathrm{p} = (2.85 \pm 0.25)\,\mathrm{mm}$. Their figure is reused with permission.

using $e_\mathrm{qe} = 0.7$ for a particle diameter of $d_\mathrm{p} = 2.8\,\mathrm{mm}$ (see Eq. (2.9)) and the adapted formulation of the critical velocity v_c,

$$v_\mathrm{c} = k_3 {E^*}^{-2} \exp\left(\frac{k_2}{2\mathcal{R}T}\right) d_\mathrm{p}^{-1/2}, \tag{4.17}$$

where $k_2 = 48.2 \times 10^3\,\mathrm{J\,mol^{-1}}$ and $k_3 = 9.664 \times 10^{17}\,\mathrm{m^{-1}\,s^{-6}\,kg^{5/2}}$ are empirical factors. The model still predicts the decreasing trend of the COR with increasing impact velocity for the original data of Higa et al. (1998), indicated by the blue curve in Fig. 4.33, and successfully predicts decreased values of the COR for the larger value of E^* the present experiments, indicated by the red curve in Fig. 4.33. The model prediction is at the lower end of the experimental data cloud, indicating that the derived exponent of -2 for the effective modulus of elasticity in Eq. (4.17) may be too small and a larger exponent like $U_\mathrm{c} \propto {E^*}^{-3/2}$ would fit the data better. However, the theoretical value of $U_\mathrm{c} \propto {E^*}^{-2}$ is kept for the discussion of impact experiments onto the wetted wall.

4.2.2.4 Effect of the Stokes Number

In the next step, the effect of the Stokes number on the normal COR e_n is discussed for particle impacts onto the wetted aluminium wall. For each experiment, the Stokes number is calculated with the water viscosity (obtained from *VDI-Wärmeatlas* 2009) for a temperature equal to the target temperature. In order to plot the particle impact experiments on the dry wall alongside the experiments with a wall film, a Stokes number is calculated with a water viscosity of $\eta = 1.768\,\mathrm{mPa\,s}$ corresponding to a temperature of $0.5\,°\mathrm{C}$. In Fig. 4.34, the normal COR e_n is plotted against the Stokes number $\mathrm{St_n}$ for particle impacts onto the wetted aluminium wall (blue and orange markers) and dry aluminium wall as reference (red markers). Data of all experimental campaigns are included with the constraint of the particle temperature being above $-12\,°\mathrm{C}$. As a reference, the adapted Higa et al. (1998) model and the model for viscous dissipation are plotted separately as red and green curves. The combined model (black dashed line) fits well the average normal COR for the particle impacts onto a liquid film, although there is a significant scatter in the data. It can be observed that for the Stokes number range of the present experiments, $\mathrm{St_n} > 100$, the model curve for e_wet lies almost on top of the curve of the adapted model of Higa et al. (1998). Currently, it is assumed that the COR is dominated by the dissipation

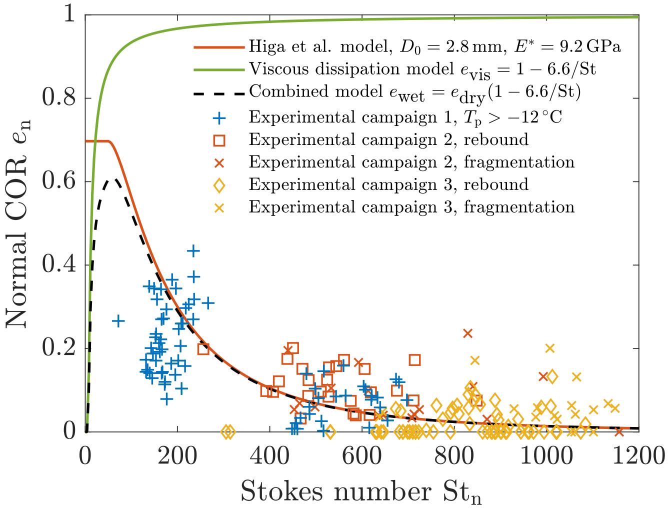

Figure 4.34: Normal COR e_n plotted against the normal Stokes number $\mathrm{St_n}$ for ice particle impacts of all present experimental campaigns, excluding particles with a temperature above $-12\,°\mathrm{C}$. The red and green curves correspond to the extended model of Higa et al. (1998) and the model for viscous dissipation, respectively. Combining both models results in the black dashed line.

resulting from plastic deformation of the ice particle in the investigated Stokes number range and the liquid water film only has a minor effect on the normal COR. This indicates, that for the context of ice crystal icing in aero engines, the dissipative behaviour of ice particles is non-negligible for larger Stokes numbers, like the ones of the present experiments. Moreover, the normal COR depends strongly on the effective elastic modulus of the particle - target material combination E^*. This is an important result which can aid in closing current research gaps in modelling the ice particle sticking behaviour. Currie (2020) performed a dedicated numerical study on ice accretion on a heated wedge shape airfoil. Next to predictions for the flow field, particle trajectories and heat transfer, he considered particle capture in a thin water film. For the sticking criterion, Currie (2020) used a critical value of the modified Stokes number St/δ^+ of Ma et al. (2013). While the general trends of the cooling rate and melt fraction are predicted well, he states that particle capture is under-predicted for near-normal particle impacts at the profile stagnation point. The present results could explain this phenomenon, since plastic deformation during ice particle impact can reduce the COR drastically, increasing the particle capture efficiency. An additional aspect that can be discussed when adapting the model of Higa et al. (1998) to an aero engine icing scenario is the particle size dependency of the critical impact velocity. In their model, Higa et al. (1998) scale the critical velocity with $v_\mathrm{c} \propto {d_\mathrm{p}}^{-1/2}$, which is close to the scaling $v \propto {d_\mathrm{p}}^{-0.58}$ reported by Hauk et al. (2015) for the breakup threshold of spherical and non-spherical ice particles with diameters ranging from $30\,\mathrm{\mu m}$ to $3.5\,\mathrm{mm}$. This similarity in the scaling exponents indicates that the model of Higa et al. (1998) can be applied also for microscopic ice particles characteristic for aero engine icing.

In future work, the dedicated model for ice impacts of Higa et al. (1998), with the adaptations of the present work, can be included in a more advanced force-balance modelling approach like the one of Buck et al. (2018). This is an important step, since capillary forces become more dominant for microscopic ice particles, which are encountered in aircraft engine icing scenarios. Specifically, the liquid bridges forming between the water film and a rebounding ice particle can further assist in the capture of ice particles, as shown in a study of Hauk (2016). In the model of Buck et al. (2018), the liquid bridge formation is treated quasi-statically, an assumption that has to be reviewed when the model is applied in the context of fast impacts of ice particles.

In addition to the normal COR, the tangential COR is investigated, which is shown in Fig. 4.35 as a function of the tangential Stokes number St_tg.

By comparing the data of the dry impacts (orange markers) to impacts onto the wetted wall (red markers), it can be observed that the values of e_tg for the dry impacts are very close to 1 while the values of e_tg for the film impacts cluster around values of $0.9 - 0.8$. This is reasonable since the liquid film slows down the tangential particle motion during impact due to viscous and inertial forces in the liquid. However, with the present experiments, no clear trend of e_tg for

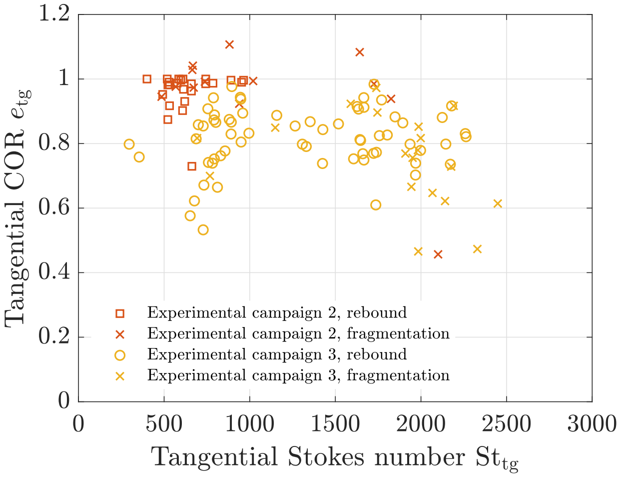

Figure 4.35: Tangential COR e_{tg} plotted against the tangential Stokes number $\mathrm{St}_{\mathrm{tg}}$. The orange markers correspond to data for impacts onto a liquid water film with varying thicknesses (campaign 2) while the red markers correspond to impact experiments onto the dry surface (campaign 3).

different Stokes numbers is visible in Fig. 4.35. The main parameters influencing the tangential COR and the deceleration of an ice particle sticking to the target after impact can be studied in future work.

4.2.3 Summary

In the present section, an experimental study of ice particle impacts onto a dry and wetted aluminium surface has been presented. A pneumatic gun or vacuum tweezers are used to impact ice spheres with diameters between $d_{\mathrm{p}} = 1.85\,\mathrm{mm}$ and $d_{\mathrm{p}} = 3.35\,\mathrm{mm}$ onto an aluminium target with normal velocities between $v_{\mathrm{p}} = 0.576\,\mathrm{m\,s^{-1}}$ and $v_{\mathrm{p}} = 6.72\,\mathrm{m\,s^{-1}}$ and impact angles between $42.4°$ and $90°$ relative to the target surface. The initial water film thickness was varied between $h = 0.095\,\mathrm{mm}$ and $h = 0.902\,\mathrm{mm}$. When using the pneumatic gun setup, a generated air stream lowered the film thickness at the instance of particle impact. However, a film thickness measurement was synchronized with recorded high-speed videos in order to determine the film thickness at the instance of impact for each experiment. Using image processing of the recorded high-speed videos, the coefficient of restitution (COR) in normal and tangential directions with respect to the target surface was determined and compared to existing models.

The model of Higa et al. (1998) for the normal COR, originally derived for ice particle impacts onto non-wetted ice targets, was rewritten to account for the increased target stiffness of aluminium compared to ice, drastically lowering the predicted normal COR. The model was found to capture the trend of the observed lower normal CORs for the first dataset of ice particle impacts onto a dry aluminium surface well. These results illustrate the importance of considering the material properties of the collision partners for an accurate modelling approach of the ice particle COR. Additionally, the rewritten model of Higa et al. (1998) was combined with a Stokes number based model of Davis et al. (1986), accounting for viscous losses in the liquid layer during particle impact onto a wetted wall. The model predictions agree well with experiments of normal and inclined ice particle impacts onto a wetted aluminium wall. In the investigated Stokes number range, the normal COR is dominated by the dissipation resulting from plastic deformation of the ice particle. These results are valuable for modelling efforts in aircraft engine icing, since they can explain an under-prediction of the particle capture efficiency as observed by Currie (2020). For future work, it is proposed to resort to a more advanced force-balance modelling approach like the one of Buck et al. (2018) for the particle deceleration due to the liquid. In this case, the effects of the water surface tension can be captured, which become increasingly important for microscopic ice particles encountered in a realistic aircraft engine icing scenario.

Finally, the tangential COR for impacts onto the dry and wetted wall has been discussed, finding the values close to one for the dry impacts and clustering around $0.9 - 0.8$ for the wetted wall impacts. A more detailed study of the dynamic tangential motion of a bouncing or sticking ice particle after impact is left for future work.

4.3 Strength Characterization of Granular Ice Layers[3]

On the internal aero engine surfaces, a certain amount of liquid water is necessary for ice accretions to form, as evident from representative icing wind tunnel investigations (Currie et al., 2013; Flegel, 2017). No ice particles with low liquid water content are captured and in the case of excess liquid, ice particles are washed away before ice agglomeration begins. Since the ice accretion develops under wet conditions, it grows as a solid matrix of stacked ice crystals with liquid water filling the remaining pores to a yet unknown amount. Further development of the ice layer is usually modelled as a balance between ice layer growth by ice crystal sticking and layer erosion caused by impacting particles (Currie et al., 2016; Trontin et al., 2017; Bucknell et al., 2019), with a crucial input for the erosion models being a strength parameter of the ice accretion (Charton et al., 2019). It has been observed that ice layer growth rates and shapes differ with for instance, higher liquid water content in the airflow. Hence, it is hypothesized that a possible reason is the varying strength of the ice layer and therefore, resistance to erosion (Currie et al., 2016).

The goal of the present work is to advance the knowledge of the ice particle impact process onto ice accretion. It is crucial to know the material properties of such granular ice layers to model a layer material response during an ice particle impact. As the ice layer material properties are currently unknown and a dedicated method to characterise them is not available, an in-situ strength measurement methodology for wet ice accretions is designed and applied in the present work. It is based on impacting a nylon sphere onto the ice layer and a subsequent evaluation of the crater depth afterwards. The reason for choosing an impact method is the ability to capture the dynamic strength of the ice layers, which presumably plays an important role during an ice particle impact onto such an ice layer. In contrast to a quasi-static strength test, e.g. inertia effects of accelerated parts of the ice layer can be captured. A nylon sphere impactor is preferred over a more realistic, nearly spherical ice particle since the shape of the latter cannot be manufactured without a small deviation from a perfectly spherical shape, possibly affecting the impact crater depth. Furthermore, a nylon particle does not fragment as easily as an ice particle, allowing the investigation of large impact velocities.

The developed impact method is applied for ice layers grown under different boundary conditions in an icing wind tunnel and for artificial ice layers manufactured in a laboratory environment. Using the proposed testing method, it can be differentiated between soft ice layers generated at positive wet-bulb temperatures in the icing wind tunnel and harder ice layers generated at negative wet-bulb temperatures. Hence, the testing method can be applied to compare wet porous ice layers at

---

[3] Parts of this chapter are based on the Bachelor-Theses of Lion Oster and Aaron Basil Jahn, and have been published (Schremb et al., 2019; Reitter et al., 2023). The original contents have been edited and/or extended for this work. The work in the icing wind tunnel of the Technische Universität Braunschweig has been performed in collaboration with Yasir A. Malik. In the wind tunnel campaign, all equipment employed has been designed in other studies, except for the particle shooting device.

different facilities with respect to their strength. For the ice layers manufactured in the laboratory, the influence of porosity, water saturation and ice crystal size on the layer strength is quantified. By carefully adjusting these parameters, the layer strength measured in the wind tunnel can be replicated, allowing to perform future studies on ice layers having a realistic strength in a laboratory environment.
Impact of nylon particles on ice layers generated in the wind tunnel and in the laboratory leads to craters of different depths depending on the material properties of the ice layers. With the use of theoretical considerations linking the crater geometry with strength parameters for the investigated ice layers, the influence of different boundary conditions under which the ice layers are generated compared to their strength is quantified.

4.3.1 Observations of Cratering Phenomena

In the experiments at the TUBS wind tunnel, impacts are performed on wetted porous ice layers generated at positive ($T_{\mathrm{wb}} = 2\,^{\circ}\mathrm{C}$, IDs 1,2,3) and negative ($T_{\mathrm{wb}} = -2\,^{\circ}\mathrm{C}$, ID 4) wet-bulb temperature (see Table 3.1). The experiments for each ice layer configuration are repeated three times. Examples of the measured slushy and glaciated ice layer topography are shown in Fig. 4.36. It can be observed, that both ice layers show a different topography. While the slushy ice layer (Fig. 4.36a)) has a large plateau region which is almost parallel to the test article surface oriented in the $x-y$ plane, the cross-section of the glaciated ice layer (Fig. 4.36b)) has a conical shape. Additionally, the ice layer in Fig. 4.36a) has a larger slope at $y = 100\,\mathrm{mm}$ next to the plateau area, compared to the ice layer in Fig. 4.36a) at $y = 100\,\mathrm{mm}$. This indicates a different impact angle dependency of the sticking and/or erosion mechanisms involved in the ice accretion growth. The data output from the 3D scanner is a three-dimensional point cloud, which is post-processed in the same way as the surface data of the artificial ice layers (see Section 3.3), using a custom code implemented in *MATLAB*. The only difference is the usage of a fifth-order polynomial surface for estimating the contour of the intact ice layer surface to account for its non-planar topography. In a manual inspection, the ice layers with IDs 1,2,3 were found to be more easily deformable than the ice layers with ID 4, possibly stemming from stronger bonds between individual ice crystals forming the solid ice matrix that is filled with liquid water in all cases.

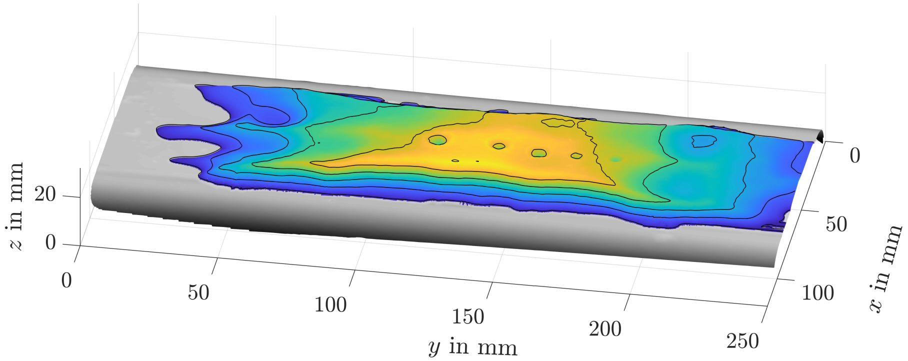

(a) Example topography of a slushy ice layer (ID=2) generated at a positive wet-bulb temperature $T_{\mathrm{wb}} = 2\,^{\circ}\mathrm{C}$. The ice layer has a large plateau region, parallel to the substrate surface.

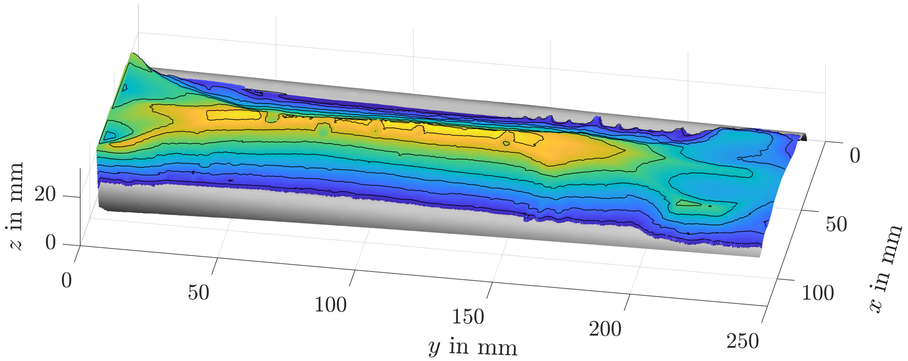

(b) Example topography of a glaciated ice layer (ID=4) generated at a negative wet-bulb temperature $T_{\mathrm{wb}} = -2\,^{\circ}\mathrm{C}$ with a conical cross section.

Figure 4.36: Example images of a slushy (a) and glaciated (b) ice layer. The lines indicate the ice layer contour at different heights, $z = 2\,\mathrm{mm}$ apart from each other.

In Fig. 4.37, two example image sequences of a nylon sphere impacting onto different ice layers generated at TUBS IWT are shown. During the impact onto the harder layer depicted in Fig. 4.37b), the diameter of the ejecta cloud near the ice layer surface is observed to be smaller compared to the softer layer depicted in Fig. 4.37a). As expected, the resulting crater depth after impact is larger for the softer layer. A minimum of five nylon spheres were shot onto each layer with different velocities ranging from $18.1\,\mathrm{m\,s^{-1}}$ to $88.7\,\mathrm{m\,s^{-1}}$.

In Fig. 4.38, the reconstructed craters for two different impact velocities are displayed. It can be observed that both craters have larger diameters compared to the

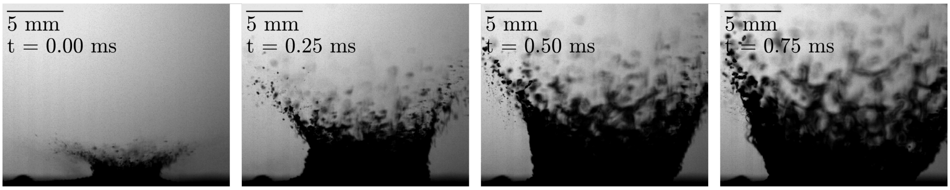

(a) Ice layer ID = 1, Impact velocity $U = 84.8\,\mathrm{m\,s^{-1}}$, Crater depth $z_c = 3.88\,\mathrm{mm}$.

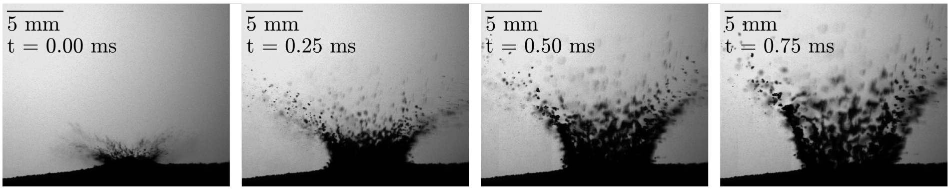

(b) Ice layer ID = 4, Impact velocity $U = 88.6\,\mathrm{m\,s^{-1}}$, Crater depth $z_c = 3.56\,\mathrm{mm}$.

Figure 4.37: Example image sequences of a $3.18\,\mathrm{mm}$ nylon sphere impact onto a slushy (a) and glaciated (b) ice layer.

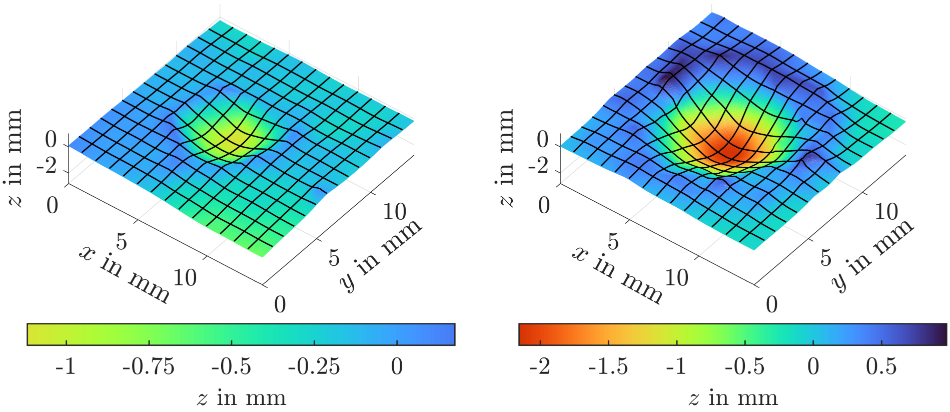

(a) Impact velocity $U = 27.8\,\mathrm{m\,s^{-1}}$; Crater depth $z_c = 0.99\,\mathrm{mm}$.

(b) Impact velocity $U = 84.8\,\mathrm{m\,s^{-1}}$; Crater depth $z_c = 2.49\,\mathrm{mm}$.

Figure 4.38: Example images of two reconstructed crater surfaces after impact of a $3.18\,\mathrm{mm}$ nylon sphere onto an slushy ice layer (ID=2) generated in the wind tunnel. The spacing between the black contour lines equals $1\,\mathrm{mm}$.

nylon sphere diameter and exhibit a ridge at their edge. Quantitative data for the crater depth is presented in the following chapter. The advantage of experiments performed at the TUBS IWT is ice accretion growth under realistic conditions. However, it remains challenging to characterize relevant ice layer properties, namely the porosity, water content and degree of sintering of the ice layer particles. Therefore, complementary experiments at TUDA IL were performed, where the aforementioned parameters are known and can be varied to capture their respective influence. An example image sequence of the impact and cratering process for two ice layers with different water content manufactured at TUDA IL is shown in Fig. 4.39. By comparing Fig. 4.39a) and Fig. 4.39b), it can be observed that by adding water to the ice layer, fewer particles are ejected during impact and the ice layer crystals form clusters holding together due to the water surface tension. Additionally, the nylon sphere rebounds from the dry layer while it penetrates deeper into the wetted layer where it eventually comes to rest. In Fig. 4.40, two reconstructed craters are displayed, generated after impact onto a dry ice layer with different velocities. As expected, With a larger impact velocity, the crater diameter and maximum depth increase.

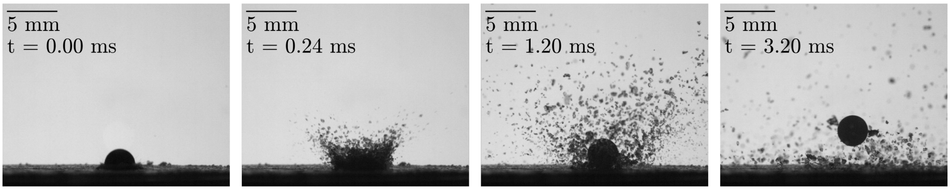

(a) Impact velocity $U = 34.8\,\mathrm{m\,s^{-1}}$; Porosity $\phi = 0.40$; Pore filling ratio $\epsilon = 0$.

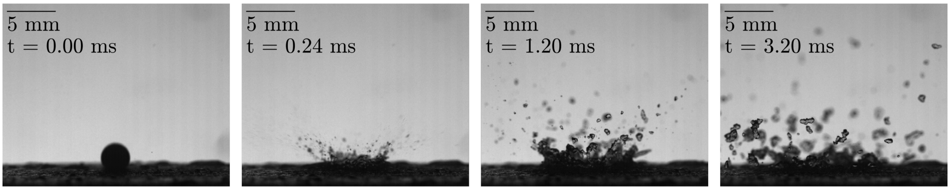

(b) Impact velocity $U = 33.6\,\mathrm{m\,s^{-1}}$; Porosity $\phi = 0.41$; Pore filling ratio $\epsilon = 0.77$.

Figure 4.39: Example image sequences of a $3.18\,\mathrm{mm}$ nylon sphere impacting onto a dry (a) and wetted (b) artificial ice layer.

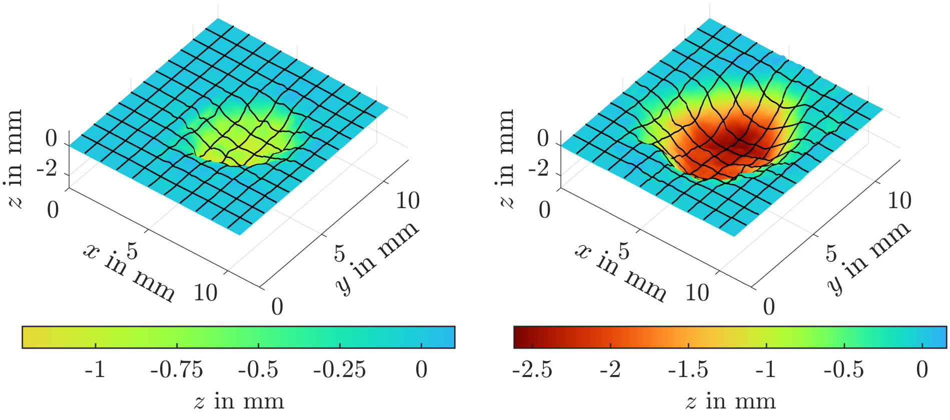

(a) Impact velocity $U = 33.6\,\mathrm{m\,s^{-1}}$; Crater depth $z_\mathrm{c} = 1.23\,\mathrm{mm}$.

(b) Impact velocity $U = 54.4\,\mathrm{m\,s^{-1}}$; Crater depth $z_\mathrm{c} = 2.62\,\mathrm{mm}$.

Figure 4.40: Example images of two reconstructed crater surfaces after the impact of a $3.18\,\mathrm{mm}$ nylon sphere onto an artificial dry ice layer with a porosity of $\Phi = 0.4$. The spacing between the black contour lines equals $1\,\mathrm{mm}$.

4.3.2 Simplified Modelling Approach for the Impact Crater Depth

A convenient way to model object penetration is by applying a phenomenological description of the penetration dynamics based on Newton's second law (Newton et al., 1850). Assuming a rigid projectile with mass m_p and instantaneous velocity v, a one-dimensional force balance for a projectile is usually derived, as reviewed by Omidvar et al. (2014), reading

$$m_\mathrm{p}\frac{\mathrm{d}v}{\mathrm{d}t} = m_\mathrm{p}g - \overline{\alpha}v^2 - \overline{\beta}v - \overline{\gamma} \tag{4.18}$$

in a generalised form. Here, t is the time and g the acceleration due to gravity. $\overline{\alpha}, \overline{\beta}$ and $\overline{\gamma}$ correspond to forces leading to the projectile deceleration. The term $\overline{\alpha}v^2$ is attributed to inertial stresses in the deforming target material, leading to a deceleration of the projectile. The contribution of a viscous resistance to deformation of the target is modelled by the term $\overline{\beta}v$ and the parameter $\overline{\gamma}$ can be interpreted as a bearing strength of the material, which has to break in order to deform. All forces are assumed to be not depending on the instantaneous penetration depth. In sand penetration experiments, usually $\overline{\beta} = 0$ is assumed, since the term $\overline{\alpha}$ dominates at large impact velocities. Additionally, the influence of the acceleration due to gravity is assumed to be negligible, reducing Eq. (4.18) to the Poncelet equation (Poncelet, 1839), given as

$$m_\mathrm{p}\frac{\mathrm{d}v}{\mathrm{d}t} = -\alpha\pi d_\mathrm{p}^2\rho v^2 - \gamma\pi d_\mathrm{p}^2 Y. \tag{4.19}$$

Here, the parameters $\overline{\alpha}$ and $\overline{\gamma}$ are transformed to dimensionless parameters α and γ, using the impacting sphere diameter d_p, the effective material density ρ and the static ice failure stress $Y_0 = 5.6\,\mathrm{MPa}$ (Tippmann et al., 2013). The effective material density ρ is computed as a function of the layer porosity ψ, and the pore filling ratio ϵ, following

$$\rho = \rho_\mathrm{i}\,(1-\psi) + \rho_\mathrm{w}\epsilon\psi, \tag{4.20}$$

where $\rho_\mathrm{i} = 916.7\,\mathrm{kg\,m^{-3}}$ and $\rho_\mathrm{w} = 999.8\,\mathrm{kg\,m^{-3}}$ are the ice and liquid water density at the freezing point, respectively (Haynes, 2015). According to Omidvar et al. (2014), recent studies suggest that α may not only be attributed to a drag coefficient as usually defined in high Reynolds number airflow, but also to a shear resistance of the granular material modelled proportionally to the dynamic pressure in the medium $\propto \rho v^2$ exerted by the projectile. The contribution of α has therefore been modelled as $\alpha \propto (1 + \eta\mu)$, where μ is an internal friction coefficient of the granular medium, and η is an adjustable constant. In the following, it has not been discerned between a drag and shear resistance term, since they cannot be separately derived from the present experimental data. However, it is hypothesized that larger differences between the parameter α for different ice layers stem mainly from different shear resistances of the ice layer compositions, since the contribution of inertial drag is assumed to be sufficiently captured using the effective density ρ. If Eq. (4.19) is integrated starting from an initial projectile velocity $v = v_\mathrm{p}$ to $v = 0$, the final penetration depth z_c can be computed as

$$z_\mathrm{c} = \frac{m_\mathrm{p}}{2\alpha\pi d_\mathrm{p}^2\rho}\ln(1 + \frac{\alpha\rho v_\mathrm{p}^2}{\gamma Y}). \tag{4.21}$$

This equation is used for fitting the experimental data of different crater depths depending on the impact velocity for all investigated ice layers. As a result, values for α and γ are obtained, which are discussed in the following.

4.3.3 Results and Interpretation of the Impact Crater Depth

In Fig. 4.41, the experimental results for the ice layers generated at the TUBS IWT are shown, where the crater depth is plotted over the impact velocity. It can be observed that the craters are generally deeper for the slushy ice layers generated at positive wet-bulb temperatures (IDs 1,2,3) compared to the harder ice layers (ID 4) generated at negative wet-bulb temperatures. When comparing the ice layers with different heating power supplied to the exposed flat plate (IDs 1,2,3), only a small difference between the crater depth trends is observed at high velocity impacts. Hence, in the positive wet-bulb temperature regime of the present experiments, a larger heating power, which generates more liquid water at the contact between ice layer and substrate, does not lead to a major variation in ice layer strength. Only a small trend is observed at large impact velocities. It can be hypothesized that either the ice layer is saturated with water in all cases, excess melt water is

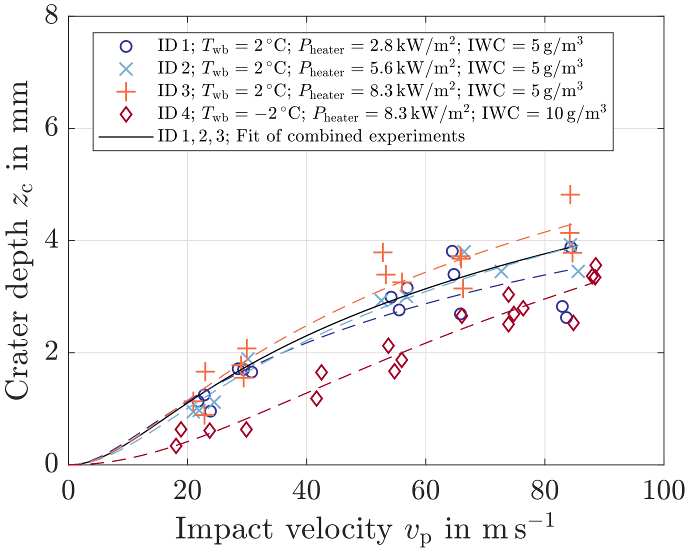

Figure 4.41: Maximum crater depth z_c plotted against the impact velocity for all experiments performed at TUBS IWT. The symbols represent one impact experiment each, and for comparison, the fitted curves of Eq. (4.21) are displayed in the same plot.

transported away, and the heating power has an effect on the strength of the solid ice structure, or the water saturation varies by a small amount, leading to a variation of the ice layer strength at large impact velocities. Judging the finding for the ice layers investigated at TUDA IL as discussed below, liquid water may lubricate particle contacts during penetration, affecting the ice layer strength mainly at high velocities. Hence, the latter hypothesis seems more plausible.

The dashed lines in Fig. 4.41 represent fits of Eq. (4.21) to the data of each ice layer ID, using a non-linear least squares regression algorithm pre-implemented in *MATLAB*. The fits follow the trends of the data well, justifying the first, rather simple modelling approach using the well-known Poncelet equation. Since the exact values of the porosity and water saturation are not known for IDs 1-4, values of $\psi^* = 0.4$ and $\epsilon^* = 0.8$ are chosen, leading to an effective density of $\rho = 870\,\mathrm{kg\,m^{-3}}$. These values correspond to the values of the ice layers manufactured at TUDA IL, which match their strength best, as discussed below. In Table 4.4, the obtained values for α and γ are summarised. Since the measured values for IDs 1-3 are quite similar, the obtained values for α and γ do not differ much from each other. For larger impact velocities, the fitted curves start to diverge and accordingly, a trend can be seen for the parameter α, which decreases for larger heating power. However, the data for IDs 1-3 is still showing a similar trend in contrast to ID 4, and the observed

ID	ψ^*	ϵ^*	α	γ
1	0.4	0.8	0.363	9.40×10^{-3}
2	0.4	0.8	0.274	1.33×10^{-2}
3	0.4	0.8	0.254	1.13×10^{-2}
4	0.4	0.8	0.184	4.46×10^{-2}
$\{1, 2, 3\}$	0.4	0.8	0.293	1.12×10^{-2}

Table 4.4: Summary of the values obtained by fitting Eq. (4.21) to the impact experiments onto ice layers with IDs 1-4 generated at the TUBS IWT.

differences between IDs 1,2 and 3 are small when compared to ID 4. Hence, the corresponding results for IDs 1,2 and 3 are combined for the subsequent analysis. The value $\alpha_{\{1,2,3\}} = 0.293$ is $\approx 60\%$ larger than $\alpha_4 = 0.184$, but it has to be noted that values of ψ^* and ϵ^* are unknown and retroactively estimated for these ice layers. Hence, the effective density ρ of the ice layers is unknown and may differ. The ice layer with ID 4 may be less saturated with melt water than the ones with IDs 1-3, since the ambient temperature is sub freezing and melt water is exclusively generated at the test article - ice layer interface. Hence, the effective density of ID 4 may be lower and since ρ is directly proportional to α in Eq. (4.21), a lower value of ρ would lead to a larger value of α in this case, decreasing the discrepancy between $\alpha_{\{1,2,3\}}$ and α_4.

Since this hypothesis cannot be tested, the need for a measurement method of the ice layer porosity and water saturation in the wind tunnel for future studies is evident. A clear conclusion for the parameters α cannot be drawn yet, since their difference can also stem from a false assumption of the effective density. It is possible that the effective densities also differ by $\approx 60\%$ (e.g. for $\psi = 0.4, \epsilon = 0.8$ vs. $\psi = 0.5, \epsilon = 0.2$), which would lead to similar values of α.

The differences between the parameters γ are more pronounced with $\gamma_4 = 4.46 \times 10^{-2}$ being 4 times as large as $\gamma_{\{1,2,3\}} = 1.12 \times 10^{-2}$. Additionally, the obtained values of γ are independent of the choice of the apparent density. With γ representing an apparent yield strength of the material, the significantly larger value of γ_4 is in line with manual inspections of the ice layers, indicating that ice layers with ID 4 are stronger and not as easily deformed as the others. This behaviour is attributed to stronger, solid inter-particle bonds inside the ice layer generated as the individual particles freeze together during the ice layer accretion. Nevertheless, the absolute values of γ indicate that the apparent yield strength of the ice layer is smaller than the static failure stress of ice by two orders of magnitude. Two reasons may be accountable for this observation. First, the total area of ice that has to break is small since it consists only of individual particle connections. Second, there can be a significant stress concentration at the notch-like geometry of inter-particle connections. Therefore, it is not surprising that the derived strength values of the entire layer are significantly lower than the strength of bulk ice.

In contrast to the ice layers generated at the TUBS IWT, the ice layer porosity and water saturation in the TUDA IL are known precisely. It can be hypothesized that if α and γ are similar for an ice layer generated at the TUBS IWT and in the TUDA IL, their properties affecting their strength are similar, too. As a result, realistic ice layers can be replicated in a laboratory environment, enabling further dedicated experimental studies on sticking and erosion processes to be conducted with significantly less effort and comparable strength values. In Fig. 4.42, the crater depth as a function of different impact velocities is shown for all experiments conducted at TUDA IL. Experiments with the same conditions are repeated five times.

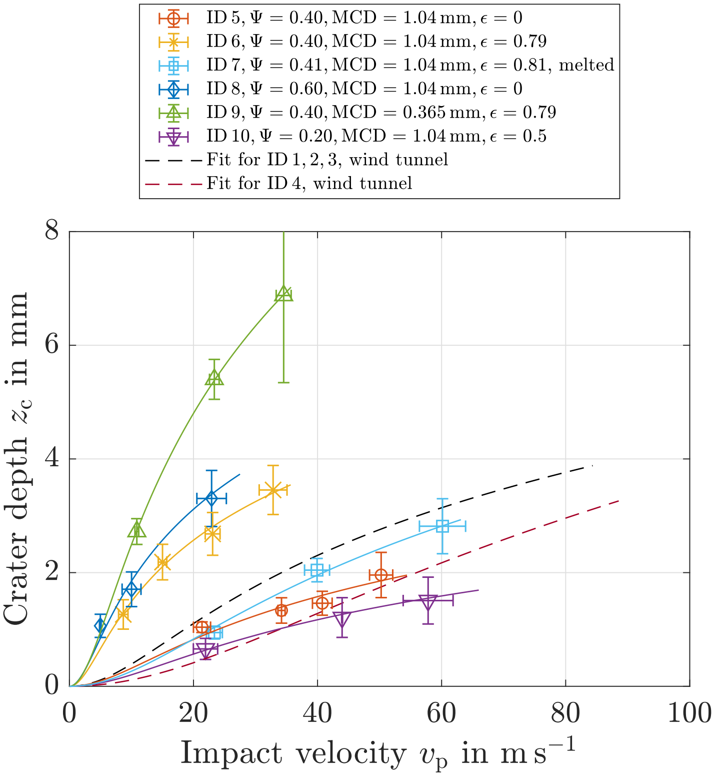

Figure 4.42: Maximum crater depth z_c plotted against the impact velocity for all experiments performed at TUDA IL. The symbols and error bars represent the mean values and one standard deviation of 5 experimental repetitions, respectively. For comparison, the fitted curves of Eq. (4.21) for the experiments conducted at the TUBS IWT are included.

For the sake of clarity, only the mean value and standard deviation of each data group are displayed in the plot as markers and error bars, respectively. For fitting Eq. (4.21) to the data, the individual data points are used. The fitting curves for the experiments in the TUBS IWT with IDs 1-3 and ID 4 are included as black and red dashed lines for comparison. In the following, the graphs are discussed together with the obtained values for α and γ, summarised in Table 4.5. The ice layers for the first three sets of experiments with ID 5-7 were manufactured with a comparatively low porosity of $\psi = 0.4$. It is assumed that this condition represents the individual ice crystals in a realistic ice accretion which are densely stacked due to the nature of an accretion growing by the repeated impact of ice crystals onto it. These manufactured ice layers consist of ice crystals with an average diameter of MCD=$1.04\,\mathrm{mm}$. The ice layer with ID 5 was not filled with water, intending this to be a reference case. Its strength is already in the same order of magnitude as that of the ice layers with IDs 1-4, since the values for the crater depth are located between the black and red dashed lines. This is also reflected in a value for $\gamma_5 = 1.27\times10^{-2}$ close to $\gamma_{\{1,2,3\}} = 1.12\times10^{-2}$. During compression of the ice crystal ensemble in the manufacturing process, it is assumed that the individual crystals are sintered together, forming inter-particle bonds that explain the observed value of γ_5. The value of $\alpha_5 = 0.801$ however, is significantly larger than $\alpha_{\{1,2,3\}} = 0.293$. As discussed above, the penetration resistance characterized by the parameter α can be split into a contribution of resistance due to the inertia of the accelerated medium and a contribution of frictional forces between particles of the medium. Since no liquid water fills the pores of the ice layer, the particle contacts are not lubricated after they are broken out of the ice matrix. Hence, the friction between particles is assumed to be larger, leading to the large value of $\alpha_5 = 0.801$.

ID	ψ	**MCD**	ϵ	α	γ
5	0.40	1.04	0	0.801	1.27×10^{-2}
6	0.40	1.04	0.79	0.387	1.31×10^{-3}
7	0.41	1.04	0.81	0.268	1.76×10^{-2}
8	0.60	1.04	0	0.791	9.74×10^{-4}
9	0.40	0.365	0.79	0.166	1.06×10^{-3}
10	0.20	1.04	0.50	0.615	2.13×10^{-2}

Table 4.5: Summary of the values obtained by fitting Eq. (4.21) to the impact experiments onto artificial ice layers with IDs 5-10 generated at the TUDA IL.

When the ice layer is manufactured the same way but filled with water before the cratering experiment (ID 6), a low value of $\alpha_6 = 0.387$ is obtained again. However, significantly deeper craters in the ice layer are observed, leading to a value of $\gamma_6 = 1.31 \times 10^{-3}$ that is one order of magnitude smaller when compared to $\gamma_5 = 1.27 \times 10^{-2}$. On the one hand, this may be attributed to the process of filling the layer with water near the freezing temperature, which leads to melting of the small inter-particle connections that strengthen the ice layer. On the other hand, the added water may change the ice layer behaviour during penetration due to, e.g. stresses being transmitted by the pore fluid, which may lead to earlier failure of the particle bonds. Either way, the ice layer is weaker and does not replicate the strength of ice layers generated in the TUBS IWT, which are deemed representative of ice layers accreting inside aero-engines.

In order to reach the goal of a representative ice layer strength, warm air is directed through the dry ice layer, partially melting it. Due to capillary forces, the melt water tends to relocate itself to the narrow areas where ice particles are connected in order to reduce its free surface area. After re-freezing the water, the inter-particle bonds are therefore strengthened, while the average layer porosity stays the same. Again, water is filled into the layers manufactured this way (ID 7). Now, the crater depths are comparable with the ones for IDs 1-3 and the values of $\alpha_7 = 0.268$ and $\gamma_7 = 1.76 \times 10^{-2}$ are very similar to $\alpha_{\{1,2,3\}} = 0.293$ and $\gamma_{\{1,2,3\}} = 1.12 \times 10^{-2}$, respectively. This suggests, that the strongly connected matrix of individual ice particles in the ice layers with ID 4 and also the slushy ice layers with IDs 1-3 is a characteristic property. These ice layers can not be replicated by loosely mixing ice particles and water, since it would lead to a softer ice layer.

For the ice layers with IDs 1-3, this means in turn, that a strong matrix is formed during the ice accretion processes. Since the test article is heated and the ambient air is at a wet-bulb temperature of $2\,^{\circ}\mathrm{C}$ in that case, it is possible that the cores of the ice particles impacting the accretion are still at sub freezing temperature. As a sticking ice particle warms up and reaches thermal equilibrium with the wet ice layer being at freezing temperature, a part of the needed energy is supplied by the latent heat of water, freezing near the particle contact with the ice matrix. This process might similarly happen for the ice layers with ID 4, where additional cooling of the ice layer due to an air wet-bulb temperature of $-2\,^{\circ}\mathrm{C}$ occurs.

Further experiments were conducted at TUDA IL to investigate the influence of a higher and lower porosity and a smaller ice crystal size (IDs 8-10). With a high porosity of $\psi = 0.6$, the non-wetted ice layer with ID 8 is very soft to begin with, albeit it remains compact, and no ice particles fall out of it when the ice layer cup is held upside down. As expected, the value of $\gamma_8 = 9.74 \times 10^{-4}$ is low and it is even comparable to the value $\gamma_6 = 1.31 \times 10^{-3}$ of the non-reinforced, wetted ice layer with lower porosity. The value of $\alpha_8 = 0.791$ is comparable to $\alpha_5 = 0.801$ of the other non-wetted ice layer, supporting the hypothesis that large values of α are driven by large friction between particles as a lubricating fluid is missing.

When smaller ice crystals are used to manufacture the ice layer (ID 9), but the solid ice matrix is not reinforced using the warm-air method, the layer is even softer than its counterpart with larger ice crystals (ID 6). This is an important result since the ice layers accreted in the TUBS IWT also consist of smaller ice particles. It seems that the main contributor for increasing the strength of the ice layer is indeed the amount of reinforcement of the particle connections.

In the last series of experiments (ID 10) the ice layer was strongly hardened by wetting a dry ice layer, drawing out the water again and subsequently re-freezing the residual water. As a result, a low porosity of $\psi = 0.2$ was obtained and the pores could only be filled again by 50% with water. The craters in these layers are very small and the obtained value of $\gamma_{10} = 2.13 \times 10^{-2}$ is large, as expected. Although water is present to lubricate the particle contacts, a larger value of $\alpha_{10} = 0.615$ is obtained, possibly originating from the jamming of irregularly shaped particles that are broken out of the solid ice matrix.

By systematically varying the ice layer properties in the TUDA IL, light is shed onto the correlation between the ice layer strength and the ice layer water content, porosity, ice crystal size and most importantly, the connection strength between individual ice particles. Characterizing the ice layer strength with two parameters, α attributed to the ice layer inertial resistance and internal friction and γ, attributed to the apparent yield strength, suggests that liquid water inside the ice layer lubricates the ice particle contacts, reducing the ice layer resistance to deformation. In order to replicate the apparent yield strength of realistic ice layers, the inter-particle connections have to be reinforced appropriately.

4.3.4 Summary

In the present work, a dynamic strength measurement methodology for dry and wet granular ice layers was designed that is based on impacting a nylon sphere onto them. Using the same shooting device, ice layers generated in a wind tunnel under conditions representative of aero-engine icing were impacted, as well as various artificial ice layers generated in a laboratory environment. In both cases, the crater depth was measured using 3D scanning methods.

The well-known Poncelet penetration depth equation, describing the crater depth as a function of the impact velocity, was used to fit the experimental data. As a result, two dimensionless parameters, α and γ, are obtained from each fit, describing the ice layer resistance to penetration due to inertial forces and an apparent yield strength of the ice layer, respectively. Analyzing these parameters, it can be differentiated between soft ice layers generated in the icing wind tunnel at positive wet-bulb temperatures and harder ice layers generated at negative wet-bulb temperatures. Hence, the testing method can be applied to compare wet porous ice layers at different facilities with respect to their strength. It was found that a characteristic property of all ice layers generated in the wind tunnel is a strongly connected matrix of the individual ice particles it contains. For the ice layers generated in the laboratory, the influence of porosity, water saturation, ice matrix strength and ice crystal size on the parameters α and γ was quantified. It was found that adding water leads to lower values of α, suggesting that this can be attributed to lower friction inside the ice layer due to lubricated particle contacts.

Realistic ice layers cannot be replicated in the laboratory by loosely mixing ice particles and water, only by re-enforcing the inter-particle bonds by partly melting the ice matrix and refreezing it again. This suggests that a similar sintering process is taking place in realistic ice layers during their accretion. Finally, the strength of the ice layers generated in the wind tunnel, characterized by α and γ, can be replicated, allowing to perform future studies on ice layers having a realistic strength in a laboratory environment.

5 Summary and Conclusion

Three distinct impact phenomena relevant to aircraft engine icing were studied experimentally in the present work: The ice particle fragmentation after impact onto a dry cold and heated substrate, ice particle sticking and rebound after impact onto a wetted substrate and the crater formation after particle impact onto dry and wet granular ice layers. For each topic, separate experimental setups and methodologies were developed, allowing investigation of the three phenomena beyond the state of the art. The present work contributes to a better understanding of impact phenomena relevant to aircraft engine icing, which may finally help to improve the accuracy of comprehensive ice crystal icing models.

Ice Particle Impact Onto a Dry Substrate In an engine icing scenario, ice particles first impact onto dry surfaces at a sub-freezing temperature. They fragment, and a debris cloud further traverses the engine. In the present work, the ice particle impact onto a dry substrate was investigated since it is of vital importance for accurately modelling the particle size distribution for predicting ice crystal icing.
In an extensive experimental study, the ice particle impact velocity, diameter, temperature, and target temperature were varied systematically, employing a full factorial experimental design. Two key results of the fragmentation process of spherical ice particles were investigated. First, the amount of a small mass of ice fragments, termed residual mass, was observed to adhere to the target and was quantified precisely for the first time. Second, the fragment size distribution was quantified by employing an advanced post processing methodology comprising a multi-object fragment tracking in the recorded high-speed videos and a maximum likelihood volume estimation for the non-spherical fragment shapes.
The residual mass was observed to adhere strongly to the target even at subfreezing temperatures, suggesting that impact induced melting is the cause. Two possible involved mechanisms are identified, namely dissipative heating during the deformation of the particle and subsequently the fragment agglomeration as well as a pressure induced melting point depression. To clarify the contribution of these effects in conclusion, detailed numerical simulations could be conducted in future work, capturing thermodynamic processes like frictional heating at fragment contacts next to the particle fracture mechanics incorporating a detailed equation of state model for ice. Such simulations were out of scope of the present thesis.
At a 5% significance level, all varied parameters were found to significantly influence the amount of adhering residual mass. The residual mass was up to 5% of

the initial particle mass for the investigated parameters and was found to increase for increasing impact velocities, target and particle temperatures. By employing an existing hydrodynamic model of Roisman (2022) for the ice particle impact, characteristic length scales were estimated to model the volume of the residual mass for sub-freezing target temperatures. Despite the low amount of residual mass relative to the initial ice particle mass, it can influence the heat balance of heated substrates drastically when it melts and contributes to the formation of liquid water on heated substrates. The present results have already been incorporated into numerical codes, improving the models for ice accretion prediction. Hereby, the ice mass sticking efficiency was modified in such a way, that 2% of an ice particle mass sticks to the surface even without liquid water present. In future work, the present model for the amount of sticking residual mass can be potentially extended for the description of the heat flux during the collision of an ice particle with a hot solid substrate.

For the investigation of the fragment volume distribution, a doubly truncated power law was fitted to the data employing an adapted maximum-likelihood estimation method. The shape of the fragment volume distribution is characterised by the power-law exponent, also termed fragment distribution parameter. In the present experiments, the fragment distribution parameter is dominated by the particle impact velocity within the investigated parameter range. A temperature variation of the particle and target within a range of $-35\,^{\circ}\mathrm{C}$ to $-5\,^{\circ}\mathrm{C}$ and $-10\,^{\circ}\mathrm{C}$ to $10\,^{\circ}\mathrm{C}$, respectively, showed no significant effect on the fragment volume distribution at a 5% significance level. It was found that the power-law parameter increases with increasing impact velocity, a phenomenon also observed for fragmentation simulations of brittle spheres. This observation may be attributed to the increasing dominance of secondary cracks that form after the initial break-up of the ice particle. Under the premise that all ice fragmentation processes are fractal in nature and thus scale invariant, the present high strain-rate experiments are compared to lower strain-rate fracture of ice floes. An extrapolation of the observed strain rate dependency of the fragment distribution parameter to low strain rates arrives at the fragment distribution parameter reported for the lower strain-rate ice fracture of ice floes. This result suggests that ice fragment size distributions can be described using a unified power-law with a strain-rate dependent fragment distribution parameter.

Ice Particle Impact Onto a Wetted Substrate Accretion of macroscopic ice layers in aircraft engines is initiated with the capture of ice particles in a liquid water film. Since the amount of captured ice particles controls the cooling rate of the liquid film and the surface beneath it, ice particle capture in liquid films is a key phenomenon which has to be understood for the modelling of ice crystal icing.

The dissipation of energy during a particle wall collision and thus, its tendency to stick is usually characterized by the coefficient of restitution, a ratio of the particle velocity after and prior to impact. During impact, mainly viscous forces in the water film, plastic deformation of the ice particle and surface tension forces cause the dissipation of the total energy of the ice particle, which rebounds with a lower velocity. In the present work, the normal and oblique impact of ice spheres onto a dry and wetted wall were studied experimentally to advance the knowledge of phenomena leading to the inception of ice accretion.

Using image processing of the recorded high-speed videos, the coefficient of restitution of spherical ice particles in normal and tangential directions was determined. In the experiments, the particle diameter, impact velocity, impact angle, and temperature were varied next to the water film thickness on the temperature controlled target. The model of Higa et al. (1998) for the normal coefficient of restitution, dedicated to ice particle impacts on a non-wetted ice target, was rewritten to account for the increased stiffness of the present aluminium target. As a result, lower normal coefficients of restitution are predicted, which were also observed in experiments on the dry aluminium target.

Additionally, the rewritten model of Higa et al. (1998) was combined with an existing model of Davis et al. (2002) accounting for an energy dissipation in the liquid layer during particle impact onto a wetted wall. The model predictions for the normal coefficient of restitution agree well with a second experimental data set of normal and inclined ice particle impacts onto a wetted aluminium wall. However, in the investigated Stokes number range, the normal COR is dominated by the dissipation resulting from the plastic deformation of the ice particle. These results are valuable for modelling efforts in aircraft engine icing, since they can explain an under-prediction of the particle capture efficiency as observed by Currie (2020).

For future work, it is proposed to resort to a more advanced force-balance modelling approach like the one of Buck et al. (2018) for the particle deceleration due to the liquid. In this case, the effects of the water surface tension can be captured, which become increasingly important for microscopic ice particles encountered in a realistic aircraft engine icing scenario. Finally, the tangential COR for impacts onto the dry and wetted wall has been discussed, finding the values close to one for the dry impacts and clustering around $0.9 - 0.8$ for the wetted wall impacts. A more detailed study of the dynamic tangential motion of a bouncing or sticking ice particle after impact is left for future work.

Strength Characterization of Granular Ice Layers In an aero-engine icing scenario, ice accretion may form as a porous structure of ice crystals wetted with melt water. For advanced modelling of the ice layer growth and erosion due to impinging ice crystals, it is crucial to have information about the ice layer composition and material properties, which is not available in the present literature. In order to close this research gap, a dynamic strength measurement methodology for dry and wet granular ice layers was designed that is based on impacting a nylon sphere onto them. Using the same shooting device, ice layers generated in a wind tunnel under conditions representative of aero-engine icing were impacted, as well as various artificial ice layers generated in a laboratory environment. In both cases, the crater depth was measured using 3D scanning methods.

The well-known Poncelet penetration depth equation, describing the crater depth as a function of the impact velocity, was used to fit the experimental data. As a result, two dimensionless parameters, α and γ, are obtained from each fit, describing the ice layer resistance to penetration due to inertial forces and apparent yield strength of the ice layer, respectively. Analyzing these parameters, it can be differentiated between soft ice layers generated in the icing wind tunnel at positive wet-bulb temperatures and harder ice layers generated at negative wet-bulb temperatures. Hence, the testing method can be applied to compare wet porous ice layers at different facilities with respect to their strength. It was found that a characteristic property of all ice layers generated in the wind tunnel is a strongly connected matrix of the individual ice particles it consists of. For the ice layers generated in the laboratory, the influence of porosity, water saturation, ice matrix strength and ice crystal size on the parameters α and γ was quantified. It was found that adding water leads to lower values of α, suggesting this is attributed to lower friction inside the ice layer due to lubricated particle contacts.

Realistic ice layers can not be replicated in the laboratory by loosely mixing ice particles and water, only by re-enforcing the inter-particle bonds by partly melting the ice matrix and refreezing it again. This suggests that a similar sintering process is taking place in realistic ice layers during their accretion. The strength of the ice layers generated in the wind tunnel, characterized by α and γ, can be replicated, allowing to perform future studies on ice layers having a realistic strength in a laboratory environment.

Within the scope of this work, significant progress has been made regarding three sub-processes of ice crystal icing in aero-engines. The present results have enhanced the understanding of the ice particle impact on dry, wet and granular substrates. In parts, the results have already been incorporated in predictive numerical tools for ice crystal icing, making them more robust also for an application to possibly disruptive engine technologies in the future.

Bibliography

Alvarez, M., Kreeger, R. E., and Palacios, J. (2019). “Experimental Evaluation of the Impact Behavior of Partially Melted Ice Particles”. *International Journal of Impact Engineering* 123, pp. 70–76. DOI: `10.1016/j.ijimpeng.2018.09.008`.

Andrews, E. and Kim, K.-S. (1998). “Threshold Conditions for Dynamic Fragmentation of Ceramic Particles”. *Mechanics of Materials* 29.3-4, pp. 161–180. DOI: `10.1016/S0167-6636(98)00014-3`.

Anisimov, S., Jedlikowski, A., and Pandelidis, D. (2015). “Frost formation in the cross-flow plate heat exchanger for energy recovery”. *International Journal of Heat and Mass Transfer* 90, pp. 201–217. DOI: `10.1016/j.ijheatmasstransfer.2015.06.056`.

Antonyuk, S., Heinrich, S., Deen, N., and Kuipers, H. (2009). “Influence of liquid layers on energy absorption during particle impact”. *Particuology* 7.4, pp. 245–259. DOI: `10.1016/j.partic.2009.04.006`.

Antonyuk, S., Heinrich, S., Tomas, J., Deen, N. G., Van Buijtenen, M. S., and Kuipers, J. (2010). “Energy absorption during compression and impact of dry elastic-plastic spherical granules”. *Granular Matter* 12.1, pp. 15–47. DOI: `10.1007/s10035-009-0161-3`.

Arakawa, M., Kagi, H., Fernandez-Baca, J. A., Chakoumakos, B. C., and Fukazawa, H. (2011). “The Existence of Memory Effect on Hydrogen Ordering in Ice: The Effect Makes Ice Attractive”. *Geophysical Research Letters* 38.16. DOI: `10.1029/2011GL048217`.

Ashby, M. F. (1989). “Materials selection in conceptual design”. *Materials Science and Technology* 5.6, pp. 517–525. DOI: `10.1179/mst.1989.5.6.517`.

Baehr, H. D. and Stephan, K. (2011). *Heat and Mass Transfer*. Heidelberg: Springer Berlin. DOI: `10.1007/978-3-642-20021-2`.

Bagherifard, S. (2019). “Enhancing the structural performance of lightweight metals by shot peening”. *Advanced Engineering Materials* 21.7, p. 1801140. DOI: `10.1002/adem.201801140`.

Bahaloo, H., Eidevåg, T., Gren, P., Casselgren, J., Forsberg, F., Abrahamsson, P., and Sjödahl, M. (2022). “Ice Sintering: Dependence of Sintering Force on Temperature, Load, Duration, and Particle Size”. *Journal of Applied Physics* 131.2, p. 025109. DOI: `10.1063/5.0073824`.

Bansmer, S. E., Baumert, A., Sattler, S., Knop, I., Leroy, D., Schwarzenboeck, A., Jurkat-Witschas, T., Voigt, C., Pervier, H., and Esposito, B. (2018). "Design, Construction and Commissioning of the Braunschweig Icing Wind Tunnel". *Atmospheric Measurement Techniques* 11.6, pp. 3221–3249. DOI: 10.5194/amt-11-3221-2018.

Barnocky, G. and Davis, R. H. (1988). "Elastohydrodynamic collision and rebound of spheres: experimental verification". *The Physics of Fluids* 31.6, pp. 1324–1329. DOI: 10.1063/1.866725.

Baumert, A. (2019). "Experimental and Numerical Studies on Ice Crystal Icing of Civil Aircraft". PhD thesis. Technische Universität Braunschweig.

Baumert, A., Bansmer, S., Sattler, S., Pervier, H., and Esposito, B. (2016). "Simulating Natural Ice Crystal Cloud Conditions for Icing Wind Tunnel Experiments-A Review on the Design, Commissioning and Calibration of the TU Braunschweig Ice Crystal Generation System". *8th AIAA Atmospheric and Space Environments Conference*, p. 4053. DOI: 10.2514/6.2016-4053.

Blackford, J. R. (2007). "Sintering and Microstructure of Ice: A Review". *Journal of Physics D: Applied Physics* 40.21, R355–R385. DOI: 10.1088/0022-3727/40/21/r02.

Bless, S., Ads, A., Iskander, M., and Omidvar, M. (2020). "Impact and Penetration of a Transparent Cohesive Soil". *AIP Conference Proceedings*. Vol. 2272. AIP Publishing LLC, p. 120002. DOI: 10.1063/12.0000896.

Børvik, T., Dey, S., and Olovsson, L. (2015). "Penetration of Granular Materials by Small-Arms Bullets". *International Journal of Impact Engineering* 75, pp. 123–139. DOI: 10.1016/j.ijimpeng.2014.07.016.

Bräunling, W. J. (2009). "Flugzeugtriebwerke. Grundlagen, Aero-Thermodynamik, ideale und reale Kreisprozesse, Thermische Turbomaschinen, Komponenten, Emissionen und Systeme". DOI: 10.1007/978-3-540-76370-3.

Bravin, M., Strapp, J. W., and Mason, J. (2015). "An Investigation into Location and Convective Lifecycle Trends in an Ice Crystal Icing Engine Event Database". *SAE 2015 International Conference on Icing of Aircraft, Engines, and Structures*. SAE International. DOI: 10.4271/2015-01-2130.

Buck, B. and Heinrich, S. (2019). "Collision dynamics of wet particles: Comparison of literature models to new experiments". *Advanced Powder Technology* 30.12, pp. 3241–3252. DOI: 10.1016/j.apt.2019.09.033.

Buck, B., Lunewski, J., Tang, Y., Deen, N. G., Kuipers, J., and Heinrich, S. (2018). "Numerical investigation of collision dynamics of wet particles via force balance". *Chemical Engineering Research and Design* 132, pp. 1143–1159. DOI: 10.1016/j.cherd.2018.05.014.

Bucknell, A., McGilvray, M., Gillespie, D., Yang, X., Jones, G., and Collier, B. (2019). "ICICLE: A Model for Glaciated & Mixed Phase Icing for Application to Aircraft Engines". *SAE Technical Papers*. DOI: 10.4271/2019-01-1969.

Burchell, M. J. and Johnson, E. (2005). “Impact Craters on Small Icy Bodies Such as Icy Satellites and Comet Nuclei”. *NOTmonthly Notices of the Royal Astronomical Society* 360.2, pp. 769–781. DOI: `10.1111/j.1365-2966.2005.09122.x`.

Burroughs, S. and Tebbens, S. (2001). “Upper-Truncated Power Laws in Natural Systems”. *Pure and Applied Geophysics* 158.4, pp. 741–757. DOI: `10.1007/PL00001202`.

Caccia, F. and Guardone, A. (2023). “Numerical simulations of ice accretion on wind turbine blades: are performance losses due to ice shape or surface roughness?” *Wind Energy Science* 8.3, pp. 341–362. DOI: `10.5194/wes-8-341-2023`.

Cao, Y. and Chen, K. (2010). “Helicopter icing”. *The Aeronautical Journal* 114.1152, pp. 83–90. DOI: `10.1017/S0001924000003559`.

Cao, Y., Tan, W., and Wu, Z. (2018). “Aircraft icing: An ongoing threat to aviation safety”. *Aerospace science and technology* 75, pp. 353–385. DOI: `10.1016/j.ast.2017.12.028`.

Cao, Y., Wu, Z., Su, Y., and Xu, Z. (2015). “Aircraft flight characteristics in icing conditions”. *Progress in Aerospace Sciences* 74, pp. 62–80. DOI: `10.1016/j.paerosci.2014.12.001`.

Carmona, H. A., Guimarães, A. V., Andrade, J. S., Nikolakopoulos, I., Wittel, F. K., and Herrmann, H. J. (2015). “Fragmentation Processes in Two-Phase Materials”. *Physical Review E: Statistical Physics, Plasmas, Fluids, and Related Interdisciplinary Topics* 91.1, p. 012402. DOI: `10.1103/PhysRevE.91.012402`.

Carmona, H. A., Wittel, F. K., Kun, F., and Herrmann, H. J. (2008). “Fragmentation Processes in Impact of Spheres”. *Physical Review E* 77.5, p. 051302. DOI: `10.1103/PhysRevE.77.051302`.

Caudle, W., Pope, A., McNeill, R., and Margason, B. (1967). *The feasibility of rapid soil investigations using high-speed, earth-penetrating projectiles*. Tech. rep. Sandia Corp., Albuquerque, N. Mex.

Charton, V. (2020). “Modélisation de l’accrétion de glace dans les turboréacteurs en conditions cristaux”. PhD thesis. Universite de Toulouse.

Charton, V., Trontin, P., Villedieu, P., and Aouizerate, G. (2019). “Semi-Empirical Modelling of Erosion Phenomena for Ice Crystal Icing Numerical Simulation”. *SAE International Journal of Advances and Current Practices in Mobility* 2.1, pp. 106–114. DOI: `10.4271/2019-01-1967`.

Clauset, A., Shalizi, C. R., and Newman, M. E. J. (2009). “Power-Law Distributions in Empirical Data”. *SIAM Review* 51.4, pp. 661–703. DOI: `10.1137/070710111`.

Cleary, P., Sinnott, M., and Morrison, R. (2008). “DEM prediction of particle flows in grinding processes”. *International Journal for numerical methods in fluids* 58.3, pp. 319–353. DOI: `10.1002/fld.1728`.

Colbeck, S. C. (1995). “Pressure melting and ice skating”. *American Journal of Physics* 63.10, pp. 888–890. DOI: `10.1119/1.18028`.

Combescure, A., Chuzel-Marmot, Y., and Fabis, J. (2011). “Experimental Study of High-Velocity Impact and Fracture of Ice”. *International Journal of Solids and Structures* 48.20, pp. 2779–2790. DOI: `10.1016/j.ijsolstr.2011.05.028`.

Currie, T. C. and Fuleki, D. (2016). “Experimental Results for Ice Crystal Icing on Hemispherical and Double Wedge Geometries at Varying Mach Numbers and Wet Bulb Temperatures”. *8th AIAA Atmospheric and Space Environments Conference*, p. 3740. DOI: 10.2514/6.2016-3740.

Currie, T. C., Fuleki, D., Knezevici, D. C., and MaCleod, J. D. (2013). “Altitude Scaling of Ice Crystal Accretion”. *5th AIAA Atmospheric and Space Environments Conference*, p. 2677. DOI: 10.2514/6.2013-2677.

Currie, T. and Fuleki, D. (2015). *Development and Application of an Impedance-Based Instrument for Measuring the Liquid Fraction and Thickness of Ice Crystal Accretions*. Tech. rep. SAE Technical Paper. DOI: 10.4271/2015-01-2134.

Currie, T. C. (2020). “A physics-based model for predicting warm surface cool-down resulting from particle impingement in ice crystal icing”. *AIAA AVIATION 2020 FORUM*, p. 2829. DOI: 10.2514/6.2020-2829.

Darabi, P., Pougatch, K., Salcudean, M., and Grecov, D. (2009). “A novel coalescence model for binary collision of identical wet particles”. *Chemical Engineering Science* 64.8, pp. 1868–1876. DOI: 10.1016/j.ces.2009.01.017.

Dash, J., Rempel, A., and Wettlaufer, J. (2006). “The physics of premelted ice and its geophysical consequences”. *Reviews of modern physics* 78.3, p. 695. DOI: 10.1103/RevModPhys.78.695.

Davis, D. R. and Ryan, E. V. (1990). “On Collisional Disruption: Experimental Results and Scaling Laws”. *Icarus* 83.1, pp. 156–182. DOI: 10.1016/0019-1035(90)90012-X.

Davis, R. H., Rager, D. A., and Good, B. T. (2002). “Elastohydrodynamic rebound of spheres from coated surfaces”. *Journal of Fluid Mechanics* 468, pp. 107–119. DOI: 10.1017/S0022112002001489.

Davis, R. H., Serayssol, J.-M., and Hinch, E. J. (1986). “The elastohydrodynamic collision of two spheres”. *Journal of Fluid Mechanics* 163, pp. 479–497. DOI: 10.1017/S0022112086002392.

Dean, A., Draguljić, D., and Voss, D. (2017). *Design and Analysis of Experiments*. 2nd ed. 2017. Springer Texts in Statistics. Cham: Springer International Publishing : Imprint: Springer. DOI: 10.1007/978-3-319-52250-0.

Deluca, A. and Corral, Á. (2013). “Fitting and Goodness-of-Fit Test of Non-Truncated and Truncated Power-Law Distributions”. *Acta Geophysica* 61.6, pp. 1351–1394. DOI: 10.2478/s11600-013-0154-9.

Dilley, J. P. (1993). “Energy loss in collisions of icy spheres: Loss mechanism and size-mass dependence”. *Icarus* 105.1, pp. 225–234. DOI: 10.1006/icar.1993.1120.

Dong, H. and Moys, M. (2006). “Experimental study of oblique impacts with initial spin”. *Powder Technology* 161.1, pp. 22–31. DOI: 10.1016/j.powtec.2005.05.046.

Dzyaloshinskii, I. E., Lifshitz, E. M., and Pitaevskii, L. P. (1961). “The general theory of van der Waals forces”. *Advances in Physics* 10.38, pp. 165–209. DOI: 10.1080/00018736100101281.

EASA (2015). *CS 25 Book 1 Appendix P, Annex to Executive Director Decision 2015/008/R of 12 March 2015 Amending Certification Specifications and Acceptable Means of Compliance for Large Aeroplanes CS-25 at Amendment 16*. https://www.easa.europa.eu/document-library/certification-specifications/cs-25-amendment-16.

Eidevåg, T., Thomson, E. S., Sollén, S., Casselgren, J., and Rasmuson, A. (2021). "Collisional damping of spherical ice particles". *Powder Technology* 383, pp. 318–327. DOI: 10.1016/j.powtec.2021.01.025.

Elbaum, M. and Schick, M. (1991). "Application of the theory of dispersion forces to the surface melting of ice". *Physical review letters* 66.13, p. 1713. DOI: 10.1103/PhysRevLett.66.1713.

Ene, A. and Teodosiu, C. (2021). "Studies dealing with defogging and de-icing phenomena on vehicles' windshield: a review". *IOP Conference Series: Earth and Environmental Science*. Vol. 664. 1. IOP Publishing, p. 012071. DOI: 10.1088/1755-1315/664/1/012071.

Ennis, B. J., Tardos, G., and Pfeffer, R. (1991). "A microlevel-based characterization of granulation phenomena". *Powder Technology* 65.1-3, pp. 257–272. DOI: 10.1016/0032-5910(91)80189-P.

FAA (2014). *Title 14 Code of Federal Regulations, Part 25 and 33 Appendix D. Airplane and Engine Certification Requirements in Supercooled Large Drop, Mixed Phase, and Ice Crystal Icing Conditions*. Docket No. FAA-2010-0636; Amendment Nos. 25-140 and 33-34, Published by the Office of the Federal Register, National Archives and Records Administration, Washington, DC, Effective Nov. 4.

Fan, X., Ten, P., Clarke, C., Bramley, A., and Zhang, Z. (2003). "Direct measurement of the adhesive force between ice particles by micromanipulation". *Powder technology* 131.2-3, pp. 105–110. DOI: 10.1016/S0032-5910(02)00339-X.

Farzaneh, M. and Chisholm, W. A. (2022). "Systems for De-Icing Overhead Power Line Conductors and Ground Wires". *Techniques for Protecting Overhead Lines in Winter Conditions: Dimensioning, Icephobic Surfaces, De-Icing Strategies*. Springer, pp. 157–194. DOI: 10.1007/978-3-030-87455-1\textunderscore5.

Feder, J. (2013). *Fractals*. New York, NY: Springer. ISBN: 978-1-4899-2124-6.

Feistel, R. and Wagner, W. (2006). "A New Equation of State for H2O Ice Ih". *Journal of Physical and Chemical Reference Data* 35.2, pp. 1021–1047. DOI: 10.1063/1.2183324.

Flegel, A. B. (2017). "Ice Crystal Icing Research at NASA Glenn Research Center". *9th AIAA Atmospheric and Space Environments Conference*, p. 4085. DOI: 10.2514/6.2017-4085.

Flegel, A. B. (2021). "Ice-Crystal Icing Investigation on a Honeywell Uncertified Research Engine in an Altitude Simulation Icing Facility". *Journal of Turbomachinery* 143.10. DOI: 10.1115/1.4050669.

Franks, F. (2003). "Nucleation of ice and its management in ecosystems". *Philosophical Transactions of the Royal Society of London. Series A: Mathematical, Physical and Engineering Sciences* 361.1804, pp. 557–574. DOI: 10.1098/rsta.2002.1141.

Gammon, P., Kiefte, H., Clouter, M., and Denner, W. (1983). “Elastic constants of artificial and natural ice samples by Brillouin spectroscopy”. *Journal of Glaciology* 29.103, pp. 433–460. DOI: 10.3189/S0022143000030355.

Garwood, K. R. and Research Advisory Group for Aerospace and Development (AGARD) (1995). “AGARD-AR-332 - Recommended practices for the assessment of the effects of atmospheric water ingestion on the performance and operability of gas turbine engines”.

Gloerfeld, M. G. (2022). “Hydrodynamics of Supercooled Drops Encountering Solidification at Various Moments of Impact”. PhD thesis. Technische Universität Darmstadt. DOI: 10.26083/tuprints-00022996.

Gold, L. W. (1977). “Engineering Properties of Fresh-Water Ice”. *Journal of Glaciology* 19.81, pp. 197–212. DOI: 10.3189/S0022143000215608.

Gollwitzer, F., Rehberg, I., Kruelle, C. A., and Huang, K. (2012). “Coefficient of restitution for wet particles”. *Physical Review E* 86.1, p. 011303. DOI: 10.1103/PhysRevE.86.011303.

Gonzato, G., Mulargia, F., and Marzocchi, W. (1998). “Practical Application of Fractal Analysis: Problems and Solutions”. *Geophysical Journal International* 132.2, pp. 275–282. DOI: 10.1046/j.1365-246x.1998.00461.x.

Goodwin, R. V. and Dischinger, D. G. (2014). “Turbofan ice crystal rollback investigation and preparations leading to inaugural ice crystal engine test at NASA PSL-3 test facility”. *6th AIAA Atmospheric and Space Environments Conference*, p. 2895. DOI: 10.2514/6.2014-2895.

Goodwin, R. V. and Fuleki, D. (2016). “Engine Preparation and Instrumentation for the Second Ice Crystal Engine Test at NASA PSL-3 Test Facility”. *8th AIAA Atmospheric and Space Environments Conference*, pp. 13–17. DOI: 10.2514/6.2016-3892.

Grazioli, J., Ghiggi, G., Billault-Roux, A.-C., and Berne, A. (2022). “MASCDB, a database of images, descriptors and microphysical properties of individual snowflakes in free fall”. *Scientific Data* 9.1, p. 186. DOI: 10.1038/s41597-022-01269-7.

Griffith, A. A. (1924). “Theory of rupture”. *Proc. 1st. Int. Cong. Appl. Mech., Delft*, pp. 55–63.

Grzych, M. L. and Mason, J. G. (2010a). “Weather conditions associated with jet engine power loss and damage due to ingestion of ice particles: What we’ve learned through 2009”. *14th Conf. on Aviation, Range and Aerospace Meteorology*.

Grzych, M. L. (2010b). *Avoiding Convective Weather Linked to Ice Crystal Icing Events*. https://www.boeing.com/commercial/aeromagazine/articles/qtr_01_10/5.

Guégan, P., Othman, R., Lebreton, D., Pasco, F., Villedieu, P., Meyssonnier, J., and Wintenberger, S. (2012). “Critical Impact Velocity for Ice Fragmentation”. *Proceedings of the Institution of Mechanical Engineers, Part C: Journal of Mechanical Engineering Science* 226.7, pp. 1677–1682. DOI: 10.1177/0954406211426639.

Guégan, P., Othman, R., Lebreton, D., Pasco, F., Villedieu, P., Meyssonnier, J., and Wintenberger, S. (2011). "Experimental Investigation of the Kinematics of Post-Impact Ice Fragments". *International Journal of Impact Engineering* 38.10, pp. 786–795. DOI: `10.1016/j.ijimpeng.2011.05.003`.

Haggerty, J., Defer, E., De Laat, A., Bedka, K., Moisselin, J.-M., Potts, R., Delanoë, J., Parol, F., Grandin, A., and Divito, S. (2019). "Detecting clouds associated with jet engine ice crystal icing". *Bulletin of the American Meteorological Society* 100.1, pp. 31–40. DOI: `10.1175/BAMS-D-17-0252.1`.

Hartmann, W. K. (1969). "Terrestrial, Lunar, and Interplanetary Rock Fragmentation". *Icarus* 10.2, pp. 201–213. DOI: `10.1016/0019-1035(69)90022-0`.

Hauk, T., Bonaccurso, E., Roisman, I. V., and Tropea, C. (2015). "Ice Crystal Impact onto a Dry Solid Wall. Particle Fragmentation". *Proceedings of the Royal Society A: Mathematical, Physical and Engineering Sciences* 471.2181, p. 20150399. DOI: `10.1098/rspa.2015.0399`.

Hauk, T., Grün, M. von der, Roisman, I. V., and Tropea, C. (2014). "Investigation of the coefficient of restitution of spheres impacting on a water film". *26th Annual Conference on Liquid Atomization and Spray Systems, ILASS – Europe*.

Hauk, T. (2016). "Investigation of the Impact and Melting Process of Ice Particles". PhD thesis. Technische Universität Darmstadt.

Haynes, W. M. (2015). *CRC Handbook of Chemistry and Physics, 95th Edition*. 95th ed. Hoboken: CRC Press. ISBN: 978-1-4822-0867-2.

Hearst, J. and Lynch, C. (1994). "Measurement of in Situ Strength Using Projectile Penetration". *International Journal of Rock Mechanics and Mining Sciences & Geomechanics Abstracts*. Vol. 31. Elsevier, pp. 243–251. DOI: `10.1016/0148-9062(94)90468-5`.

Heißelmann, D., Blum, J., Fraser, H. J., and Wolling, K. (2010). "Microgravity Experiments on the Collisional Behavior of Saturnian Ring Particles". *Icarus* 206.2, pp. 424–430. DOI: `10.1016/j.icarus.2009.08.009`.

Hertz, H. (1882). "Ueber die Berührung fester elastischer Körper." 1882.92, pp. 156–171. DOI: `10.1515/crll.1882.92.156`.

Hessert, R., Bamberg, J., Satzger, W., and Taxer, T. (2008). "Ultrasonic impact treatment for surface hardening of the aero-engine material IN718". *Proceeding ofthe 10th international conference on shot peening ICSP*, pp. 410–415.

Higa, M., Arakawa, M., and Maeno, N. (1996). "Measurements of Restitution Coefficients of Ice at Low Temperatures". *Planetary and Space Science* 44.9, pp. 917–925. DOI: `10.1016/0032-0633(95)00133-6`.

Higa, M., Arakawa, M., and Maeno, N. (1998). "Size Dependence of Restitution Coefficients of Ice in Relation to Collision Strength". *Icarus* 133.2, pp. 310–320. DOI: `10.1006/icar.1998.5938`.

Hobbs, P. V. and Mason, B. (1964). "The sintering and adhesion of ice". *Philosophical Magazine* 9.98, pp. 181–197. DOI: `10.1080/14786436408229184`.

Hunter, S. C. (1957). “Energy absorbed by elastic waves during impact”. *Journal of the Mechanics and Physics of Solids* 5.3, pp. 162–171. DOI: 10.1016/0022-5096(57)90002-9.

Ide, R., Reehorst, A., Ranaudo, R., Mikkelsen, K., and McKnight, R. (1986). “The measurement of aircraft performance and stability and control after flight through natural icing conditions”. *3rd Flight Testing Conference and Technical Display*, p. 9758. DOI: 10.2514/6.1986-9758.

Iveson, S. M., Litster, J. D., Hapgood, K., and Ennis, B. J. (2001). “Nucleation, Growth and Breakage Phenomena in Agitated Wet Granulation Processes: A Review”. *Powder Technology* 117.1-2, pp. 3–39. DOI: 10.1016/S0032-5910(01)00313-8.

Jäckel, R., Gutiérrez-Urueta, G., and Tapia, F. (2021). “A review on Pitot tube icing in aeronautics: Research-design and characterization–future trends”. *Flow Measurement and Instrumentation* 81, p. 102033. DOI: 10.1016/j.flowmeasinst.2021.102033.

Jasinski, W. J., Noe, S. C., Selig, M. S., and Bragg, M. B. (1998). “Wind Turbine Performance Under Icing Conditions”. *Journal of Solar Energy Engineering* 120.1, pp. 60–65. DOI: 10.1115/1.2888048.

Johnson, K. L. (1985). *Contact Mechanics*. Cambridge: Cambridge University Press. ISBN: 0-521-25576-7.

Johnson, N. L. (1949). “Systems of Frequency Curves Generated by Methods of Translation”. *Biometrika* 36.1/2, pp. 149–176. DOI: 10.2307/2332539.

Jorgenson, P. C. E., Veres, J. P., Nili, S., Bommireddy, S. R., and Suder, K. L. (2020). “Analysis of the Honeywell Uncertified Research Engine with Ice Crystal Cloud Ingestion at Simulated Altitudes”. *Journal of Turbomachinery* 142.6. DOI: 10.1115/1.4047187.

Joseph, G., Zenit, R., Hunt, M., and Rosenwinkel, A. (2001). “Particle–wall collisions in a viscous fluid”. *Journal of Fluid Mechanics* 433, pp. 329–346. DOI: 10.1017/S0022112001003470.

Juan Gallego-Juarez, K. G., ed. (2015). *Power Ultrasonics: Applications of High-Intensity Ultrasound*. Cambridge: Woodhead Publishing. DOI: 10.1016/C2013-0-16435-5.

Jung, S., Tiwari, M. K., Doan, N. V., and Poulikakos, D. (2012). “Mechanism of supercooled droplet freezing on surfaces”. *Nature communications* 3.1, p. 615. DOI: 10.1038/ncomms1630.

Kantak, A. A., Galvin, J. E., Wildemuth, D. J., and Davis, R. H. (2005). “Low-velocity collisions of particles with a dry or wet wall”. *Microgravity Science and Technology* 17.1, pp. 18–25. DOI: 10.1007/BF02870971.

Karpen, N., Cuco, A., Kuenstler, D., Bonaccurso, E., Reitter, L. M., Roisman, I. V., and Tropea, C. (2021). “Characterizing Microscopic Ice Particle Impacts onto a Rigid Surface: Wind Tunnel Setup and Analysis”. *AIAA AVIATION 2021 FORUM*. DOI: 10.2514/6.2021-2671.

Kegerreis, J. A., Ruiz-Bonilla, S., Eke, V. R., Massey, R. J., Sandnes, T. D., and Teodoro, L. F. (2022). “Immediate Origin of the Moon as a Post-impact Satellite”. *The Astrophysical Journal Letters* 937.2, p. L40. DOI: 10.3847/2041-8213/ac8d96.

Khanal, M., Schubert, W., and Tomas, J. (2004). “Ball impact and crack propagation–simulations of particle compound material”. *Granular Matter* 5.4, pp. 177–184. DOI: 10.1007/s10035-003-0149-3.

Kharaz, A., Gorham, D., and Salman, A. (2001). “An experimental study of the elastic rebound of spheres”. *Powder Technology* 120.3, pp. 281–291. DOI: 10.1016/S0032-5910(01)00283-2.

Kikuchi, K., Kameda, T., Higuchi, K., Yamashita, A., et al. (2013). “A global classification of snow crystals, ice crystals, and solid precipitation based on observations from middle latitudes to polar regions”. *Atmospheric research* 132, pp. 460–472. DOI: 10.1016/j.atmosres.2013.06.006.

Kingery, W. (1960). “Regelation, surface diffusion, and ice sintering”. *Journal of Applied Physics* 31.5, pp. 833–838. DOI: 10.1063/1.1735704.

Kintea, D. M. (2016). “Hydrodynamics and Thermodynamics of Ice Particle Accretion”. PhD thesis. Technische Universität Darmstadt.

Koch, C. and Cho, Y. (1992). “Nanocrystals by high energy ball milling”. *Nanostructured Materials* 1.3, pp. 207–212. DOI: 10.1016/0965-9773(92)90096-G.

Koszut, J., Boyina, K., Popovic, G., Carpenter, J., Wang, S., and Miljkovic, N. (2022). “Superhydrophobic heat exchangers delay frost formation and reduce defrost energy input of aircraft environmental control systems”. *International Journal of Heat and Mass Transfer* 189, p. 122669. DOI: 10.1016/j.ijheatmasstransfer.2022.122669.

Krijt, S., Güttler, C., Heißelmann, D., Dominik, C., and Tielens, A. G. G. M. (2013). “Energy dissipation in head-on collisions of spheres”. *Journal of Physics D: Applied Physics* 46.43, p. 435303. DOI: 10.1088/0022-3727/46/43/435303.

Kristensen, H., Holm, P., and Schaefer, T. (1985). “Mechanical Properties of Moist Agglomerates in Relation to Granulation Mechanisms Part I. Deformability of Moist, Densified Agglomerates”. *Powder Technology* 44.3, pp. 227–237. DOI: 10.1016/0032-5910(85)85004-X.

Lacagnina, M. (2008). “Ice Crystal Icing”. *Journal of Flight Safety Foundation*. Vol. 3, No. 6, pp. 12–16.

Langham, E. and Mason, B. J.-N. (1958). “The heterogeneous and homogeneous nucleation of supercooled water”. *Proceedings of the Royal Society of London. Series A. Mathematical and Physical Sciences* 247.1251, pp. 493–504. DOI: 10.1098/rspa.1958.0207.

Lausch*, M., Reitter*, L. M., Schremb, M., and Hussong, J. (2023). “Impact of an ice particle onto a rigid substrate: Statistical analysis of the fragment size distribution”. Submitted to: *International Journal of Impact Engineering*, *Joint first authors. DOI: 10.1016/j.ijimpeng.2023.104732.

Lawn, B. (1993). *Fracture of brittle solids*. Cambridge University Press, p. 194. ISBN: 0521401763.

Lawson, R. P., Angus, L. J., and Heymsfield, A. J. (1998). "Cloud particle measurements in thunderstorm anvils and possible weather threat to aviation". *Journal of aircraft* 35.1, pp. 113–121. DOI: 10.2514/2.2268.

Li, Y., Milton, K. A., Brevik, I., Malyi, O. I., Thiyam, P., Persson, C., Parsons, D. F., and Boström, M. (2022). "Premelting and formation of ice due to Casimir-Lifshitz interactions: Impact of improved parameterization for materials". *Physical Review B* 105.1, p. 014203. DOI: 10.1103/PhysRevB.105.014203.

Liang, G. and Mudawar, I. (2016). "Review of mass and momentum interactions during drop impact on a liquid film". *International Journal of Heat and Mass Transfer* 101, pp. 577–599. DOI: 10.1016/j.ijheatmasstransfer.2016.05.062.

Libbrecht, K. G. (2019). "A quantitative physical model of the snow crystal morphology diagram". *arXiv preprint arXiv:1910.09067*.

Libbrecht, K. G. (2005). "The physics of snow crystals". *Reports on progress in physics* 68.4, p. 855. DOI: 10.1088/0034-4885/68/4/R03.

Ma, G., Zhang, Y., Zhou, W., Ng, T.-T., Wang, Q., and Chen, X. (2018a). "The Effect of Different Fracture Mechanisms on Impact Fragmentation of Brittle Heterogeneous Solid". *International Journal of Impact Engineering* 113, pp. 132–143. DOI: 10.1016/j.ijimpeng.2017.11.016.

Ma, G., Zhou, W., Zhang, Y., Wang, Q., and Chang, X. (2018b). "Fractal Behavior and Shape Characteristics of Fragments Produced by the Impact of Quasi-Brittle Spheres". *Powder Technology* 325, pp. 498–509. DOI: 10.1016/j.powtec.2017.11.030.

Ma, J., Liu, D., and Chen, X. (2013). "Experimental study of oblique impact between dry spheres and liquid layers". *Physical Review E* 88.3, p. 033018. DOI: 10.1103/PhysRevE.88.033018.

Makkonen, L. (1987). "Salinity and growth rate of ice formed by sea spray". *Cold Regions Science and Technology* 14.2, pp. 163–171. DOI: 10.1016/0165-232X(87)90032-2.

Malik, Y. A., Bennani, L., Bansmer, S., Trontin, P., and Villedieu, P. (2023). "Experimental and Numerical Investigation of Accretion Inception and Heat Transfer Physics in Ice Crystal Icing". Submitted to: *International Journal of Heat and Mass Transfer*. DOI: 10.2139/ssrn.4385886.

Marconnet, D., Norden, C., and Vidal, L. (2016). *Optimum use of weather radar*. https://safetyfirst.airbus.com/optimum-use-of-weather-radar.

Marston, J., Vakarelski, I. U., and Thoroddsen, S. T. (2012). "Sphere Impact and Penetration into Wet Sand". *Physical Review E* 86.2, p. 020301. DOI: 10.1103/PhysRevE.86.020301.

Mason, J., Strapp, W., and Chow, P. (2006). "The Ice Particle Threat to Engines in Flight". *44th AIAA Aerospace Sciences Meeting and Exhibit*. American Institute of Aeronautics and Astronautics, p. 2. DOI: 10.2514/6.2006-206.

Mason, J. G., Chow, P., and Fuleki, D. M. (2010). “Understanding ice crystal accretion and shedding phenomenon in jet engines using a rig test”. *Turbo Expo: Power for Land, Sea, and Air*. Vol. 43963, pp. 169–178. DOI: `10.1115/GT2010-22550`.

Mitarai, N. and Nori, F. (2006). “Wet Granular Materials”. *Advances in Physics* 55.1-2, pp. 1–45. DOI: `10.1080/00018730600626065`.

Müller, T. and Huang, K. (2016). “Influence of the liquid film thickness on the coefficient of restitution for wet particles”. *Physical Review E* 93.4, p. 042904. DOI: `10.1103/PhysRevE.93.042904`.

Nakamura, A. M. (2017). “Impact Cratering on Porous Targets in the Strength Regime”. *Planetary and Space Science* 149, pp. 5–13. DOI: `10.1016/j.pss.2017.09.001`.

Nakano, R., Hirabayashi, M., Agrusa, H. F., Ferrari, F., Meyer, A. J., Michel, P., Raducan, S. D., Sánchez, P., and Zhang, Y. (2022). “NASA’s Double Asteroid Redirection Test (DART): Mutual Orbital Period Change Due to Reshaping in the Near-Earth Binary Asteroid System (65803) Didymos”. *The Planetary Science Journal* 3.7, p. 148. DOI: `10.3847/PSJ/ac7566`.

Nasr, A., Björnsson, I., Honfi, D., Larsson Ivanov, O., Johansson, J., and Kjellström, E. (2021). “A review of the potential impacts of climate change on the safety and performance of bridges”. *Sustainable and Resilient Infrastructure* 6.3-4, pp. 192–212. DOI: `10.1080/23789689.2019.1593003`.

Newton, I. and Chittenden, N. (1850). *Newton’s principia: The mathematical principles of natural philosophy*. Geo. P. Putnam.

Oliver, M. J. (2014). “Validation Ice Crystal Icing Engine Test in the Propulsion Systems Laboratory at NASA Glenn Research Center”. *AIAA Aviation*, p. 6. DOI: `10.2514/6.2014-2898`.

Omidvar, M., Iskander, M., and Bless, S. (2014). “Response of Granular Media to Rapid Penetration”. *International Journal of Impact Engineering* 66, pp. 60–82. DOI: `10.1016/j.ijimpeng.2013.12.004`.

Palacios, J., Yan, S., Tan, C., and Kreeger, R. E. (2014). “Experimental Measurement of Frozen and Partially Melted Water Droplet Impact Dynamics”. *6th AIAA Atmospheric and Space Environments Conference* 51. DOI: `10.2514/6.2014-3047`.

Pan, H. and Render, P. M. (1996). “Impact Characteristics of Hailstones Simulating Ingestion by Turbofan Aeroengines”. *Journal of Propulsion and Power* 12.3, pp. 457–462. DOI: `10.2514/3.24057`.

Pedregosa, F., Varoquaux, G., Gramfort, A., Michel, V., Thirion, B., Grisel, O., Blondel, M., Prettenhofer, P., Weiss, R., Dubourg, V., Vanderplas, J., Passos, A., Cournapeau, D., Brucher, M., Perrot, M., and Duchesnay, E. (2011). “Scikit-Learn: Machine Learning in Python”. *Journal of Machine Learning Research* 12, pp. 2825–2830.

Petrenko, V. F. and Whitworth, R. W. (1999). *Physics of ice*. Oxford: Oxford University Press.

Pierrat, P., Agrawal, D. K., and Caram, H. S. (1998). “Effect of Moisture on the Yield Locus of Granular Materials: Theory of Shift”. *Powder Technology* 99.3, pp. 220–227. DOI: `10.1016/S0032-5910(98)00111-9`.

Pinzer, B. R. and Schneebeli, M. (2009). “Snow Metamorphism under Alternating Temperature Gradients: Morphology and Recrystallization in Surface Snow”. *Geophysical Research Letters* 36.23. DOI: 10.1029/2009GL039618.

Poncelet, J. V. (1839). *Introduction à La Mécanique Industrielle, Physique Ou Expérimentale*. Thiel.

Presles, B., Debayle, J., and Pinoli, J.-C. (2012). “Size and Shape Estimation of 3-D Convex Objects from Their 2-D Projections: Application to Crystallization Processes”. *Journal of Microscopy* 248.2, pp. 140–155. DOI: 10.1111/j.1365-2818.2012.03658.x.

Ramesh, K., Hogan, J. D., Kimberley, J., and Stickle, A. (2015). “A review of mechanisms and models for dynamic failure, strength, and fragmentation”. *Planetary and Space Science* 107, pp. 10–23. DOI: 10.1016/j.pss.2014.11.010.

Refloch, A., Courbet, B., Murrone, A., Villedieu, P., Laurent, C., Gilbank, P., Troyes, J., Tessé, L., Chaineray, G., Dargaud, J., et al. (2011). “CEDRE software”. *Aerospace Lab* 2, p–1.

Reitter, L., Lohmann, H., Schremb, M., Roisman, I., Hussong, J., and Tropea, C. (2022a). “Impact of an Ice Particle onto a Dry Rigid Substrate: Dynamic Sintering of a Residual Ice Cone”. *Cold Regions Science and Technology* 194, p. 103416. DOI: 10.1016/j.coldregions.2021.103416.

Reitter, L., Malik, Y., Jahn, A., Roisman, I., and Hussong, J. (2023). “Penetration of a solid spherical particle into artificial and natural wet granular ice layers: Dynamic strength characterization”. *International Journal of Impact Engineering*, p. 104791. DOI: 10.1016/j.ijimpeng.2023.104791.

Reitter, L. M., Mayrhofer, A., Tropea, C., and Hussong, J. (2022b). “Experimental Investigation of Normal and Oblique Impact of Ice Particles onto a Wetted Wall”. *AIAA AVIATION 2022 Forum*, p. 3533. DOI: 10.2514/6.2022-3533.

Reitter, L. M., Schremb, M., Lohmann, H., and Tropea, C. (2021). “Experimental Investigation of Ice Particle Impacts onto a Rigid Substrate”. *AIAA AVIATION 2021 FORUM*. DOI: 10.2514/6.2021-2670.

Rioboo, R., Marengo, M., and Tropea, C. (2002). “Time evolution of liquid drop impact onto solid, dry surfaces”. *Experiments in Fluids* 33.1, pp. 112–124. DOI: 10.1007/s00348-002-0431-x.

Roisman, I. V. (2022). “Hydrodynamic Model of a Collision of a Spherical Plastic Ice Particle with a Perfectly Rigid Substrate”. *International Journal of Impact Engineering* 159, p. 104019. DOI: 10.1016/j.ijimpeng.2021.104019.

Rosenberg, R. (2005). “Why is ice slippery?” *Physics Today* 58.12, p. 50.

Ruiz-Suárez, J. (2013). “Penetration of Projectiles into Granular Targets”. *Reports on Progress in Physics* 76.6, p. 066601. DOI: 10.1088/0034-4885/76/6/066601.

Ryerson, C. C. and Gow, A. J. (2000). *Ship superstructure icing: crystalline and physical properties*. Tech. rep. Cold Regions Research and Engineering Laboratory (US).

Samuelsen, E. M. (2018). “Ship-icing prediction methods applied in operational weather forecasting”. *Quarterly Journal of the Royal Meteorological Society* 144.710, pp. 13–33. DOI: 10.1002/qj.3174.

Sarli, B. V., Ozimek, M. T., Atchison, J. A., Englander, J. A., and Barbee, B. W. (2017). “Nasa double asteroid redirection test (dart) trajectory validation and robustness”. *AAS/AIAA Space Flight Mechanics Meeting*. GSFC-E-DAA-TN38510.

Savvateev, A., Budin, A., Kolikov, V., and Rutberg, P. G. (2001). “High-Speed Penetration into Sand”. *International Journal of Impact Engineering* 26.1-10, pp. 675–681. DOI: 10.1016/S0734-743X(01)00132-4.

Schmider, E., Ziegler, M., Danay, E., Beyer, L., and Bühner, M. (2010). “Is it really robust?” *Methodology*. DOI: 10.1027/1614-2241/a000016.

Schremb, M. (2018). “Hydrodynamics and Thermodynamics of Ice Accretion through Impact of Supercooled Large Droplets: Experiments, Simulations and Theory”. PhD thesis. Darmstadt: Technische Universität Darmstadt.

Schremb, M., Malicevic, K., Reitter, L., Roisman, I., and Tropea, C. (2019). *Material Properties of Granular Ice Layers Characterized Using a Rigid-Body-Penetration Method: Experiments and Modeling*. Tech. rep. SAE Technical Paper. DOI: 10.4271/2019-01-2034.

Schubert, H., Herrmann, W., and Rumpf, H. (1975). “Deformation Behaviour of Agglomerates under Tensile Stress”. *Powder Technology* 11.2, pp. 121–131. DOI: 10.1016/0032-5910(75)80037-4.

Schulson, E. M. and Hibler, W. D. (1991). “The Fracture of Ice on Scales Large and Small: Arctic Leads and Wing Cracks”. *Journal of Glaciology* 37.127, pp. 319–322. DOI: 10.3189/S0022143000005748.

Schulson, E. M. and Duval, P. (2009). *Creep and Fracture of Ice*. Cambridge: Cambridge university press.

Schulson, E. M. (2001). “Brittle Failure of Ice”. *Engineering Fracture Mechanics* 68.17, pp. 1839–1887. DOI: 10.1016/S0013-7944(01)00037-6.

Schultz, P. H., Eberhardy, C. A., Ernst, C. M., A’Hearn, M. F., Sunshine, J. M., and Lisse, C. M. (2007). “The Deep Impact Oblique Impact Cratering Experiment”. *Icarus* 191.2, pp. 84–122. DOI: 10.1016/j.icarus.2007.06.031.

Senoner, J.-M., Trontin, P., Reitter, L. M., Karpen, N., Schremb, M., Vargas, M., and Villedieu, P. (2022). “Ice Particle Impact on Solid Walls: Size Modeling of Reemited Fragments”. *International Journal of Impact Engineering*. DOI: 10.1016/j.ijimpeng.2022.104322.

Shazly, M., Prakash, V., and Lerch, B. A. (2009). “High Strain-Rate Behavior of Ice under Uniaxial Compression”. *International Journal of Solids and Structures* 46.6, pp. 1499–1515. DOI: 10.1016/j.ijsolstr.2008.11.020.

Shimaki, Y. and Arakawa, M. (2012). “Low-Velocity Collisions between Centimeter-Sized Snowballs: Porosity Dependence of Coefficient of Restitution for Ice Aggregates Analogues in the Solar System”. *Icarus* 221.1, pp. 310–319. DOI: 10.1016/j.icarus.2012.08.005.

Slater, B. and Michaelides, A. (2019). “Surface premelting of water ice”. *Nature Reviews Chemistry* 3.3, pp. 172–188. DOI: `10.1038/s41570-019-0080-8`.

Strapp, J. W., Schwarzenboeck, A., Bedka, K., Bond, T., Calmels, A., Delanoe, J., Dezitter, F., Grzych, M., Harrah, S., Korolev, A., et al. (2021). “Comparisons of cloud in situ microphysical properties of deep convective clouds to appendix D/P using data from the high-altitude ice crystals-high ice water content and high ice water content-RADAR I flight campaigns”. *SAE International Journal of Aerospace* 14.01-14-02-0007, pp. 127–159. DOI: `10.4271/01-14-02-0007`.

Strapp, J., Korolev, A., Ratvasky, T., Potts, R., Protat, A., May, P., Ackerman, A., Fridlind, A., Minnis, P., Haggerty, J., Riley, J. T., Lilie, L. E., and Isaac, G. (2016). “The high ice water content study of deep convective clouds: Report on science and technical plan”. *Tech. Rep. DOT/FAA/TC-14/31*.

Struk, P. M., Broeren, A. P., Tsao, J.-C., Vargas, M., Wright, W. B., Currie, T., Knezevici, D., and Fuleki, D. (2012). “Fundamental ice crystal accretion physics studies”. *International Conference on Aircraft and Engine Icing and Ground Deicing*. E-18119.

Sutkar, V. S., Deen, N. G., Padding, J. T., Kuipers, J., Salikov, V., Crüger, B., Antonyuk, S., and Heinrich, S. (2015). “A novel approach to determine wet restitution coefficients through a unified correlation and energy analysis”. *AIChE Journal* 61.3, pp. 769–779. DOI: `10.1002/aic.14693`.

Szabo, D. and Schneebeli, M. (2007). “Subsecond Sintering of Ice”. *Applied Physics Letters* 90.15, p. 151916. DOI: `10.1063/1.2721391`.

Tan, Q., Hosseini, S., Seidel-Morgenstern, A., Thévenin, D., and Lorenz, H. (2022). “Modeling ice crystal growth using the lattice Boltzmann method”. *Physics of Fluids* 34.1, p. 013311. DOI: `10.1063/5.0072542`.

Tavares, F. (2022). *Collision May Have Formed the Moon in Mere Hours, Simulations Reveal*. https://www.nasa.gov/feature/ames/lunar-origins-simulations.

Tavares, L. M. (2007). “Chapter 1 Breakage of Single Particles: Quasi-Static”. *Particle Breakage*. Ed. by A. D. Salman, M. Ghadiri, and M. J. Hounslow. Vol. 12. Handbook of Powder Technology. Elsevier Science B.V., pp. 3–68. DOI: `10.1016/S0167-3785(07)12004-2`.

Terry, L. G., Conaway, K., Rebar, J., and Graettinger, A. J. (2020). “Alternative deicers for winter road Maintenance—A Review”. *Water, Air, & Soil Pollution* 231, pp. 1–29. DOI: `10.1007/s11270-020-04773-x`.

Tetteh, E., Loth, E., Neuteboom, M. O., and Fisher, J. (2022). “In-Flight Gas Turbine Engine Icing”. *AIAA Journal* 60.10, pp. 5610–5632. DOI: `10.2514/1.J061523`.

Tippmann, J. D., Kim, H., and Rhymer, J. D. (2013). “Experimentally Validated Strain Rate Dependent Material Model for Spherical Ice Impact Simulation”. *International Journal of Impact Engineering* 57, pp. 43–54. DOI: `10.1016/j.ijimpeng.2013.01.013`.

Tomas, J., Schreier, M., Gröger, T., and Ehlers, S. (1999). “Impact Crushing of Concrete for Liberation and Recycling”. *Powder Technology* 105.1, pp. 39–51. DOI: `10.1016/S0032-5910(99)00116-3`.

Trimble, S. (2013). *GEnx icing issue prompts 747-8, 787 restriction, route withdrawals*. https://www.flightglobal.com/genx-icing-issue-prompts-747-8-787-restriction-route-withdrawals/111810.article.

Trontin, P., Blanchard, G., Kontogiannis, A., and Villedieu, P. (2017). "Description and Assessment of the New ONERA 2D Icing Suite IGLOO2D". *9th AIAA Atmospheric and Space Environments Conference*, p. 3417. DOI: 10.2514/6.2017-3417.

Tsao, J.-C. (2017). "Preliminary Evaluation of Altitude Scaling for Turbofan Engine Ice Crystal Icing". *9th AIAA Atmospheric and Space Environments Conference*, p. 4086. DOI: 10.2514/6.2017-4086.

Tsujido, S., Arakawa, M., Suzuki, A. I., and Yasui, M. (2015). "Ejecta Velocity Distribution of Impact Craters Formed on Quartz Sand: Effect of Projectile Density on Crater Scaling Law". *Icarus* 262, pp. 79–92. DOI: 10.1016/j.icarus.2015.08.035.

Turcotte, D. L. (1997). *Fractals and Chaos in Geology and Geophysics*. Second. Cambridge: Cambridge University Press. DOI: 10.1017/CBO9781139174695.

Uenishi, K., Hasegawa, T., Yoshida, T., Sakauguchi, S., and Suzuki, K. (2019). "Dynamic Fracture and Fragmentation of Ice Materials". *Proceedings of the First International Conference on Theoretical, Applied and Experimental Mechanics*. Ed. by E. E. Gdoutos. Springer International Publishing, pp. 242–243. DOI: 10.1007/978-3-319-91989-8_54.

Uenishi, K., Yoshida, T., Ionescu, I. R., and Suzuki, K. (2018). "Dynamic Fragmentation of Ice Spheres: Two Specific Fracture Patterns". *Procedia Structural Integrity* 13, pp. 670–675. DOI: 10.1016/j.prostr.2018.12.111.

Umbanhowar, P. and Goldman, D. I. (2010). "Granular Impact and the Critical Packing State". *Physical Review E: Statistical Physics, Plasmas, Fluids, and Related Interdisciplinary Topics* 82.1, p. 010301. DOI: 10.1103/PhysRevE.82.010301.

Vanapalli, S., Fredlund, D., Pufahl, D., and Clifton, A. (1996). "Model for the Prediction of Shear Strength with Respect to Soil Suction". *Canadian Geotechnical Journal* 33.3, pp. 379–392. DOI: 10.1139/t96-060.

Vargas, M., Ruggeri, C., Struk, P., Pereira, M., Revilock, D., and Kreeger, R. (2015). "Ice Particle Impacts on a Flat Plate". *SAE Technical Paper Series*. 400 Commonwealth Drive, Warrendale, PA, United States: SAE International. DOI: 10.4271/2015-01-2099.

Vargas, M. M., Ruggeri, C. R., Pereira, M., and Revilock, D. M. (2020). "Ice Particles Impacting on a Flat Plate: Temperature and Velocity Effect". *AIAA AVIATION 2020 FORUM*. DOI: 10.2514/6.2020-2843.

VDI-Wärmeatlas (2009). Springer Berlin, Heidelberg. DOI: 10.1007/978-3-540-32218-4.

Veres, J. P., Jorgenson, P., and Jones, S. M. (2016). "Modeling of Highly Instrumented Honeywell Turbofan Engine Tested with Ice Crystal Ingestion in the NASA Propulsion System Laboratory". *8th AIAA Atmospheric and Space Environments Conference*. DOI: 10.2514/6.2016-3895.

Vogt, C., Laihem, K., and Wiebusch, C. (2008). “Speed of sound in bubble-free ice”. *The Journal of the Acoustical Society of America* 124.6, pp. 3613–3618. DOI: 10.1121/1.2996304.

Wagner, W., Riethmann, T., Feistel, R., and Harvey, A. H. (2011). “New Equations for the Sublimation Pressure and Melting Pressure of H2O Ice Ih”. *Journal of Physical and Chemical Reference Data* 40.4, p. 043103. DOI: 10.1063/1.3657937.

Weeber, A. and Bakker, H. (1988). “Amorphization by ball milling. A review”. *Physica B: Condensed Matter* 153.1, pp. 93–135. DOI: 10.1016/0921-4526(88)90038-5.

Weiss, J. (2001). “Fracture and Fragmentation of Ice: A Fractal Analysis of Scale Invariance”. *Engineering Fracture Mechanics* 68.17, pp. 1975–2012. DOI: 10.1016/S0013-7944(01)00034-0.

Wettlaufer, J. (1999). “Ice surfaces: macroscopic effects of microscopic structure”. *Philosophical Transactions of the Royal Society of London. Series A: Mathematical, Physical and Engineering Sciences* 357.1763, pp. 3403–3425. DOI: 10.1098/rsta.1999.0500.

Wildeman, S., Sterl, S., Sun, C., and Lohse, D. (2017). “Fast Dynamics of Water Droplets Freezing from the Outside In”. *Physical Review Letters* 118.8, p. 084101. DOI: 10.1103/PhysRevLett.118.084101.

Wu, X. and Prakash, V. (2015). “Dynamic Compressive Behavior of Ice at Cryogenic Temperatures”. *Cold Regions Science and Technology* 118, pp. 1–13. DOI: 10.1016/j.coldregions.2015.06.004.

Yarin, A. L. (2006). “Drop impact dynamics: splashing, spreading, receding, bouncing…” *Annu. Rev. Fluid Mech.* 38, pp. 159–192. DOI: 10.1146/annurev.fluid.38.050304.092144.

Yarin, A. L., Roisman, I. V., and Tropea, C. (2017). *Collision Phenomena in Liquids and Solids*. Cambridge: Cambridge University Press. ISBN: 978-1-107-14790-4. DOI: 10.1017/9781316556580.

Yasui, M., Hayama, R., and Arakawa, M. (2014). “Impact Strength of Small Icy Bodies That Experienced Multiple Collisions”. *Icarus* 233, pp. 293–305. DOI: 10.1016/j.icarus.2014.02.008.

Zhao, Q., Liu, Z., Yu, P., Chen, L., and Guan, F. (2022). “Review of Transmission Line Icing and Anti-icing Technologies”. *The proceedings of the 16th Annual Conference of China Electrotechnical Society: Volume II*. Springer, pp. 1224–1232. DOI: 10.1007/978-981-19-1870-4_129.

Zheng, J. and d. Hryciw, R. (2015). “Traditional Soil Particle Sphericity, Roundness and Surface Roughness by Computational Geometry”. *Géotechnique* 65.6, pp. 494–506. DOI: 10.1680/geot.14.P.192.